

**Space-borne observations of meteoric metal
layers in the upper atmosphere**

by

Erin C. M. Dawkins

Submitted in accordance with the requirements for the degree of Doctor of Philosophy

University of Leeds

School of Earth and Environment

October 2014

Declaration of Authorship

The candidate confirms that the work submitted is her own, except where work which has formed part of jointly-authored publications has been included. The contribution of the candidate and the other authors to this work has been explicitly indicated below. The candidate confirms that appropriate credit has been given within the thesis where reference has been made to the work of others.

The work contained in *Chapter 3* and *Chapter 4* forms the basis of a jointly-authored manuscript [Dawkins *et al.*, 2014] which has been accepted for publication in *Geophysical Research Letters*. The candidate performed all the analyses for the paper, and prepared the manuscript with guidance from the co-authors. The candidate developed the K retrieval outlined in the paper, which is based on an original Na retrieval developed by J. Gumbel and J. Hedin. J. Höffner and J. Friedman provided lidar data which is included in the paper.

Dawkins, E. C. M., Plane, J. M. C., Chipperfield, M. P., Feng, W., Gumbel, J., Hedin, J., Höffner, J. and Friedman, J. S. (2014). First global observations of the mesospheric potassium layer. *Geophysical Research Letters*, 41(15), 5653-5661.

The results in *Chapter 5* pertaining to the new potassium chemistry form part of a jointly-authored manuscript [Plane *et al.*, 2014a], which has been published in *Geophysical Research Letters*. Work by the candidate – the observation of the near-global semi-annual seasonality seen in the OSIRIS K data – served as an impetus for this paper, which presents an explanation for the different summertime behaviours of K and Na. The candidate assisted W. Feng in analysing output from WACCM which is used in this paper, and provided comments on the manuscript.

Plane, J. M. C., Feng, W., Dawkins, E., Chipperfield, M. P., Höffner, J., Janches, D., and Marsh, D. R. (2014a). Resolving the strange behavior of extraterrestrial potassium in the upper atmosphere. *Geophysical Research Letters*, 41(13), 4753-4760.

The background section in *Chapter 5* pertaining to the long-term changes to, and sensitivity of, the upper mesosphere/lower thermosphere region forms part of an invited jointly-authored manuscript [Plane et al., 2014b], which has been submitted for publication in *Chemical Reviews*. The candidate performed an extensive literature review and prepared the Section 2.3 ‘Sensitivity to change’, as well as providing comments on the manuscript.

Plane, J. M. C., Feng, W. and Dawkins, E. C. M., (2014b). Mesosphere and Metals: Chemistry and Changes. *Chemical Reviews*. Submitted: 4th September 2014.

This copy has been supplied on the understanding that it is copyright material and no quotation from the thesis may be published without proper acknowledgement.

The right of Erin C. M. Dawkins to be identified as Author of this work has been asserted by her in accordance with the Copyright, Designs and Patents Act 1988.

© The University of Leeds and Erin C. M. Dawkins

Acknowledgements

Firstly, I would like to thank my supervisors – Prof. John Plane and Prof. Martyn Chipperfield – who have mentored and guided me throughout this whole process, and have provided a constant source of inspiration to me. Without their guidance, this work and the production of this thesis would not be possible. I would also like to thank Wuhu Feng who works tirelessly and is always ready to help; he has provided me with a great deal of support over these four years, as well as his friendship. Additionally, I would like to extend special thanks to Jörg Gumbel, Jonas Hedin, Josef Höffner and Jonathan Friedman, all of whom have provided data and a tremendous amount of advice, necessary for the completion of all this work. I would also like to acknowledge the help and advice I have received from the wider satellite retrieval community.

A big thank you to all the friends I have made while at Leeds, with specific mentions to everyone from both of my research groups, everyone on Level 10 and particularly those in 10.126, both past and present. Thank you for all your support and friendship over the years – it has meant a lot. I would also like to give an extra-special mention to Soph, Cat, Ross and Ed, and an extra extra-special mention to Tim. These past few years have had their up's and down's, but I know I have friends for life in all of you.

Finally, I would like to give my sincerest thank you to both my parents and my brother. You have always provided me with unwavering support in whatever I have decided to do and I am eternally indebted.

Abstract

The upper mesosphere/lower thermosphere (MLT) is an important transition region. However, it remains poorly understood relative to other parts of the Earth's atmosphere, largely due to a lack of observations. Metal species, produced by meteoric ablation act as useful tracers of upper atmospheric dynamics and chemistry. Of these meteoric metals, K has long been an enigma. Limited lidar data at extra-tropical latitudes shows that the K layer displays a semi-annual seasonal variation rather than the annual pattern seen in other metals such as Na and Fe. This is a rather surprising feature as both Na and K are Group 1 alkali metals and, thus, should exhibit similar behaviour.

The aim of this thesis was to produce the first near-global K retrieval which could be used to evaluate this unusual behaviour, as well as providing a new dataset with which to test our understanding of the MLT region. The K retrieval uses dayglow measurements of K at ~ 770 nm from the Optical Spectrograph and InfraRed Imager System (OSIRIS) instrument on-board the Odin satellite. This retrieval is shown to be capable of retrieving K number density profiles with a 2 km vertical resolution and a typical peak layer error of $\pm 15\%$. It is shown to compare well with the limited available lidar data.

A first near-global look at the global K layer is presented, which shows that the unusual semi-annual seasonal behaviour is global in extent. The OSIRIS data is used to validate the National Center of Atmospheric Research (NCAR) Whole Atmosphere Community Climate Model (WACCM) modelled K layer; showing good overall agreement and providing support for a new K chemistry scheme which is included in the model. Both OSIRIS and WACCM datasets are used to examine the response of the Na and K metal layers to the 11-year solar cycle. Unlike Na, K shows an anti-correlation with the 11-year solar cycle. The associated temperatures appear to be the predominant source of this anti-correlation. Finally, the response of the WACCM modelled K, Na and Fe layers is examined with respect to longer-term (50-year) changes within the MLT region. K is

the only metal to demonstrate a pronounced response to the recent cooling temperature trend.

Table of Contents

Declaration of Authorship	iii
Abstract	v
Acknowledgments	vii
List of Figures	xiv
List of Tables.....	xxvii
Abbreviations	xxxi
1 INTRODUCTION	1
1.1 Overview	1
1.2 The Earth's upper atmosphere	2
1.2.1 Overall structure	2
1.2.2 The Mesosphere/Lower Thermosphere (MLT)	4
1.2.3 Climate change in the upper atmosphere	13
1.3 The Neutral Metal layers	14
1.3.1 Observations of the meteoric metal layers	14
1.3.2 Meteoroids and the input of cosmic dust into the terrestrial atmosphere	18
1.3.3 The use of the metal layers as tracers	21
1.3.4 The unusual behaviour of potassium	22
1.3.5 Other phenomena related to the metal layers.....	23
1.4 Thesis aims and objectives	25
1.5 Thesis layout.....	26
2 OSIRIS INSTRUMENT AND DATASETS.....	28
2.1 Introduction	28
2.2 Odin satellite.....	29

2.2.1	Mission objectives.....	29
2.2.2	Odin Orbit	29
2.2.3	Satellite Configuration	30
2.3	The OSIRIS instrument	32
2.4	OSIRIS Data Processing.....	36
2.5	Mass Spectrometer Incoherent Scatter model (MSISE-00).....	37
2.6	ECMWF ERA-Interim.....	37
2.7	OSIRIS Na data	38
2.8	NCAR Whole Atmosphere Community Climate Model (WACCM).....	38
2.9	TIMED/SABER instrument.....	39
2.10	Solar F10.7 radio flux	40
2.11	Lidar data	40
3	THE POTASSIUM RETRIEVAL METHODOLOGY.....	41
3.1	Introduction.....	41
3.2	Optimal estimation method.....	41
3.2.1	Introduction	41
3.2.2	The inversion method.....	42
3.3	The forward model	43
3.3.1	Model Description.....	43
3.3.2	Phase function	46
3.3.3	Spectroscopic properties of K	47
3.3.4	Determining the solar irradiance	52
3.3.5	Calculating the local albedo	58
3.3.6	Polarisation.....	60
3.3.7	The forward model resolution	61

3.3.8	Choice of retrieval grid resolution	62
3.3.9	The a priori profile	63
3.3.10	Consideration of limb geometry	65
3.3.11	Forward model input parameters	65
3.4	Measurement of potassium radiance values	66
3.4.1	Extracting K radiance values	67
3.4.2	Quality-control of radiance profiles	70
3.4.3	The Ring effect	72
3.4.4	The weighting and contribution functions	75
3.5	Summary	76
4	ERROR ANALYSIS AND VALIDATION	78
4.1	Introduction	78
4.2	Characterisation of error	78
4.2.1	Measurement noise	79
4.2.2	Forward model error	81
4.2.3	Forward model parameter error	82
4.2.4	Smoothing error	86
4.2.5	Total retrieval error	88
4.3	Ground-truth for K retrievals	90
4.3.1	Comparison with Arecibo (18°N)	91
4.3.2	Comparison with Kühlungsborn lidar (54°N)	102
4.3.3	Comparison with Tenerife lidar data (28°N)	103
4.4	Summary	104
5	THE GLOBAL POTASSIUM LAYER	105
5.1	Introduction	105
5.2	A first look at the near-global K layer	105
5.2.1	Column abundance	105

5.2.2	Monthly mean density profiles.....	108
5.2.3	Peak layer height plots	110
5.2.4	Layer width variations.....	112
5.3	The different behaviours of K and Na	114
5.4	Explanation for the unusual behaviour of K.....	115
5.4.1	Comparison of OSIRIS versus WACCM K column densities.....	120
5.5	The relationship between temperature and K	121
5.5.1	MLT temperature: how well does WACCM compare to SABER?	121
5.5.2	Relationship between temperature & K column density versus latitude.....	126
5.5.3	The differential response of modelled Na and K to temperature	127
5.6	The diurnal behaviour of K.....	131
5.7	Polar depletion of the K layer	137
5.8	Sporadic layer activity of K.....	140
5.8.1	Overview	140
5.8.2	Sporadic K Layers.....	141
5.9	Chapter summary	150
6	SOLAR CYCLE EFFECTS AND LONG-TERM TRENDS.....	153
6.1	Overview.....	153
6.2	Response of the metal layers to the solar cycle	154
6.2.1	The solar cycle and the response of the MLT region	154
6.2.2	Solar cycles 23 and 24.....	155
6.2.3	The solar cycle response of the Na and K metal layers: OSIRIS versus WACCM.....	158
6.3	Longer-term trends in the metal layers	173
6.3.1	Longer-term changes within the MLT region	174
6.3.2	Longer-term trends in the modelled metal layers.....	182

6.4	Chapter summary	207
7	CONCLUSIONS AND RECOMMENDATIONS	209
7.1	Major findings	209
7.2	Recommendations	212
7.3	Concluding remarks	214
8	REFERENCES	215

List of Figures

- Figure 1-1: *The structure of the Earth's atmosphere. Reproduced from <http://www.geogrify.net/GEO1/Lectures/IntroPlanetEarth/FourSpheres.html>.3*
- Figure 1-2: *Mixing ratios of species found in the MLT with (a) no diurnal variation and (b) for species which exhibit significant diurnal variation. Solid lines indicate the daytime profiles and broken lines indicate night-time profiles. Reproduced from Plane [2003].5*
- Figure 1-3: *The ionospheric D, E and F layers. Reproduced from <http://www.fas.org/man/dod-101/navy/docs/es310/propagat/IMG00024.GIF>.7*
- Figure 1-4: *Vertical profiles of the electron and major positive ion densities in the MLT during January 1999 during (a) daytime and (b) night-time. Reproduced from Plane [2003].9*
- Figure 1-5: *Meridional wind vectors as a function of altitude and latitude. A summertime upwelling as a result of gravity wave activity and wintertime downwelling characterised the MLT meridional circulation. Reproduced from Plane [2003].10*
- Figure 1-6: *Summary of the various vertical couplings between atmospheric regions. Reproduced from Summers [1999].12*
- Figure 1-7: *Locations of ground-based metal resonance lidar observatories with significant records on Na, Fe, Ca or Ca⁺ [personal communication].16*
- Figure 1-8: *Example of meteoric input flux (MIF) for Fe. Reproduced from Feng et al., [2014].20*
- Figure 1-9: *Elemental ablation profiles of a 5 μm meteoroid entering at 20 km s⁻¹ as predicted by the Chemical Ablation Model (CABMOD). Reproduced from Plane et al. [2012].21*
- Figure 1-10:** *Three-dimensional plot of the annual variation (altitude, month, density) of metal layers for Ca (from Kühlungsborn (54°N 12°E), Fe (54°N 12°E), K (54°N 12°E)*

<i>and Na (Fort Collins (41°N 105°W). Reproduced from Plane [2003], which is based on Gerding et al. [2000].</i>	23
Figure 2-1: <i>The Odin satellite payload. Reproduced from Murtagh et al. [2002].</i>	30
Figure 2-2: <i>Nominal division of time for Odin astronomy and aeronomy modes. Reproduced from Murtagh et al. [2002].</i>	32
Figure 2-3: <i>Configuration of the OSIRIS instrument. Reproduced from Llewellyn et al. [2004].</i>	33
Figure 2-4: <i>Photograph of the OSIRIS instrument. Reproduced from https://directory.eoportal.org/documents/163813/198303/Odin_Auto1.</i>	33
Figure 2-5: <i>Optics configuration of the OSIRIS instrument. Reproduced from Warshaw et al. [1996].</i>	34
Figure 2-6: <i>Tested mean optical spectrograph sensitivity within the UV/VIS wavelength range. Reproduced from Llewellyn et al. [2004].</i>	35
Figure 2-7: <i>Polarisation response of OSIRIS UV/VIS spectrograph. Reproduced from McLinden et al. [2002].</i>	36
Figure 3-1: <i>Schematic of the limb-viewing geometry in a spherical atmosphere. Adapted from Strong et al. [2002].</i>	44
Figure 3-2: <i>Grotrian diagram to show the $K(D_1)$ and $K(D_2)$ line transitions. Note that the $K(D_2)$ (at $\sim 766.5\text{nm}$) cannot be resolved in the OSIRIS spectra due to its proximity to the O_2 A-band (760-765 nm).</i>	48
Figure 3-3: <i>The variation of the backscatter cross-section of the $K(D_1)$ transition at $\sim 770\text{nm}$ for different temperatures [K]. The positions and relative strengths of the hyperfine split lines is shown for each of the main potassium isotopes (^{39}K and ^{41}K). Reproduced from von Zahn and Höffner [1996].</i>	48
Figure 3-4: <i>$K(D_1)$ line cross-section calculated for $T = 200\text{K}$.</i>	50

Figure 3-5: [Left] The Doppler broadening (units: pm) as a function of altitude (km) for $T = 200$ K. [Right] The Doppler broadening (pm) as a function of temperature (K).51

Figure 3-6: Transmission and self-absorption by the K atom as a function of number density and path length. The line values represent the transmission. When there is no absorption, the transmission is equal to 1. N.B. the path lengths used in the calculation are in units of cm. These are converted to units of km in this, for reasons of clarity only.52

Figure 3-7: The vacuum wavelength solar irradiance spectrum (at 0.01 nm resolution) for wavelength ranges 760-780 nm [top panel] and 760-774 nm [lower panel]. The data is described in Chance and Kurucz [2010] and is available from <http://www.cfa.harvard.edu/atmosphere/links/sao2010.solref.converted>.53

Figure 3-8: Comparison of the K(D_1) Fraunhofer line to the Na solar D lines. The K solar line is much shallower than the Na line, as well as being much narrower. The Na solar D lines have been vertically offset in order for clearer comparison with the K line.54

Figure 3-9: The determination of the absolute solar flux at the Fraunhofer line centre for [top panel] Na and [lower panel] K.55

Figure 3-10: Example of the base of the Na(D_1) line at 589 nm. The solid line represents the calculated solar spectrum, with the circles represent empirical data. Reproduced from McNutt and Mack [1963].56

Figure 3-11: Modelling the solar Fraunhofer line at 770 nm. The Chance and Kurucz spectrum is shown versus the simulated spectrum which is calculated from different values for x_e and A parameters (here, labelled x_eF and AF, respectively).57

Figure 3-12: Sensitivity of the retrieved K number density profile for choice of x_e [top panel, here labelled x_eF] and A parameters [lower panel, labelled AF].58

Figure 3-13: Effect of changing the retrieval grid resolution on the final retrieved K number density profiles for [left] vertical grid resolutions of 1, 1.5, 2, 3 and 4 km and

<i>[right] for resolutions of 2, 3 and 4 km only (omitting profiles for 1 and 1.5 km for clarity).</i>	63
Figure 3-14: <i>The a priori and its associated covariance.</i>	64
Figure 3-15: <i>Illustrating the effect of different a priori (here, referred to as x_a) profiles on final retrieved K number density profiles.</i>	65
Figure 3-16: <i>An OSIRIS limb radiance spectrum at 90 km the relative levels of K at 770 nm and Na at 589 nm.</i>	67
Figure 3-17: <i>OSIRIS limb spectra at tangent heights between 40-104 km at a solar zenith angle of 88.0°.</i>	68
Figure 3-18: <i>Extracting the K emission signal. An example normalised 90 km limb radiance spectrum is presented showing the $K(D_1)$ line at ~ 770 nm.</i>	70
Figure 3-19: <i>Example vertical radiance profile derived from OSIRIS limb spectra.</i>	70
Figure 3-20: <i>Correcting for the Ring effect. Left panel: A example limb radiance for 90 km, which has been normalised by a 40 km, corrected for a variety of RRS contributions (2%, 4%, 6% and 8%). Right panel: The vertical radiance profiles which result from different Ring effect correction values.</i>	74
Figure 3-21: <i>A typical calculated weighting function.</i>	75
Figure 3-22: <i>A typical contribution function.</i>	76
Figure 4-1: <i>Example retrieved number density profile with associated measurement error contribution indicated by horizontal bars.</i>	80
Figure 4-2: <i>Sensitivity of retrieved profile to measurement error, Δy (referred to as dy in plot).</i>	81
Figure 4-3: <i>Sensitivity of the retrieval to a change in the forward model parameters.</i> ...	84

Figure 4-4: <i>Effect of changing the x_e and A parameters (referred to in plot as x_eF and AF, respectively).</i>	85
Figure 4-5: <i>Contributions to the forward model parameter error. Need to understand why temperature results in a negative profile at 83 km.</i>	86
Figure: 4-6: <i>Example averaging kernel.</i>	87
Figure 4-7: <i>Retrieved K number density profile with associated smoothing error contribution indicated by horizontal bars.</i>	88
Figure 4-8: <i>Contributions from different error sources to the final retrieved profile.</i>	89
Figure 4-9: <i>Relative contributions from the different error sources to the final retrieved profile.</i>	90
Figure 4-10: <i>The global lidar network. The K lidars at Arecibo and Kühlungsborn (Kb) are indicated by blue stars. Reproduced from the 4M proposal [J. Plane, pers. comm].</i>	91
Figure 4-11: <i>OSIRIS K profile (16.86°N, 286.09°E, 16th May 2004) versus Arecibo lidar (15th May 2004). [Left panel] OSIRIS single profile in black, all Arecibo lidar profiles in red. [Right panel] OSIRIS single profile in black, mean Arecibo lidar profile in red (± 1 standard deviation, shaded area).</i>	93
Figure 4-12: <i>OSIRIS K profile (16.63°N, 297.95°E, 15th Aug 2007) versus Arecibo lidar (15th Aug 2007). [Left panel] As in figure above (OSIRIS single profile in black, all Arecibo lidar profiles in red). [Right panel] As above (OSIRIS single profile in black, mean Arecibo lidar profile in red (± 1 standard deviation, shaded area)).</i>	93
Figure 4-13: <i>OSIRIS K profile (16.91°N, 300.31°E, 25th Jan 2008) versus Arecibo lidar (23rd Jan 2008). [Left and right panels] As above.</i>	94
Figure 4-14: <i>OSIRIS K profile (16.91°N, 300.31°E, 25th Jan 2008) versus Arecibo lidar (24th Jan 2008). [Left and right panels] As above.</i>	94

Figure 4-15: <i>March 2004. OSIRIS zonal (13-23°N) mean profile (blue, ±1 standard deviation) [17 profiles] versus Arecibo (18°N) (red, ±1 standard deviation) [2 profiles].</i>	95
Figure 4-16: <i>April 2004. As Figure 4-15, but OSIRIS profile [4 profiles] versus Arecibo [1 profile].</i>	96
Figure 4-17: <i>May 2004. As before, but OSIRIS [15 profiles] versus Arecibo [2 profiles].</i>	96
Figure 4-18: <i>June 2004. As before, but OSIRIS [22 profiles] versus Arecibo [3 profiles].</i>	97
Figure 4-19: <i>July 2004. As before, but OSIRIS [12 profiles] versus OSIRIS [6 profiles].</i>	97
Figure 4-20: <i>August 2004. As before, but OSIRIS [4 profiles] versus Arecibo [7 profiles].</i>	98
Figure 4-21: <i>October 2004. As before, but OSIRIS [9 profiles] versus Arecibo [1 profile].</i>	98
Figure 4-22: <i>November 2004. As before, OSIRIS [4 profiles] versus Arecibo [1 profile].</i>	99
Figure 4-23: <i>Comparison of OSIRIS versus Arecibo monthly mean column densities for 2004. The OSIRIS monthly mean column density for 18±5°N is shown in blue, along with the corresponding error of the mean (2σ, vertical bars), while the Arecibo monthly mean column density along with the associated variation (1σ, shaded area) is shown in red.</i>	101
Figure 4-24: <i>Comparison of OSIRIS versus Kühlungsborn monthly mean column densities for 2005. The OSIRIS monthly mean column density for 54±5°N is shown in blue, along with the corresponding error of the mean (2σ, vertical bars), while the Kühlungsborn monthly mean column density along with the associated variation (1σ,</i>	

shaded area) is shown in red. Only data between 75-97 km is used in order to minimise the impact of sporadic K layers on the analysis.102

Figure 4-25: Comparison of OSIRIS versus Tenerife [Fricke-Begemann et al., 2002] monthly mean column densities. The OSIRIS multi-year mean (2004-2011) monthly mean column density for $28\pm 5^\circ N$ is shown in blue, along with the corresponding error of the mean (2σ , vertical bars). The Tenerife data consists of 55 nights of measurements made during Mar-Nov 1999; the monthly mean column density is determined and is shown, along with associated variation (1σ , shaded area), in red. Only OSIRIS data between 75-97 km is used in order to minimise the impact of sporadic K layers on the analysis.103

Figure 5-1: Grid plot of the monthly averaged total OSIRIS K column density zonally averaged in 10° latitude bins for 2004-2013. [Units: $K \text{ atoms cm}^{-2}$].106

Figure 5-2: The K injection flux [units: $K \text{ atoms cm}^{-2} \text{ s}^{-1}$]. From W. Feng (pers. communication).....107

Figure 5-3: OSIRIS K zonal mean monthly mean column density profiles (2004-2013), binned into 30° latitude bands. NB: the OSIRIS latitude coverage only extends up to $82^\circ N$ and $82^\circ S$. Vertical error bars represent the error of the mean ($2\sigma/\sqrt{N}$, where N = no. of observations within the month). Only data from profiles <97 km is considered. [Units: $K \text{ atoms cm}^{-2}$].108

Figure 5-4: Seasonal variation of the OSIRIS mean monthly K layer, as a function of month and altitude, in 30° latitude bins (with the exception of 60 - 82° profiles). White gaps indicate either no OSIRIS coverage, or no available data. [Colour bar units: $K \text{ atoms cm}^{-3}$]......110

Figure 5-5: Centroid altitude profiles of the OSIRIS zonal mean monthly mean K layer (2004-2013), binned into 30° latitude bands. NB: the OSIRIS latitude coverage only extends up to $82^\circ N$ and $82^\circ S$. Vertical error bars represent the error of the mean.112

Figure 5-6: *RMS-width profiles of the OSIRIS zonal mean monthly mean K layer (2004-2013), binned into 30° latitude bands (with the exception of the 60-82° bands). Vertical error bars represent the error of the mean. [Units: km].*..... 114

Figure 5-7: *Global gridded column density retrieved from OSIRIS (2004-2013) binned into 10° latitude bands for, [top panel] K and [lower panel] Na. [Units: metal atoms cm⁻²].*..... 115

Figure 5-8: *Schematic of the main K layer chemistry [reproduced from Plane et al., (2014)]. Pink boxes indicate the ultimate sources and sinks of the K atoms; meteoric ablation being the original source of the K atoms, and polymerisation of K compounds into meteoric smoke particles resulting in removal. The blue boxes indicate reservoir species on the topside of the neutral K layer, green boxes indicate metallic reservoir compounds on the bottom side of the layer. Solid lines indicate chemical reactions and broken lines indicate photochemical reactions.* 116

Figure 5-9: *Schematic of the main Na layer chemistry. Reproduced from Plane [2003].* 119

Figure 5-10: *Comparison of OSIRIS (top panel) and WACCM (lower panel) K column densities, as a function of month and latitude for 2004. [Units: K atoms cm⁻²].* 121

Figure 5-11: *Mean temperature at 90 km for a 6-year period (2004-2009) derived from WACCM-ERA (top panel) and SABER (lower panel) data. [Units: K].* 122

Figure 5-12: *Temperature difference between WACCM-ERA and SABER (WACCM-ERA minus SABER) at 90 km. [Units: K].* 123

Figure 5-13: *SABER observed mean vertical temperature profiles (2004-2009) for selected latitude bands. White gaps indicate no data is available due to a lack of satellite coverage as a result of the alternating yaw cycles outlined in Chapter 2. [Units: K].*.. 125

Figure 5-14: *WACCM-ERA simulated mean vertical temperature profiles (2004-2009) for selected latitude bands. [Units: K].* 126

Figure 5-15: Comparison of the K versus Na zonal mean monthly mean profiles, using WACCM-ERA data (2004-2009) as a function of altitude and latitude. [Units: metal atoms cm^{-3}].	128
Figure 5-16: WACCM-ERA zonal mean monthly mean temperature profiles (2004-2009) as a function of altitude and latitude. [Units: K].	129
Figure 5-17: Correlation analysis between WACCM K (top panel) and Na (lower panel) number densities, and temperature, for all months between 2004-2009, as a function of latitude and altitude. The independent variable is time.	131
Figure 5-18: OSIRIS diurnal difference (a.m. minus p.m) in the K number density as a function of altitude and latitude, for March, July, October and December. Multi-year mean over 2004-2009 period. [Units: K atoms cm^{-3}].	132
Figure 5-19: WACCM diurnal difference (a.m. minus p.m) in the K number density as a function of altitude, for a selection of available latitudes (78°N , 54°N , 18°N and 78°S), for March, July, October and December 2004. [Units: K atoms cm^{-3}].	133
Figure 5-20: Diurnal mean profiles of various WACCM chemical species related to K chemistry as a function of altitude and local time. All profiles are for a low latitude (18°N) location and for 2004.	135
Figure 5-21: Comparison of WACCM-simulated morning (0600 LT) and evening (1800 LT) profiles of the main chemistry species relevant to the neutral K layer chemistry. The concentration is on a log scale for a clear comparison.	137
Figure 5-22: The seasonal mean OSIRIS K layer at latitudes corresponding with the Spitsbergen (78°N), Kuhlungsborn (54°N), Tenerife (28°N) and Arecibo (18°N) lidar stations, all $\pm 5^{\circ}$.	139
Figure 5-23: Comparison of zonal mean OSIRIS K layer column density centred about Spitsbergen (78°N), Kuhlungsborn (54°N), Tenerife (28°N) and Arecibo (18°N), all $\pm 5^{\circ}$. Vertical bars indicate the error of the mean (2σ). [Units: K cm^{-2}].	140

Figure 5-24: *Frequency occurrences of sporadic K layers at Arecibo for a total of 1312 hours of measurements across 147 different nights between Feb 2002 and Dec 2005. Adapted from Delgado [2011].* 142

Figure 5-25: *Example sporadic K layers as detected by OSIRIS (blue, solid line). The standard mean K layer is derived from the associated mean monthly zonal mean ($\pm 5^\circ$ either side of the possible sporadic K layer) profile (red, broken). [Units: K atoms cm^{-3}].* 143

Figure 5-26: *Comparison of sporadic K layer occurrence probability observed at Arecibo [Delgado, 2011] and by OSIRIS.* 144

Figure 5-27: *Percentage occurrence of OSIRIS-detected sporadic K layers as a function of month and latitude (10° bins). The data comprises of the mean percentage occurrence for all years 2004-2011.* 146

Figure 5-28: *Percentage occurrence of OSIRIS-detected sporadic K layers as a function of latitude (10° bins) and longitude (30° bins). The data comprises of the mean percentage occurrence for all years 2004-2011.* 147

Figure 5-29: *Percentage occurrence of sporadic E layers. Reproduced from Chu et al. [2014].* 150

Figure 6-1: *The F10.7 solar flux is shown as a function of time. The most recent solar minimum period (2008-2010) is unusually quiet. Reproduced from: www.swpc.noaa.gov/forecast_verification/Assets/F10/F10ObsPlot.html. Annotated to include solar cycle numbers.* 156

Figure 6-2: *Long-term times series of sun spot observations for the period 1750-2014. Reproduced from <http://solarscience.msfc.nasa.gov/>.* 157

Figure 6-3: *Comparison between the OSIRIS versus WACCM monthly mean global K column densities between 2004-2013. Vertical lines added to help guide the eye. [Units: K atoms cm^{-2}].* 159

Figure 6-4: Comparison between the OSIRIS versus WACCM monthly global K anomalies between 2004-2013. [%, relative to the multi-year monthly mean K column density]. Vertical lines added to guide the eye.160

Figure 6-5: Comparison between the OSIRIS versus WACCM monthly mean global Na column densities between 2004-2013. [Units: Na atoms cm⁻²].161

Figure 6-6: Comparison between the OSIRIS versus WACCM monthly global Na anomalies between 2004-2013 [%, relative to the multi-year monthly mean Na column density].....162

Figure 6-7: Mean monthly F10.7 radio flux for 2004-2013 period.163

Figure 6-8: 11-year solar cycle variation in the SABER temperature data. [Left panel] Mean global SABER temperature profiles for solar maximum (2012, solid red line) versus solar minimum (2008, broken black line), as a function of height. [Right panel] Temperature difference (solar max - solar min) as a function of altitude. [Units: K]. .164

Figure 6-9: Mean monthly global SABER temperatures for 2004-2013, for [top panel] 95 km, [middle] 90 km, and [bottom] 87 km. [Units: K].....165

Figure 6-10 [Top panel] Response of the K layer to the 11-yr solar cycle. All results have been normalised (divided by their means) to allow for easy comparison. The solar flux (represented by the F10.7 radio flux) is shown as the light blue dashed line. The normalised modelled K column density (between 75-105 km) is shown as the solid blue line (with circles), the green line (with triangles) and the red lines (with crosses) represent the K⁺ and KHCO₃ column densities, respectively. [Lower panel] As above, but with an expanded y-axis.171

Figure 6-11: [Top panel] The response of the Na layer and related variables to the 11-yr solar cycle. The normalised modelled Na column density (between 75-105 km) is shown as the solid blue line (with circles), the green line (with triangles) and the red lines (with crosses) represent the Na⁺ and NaHCO₃ column densities, respectively. [Lower panel] As above, but with an expanded y-axis.172

Figure 6-12: Schematic of the long-term changes within the whole atmosphere. Red arrows indicate warming trends, blue arrows indicate cooling, and green arrows indicate regions where the long-term trends are uncertain. Black arrows indicate the sign of changes within the ionospheric electron concentration. Adapted from Lastovicka [2008]. 175

Figure 6-13: Comparison of differential estimates of the mean long-term temperature trend [$K \text{ decade}^{-1}$] within the mesosphere across the tropics, covering four decades of different measurements (1969-2009). The shaded horizontal lines represent the approximate range of trends as revealed within the last two decades. Reproduced from Beig et al. [2011]. 177

Figure 6-14: Comparison of the seasonal PMC frequency of occurrence as observed by the SBUV and SBUV2 instruments, as a function of latitude band ($54\text{-}64^\circ\text{N}$, $64\text{-}74^\circ\text{N}$, $74\text{-}82^\circ\text{N}$). The solid lines represent a linear regression fit. The vertical error bars represent the confidence limits in the individual seasonal mean values based on counting statistics. Reproduced from Shettle et al. [2009]. 180

Figure 6-15: [Left panel] Example decadal temperature trend [$K \text{ decade}^{-1}$] as simulated by WACCM for $30\text{-}60^\circ\text{S}$, across the period 1955-2005. [Right panel] Equivalent plot for decadal O_3 trend. 183

Figure 6-16: Example fitting routine for K [panel a], Na [panel b] and Fe [panel c]. The original metal annual mean column time series is shown as a solid black line [Units: metal atoms cm^{-2}]. The non-linear regression model is shown as the red dashed line. The linear component of the fitted model is shown in a green line. The annual linear trend (across 50-years) indicated in red text [Units: $\% \text{ yr}^{-1}$]. 186

Figure 6-17: Fast-Fourier transform analysis of periodicities of K, Na and Fe WACCM model output. Each inset plot presents an expanded y-axis for clarity. [Units of frequency: yr^{-1}]. 187

Figure 6-18: *Normalised time-series of the K, Na and Fe annual mean column densities for 60-90°N. The normalised time-series is presented as colour-coded broken lines, and the corresponding linear trends are presented as solid lines. The uncertainty associated with each derived linear trend is provided in brackets.*188

Figure 6-19: *As above, but for 30-60°N.*189

Figure 6-20: *As above, but for 0-30°N.*189

Figure 6-21: *As above, but for 0-30°S.*189

Figure 6-22: *As above, but for 30-60°S.*190

Figure 6-23: *As above, but for 60-90°S.*190

Figure 6-24: *Long-term linear trends in modelled metals [top panel], temperature [middle panel] and temperature and MLT region O₃, CO₂ and H₂O. All as a function of latitude band. [Units: % yr⁻¹].*198

Figure 6-25: *A comparison of the long-term response of K (top panel), Na (middle panels) and Fe (lowest panels) across a 50-year period (1955-2005). All profiles show the respective mean metal number density across either 1955-1965 (blue profiles) or 1995-2005 (red profiles), as a function of altitude. The left-hand column indicates zonal mean profiles for 60-90°N, and the right-hand column indicates zonal mean profiles for 60-90°S.*199

Figure 6-26: *Normalised time-series for Na, K and Fe centroid altitude, as a function of latitude. For each plot, the normalised time-series is presented (colour-coded broken lines), along with the associated linear trend (solid lines).*200

Figure 6-27: *Long-term linear trends in the centroid altitude of the WACCM modelled K, Na, and Fe metal layers for 1955-2005, as a function of latitude band. [Units: % yr⁻¹].*206

Figure 6-28: *Long-term linear trends in the RMS-width of the WACCM modelled K, Na, and Fe metal layers for 1955-2005, as a function of latitude band. [Units: % yr⁻¹].*206

List of Tables

Table 1-1: <i>Summary of dominant ions in the D, E and F ionospheric regions. Adapted from Plane (2003).</i>	8
Table 1-2: <i>Estimates of the global cosmic dust input rate to the Earth's atmosphere (deep blue = extra-terrestrial estimate; light blue = middle atmosphere estimate; grey = ice core/deep-sea estimate). Based on Plane [2012].</i>	19
Table 3-1: <i>Calculating the E1 and E2 constants. Reproduced from Chandrasekhar [1960].</i>	46
Table 4-1: <i>List of simultaneous OSIRIS and Arecibo lidar measurements.</i>	92
Table 6-1: <i>Correlation analysis between OSIRIS and WACCM global mean K column densities and the solar F10.7 flux (F10.7) and global mean SABER temperatures at 87 km (T87), 90 km (T90) and 95 km (T95) respectively. All data covers the period 2004-2013. The significance values of each correlation coefficient is indicated in brackets. Results in bold indicate a significance with a confidence level of $\geq 95\%$. Blue cell shading represents a significant anti-correlation. Red cell shading indicates a significant positive correlation. All correlations to 2 d.p.</i>	167
Table 6-2: <i>As above, but for Na.</i>	167
Table 6-3: <i>Linear trends in the WACCM metal layers [Units: $\% \text{ yr}^{-1}$] as a function of latitude band (90°N to 90°S, in 30° intervals). The associated uncertainty is indicated in brackets. This has been calculated by determining the difference in a linear trend which takes into account the solar cycle contribution (as used here) and a simple first-order polynomial fit. Positive trends are indicated by red shading whilst negative trends are indicated by blue shading. All values are provided to 3 d.p.</i>	191
Table 6-4: <i>Summary of derived linear trends for the metals and associated variables, within the 50-year WACCM time-series, as a function of latitude band. The associated uncertainties are given in brackets. As before, negative trends are colour-coded blue, while positive trends are shaded red. All values provided to 3 d.p.</i>	193

Table 6-5: <i>Correlations between temperature (at 87, 90, and 95 km) and stratospheric and mesospheric O₃, and MLT region CO₂ and H₂O. All simulated by WACCM. All to 3 d.p.</i>	194
Table 6-6: <i>Correlation coefficients between the metals and various related parameters. The significance values are indicated in brackets. Red shading indicates significant (>95% confidence) positive correlations, blue shading indicates significant negative correlations. All to 3 d.p.</i>	196
Table 6-7: <i>Long-term linear trends in the centroid altitude of the metal layers, as a function of latitude band [units: % yr⁻¹]. Associated uncertainties are provided in brackets. All to 3 d.p.</i>	201
Table 6-8: <i>Summary of correlations between the metal layer centroid altitudes and temperature and relevant chemical species. The associated significance values are provided in brackets. All those significant at the >95% level are shaded and in bold.</i> 202	
Table 6-9: <i>Long-term linear trends in the RMS-width of the metal layers, as a function of latitude band [units: % yr⁻¹]. Associated uncertainties are provided in brackets. All to 3 d.p.</i>	204
Table 6-10: <i>Summary of correlations between the metal layer centroid altitudes and temperature and relevant chemical species. The associated significance values are provided in brackets. All those significant at the >95% level are shaded and in bold. All to 3 d.p.</i>	204

Abbreviations

AIM	<u>A</u> eronomy of <u>I</u> ce in the <u>M</u> esosphere
albrat	<u>al</u> bedo <u>rat</u> io
AZ	<u>AZ</u> imuth angle
CABMOD	<u>C</u> hemical <u>AB</u> lation <u>MO</u> del
CCD	<u>C</u> harge <u>C</u> oupled <u>D</u> evice
CCN	<u>C</u> loud <u>C</u> ondensation <u>N</u> uclei
CESM	<u>C</u> ommunity <u>E</u> arth <u>S</u> ystem <u>M</u> odel
CIRA	<u>C</u> ommittee on <u>S</u> pace <u>R</u> esearch <u>I</u> nternational <u>R</u> eference <u>A</u> tmosphere
CNES	<u>C</u> entre <u>N</u> ational d' <u>E</u> tudes <u>S</u> patiales
COSMIC	<u>C</u> onstellation <u>O</u> bserving <u>S</u> ystem for <u>M</u> eteorology, <u>I</u> onosphere and <u>C</u> limate
COSPAR	<u>C</u> ommittee on <u>S</u> P <u>A</u> ce <u>R</u> esearch
CSA	<u>C</u> anadian <u>S</u> pace <u>A</u> gency
E-UV	<u>E</u> xtrême <u>U</u> ltra <u>V</u> iolet
ECMWF	<u>E</u> uropean <u>C</u> entre for <u>M</u> edium- <u>R</u> ange <u>W</u> eather <u>F</u> orecasts
Envisat	<u>E</u> nvironmental <u>sat</u> ellite
E_s	sporadic <i>E</i>
ESA	<u>E</u> uropean <u>S</u> pace <u>A</u> gency
FFT	<u>F</u> ast <u>F</u> ourier <u>T</u> ransform
FOV	<u>F</u> ield- <u>of</u> - <u>V</u> iew
FWHM	<u>F</u> ull- <u>W</u> idth <u>H</u> alf- <u>M</u> aximum
GOMOS	<u>G</u> lobal <u>O</u> zone <u>M</u> onitoring by <u>O</u> ccultation of <u>S</u> tars

IR	<u>I</u> n <u>f</u> r <u>a</u> - <u>R</u> ed
K _s	sporadic K
LIDAR	<u>L</u> i <u>g</u> h <u>t</u> <u>D</u> e <u>t</u> e <u>c</u> t <u>i</u> o <u>n</u> <u>A</u> n <u>d</u> <u>R</u> a <u>n</u> g <u>i</u> n <u>g</u> , hereafter referred to as 'lidar'
LF	<u>L</u> o <u>w</u> <u>F</u> re <u>q</u> u <u>e</u> n <u>c</u> y
LOS	<u>L</u> i <u>n</u> e- <u>o</u> f- <u>S</u> i <u>g</u> h <u>t</u>
LT	<u>L</u> o <u>c</u> a <u>l</u> <u>T</u> i <u>m</u> e
MIF	<u>M</u> e <u>t</u> e <u>o</u> r <u>i</u> c <u>I</u> n <u>p</u> u <u>t</u> <u>F</u> u <u>n</u> c <u>t</u> i <u>o</u> n
MLT	upper <u>M</u> e <u>s</u> o <u>s</u> p <u>h</u> e <u>r</u> e- <u>L</u> o <u>w</u> e <u>r</u> <u>T</u> h <u>e</u> r <u>m</u> o <u>s</u> p <u>h</u> e <u>r</u> e region
MPP	<u>M</u> u <u>l</u> t <u>i</u> - <u>P</u> i <u>n</u> n <u>e</u> d <u>P</u> h <u>a</u> s <u>e</u>
MSISE	<u>M</u> a <u>s</u> s <u>S</u> p <u>e</u> c <u>t</u> r <u>o</u> m <u>e</u> t <u>e</u> r - <u>I</u> n <u>c</u> o <u>h</u> e <u>r</u> e <u>n</u> t <u>S</u> c <u>a</u> t <u>t</u> e <u>r</u> <u>E</u> x <u>t</u> e <u>n</u> s <u>i</u> o <u>n</u>
Na _s	sporadic Na
NASA	<u>N</u> a <u>t</u> i <u>o</u> n <u>a</u> l <u>A</u> e <u>r</u> o <u>n</u> a <u>t</u> i <u>c</u> s <u>a</u> n <u>d</u> <u>S</u> p <u>a</u> c <u>e</u> <u>A</u> d <u>m</u> i <u>n</u> i <u>s</u> t <u>r</u> a <u>t</u> i <u>o</u> n
NH	<u>N</u> o <u>r</u> t <u>h</u> e <u>r</u> n <u>H</u> e <u>m</u> i <u>s</u> p <u>h</u> e <u>r</u> e
NIST	<u>N</u> a <u>t</u> i <u>o</u> n <u>a</u> l <u>I</u> n <u>s</u> t <u>i</u> t <u>u</u> t <u>e</u> o <u>f</u> <u>S</u> t <u>a</u> n <u>d</u> a <u>r</u> d <u>s</u> <u>a</u> n <u>d</u> <u>T</u> e <u>c</u> h <u>n</u> o <u>l</u> o <u>g</u> y
NLC	<u>N</u> o <u>c</u> t <u>i</u> l <u>u</u> c <u>e</u> n <u>t</u> <u>C</u> l <u>o</u> u <u>d</u>
NRL	<u>N</u> a <u>v</u> a <u>l</u> <u>R</u> e <u>s</u> e <u>a</u> r <u>c</u> h <u>L</u> a <u>b</u> o <u>r</u> a <u>t</u> o <u>r</u> y
NSERC	<u>N</u> a <u>t</u> u <u>r</u> a <u>l</u> <u>S</u> c <u>i</u> e <u>n</u> c <u>e</u> s <u>a</u> n <u>d</u> <u>E</u> n <u>g</u> i <u>n</u> e <u>e</u> r <u>i</u> n <u>g</u> <u>R</u> e <u>s</u> e <u>a</u> r <u>c</u> h <u>C</u> o <u>n</u> c <u>i</u> l
OSIRIS	<u>O</u> p <u>t</u> i <u>c</u> a <u>l</u> <u>S</u> p <u>e</u> c <u>t</u> r <u>o</u> g <u>r</u> a <u>p</u> h <u>a</u> n <u>d</u> <u>I</u> n <u>f</u> r <u>a</u> <u>R</u> e <u>d</u> <u>I</u> m <u>a</u> g <u>e</u> r <u>S</u> y <u>s</u> t <u>e</u> m
PDC	<u>P</u> a <u>r</u> a <u>l</u> l <u>e</u> l <u>D</u> a <u>t</u> a <u>C</u> e <u>n</u> t <u>e</u> r
PMC	<u>P</u> o <u>l</u> a <u>r</u> <u>M</u> e <u>s</u> o <u>s</u> p <u>h</u> e <u>r</u> i <u>c</u> <u>C</u> l <u>o</u> u <u>d</u>
PMSE	<u>P</u> o <u>l</u> a <u>r</u> <u>M</u> e <u>s</u> o <u>s</u> p <u>h</u> e <u>r</u> i <u>c</u> <u>S</u> u <u>m</u> m <u>e</u> r <u>E</u> c <u>h</u> o <u>e</u> s
PSC	<u>P</u> o <u>l</u> a <u>r</u> <u>S</u> t <u>r</u> a <u>t</u> o <u>s</u> p <u>h</u> e <u>r</u> i <u>c</u> <u>C</u> l <u>o</u> u <u>d</u>
QC	<u>Q</u> u <u>a</u> l <u>i</u> t <u>y</u> - <u>C</u> o <u>n</u> t <u>r</u> o <u>l</u>
RMS	<u>R</u> o <u>o</u> t- <u>M</u> e <u>a</u> n- <u>S</u> q <u>u</u> a <u>r</u> e
RRS	<u>R</u> o <u>t</u> a <u>t</u> i <u>o</u> n <u>a</u> l <u>R</u> i <u>n</u> g <u>S</u> c <u>a</u> t <u>t</u> e <u>r</u> i <u>n</u> g
SABER	<u>S</u> o <u>u</u> n <u>d</u> i <u>n</u> g o <u>f</u> t <u>h</u> e <u>A</u> t <u>m</u> o <u>s</u> p <u>h</u> e <u>r</u> e u <u>s</u> i <u>n</u> g <u>B</u> r <u>o</u> a <u>d</u> b <u>a</u> n <u>d</u> <u>E</u> m <u>i</u> s <u>s</u> i <u>o</u> n <u>R</u> a <u>d</u> i <u>o</u> m <u>e</u> t <u>r</u> y
SCIAMACHY	<u>S</u> c <u>a</u> n <u>n</u> i <u>n</u> g <u>I</u> m <u>a</u> g <u>i</u> n <u>g</u> <u>A</u> b <u>s</u> o <u>r</u> p <u>t</u> i <u>o</u> n <u>s</u> p <u>e</u> c <u>t</u> r <u>o</u> m <u>e</u> t <u>e</u> r f <u>o</u> r <u>A</u> t <u>m</u> o <u>s</u> p <u>h</u> e <u>r</u> i <u>c</u>

	<u>C</u> <u>H</u> <u>a</u> <u>r</u> <u>t</u> <u>o</u> <u>g</u> <u>r</u> <u>a</u> <u>p</u> <u>h</u> <u>y</u>
s.f.u.	<u>s</u> <u>o</u> <u>l</u> <u>a</u> <u>r</u> <u>f</u> <u>l</u> <u>u</u> <u>x</u> <u>u</u> <u>n</u> <u>i</u> <u>t</u> <u>s</u>
SH	<u>S</u> <u>o</u> <u>u</u> <u>t</u> <u>h</u> <u>e</u> <u>r</u> <u>n</u> <u>H</u> <u>e</u> <u>m</u> <u>i</u> <u>s</u> <u>p</u> <u>h</u> <u>e</u> <u>r</u> <u>e</u>
SMR	<u>S</u> <u>u</u> <u>b</u> - <u>M</u> <u>i</u> <u>l</u> <u>l</u> <u>i</u> <u>m</u> <u>e</u> <u>t</u> <u>r</u> <u>e</u> <u>R</u> <u>a</u> <u>d</u> <u>i</u> <u>o</u> <u>m</u> <u>e</u> <u>t</u> <u>e</u> <u>r</u>
SNSB	<u>S</u> <u>w</u> <u>e</u> <u>d</u> <u>i</u> <u>s</u> <u>h</u> <u>N</u> <u>a</u> <u>t</u> <u>i</u> <u>o</u> <u>n</u> <u>a</u> <u>l</u> <u>S</u> <u>p</u> <u>a</u> <u>c</u> <u>e</u> <u>B</u> <u>o</u> <u>a</u> <u>r</u> <u>d</u>
SOFIE	<u>S</u> <u>o</u> <u>l</u> <u>a</u> <u>r</u> <u>O</u> <u>cc</u> <u>u</u> <u>l</u> <u>t</u> <u>a</u> <u>t</u> <u>i</u> <u>o</u> <u>n</u> <u>f</u> <u>o</u> <u>r</u> <u>I</u> <u>c</u> <u>e</u> <u>E</u> <u>x</u> <u>p</u> <u>e</u> <u>r</u> <u>i</u> <u>m</u> <u>e</u> <u>n</u> <u>t</u>
SSC	<u>S</u> <u>w</u> <u>e</u> <u>d</u> <u>i</u> <u>s</u> <u>h</u> <u>S</u> <u>p</u> <u>a</u> <u>c</u> <u>e</u> <u>C</u> <u>o</u> <u>r</u> <u>p</u> <u>o</u> <u>r</u> <u>a</u> <u>t</u> <u>i</u> <u>o</u> <u>n</u>
SZA	<u>S</u> <u>o</u> <u>l</u> <u>a</u> <u>r</u> <u>Z</u> <u>e</u> <u>n</u> <u>i</u> <u>t</u> <u>h</u> <u>A</u> <u>n</u> <u>g</u> <u>l</u> <u>e</u>
TIMED	<u>T</u> <u>h</u> <u>e</u> <u>r</u> <u>m</u> <u>o</u> <u>s</u> <u>p</u> <u>h</u> <u>e</u> <u>r</u> <u>e</u> <u>I</u> <u>o</u> <u>n</u> <u>o</u> <u>s</u> <u>p</u> <u>h</u> <u>e</u> <u>r</u> <u>e</u> <u>M</u> <u>e</u> <u>s</u> <u>o</u> <u>s</u> <u>p</u> <u>h</u> <u>e</u> <u>r</u> <u>e</u> <u>E</u> <u>n</u> <u>e</u> <u>r</u> <u>g</u> <u>e</u> <u>t</u> <u>i</u> <u>c</u> <u>s</u> <u>a</u> <u>n</u> <u>d</u> <u>D</u> <u>y</u> <u>n</u> <u>a</u> <u>m</u> <u>i</u> <u>c</u> <u>s</u>
TOA	<u>T</u> <u>o</u> <u>p</u> - <u>o</u> <u>f</u> - <u>A</u> <u>t</u> <u>m</u> <u>o</u> <u>s</u> <u>p</u> <u>h</u> <u>e</u> <u>r</u> <u>e</u>
TOMS	<u>T</u> <u>o</u> <u>t</u> <u>a</u> <u>l</u> <u>O</u> <u>z</u> <u>o</u> <u>n</u> <u>e</u> <u>M</u> <u>a</u> <u>p</u> <u>p</u> <u>i</u> <u>n</u> <u>g</u> <u>S</u> <u>p</u> <u>e</u> <u>c</u> <u>t</u> <u>r</u> <u>o</u> <u>m</u> <u>e</u> <u>t</u> <u>e</u> <u>r</u>
UARS	<u>U</u> <u>p</u> <u>p</u> <u>e</u> <u>r</u> <u>A</u> <u>t</u> <u>m</u> <u>o</u> <u>s</u> <u>p</u> <u>h</u> <u>e</u> <u>r</u> <u>e</u> <u>R</u> <u>e</u> <u>s</u> <u>e</u> <u>a</u> <u>r</u> <u>c</u> <u>h</u> <u>S</u> <u>a</u> <u>t</u> <u>e</u> <u>l</u> <u>l</u> <u>i</u> <u>t</u> <u>e</u>
UV	<u>U</u> <u>l</u> <u>t</u> <u>r</u> <u>a</u> - <u>V</u> <u>i</u> <u>o</u> <u>l</u> <u>e</u> <u>t</u>
VIS	<u>V</u> <u>I</u> <u>S</u> <u>i</u> <u>b</u> <u>l</u> <u>e</u>

1 INTRODUCTION

1.1 Overview

The presence of neutral metal atoms in the Earth's upper atmosphere has been known for a long time. Slipher [1929] was the first to report that radiation measured in the nightglow spectrum at 589 nm was due to the sodium ($3^2P_J-3^2S_{1/2}$) transition and the source was located within the Earth's atmosphere. Since then, similar observations have raised a number of important questions regarding the presence of neutral metal atoms in the upper atmosphere. As outlined in Plane [2003], these include:

- Why do the metals appear as layers of neutral metal atoms at about 90 km?
- Why are these layers only a few kilometres thick?
- Why is the relative abundance of the metals in the layers quite different from their relative abundances in common types of meteorites?
- How can the different seasonal behaviour of the metals be explained?
- What is the source of metal atoms from which sudden or sporadic layers form, often explosively?
- How do dynamical processes, such as atmospheric gravity waves and tides, affect the chemistry that governs the metal layers?
- Finally, do the metal layers act as sensitive indicators of climate change in the mesosphere, either directly or through their relationship with noctilucent clouds, and do the metals have any impact in the stratosphere and troposphere?

The upper atmospheric abundance of a number of meteoric metals has previously been measured using ground based lidar (Na, Fe, K, Ca and Ca^+) [e.g. Megie and Blamont, 1977; Alpers *et al.*, 1990; Höffner and Lübken, 2004; Chu *et al.*, 2011; Raizada *et al.*, 2012] and satellite measurements (Na, Mg) [e.g. Gumbel *et al.*, 2007; Langowski *et al.*, 2014a,b]. To date, only relatively spatially sparse measurements of potassium (K) have

been measured using lidar, but they indicate that potassium displays a seasonality quite unlike the other metals, which cannot currently be explained [e.g. Eska *et al.*, 1999; Delgado *et al.*, 2006].

The main purpose of the work described in this thesis is to derive upper atmospheric density profiles for K using the Optical Spectrograph InfraRed Imager System (OSIRIS) ultraviolet/visible spectrometer on board the Odin satellite, and to investigate the latitudinal extent of this unusual seasonality and associated phenomena. This chapter provides an introduction to the subject. In Section 1.2, a brief overview is provided of the chemistry and dynamics of the Earth's upper atmosphere. The neutral metal layers are introduced and discussed in Section 1.3. The specific aims and objectives of this thesis are presented in Section 1.4, and finally, the thesis layout is outlined in Section 1.5.

1.2 The Earth's upper atmosphere

1.2.1 Overall structure

The overall structure of the Earth's atmosphere up to 120 km is shown in Figure 1-1. It is divided into four distinct layers: the troposphere, the stratosphere, the mesosphere and the thermosphere based on whether the lapse rate (rate of change in temperature with altitude) is positive or negative.

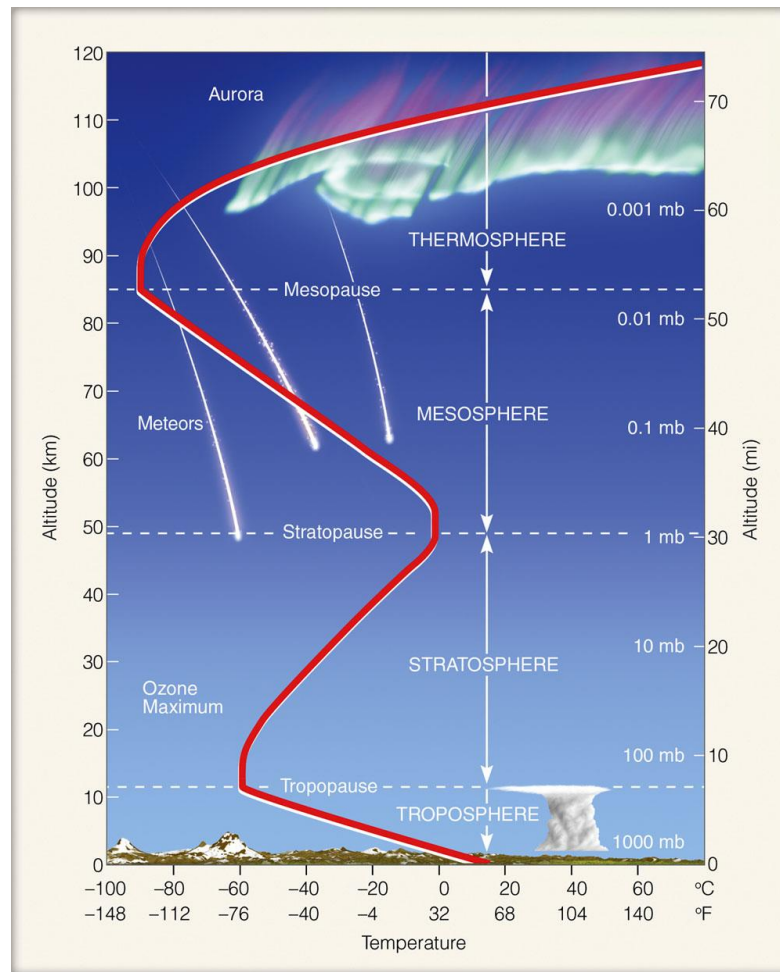


Figure 1-1: The structure of the Earth's atmosphere. Reproduced from <http://www.geogrify.net/GEO1/Lectures/IntroPlanetEarth/FourSpheres.html>.

The troposphere is characterised by a negative lapse rate and extends from the Earth's surface to between 7-8 km at the poles and between 16-18 km at the equator. Most of the weather phenomena take place within this layer. The troposphere contains about 70% to 80% of the total mass of the Earth's atmosphere and about 99% of the water vapour.

The stratosphere is separated from the troposphere by an isothermal layer known as the tropopause. The stratosphere extends from the tropopause up to an altitude of about 50 km and is characterised by a positive lapse rate due to absorption of solar UV radiation by ozone, which provides a shield to life on Earth from this harmful radiation. This layer of the atmosphere is characterised by intense interactions between radiative, dynamical and chemical processes.

The mesosphere is separated from the stratosphere by the stratopause where the highest temperature in the middle atmosphere (encompassing both the stratosphere and mesosphere) occurs. The mesosphere extends upwards to an altitude of about 85 km and is characterised by a negative lapse rate. Noctilucent clouds are located in the mesosphere and the upper mesosphere is also the region of the ionosphere known as the *D* layer.

Above this is the thermosphere, which is separated from the mesosphere by the mesopause, a region in which the lowest temperatures within the terrestrial atmosphere occurs. The thermosphere extends upwards to an altitude of around 500 km, and is characterised by a positive lapse rate which is due to the absorption of highly energetic solar radiation by atmospheric molecules. This radiation also produces ionisation of the air molecules and results in the *E* and *F* layers of the ionosphere.

1.2.2 The Mesosphere/Lower Thermosphere (MLT)

1.2.2.1 Major atmospheric constituents of the MLT

The upper mesosphere/lower thermosphere (MLT) region extends from between about 70-110 km. It forms an important transition region, sandwiched between the effects of incoming X-ray and extreme UV (E-UV) radiation from space ($<1.27 \mu\text{m}$) above and the effect of the lower atmosphere below. Whilst turbulent mixing dominates the atmosphere below 110 km, above this height, the mean free path of air molecules is of the order of 1 m and bulk motion of air cannot be sustained. This means that gravitational settling by molecular mass is able to occur and molecular diffusion dominates. Thus, the MLT region is a transition zone between these two starkly differing mixing regimes.

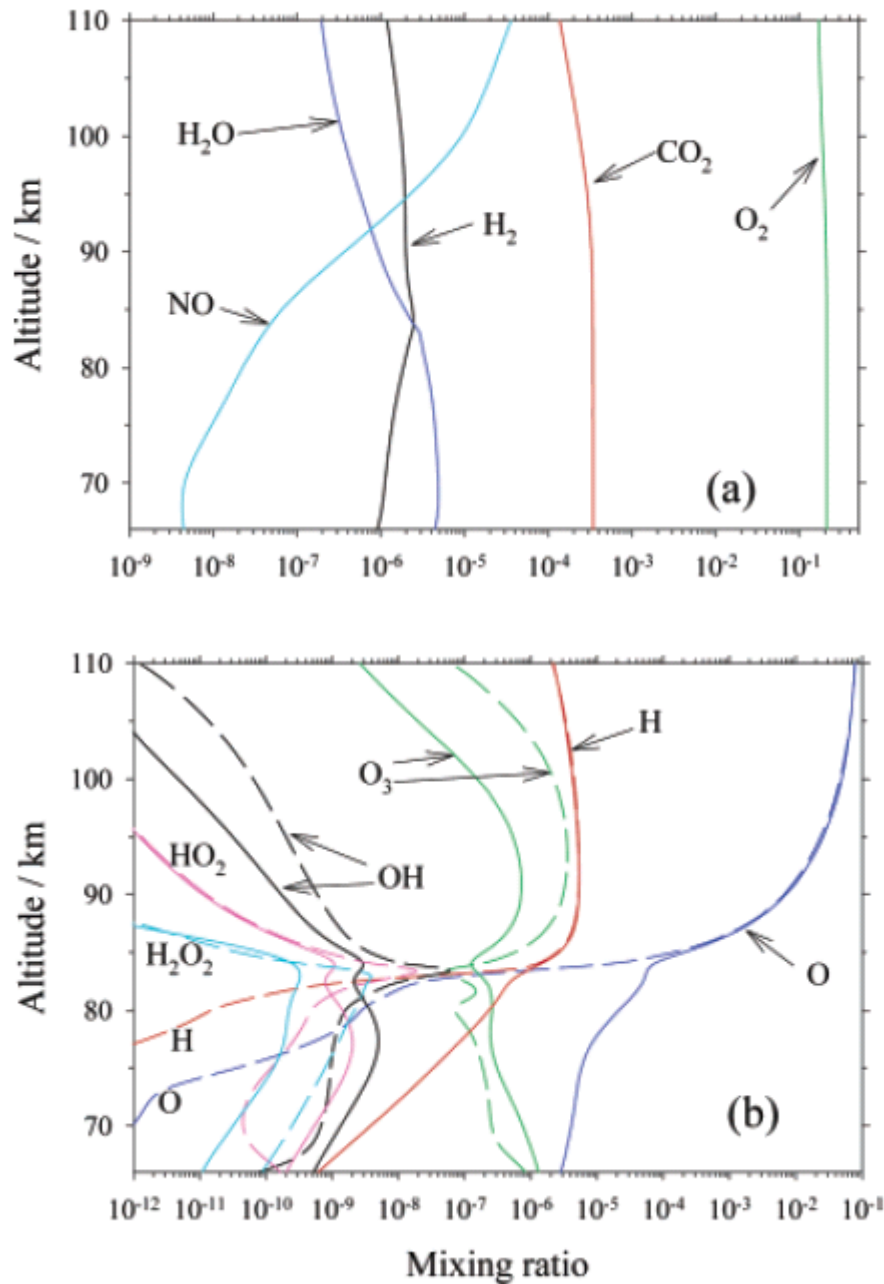
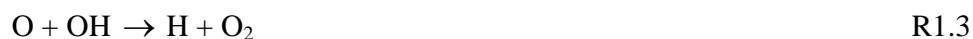
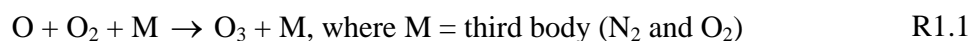


Figure 1-2: *Mixing ratios of species found in the MLT with (a) no diurnal variation and (b) for species which exhibit significant diurnal variation. Solid lines indicate the daytime profiles and broken lines indicate night-time profiles. Reproduced from Plane [2003].*

Plane [2003] provides an excellent overview of the chemistry of this region. Atomic oxygen is the dominant reaction species in the MLT region (shown in Figure 1-2) with a significant diurnal variation below 82 km. It is produced during the daytime via photolysis of O_2 , and its removal is a result of the following series of reactions:



The dominant rate dependent reaction governing the removal of atomic O, is the pressure-dependent recombination of atomic O and O₂ to form O₃ (Reaction R1.1). Above 82 km, chemical energy stored as a result of the daytime absorption of solar UV is available during the night-time. As a result, the time constant of this reaction exceeds 12 hours allowing a layer of atomic O to persist through the night, resulting in little diurnal variation of atomic O. Below 82 km, the atomic O layer experiences significant diurnal variation. This sharp transition region is known as the atomic oxygen shelf [Plane, 2003] and is significant for the chemistry of this reaction.

Atomic H is another important atmospheric constituent at these altitudes and has a very similar vertical profile to atomic O, with a sharp transition region below 82 km. It is produced as a result of the photolysis of H₂O, which is itself produced from the oxidation of CH₄, which is transported up from the stratosphere.

Other relevant species include O₃, H₂, H₂O and NO. Above 82 km, daytime photolysis means that the O₃ layer experiences a night-time maximum. In addition to this, O₃ is involved in two catalytic cycles involving H (both Reactions R1.2 and R1.3, and R1.4-R1.6). Below 82 km, there is little difference between the daytime and night-time profiles. H₂ is formed through R1.6 and is at a maximum around 82 km. The H₂O

mixing ratio decreases above 80 km, as a result of photolysis by solar Lyman-alpha radiation at 121.6 nm which extends down to this altitude.

The production of nitric oxide (NO) arises predominantly as a result of the reaction of electronically excited atomic nitrogen atoms,



Whereas $\text{N}({}^2\text{D})$ results from a number of exothermic ion-molecule reactions (such as $\text{N}_2^+ + \text{O} \rightarrow \text{N}({}^2\text{D}) + \text{NO}^+$), reaction R1.7 results in an increasing vertical NO mixing ratio with a significant source in the lower thermosphere (seen in Figure 1-2).

1.2.2.2 The ionosphere

Ion chemistry also plays an important role in the MLT region. The MLT is bombarded by high energy solar photons which generate significant plasma concentrations above 70 km, to form the ionosphere (shown in Figure 1-3). The ionosphere can be split up into three distinct regions; the *D* region (70-95 km), *E* region (95-170 km) and *F* region (170-500 km) (shown in Figure 1-3). Each of these layers is characterised by different ions concentrations and these are summarised in Table 1-1.

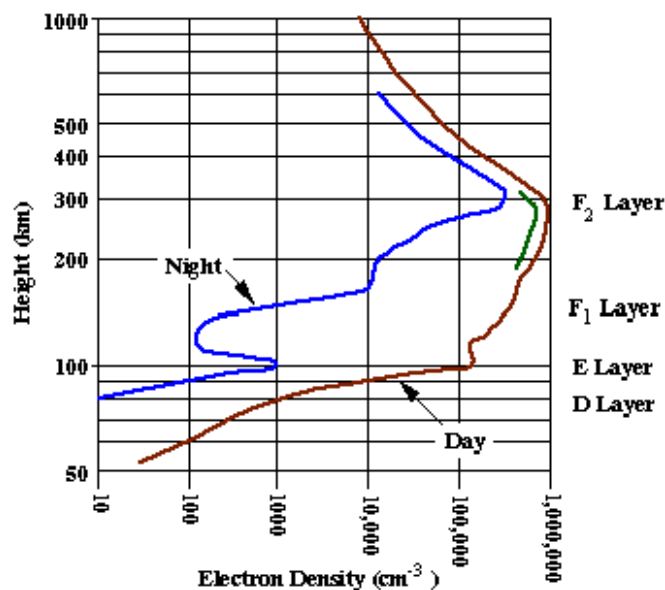


Figure 1-3: The ionospheric D, E and F layers. Reproduced from <http://www.fas.org/man/dod-101/navy/docs/es310/propagat/IMG00024.GIF>.

Table 1-1: Summary of dominant ions in the *D*, *E* and *F* ionospheric regions.
Adapted from Plane [2003].

	Dominant ions	
<i>D</i> region (70-95 km)	Proton hydrates, such as $H^+(H_2O)_n$, $n \geq 1$, negative ions and negatively charged meteoric smoke particles (MSPs).	<p>Primary source is the photo-ionisation of NO by Lyman-α. Galactic cosmic rays are a significant source of ionisation.</p> <p>As a result of the increased atmospheric density, the ion chemistry of the <i>D</i> region is extremely complex relative to either the <i>E</i> or <i>F</i> regions.</p> <p>Proton hydrates are formed by the clustering of positive ions which form weak ligands and ultimately switch with H_2O.</p> <p>Electrons may attach to O_2, which then react with O_3, to form both O_2^- and O^-. These negative ions are able to form the more stable HCO_3^-, NO_3^- and Cl^- ions.</p> <p>Above 85 km, the large concentrations of ambient O result in these negative ions being rapidly destroyed either by detachment, or by associative attachment, e.g. $O^{2-} + O \rightarrow O_3 + e^-$.</p>
<i>E</i> region (95-170 km)	O_2^+ and NO^+ balanced by free electrons	<p>Primary source is from solar X-ray and E-UV radiation at wavelengths < 103 nm. <i>E</i> region, O_2^+ and NO^+ formed by photo-ionisation. N_2^+ is rapidly lost by reacting with either O or O_2 to form NO^+ and O_2^+, respectively.</p> <p>A key feature of the <i>E</i> region relevant to this thesis, is the occurrence of sporadic <i>E</i> layers. Sporadic <i>E</i> layers can occur and consist of relatively dense patches of ionised gas which appear spontaneously in local concentrations (50-150 km across) and disappear after a few hours. It is not understood why these spontaneous concentrations occur, but they can be exploited for long-distance radio propagation/communication purposes. [e.g. MacLeod, 1966; Collis and Turunen, 1987; Wu <i>et al.</i>, 2005]</p>
<i>F</i> region (170-500 km)	O^+ , N^+ , O_2^+ and NO^+ ions	Primary source is the photo-ionisation. This region has the highest concentration of electrons, which are important in radio communications.

Figure 1-4 depicts the profiles of electrons and the main positive ions between an altitude of 75 and 140 km, during both daytime and night-time. A pronounced diurnal variation exists in the electron layer and the positive atomic and molecular ions, as a result of the diurnal changes in the solar X-ray and E-UV radiation at wavelengths < 103 nm.

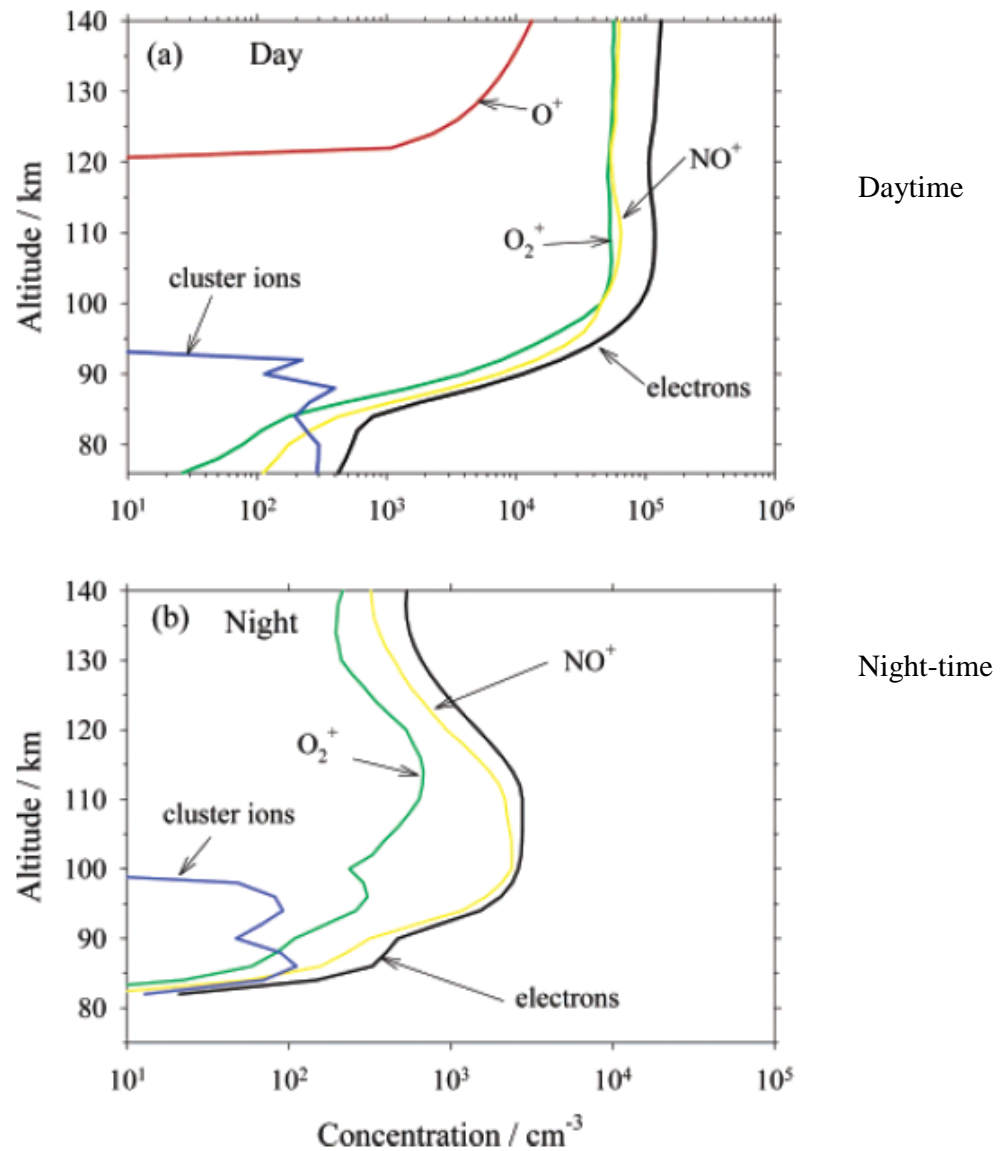


Figure 1-4: Vertical profiles of the electron and major positive ion densities in the MLT during January 1999 during (a) daytime and (b) night-time. Reproduced from Plane [2003].

1.2.2.3 Relevant dynamics of the MLT

The upper mesosphere/lower thermosphere region (MLT, ~70-110 km) forms a crucial energy transition layer between the lower atmosphere and the upper thermosphere/space boundary [e.g. Plane, 2003; Laštovička *et al.*, 2008]. It is subject to high energy solar electromagnetic radiation and energetic particles from above, and to the effect of breaking gravity waves, planetary waves and tides from the lower atmosphere below [e.g. Schoeberl *et al.*, 1983; Forbes, 1995; Garcia *et al.*, 2005; Gardner and Liu., 2010]. Wave-induced dynamical and chemical transport, turbulent eddy diffusion and the flux due to advection by the mean vertical winds (upwelling in summer, downwelling in winter with greatest effect at poles) [Summers and Siskind, 1999; Gardner and Liu, 2010] all play a role in the vertical flux within the MLT and between atmospheric regions. The winter downwelling from the meridional circulation causes a funnelling of mesospheric air and transport of minor chemical constituents down to the lower stratosphere through the Antarctic polar vortex [Plane 2003] as shown in Figure 1-5.

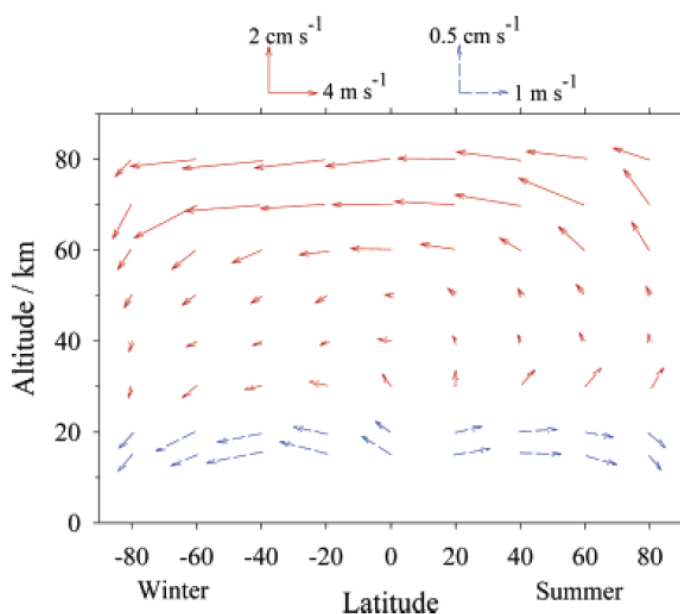


Figure 1-5: Meridional wind vectors as a function of altitude and latitude. A summertime upwelling as a result of gravity wave activity and wintertime downwelling characterised the MLT meridional circulation. Reproduced from Plane [2003].

The vertical coupling between the different regions of the atmosphere is summarised in Figure 1-6. Gravity waves generated in the lower atmosphere as a result of enhanced summer hemisphere solar heating have an important role in driving the mean meridional circulation, influencing the thermal structure of, and contributing to turbulence and mixing in the mesosphere/lower thermosphere region [e.g. see Fritts and Alexander, 2003]. The amplitude of these vertically propagating waves increases with decreasing pressure, until they eventually become unstable, breaking and delivering momentum and energy within the mesosphere. This causes a drag on the mean zonal winds near the mesopause region, driving the meridional flow towards the equator away from the summer pole. Associated upwelling and adiabatic expansion of air leads to very low temperatures in the summer polar region, whilst the corresponding downwelling at the winter pole leads to adiabatic heating and enhanced warming, in contrast to much of the rest of the atmosphere [Fritts and Alexander, 2003].

The chemical composition in the MLT is controlled by the coupled effects of solar radiation, chemical kinetics and mass transport [Allen *et al.*, 1981]. Gravity waves have a significant effect on the transport of chemical species, with the wave-driven winter downwelling causing the transport of minor chemical constituents from the upper MLT region to the lower stratosphere through the polar vortex [e.g. Hunten *et al.*, 1980; Garcia and Boville, 1994]. The interaction of planetary waves with gravity waves can serve to modify the strength of the zonal wind introducing subseasonal variation [Holton, 1983]. The photolysis of H₂O propagating up from the stratosphere produces atomic H and OH [Plane, 2003]. A major source of nitric oxide (NO) is in the lower thermosphere, where it is produced by the reaction of electronically excited nitrogen (by either solar UV or auroral electrons) with molecular oxygen, to produce NO and atomic O. Atomic H, OH and NO all play an important chemical role throughout the atmosphere, and are specifically involved in the ozone loss processes within the upper mesosphere, and stratospheric regions.

The MLT region is also important in terms of polar mesospheric and stratospheric cloud formation; particles of meteoric origin act as nuclei upon which water vapour condenses

to form cloud droplets [Murphy *et al.*, 1998; Curtius *et al.*, 2005; Megner *et al.*, 2006; Vondrak *et al.*, 2008; Saunders *et al.*, 2010]. Polar stratospheric clouds (PSCs) are associated with ozone destruction [Solomon *et al.*, 1986; Poole and McCormick, 1988; Molina *et al.*, 1993; Solomon and Chanin, 2011] and have been linked to regional tropospheric warming [Sloan and Pollard, 1998; Lachlan-Cope *et al.*, 2009]. Polar mesospheric clouds (commonly known as noctilucent clouds when seen with the naked eye), are ice clouds that form under very specific circumstances, dependent on cold temperatures and water vapour content [Garcia, 1989; DeLand *et al.*, 2006; Laštovička *et al.*, 2008; Morris and Murphy, 2008]. Their increasing occurrence in recent years has been linked to climate change [DeLand *et al.*, 2006] and it is thought that they act as sensitive indicators to such change [Garcia, 1989; DeLand *et al.*, 2006; Laštovička *et al.*, 2008; Morris and Murphy, 2008].

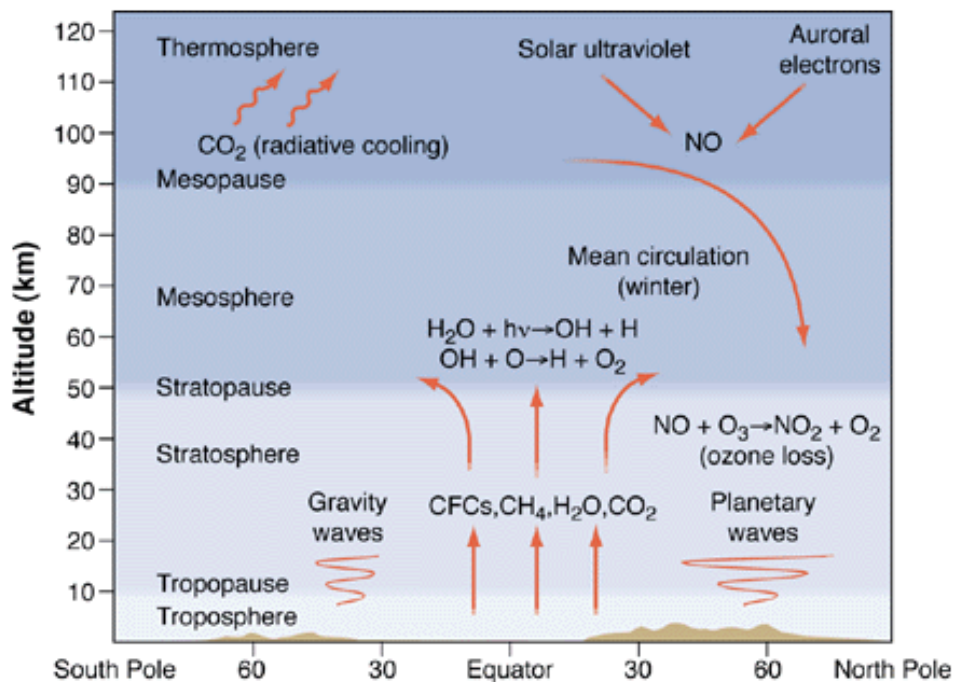


Figure 1-6: Summary of the various vertical couplings between atmospheric regions. Reproduced from Summers and Siskind [1999].

1.2.3 Climate change in the upper atmosphere

There is now increasing evidence that anthropogenic emissions of greenhouse gases are having an impact at nearly all atmospheric altitudes between ground and space. Observations of the middle and upper atmosphere indicate a net cooling [Roble and Dickinson, 1989; Rishbeth and Roble, 1992; Akmaev and Fomichev, 2000; Beig *et al.*, 2003; Laštovička *et al.*, 2008], as a result of a build-up of greenhouse gases, ongoing depletion of stratospheric ozone, and a steadily increasing water vapour content [Roble and Dickinson, 1989; Akmaev and Fomichev, 2000; Akmaev *et al.*, 2006; Laštovička *et al.*, 2008].

The MLT is sensitive to climate change, and any temperature changes are much easier to detect within the MLT region as the temperature change over the previous two decades is comparable to the diurnal temperature variation. In contrast, the diurnal temperature variation in other parts of the atmosphere far exceed the equivalent longer-term temperature changes [Plane *et al.*, 2014].

Ozone depletion results in a reduction of solar heating, and it is thought that this is of a magnitude comparable to that of the CO₂ forcing [Akmaev *et al.*, 2006]. The cooling of the middle and upper atmospheric layers will cause a hydrostatic contraction, which is likely to affect the propagation of gravity waves, atmospheric temperature distribution and the transport of water throughout much of the atmosphere [Garcia, 1989; Akmaev *et al.*, 2006]. An altered upper atmosphere may have implications for heat, momentum and mass exchange between atmospheric regions, affecting such phenomena as the quasi-biennial oscillation, the polar vortex and sudden stratospheric warming events. Currently, it is not clear how these changes will manifest themselves and what effect it will have on the mean meridional and global circulation and chemical transport patterns in the future.

1.3 The Neutral Metal layers

Upon entering the upper atmosphere, meteoroids burn up (ablate) due to frictional heating, giving rise to well-defined layers of neutral metal atoms and ions (including Na, Fe, Mg, Ca and K). These meteoric metal layers display diurnal and seasonal variation, with the metal species abundance and distribution being affected by both chemistry (photo-ionisation and sink reactions with O, O₂, O₃ and CO₂), and dynamics (gravity waves, planetary waves and tides) [Garcia *et al.*, 2005].

1.3.1 Observations of the meteoric metal layers

The interest in the upper atmospheric metal layers dates back to 1929, where Slipher first observed bright yellow radiation at 589 nm in the night sky spectrum, suggesting that it might be attributable to Na. A decade later, this was confirmed as being as a result of Na resonance, with a source located in the terrestrial atmosphere by Cabannes *et al.* [1938] and Bernard [1939]. Subsequent work by a number of authors [e.g. Hunten and Shepherd, 1954; Chamberlain, 1958, 1961] identified that the Na atoms resided in a thin layer at an altitude between 85-90 km, by making twilight observations as the solar terminator passed through the upper mesosphere and analysing the change in fluorescence.

Radiative transfer models were used to determine absolute Na number densities [Hunten, 1954; Chamberlain, 1956; Hunten, 1967]. The first real quantitative observations of the metals layers (including Na, K, Fe and Ca⁺) were performed by Chamberlain [1956], Blamont and Donahue [1961], Donahue and Meier [1967] and Sullivan and Hunten [1964], who used either ground-based or rocket-borne passive photometric techniques. However, these passive measurements could only be performed during the daytime as they relied on the solar photo-excitation of the atoms.

1.3.1.1 Lidar measurements

A great advancement in the study of the metal layers arrived with the invention of the tunable laser in the later 1960s [Bowman et al, 1969]. The lidar (LIght Detection And Ranging) technique involves the use of a pulsed laser beam tuned to the wavelength of a strongly allowed transition of the metal atom of interest. This beam is then transmitted to the target atmospheric region and the amount of backscattered radiation is recorded. The active excitation of individual atoms by the laser allowed sampling to be made over the full diurnal cycle. Much progress has been made in the last few decades in understanding the mesospheric metal layers, through a combination of laboratory studies and atmospheric modelling [e.g. Plane, 2003; Feng *et al.*, 2014; Marsh *et al.*, 2014]. However to date, the majority of information on the metal layers still comes from lidar station observations.

Lidar stations exist globally at various latitudes (see Figure 1-7), providing information on the diurnal and seasonal (and to a limited extent, latitudinal) variation of the Na, Fe, K, Ca and Ca⁺ layers. A large amount of lidar data exists for Na and Fe [e.g. Megie and Blamont, 1977; Clemesha *et al.*, 1979; Kirchoff and Clemesha, 1983; Alpers *et al.*, 1990; Clemesha *et al.*, 2004; Gardner *et al.*, 2005; 2011; Chu *et al.*, 2011], in part as a result of their use to determine upper atmospheric temperatures and wind profiles. In contrast, only a limited number of studies have been made for K, Ca and Ca⁺ [e.g. Eska *et al.*, 1998; 1999; Gerding *et al.*, 2000; Höffner and Lübken, 2004; 2007; Raizada *et al.*, 2007; Raizada *et al.*, 2011; 2012; Delgado *et al.*, 2012].

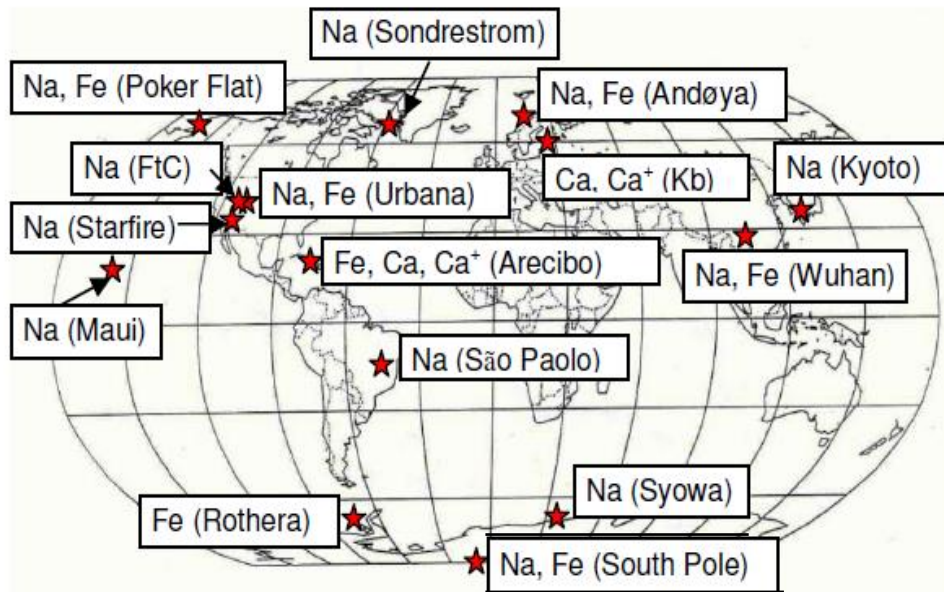


Figure 1-7: Locations of ground-based metal resonance lidar observatories with significant records on Na, Fe, Ca or Ca⁺ [J. Plane, personal communication].

1.3.1.2 Satellite observations

A key limitation of the ground-based observations is that in many cases these do not always provide continuous datasets, often being the result of short measurement campaigns, as well as being strongly biased towards Na and Fe measurements. Although station lidar measurements have very good temporal and altitude resolution, a key limitation is that there is limited global spatial coverage. For these reasons, and due to direct *in situ* measurements of the metal layers being difficult, such systematic global measurements can only be provided by space-borne instruments.

Satellite work so far has mostly focussed on atomic sodium. The first such space measurements were made by Newman [1988] who focussed on the Na nightglow from measurements from one of the polar orbiting Defence Meteorological Satellite Program (DMSP) satellites during July 1979. Whilst her data showed latitudinal and altitudinal variation in the metal layer, the work has come under criticism regarding the accuracy of obtaining data from the nightglow, where emission spectra are generated indirectly by chemiluminescent cycles involving Na, O₃ and atomic O [Clemesha *et al.*, 1990; Xu *et*

al., 2005; Fan *et al.*, 2007a]. Subsequent retrievals have focussed on dayglow where emission spectra are stimulated directly by absorption of solar radiation.

In 2004, Fussen *et al.* developed a retrieval algorithm using measurements from the stellar-occultation instrument, GOMOS, on-board Envisat for a one-year period (2003). However, they found that the retrieved Na column abundances, layer density profiles and the seasonal and latitude variations were in poor agreement with available data from ground-based lidars [Fan *et al.*, 2007a]. Much subsequent work [Fussen *et al.*, 2010] has been done to improve the retrieval, and atomic Na datasets now exist for 2002-2008.

Another independent Na retrieval scheme has been developed by Gumbel *et al.* [2007] which uses dayglow limb radiances from the OSIRIS spectrometer on-board the Odin satellite. With this they were able to produce absolute Na density profiles for 2003-2004, which depict column abundance as well as peak layer height and widths. The retrieved data was validated via overflights over the Na lidar at Fort Collins, Colorado and was found to compare well [Fan *et al.*, 2007a]. As measurements are made at 0600 and 1800 LT, Odin/OSIRIS allows the effect of the diurnal tide to be observed in the metal layers.

Recent work has also focused on retrieving information about the neutral and ionic Mg metal layers. Scharringhausen *et al.* [2007, 2008a,b] developed a retrieval which uses dayglow limb radiances from the SCIAMACHY instrument onboard Envisat, producing the first global datasets for Mg and Mg⁺ spanning 2002-2006. No ground lidar observations exists for Mg/Mg⁺ due to their strong resonance transitions at 285 nm and 280 nm being completely absorbed by stratospheric ozone. However, Scharringhausen *et al.* found that their data were in good agreement with previous measurements made from rocket sensors. They found that in contrast to other metallic species, no such pronounced seasonal variation exists in the atomic Mg layer, but a seasonal pattern (with summertime maxima) is seen for Mg⁺ [Scharringhausen, 2007; Scharringhausen *et al.*, 2008b]. Much improvement of the earlier retrieval has subsequently been performed by Langowski *et al.* [2014a, 2014b] and the Mg and Mg⁺ datasets have now been extended to April 2012.

1.3.2 Meteoroids and the input of cosmic dust into the terrestrial atmosphere

The major source of cosmic dust into the terrestrial atmosphere occurs as a result of collisions between asteroids, and also the sublimation of comets as they approach the Sun during their orbit [Plane, 2012]. Other sources of cosmic dust originate from meteor showers (such as the Perseids, Leonids and Geminids), which take place periodically as the Earth passes through a cometary trail on its orbit around the Sun. The meteoric material which burns up in the MLT are known as meteoroids, whilst the material which reaches the ground is known as meteorites.

The magnitude of cosmic dust input into the terrestrial atmosphere from these meteoroids, represents a huge source of uncertainty, with estimates ranging from 3 to nearly 300 tonnes day⁻¹ depending on the measurement technique used (see Table 1-2 for a summary of these observations). Observations of the zodiacal cloud, space-borne dust detection, deep-sea ocean sediments and ice cores indicate cosmic dust input values towards the higher end of this range. Meanwhile, measurements from high-altitude aircraft, high performance radars, meteor radars, and modelling studies indicate values towards the lower end. Depending on the true magnitude of this cosmic dust input, significant revisions may need to be made to the understanding of vertical transport within the atmosphere, in order to account for the different values [Plane, 2012].

Table 1-2: Estimates of the global cosmic dust input rate to the Earth's atmosphere (deep blue = extra-terrestrial estimate; light blue = middle atmosphere estimate; grey = ice core/deep-sea estimate). Adapted from Plane [2012].

Technique	Cosmic dust input (t d ⁻¹)	Reference	Potential problems of technique
Zodiacal dust cloud observations and modelling	270	Nesvorný <i>et al.</i> [2011]	Needs to be constrained by terrestrial meteor radars
Long Duration Exposure Facility	110±55	Love and Brownlee [1993]	Sensitive to cosmic dust velocity distribution
High performance radars	5±2	Mathews <i>et al.</i> [2001]	Possible velocity bias/selective mass range
Conventional meteor radars	44	Hughes [1978]	Extrapolation, selective mass/velocity range
Na layer modelling	20±10	Plane [2004]	Sensitive to vertical eddy diffusion transport
Fe layer modelling	6	Gardner <i>et al.</i> [2011]	Depends on vertical transport
Fe/Mg in stratospheric sulphate layer	22-104	Cziczo <i>et al.</i> [2011]	Data has limited geographic extent
Optical extinction measurements	10-40	Hervig <i>et al.</i> [2009]	Particle refractive indices uncertain
Fe in Antarctic ice core	15±5	Lanci <i>et al.</i> [2012]	Very little wet deposition by snow
Fe in Greenland ice core	175±68	Lanci and Kent [2006]	Uncertain atmospheric transport/deposition
Ir and Pt in Greenland ice core	214±82	Gabrielli <i>et al.</i> [2004]	Uncertain atmospheric transport/deposition
Os in deep-sea sediments	101±36	Peuker-Ehrenbrink [1996]	Focusing by ocean currents
Ir in deep-sea sediments	240	Wasson and Kyte [1987]	Focusing by ocean currents

The meteoric input flux (MIF) is a function of meteoroid velocity, size, density, entry angle and composition [e.g. see Janches *et al.*, 2006]. The MIF exhibits a diurnal, seasonal and latitudinal variation (see Figure 1-8) with a hemispheric springtime minima and autumn maxima [Ceplecha *et al.*, 1998].

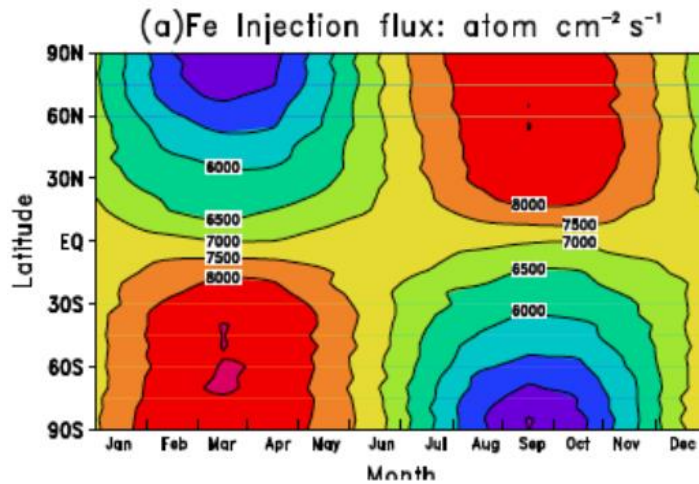


Figure 1-8: Example of meteoric input flux (MIF) for Fe. Reproduced from Feng *et al.*, [2014].

A chemical ablation model (CABMOD) [Vondrak *et al.*, 2008] can be used to estimate the ablation profiles of the constituents of incoming meteoroids for a given mass, velocity, size and entry angle. Example ablation profiles for meteoroids of 5 μg mass and an entry velocity of 20 km s⁻¹ are shown in Figure 1-9. Above 105 km, the mass loss is attributed to sputtering, and the particle has not yet melted, with temperatures <1800 K. Differential elemental ablation occurs below this altitude, with the more volatile constituents ablating sooner (e.g. Na and K at ~100 km), at higher altitudes. The least volatile elements, such as Ca, ablate further down in the atmosphere, with a peak ablation near 83 km.

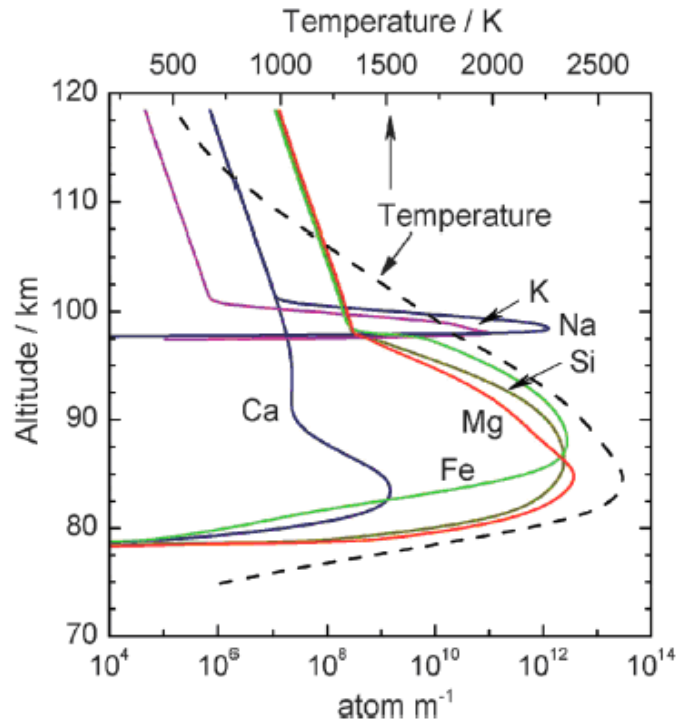


Figure 1-9: Elemental ablation profiles of a $5 \mu\text{m}$ meteoroid entering at 20 km s^{-1} as predicted by the Chemical Ablation Model (CABMOD). Reproduced from Plane *et al.* [2012].

1.3.3 The use of the metal layers as tracers

The meteoric metals exist as a layer of atoms between approximately 80-105 km altitude, and their abundance is dependent on complex interactions between chemical reactions and various different dynamics. Above 105 km, the metals persist as metal ions. Below 80 km, these metals form various compounds (e.g. carbonates, hydroxides and oxides). These compounds polymerise into nm-sized meteoric smoke particles (MSPs) which likely act as cloud condensation nuclei throughout the mesosphere and stratosphere. Here they are cycled, until eventually after approximately four years, they are deposited at the Earth's surface [Plane *et al.*, 2014]. The spatio-temporal concentrations of these metals is dependent on both chemistry and dynamics; the observation and accurate modelling of such neutral metal layers permit an increased understanding of such processes affecting the MLT region.

1.3.4 The unusual behaviour of potassium

In addition to differential ablation rates, the metal species show differences in seasonal variation and latitude-dependence of peak layer heights and densities from one another, as can be seen in Figure 1-10. While the Fe, Na and Ca layers exhibit dominant annual variation with early winter maxima and mid-summer minima at mid-latitudes, the K layers exhibit semi-annual variations with a marked second maximum during the hemispheric summer [Gerding *et al.*, 2000; Plane, 2003]. This is particularly surprising as both Na and K are Group 1 (alkali) metals and thus they would be expected to show similar behaviours. Semi-annual differences in altitude are present in all metal layers; peak densities occur at higher altitudes in the hemispheric winter for Fe and Ca [Kane and Gardner, 1993; Gerding *et al.*, 2000] and for the summer for Na and K [Kane and Gardner, 1993; Eska *et al.*, 1998; Gerding *et al.*, 2000].

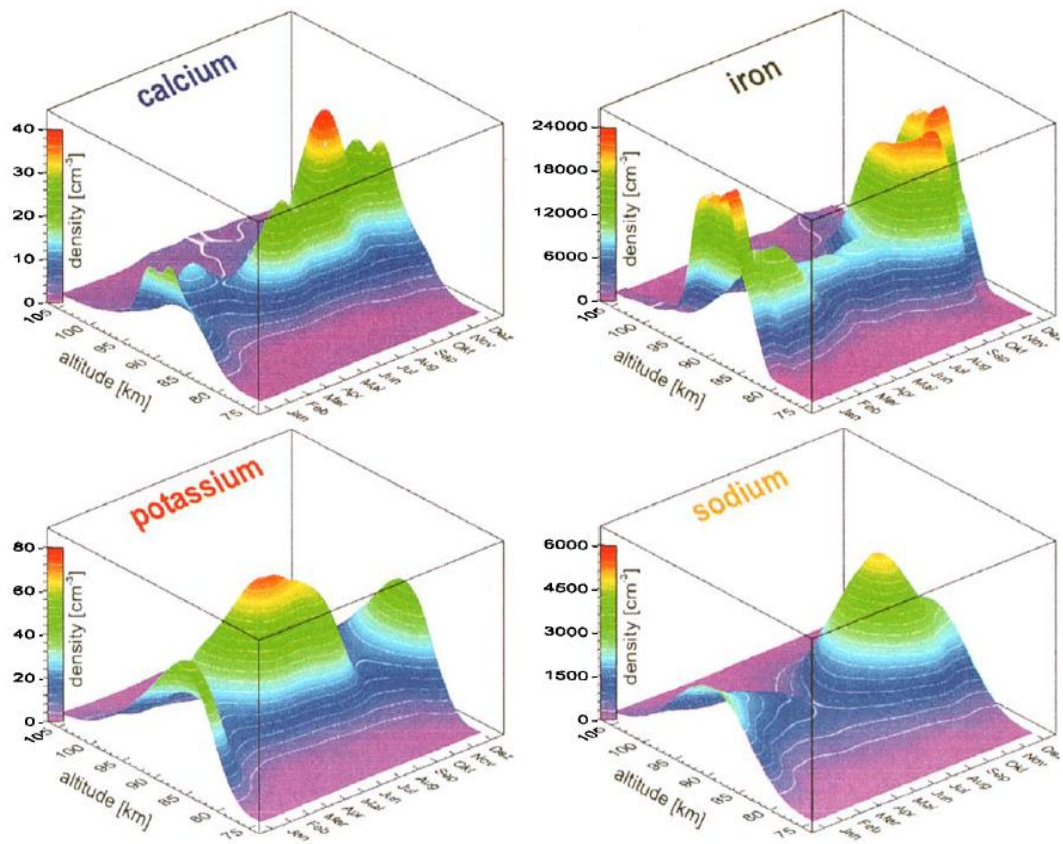


Figure 1-10: Three-dimensional plot of the annual variation (altitude, month, density) of metal layers for Ca (from Kühlungsborn ($54^{\circ}\text{N } 12^{\circ}\text{E}$), Fe ($54^{\circ}\text{N } 12^{\circ}\text{E}$), K ($54^{\circ}\text{N } 12^{\circ}\text{E}$) and Na (Fort Collins ($41^{\circ}\text{N } 105^{\circ}\text{W}$)). Reproduced from Plane [2003], which is based on Gerding et al. [2000].

1.3.5 Other phenomena related to the metal layers

Another striking phenomenon is the appearance of sporadic metal layers observed within the upper mesosphere/lower thermosphere region. These sporadic layers occur explosively within a matter of minutes usually with very narrow layer full-width half-maximum, peak heights occurring a few kilometres higher than, and with peak densities sometimes reaching more than an order of magnitude greater than the background metal

layer [Clemesha, 1995; Gardner, 1995]. They can persist for a number of hours and their horizontal extent varies.

Their appearance appears to be latitude-dependent and, at least for Na, they seem to be more prevalent in the southern hemisphere [Fan *et al.*, 2007]. Sporadic layers for atomic Na [Gardner, 1995; Fan *et al.*, 2007], Fe [Gardner, 1995], Ca [Gerding *et al.*, 1999] and K [Delgado *et al.*, 2011] have all been observed. Very recent results from Xinzhao Chu from the University of Colorado at Boulder have revealed an extreme sporadic atomic Fe layer event occurred in February 2011 with exceptionally large peak densities of $1.2 \times 10^5 \text{ cm}^{-3}$. The growth speed and peak density exceeds any other observations so far.

The causal mechanisms determining the occurrence and extent of sporadic neutral metal layers remain uncertain but possible links to the melting of polar mesospheric clouds, to geomagnetic storms, bombardment by energetic particles and neutralisation by sporadic *E* layers have been made. [e.g. Clemesha *et al.*, 1978, Beatty *et al.*, 1989; Kirkwood and Collis, 1989; von Zahn and Murad, 1990; Zhou *et al.*, 1993; Cox and Plane, 1998; Hansen and von Zahn, 1990; Delgado *et al.*, 2012].

Variations in the solar cycle (UV and E-UV portion of the solar spectrum) may impact the metal layers, by modifying the thermal structure and chemical composition of the middle atmosphere [Brasseur and Solomon, 1984]. Changes in the photo-ionisation and photolysis rates might be expected, causing potential lowering of the peak metal layer heights during solar maximum periods. Solar proton events (where very high energy protons are emitted from the solar atmosphere, penetrating the Earth's magnetosphere and causing enhanced ionisation within the terrestrial upper atmosphere) may also affect the metal layers. In his PhD thesis [2007], Marco Scharringhausen investigated the impact of both the solar cycle and solar proton events on the neutral and ion magnesium (Mg) layers. He found no significant correlation between the solar activity and Mg/Mg⁺ abundance on small times scales of five to six years prior to the solar minimum in 2007. However, he found a strong correlation between enhanced Mg and Mg⁺ densities and the solar proton events studied. The effect of the solar cycle and solar proton events on the other metal layers remains to be explored.

1.4 Thesis aims and objectives

A lack of observations of the mesosphere/lower thermosphere region has meant that this important region has been relatively poorly understood to-date, compared to other parts of the Earth's atmosphere. Lidar studies of the metal layers derived from meteoroids are numerous, but the key limitation of such data is that they represent point measurements. Remote sensing by satellites makes it possible to build up a near-global picture of these metals, which act as excellent tracers for atmospheric chemistry and dynamics within the MLT region. Of these meteoric metals, K remains the least well understood, displaying a unique semi-annual seasonality not seen in the other observable metals.

The specific aims and objectives of this thesis are listed below along with reference to the chapter which presents the relevant work;

- Produce the first global retrieval of the K layer (Chapter 3) and assess the performance of the retrieved dataset (Chapter 4)
 - Develop a satellite retrieval algorithm to derive information on the near-global neutral K layer
 - Perform a full error-analysis of the retrieved K product
 - Ground-truth the new dataset with available K lidar station data
- Assess the extent of the semi-annual seasonality in K and the sensitivity of the K layer to various atmospheric phenomena (Chapter 5)
 - Examine the seasonality of the near-global K layer, in terms of absolute number density, column abundance, peak layer height and root-mean square layer width.
 - Identify if there are latitude-dependent effects on the above parameters.

- Establish how well a whole atmosphere model can reproduce the satellite observations and the implications this may have for model chemistry and dynamics.
- Determine the global diurnal behaviour of the K layer.
- Look for evidence of sporadic metal layers in satellite datasets, in terms of their frequency and horizontal extent.
- Investigate removal of underside of the potassium metal layers by noctilucent clouds.
- Examine whether there is there a solar cycle response in the Na and K metal layers, and where there any long-term trends in such metals (Chapter 6)
 - Assess the impact of the solar cycle on the observed and modelled metal layers.
 - Examine the long-term trend in the modelled metal layers (K, Na, Fe).
 - Assess whether the sodium and potassium metal layers act as sensitive indicators of climate change in the upper atmosphere.

This work provides valuable information on answering some of the key questions presented at the start of this Chapter, namely: how can the different seasonal behaviour of the metals be explained? What is the source of metal atoms from which sudden or sporadic layers form? Do the metal layers act as sensitive indicators of climate change in the mesosphere, either directly or through their relationship with noctilucent clouds?

1.5 Thesis layout

The remaining thesis is organised as follows:

Chapter 2: Description of the OSIRIS satellite instrument which is of fundamental importance for this thesis, and all other relevant datasets used throughout this work.

- Chapter 3: Description of the new K retrieval scheme.
- Chapter 4: Description of the retrieval error analysis and validation approach.
- Chapter 5: Presentation of the first look at the near-global K layer, and examines a possible explanation for the unusual behaviour of K.
- Chapter 6: The solar cycle and longer-term response of the observed and modelled Na and K metal layers.
- Chapter 7: Summary of the results of this thesis, overall conclusions and recommendations for future work.

2 OSIRIS INSTRUMENT AND DATASETS

2.1 Introduction

This chapter provides an overview of the OSIRIS instrument and the datasets used in Chapters 3-6. An in-depth overview of the Odin satellite including the mission objectives, orbit and payload details is outlined in Section 2.2. The Optical Spectrometer and InfraRed Imager System (OSIRIS) instrument, which forms the basis of this thesis work, is described in 2.3, with the necessary data processing requirements documented in 2.4. Sections 2.5 and 2.6 outline the Mass Spectrometer Incoherent Scatter (MSISE-00) and European Centre for Medium-range Weather Forecasts (ECMWF) ERA-Interim datasets, respectively, which are both employed in the K retrieval scheme detailed in Chapter 3.

While this thesis focuses on the retrieval and use of the OSIRIS K dataset, the OSIRIS Na datasets are integral to the work performed in Chapters 5 and 6. Section 2.7 outlines the work done in this thesis to extend an existing OSIRIS Na dataset for use in this work.

Model data from the National Centre for Atmospheric Research (NCAR) Whole Atmosphere Community Climate Model (WACCM) is used throughout Chapters 5 and 6, and this model is described in Section 2.8. Temperature data from the Thermosphere Ionosphere Mesosphere Energetic and Dynamics (TIMED) Sounding of the Atmosphere using Broadband Emission Radiometry (SABER) instrument also used in Chapter 5 and 6, is described in Section 2.9. Section 2.10 details the solar F10.7 (10.7 cm wavelength) radio flux data which is used in Chapter 6. Finally, Section 2.11 briefly describes the source of the lidar data used in Chapter 4.

2.2 Odin satellite

2.2.1 Mission objectives

The Odin satellite was launched from the Svobodny Cosmodrome in far-eastern Russia in February 2001. It was designed to combine two sets of scientific objectives on one mission: the study of star formations and the early solar system (astronomy) and the study of the mechanisms behind the depletion of the ozone layer and the effects of global warming (aeronomy). The latter objectives are outlined in Murtagh *et al.* [2002].

The mission is a result of collaboration between the space agencies of Sweden (SNSB - Swedish National Space Board), Canada (CSA - Canadian Space Agency, and NSERC - Natural Sciences and Engineering Research Council), Finland (Tekes - Finnish Funding Agency for Technology and Innovation) and France (CNES - Centre National d'Etudes Spatiales). The Swedish Space Corporation (SSC) was responsible for the spacecraft system design and development and is also responsible for spacecraft operations.

The original planned mission lifetime was two years but the scientific results and condition of the space hardware has allowed the mission to be significantly extended. In 2014, the mission had been successfully running for 13 years, although limited data exists prior to 2004. The original astronomy mission was successfully concluded in 2007 and, since then, the mission has been funded as a third party mission by the European Space Agency (ESA) under its Earthnet programme.

2.2.2 Odin Orbit

The Odin platform orbits in a Sun-synchronous orbit at 620 km with an inclination of 97.8°. This results in near-global coverage (within $\pm 82^\circ$ latitude) with equator crossing times of 06:00 and 18:00 local time. A total of 15 orbits are performed during each day.

2.2.3 Satellite Configuration

A representation of the Odin spacecraft is shown in Figure 2-1. The satellite has a mass of 250 kg and is provided with 300 W of power from deployable, fixed solar arrays which are kept at an angle within 35° to the Sun to ensure both that power production is maximised and also so that the on-board instruments are shielded from direct sunlight [Murtagh *et al.*, 2002]. This configuration also helps to ensure a stable thermal operating environment for the payload [Murtagh *et al.*, 2002].

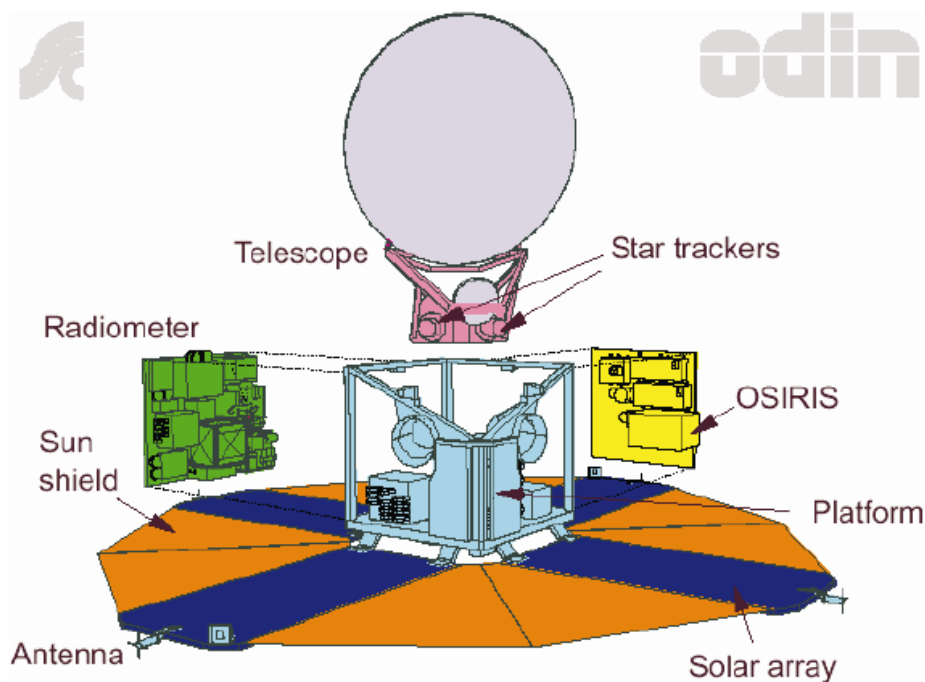


Figure 2-1: The Odin satellite payload. Reproduced from Murtagh *et al.* [2002].

The satellite is three-axis-stabilised. The attitude of the spacecraft is sensed using a combination of 3 coarse and 2 fine sun sensors, 3 gyros, 2 star trackers and two 3-axis magnetometers. The attitude of the spacecraft is controlled by using 3 orthogonal reaction wheels and 3 magnetic-torquers.

There are two instruments mounted onboard the Odin platform: the Sub-Millimetre Radiometer (SMR) and the Optical Spectrometer and Infrared Imaging System (OSIRIS). A number of species (e.g. CO, N₂O, HNO₃, NO₂ and O₃) relevant to the Odin mission objectives can be viewed in the sub-millimetre part of the electromagnetic

spectrum, with the SMR instrument being used for both astronomy and aeronomy modes. The OSIRIS instrument is predominantly used to detect aerosol layers and various species (e.g. BrO, NO₂, OCIO and O₃) relevant to the aeronomy mission. The OSIRIS instrument is described in detail in Section 2.3.

Up to the time of completion of the astronomy mission in 2007, the spacecraft was required to operate in separate modes for the astronomy and aeronomy parts of the mission. In the astronomy mode, the spacecraft is re-pointed in the direction of the required celestial object and maintained in that direction for up to 60 minutes at a time. In the aeronomy mode, the spacecraft is pointed to follow the Earth's limb and then scans the atmosphere up and down between 15 and 120 km in altitude, at a rate of up to 40 scans per orbit.

The original nominal arrangement for the 2 modes of operation was that each discipline would have 50% of the total year operating time [Murtagh *et al.*, 2002]. Generally, each discipline had a 3-day repeat cycle; Odin operated in astronomy mode one day, aeronomy mode the next, with the third day given to provide some leeway for additional observations to be made in periods of interest in either operating mode [Murtagh *et al.*, 2002]. Additional time blocks were allocated to allow for particular measurements to be made during known periods of interest, such as aeronomy atmospheric measurements during the hemispheric spring periods [Murtagh *et al.*, 2002]. A general summary of the initial allocation of operating modes is provided in Figure 2-2. An additional period was allocated during July for the study of the summer mesopause, and astronomy mode received extra time during March and September when the galactic plane and centre is visible [Murtagh *et al.*, 2002].

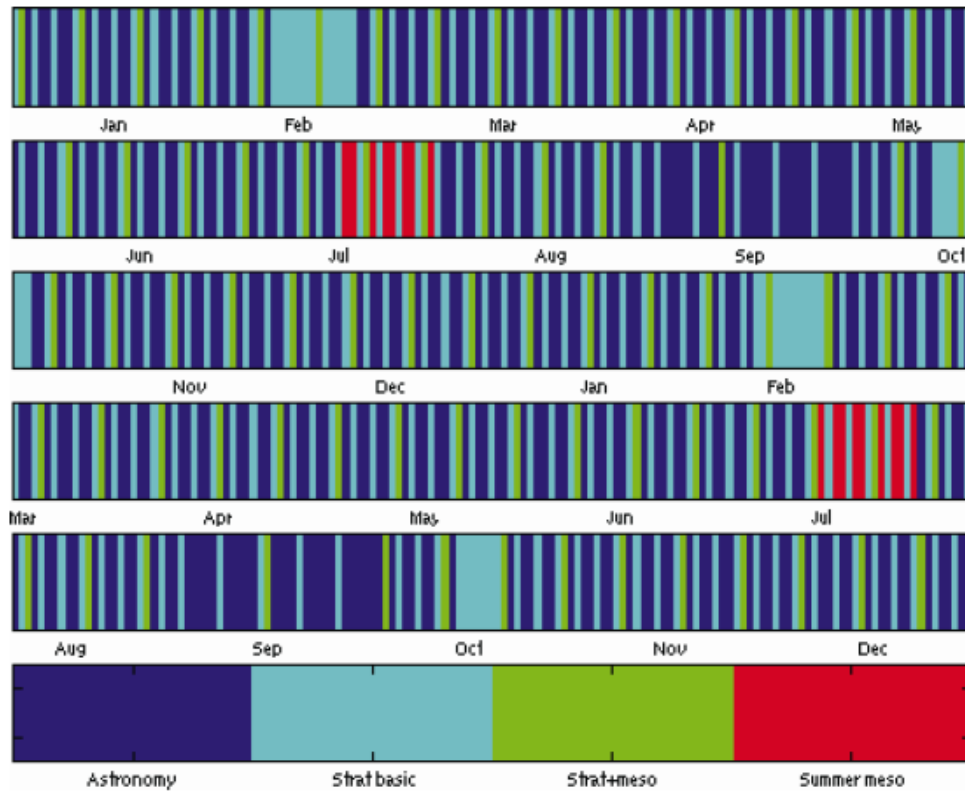


Figure 2-2: *Nominal division of time for Odin astronomy and aeronomy modes. Reproduced from Murtagh et al. [2002].*

2.3 The OSIRIS instrument

The OSIRIS instrument consists of an optical spectrograph (OS) and an infrared imager (IRI) which makes daylight limb measurements between 280-810 nm, for tangent heights between 5-110 km. The instrument has a mass of 12 kg and its power consumption is between 15-20 W depending on operating mode.

An exposed view of the instrument showing its main components is given in Figure 2-3. The OS and IRI are optically separate instruments but their fields-of-view are aligned with each other and also with the sub-millimetre SMR instrument. This thesis is mainly concerned with the wideband OS instrument which is used to measure the atmospheric radiance from K at 770 nm and Na at 589 nm. A photograph of the OSIRIS instrument is given in Figure 2-4.

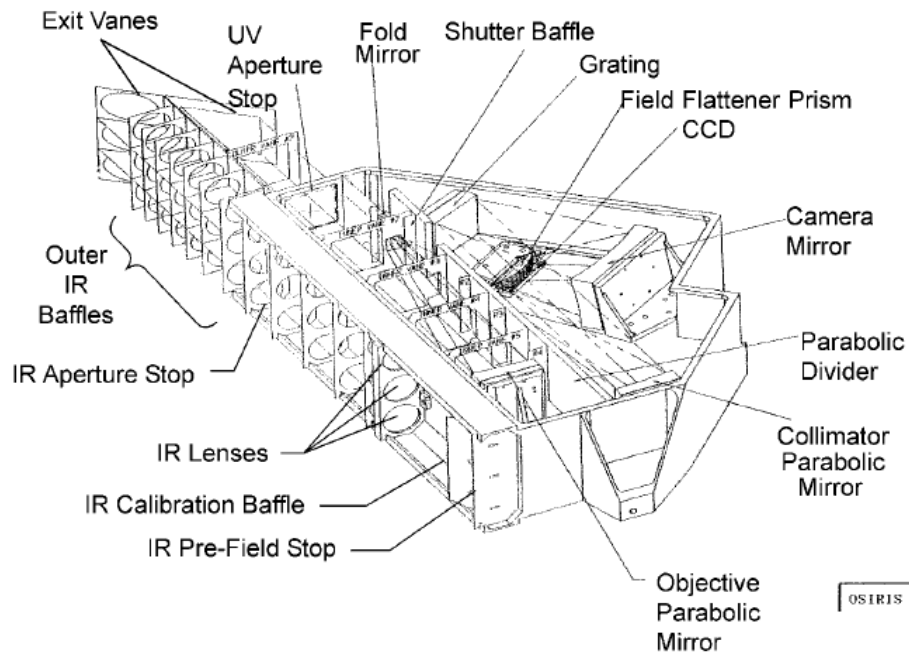


Figure 2-3: Configuration of the OSIRIS instrument. Reproduced from Llewellyn et al. [2004].

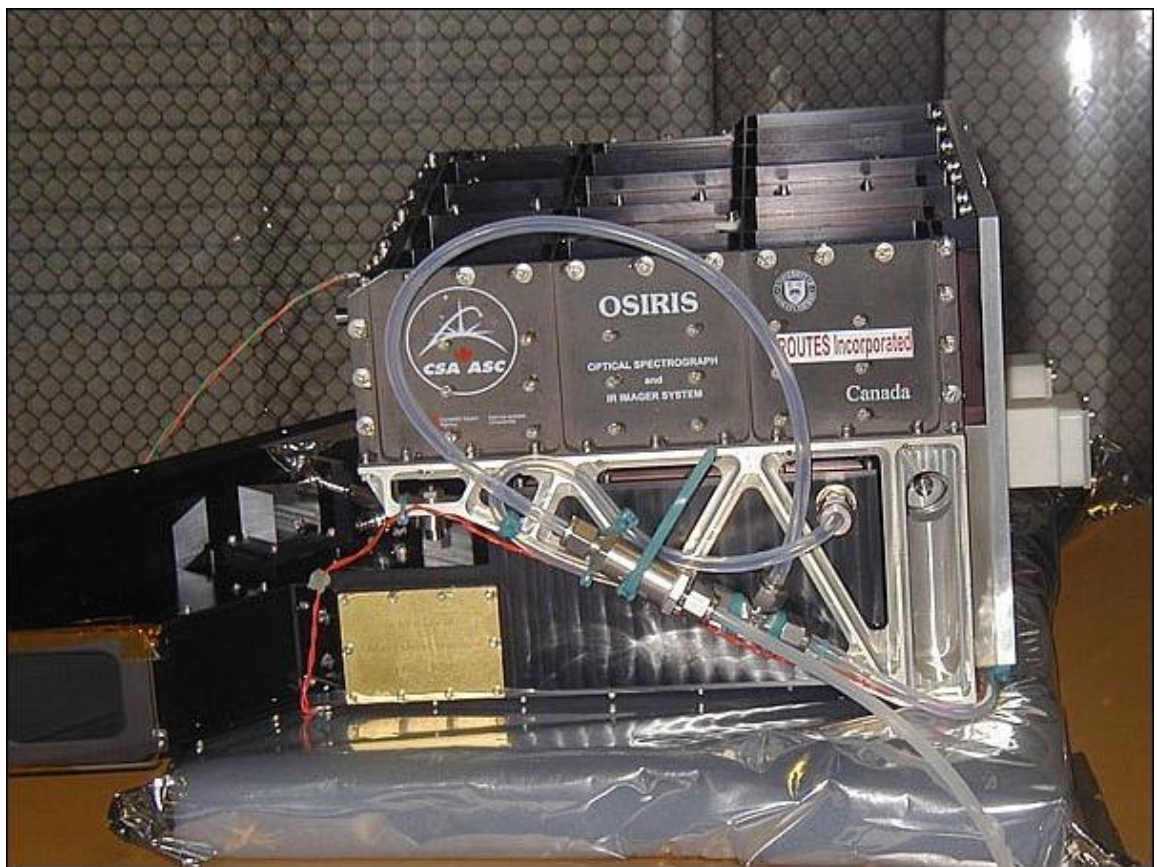


Figure 2-4: Photograph of the OSIRIS instrument. Reproduced from https://directory.eoportal.org/documents/163813/198303/Odin_Auto1.

The optical details of the OSIRIS instrument are shown in Figure 2-5. The incoming UV/VIS radiation is focussed by the objective parabolic mirror on to a plane mirror which folds the optical path. After reflection from the collimator parabolic mirror, the radiation falls on to the diffraction grating where the diffracted radiation is re-focussed out-of-plane by the camera mirror, via the field-flattening prism onto the charge-coupled detector (CCD) array. The input slit of the spectrograph is imaged on to the CCD such that the vertical columns correspond to the horizontal field-of-view (FOV) and the horizontal rows correspond to the light dispersed in wavelength.

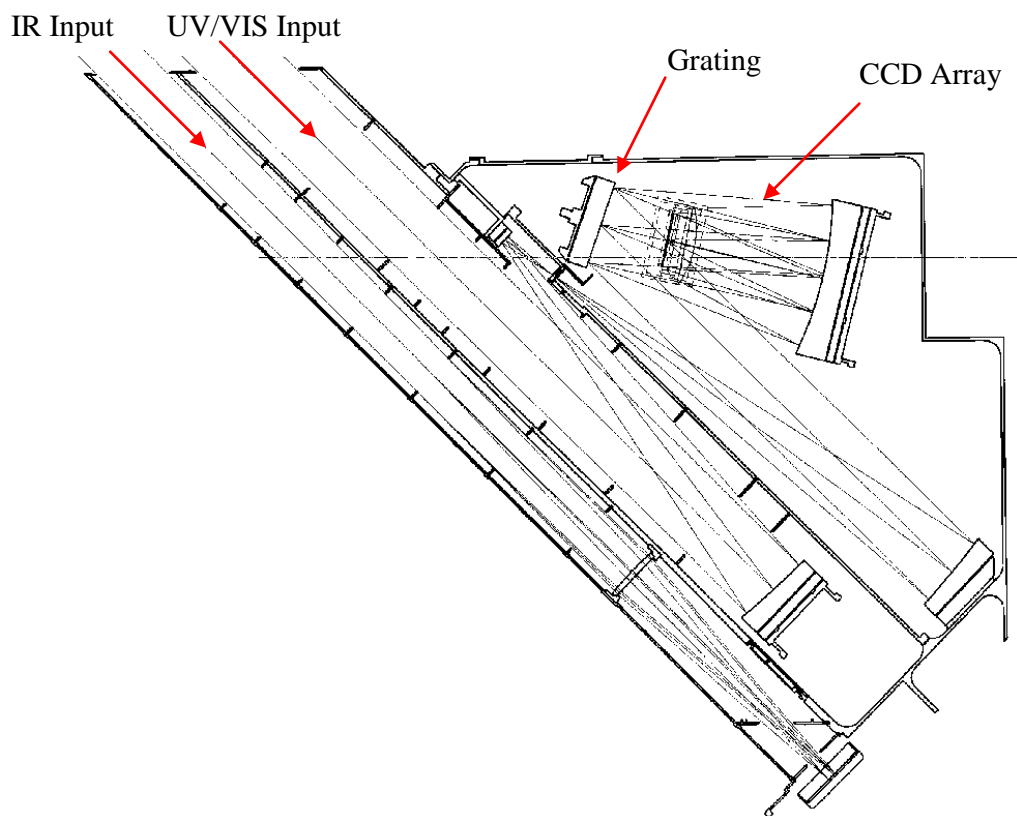


Figure 2-5: *Optics configuration of the OSIRIS instrument. Reproduced from Warsaw et al. [1996].*

The spectral response of the CCD ultimately determines the spectral passband of the UV/VIS part of the OSIRIS instrument. The CCD used is UV-enhanced with a UV anti-reflection coating giving high quantum efficiency at the UV end of the spectrum. The CCD has a frame transfer structure and is operated in multi-pinned phase (MPP) mode

with the matrix array of 1353 x 286 pixels. The row of 1353 pixels corresponds to the diffracted wavelengths within the range 280-800 nm. The spectral resolution is ~1 nm. On one side of the array, 32 column pixels are employed to detect horizontal FOV slit image brightening, while the remaining columns provide spectrograph internal scattering features.

The CCD detector is passively cooled by radiation which maintains a relatively stable thermal environment at ~-20°. In addition, maintaining the CCD at this temperature prevents the dark current from integrating to a significant level after 10 s. The CCD operates with integration times selectable from 0.1 to 10 s. Figure 2-6 displays the overall 32 pixel sensitivities of the UV/VIS spectrograph at various wavelengths during calibration. As shown, the sensitivity has degraded performance near the lower and higher wavelength boundaries.

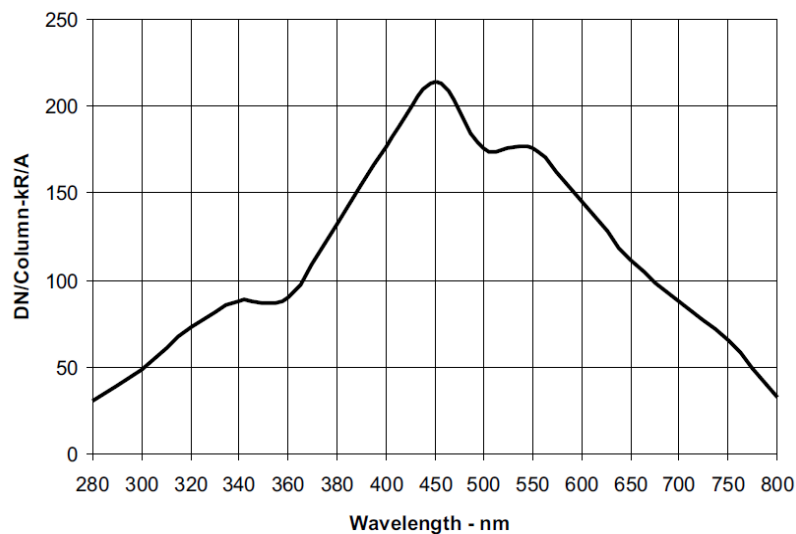


Figure 2-6: Tested mean optical spectrograph sensitivity within the UV/VIS wavelength range. Reproduced from Llewellyn et al. [2004].

There is no internal radiometric calibration provided within the UV/VIS part of the OSIRIS instrument. Instead calibration is provided by observing artificial sources emanating from the Earth during orbit. On-ground characterisation of the instrument was performed including determining the efficiency of the diffraction grating for both

horizontal and vertically polarised radiation. In Figure 2-7, the response to radiation parallel (g_{12}) and perpendicular (g_{13}) to the grating grooves is shown.

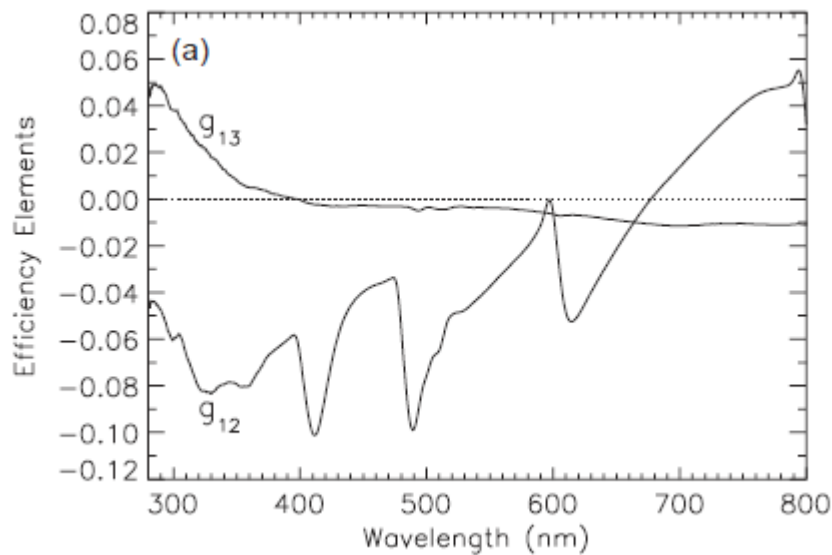


Figure 2-7: Polarisation response of OSIRIS UV/VIS spectrograph. Reproduced from McLinden et al. [2002].

2.4 OSIRIS Data Processing

The OSIRIS data is processed to levels 1 and 2 at the University of Saskatchewan, Saskatoon, Canada with the processed data stored at the Parallel Data Center (PDC) in Stockholm, Sweden. The archive of the Odin mission is located at the Royal Institute of Technology in Stockholm, Sweden.

The OSIRIS level 1 data (which consists of calibrated radiance spectra) used in this work was provided by Prof. Jörg Gumbel from Stockholm University. The fully calibrated data was supplied in '.mat' MATLAB format, pre-sorted into individual orbits.

2.5 Mass Spectrometer Incoherent Scatter Extension model (MSISE-00)

The NRL (Naval Research Laboratory) Mass Spectrometer Incoherent Scatter Extension (MSISE) empirical model [Picone *et al.*, 2002] calculates the neutral densities and temperature between 0-700 km and is based on user-specific geophysical parameters. It consists of the Committee on Space Research (COSPAR) International Reference Atmosphere (CIRA) 1986 and uses composition, density and temperature data from a number of observational datasets, including from rockets, seven different satellites (AEROS-A, AE-C, AE-D, AE-E, DE-2, ESRO 4, OGO-6 and San Marco 3) and five incoherent scatter radars (Arecibo, Jicamarca, Malvern, Millstone Hill and St. Santin). It can be used to calculate the number densities of Ar, H, He, N, N₂, O, and O₂, total mass density, neutral temperature and exospheric temperature, all of which are provided as a look-up table.

Data from the MSISE-00 model is used in Chapter 3.

2.6 ECMWF ERA-Interim

The European Centre for Medium-range Weather Forecasts (ECMWF) ERA-Interim dataset is a global atmospheric reanalysis which extends from 1st January 1979 to present. The model has a T255 spectral resolution, an approximate horizontal resolution of 0.7°, on 60 vertical levels extending from the surface up to a pressure surface of 0.1 hPa. It uses the 2006 version of the Integrated Forecasting System (IFS Cy31r2) and is continuously updated in near-real time. The reanalyses are available as gridded data products of 6-hourly atmospheric fields on model levels and pressure levels including potential temperature and potential vorticity, and both 3-hourly surface fields and daily vertical integrals. Monthly means of daily values are also available at 0, 6, 12 and 18 UTC. Further information can be found in Dee *et al.* [2011].

The ECMWF ERA-Interim data is used in Chapter 3.

2.7 OSIRIS Na data

All OSIRIS Na data used in this thesis (used in Chapters 5 and 6) has been processed by the candidate using the Na retrieval algorithm provided by Prof. Jörg Gumbel. A previous publication by Hedin and Gumbel [2011] documented the retrieved Na dataset from 2004-2010. As part of this thesis, the OSIRIS Na has been re-processed and extended from 2004 to June 2013.

2.8 NCAR Whole Atmosphere Community Climate Model (WACCM)

The National Center for Atmospheric Research (NCAR) WACCM model is a comprehensive coupled chemistry climate model and is part of the Community Earth System Model (CESM) framework. Using this common numerical framework, WACCM has been designed to provide a flexible model environment, in which the domain and component modules can be adjusted and configured for specific user requirements.

The standard model extends from the Earth's surface up to ~140 km with 66 vertical levels (vertical resolution of approximately 1.5 km in the lower atmosphere, and ~3 km in the MLT region), and a horizontal resolution of $1.9^\circ \times 2.5^\circ$ (lat-lon). WACCM consists of a fully-interactive chemistry scheme and includes shortwave heating and photolysis from Lyman- α to E-UV. Above 60 km, it incorporates non-LTE (local thermal equilibrium) IR transfer. It includes a parameterisation for gravity waves from convection and fronts (and their subsequent breaking within the mesopause region) and includes thermospheric processes such as aurora, ion chemistry and molecular diffusion.

Metal chemistry modules have been added for Na [Marsh *et al.*, 2013], Fe [Feng *et al.*, 2013] and Mg, Si and Ca (all by W. Feng).

All WACCM output data has been provided by Dr. Wuhu Feng, and WACCM data is used in Chapters 5 and 6. In Chapter 5, data from WACCM-ERA (WACCM nudged with ERA-Interim) data is used. In Chapter 6, a free-running WACCM is employed.

2.9 TIMED/SABER instrument

The Sounding of the Atmosphere using Broadband Emission Radiometry (SABER) instrument is found onboard the NASA TIMED (Thermosphere Ionosphere Mesosphere Energetics Dynamics) satellite. The overarching aim of the TIMED mission is to learn more about the MLT region, particularly with respect to the fundamental processes driving the chemistry and dynamics between 60-180 km.

The SABER instrument is one of four instruments onboard TIMED to assist in achieving this goal. SABER consists of a 10-channel broadband limb-scanning infrared radiometer which covers the spectral range 1.27-17 μm . It performs global measurements which provide information on kinetic temperature, and volume mixing ratios of various trace species including O_3 , CO_2 and H_2O .

Launched on December 7th 2001, the TIMED satellite orbits at 625 km, in a non-Sun-synchronous drifting orbit with an orbital inclination of 74.1° , and a mean orbit period of 97 minutes. As a result of this drifting orbit, the latitudinal coverage depends on a 60-day yaw cycle (the yaw manoeuvre reverses the scanning direction of the SABER instrument by 180° , in order to cover the polar regions) which results in observations of latitudes between 82°S to 52°N in the south-viewing phase, and 52°S to 82°N in the north-viewing phase. As such, continuous measurements at high latitudes are not available. The SABER instrument provides near-continuous measurements and scans between the Earth's surface to 400 km, with a vertical instantaneous FOV of approximately 2.0 km at 50 km altitude, with a vertical resolution of ~ 0.4 km.

SABER temperature data is used in Chapters 5 and 6.

2.10 Solar F10.7 radio flux

The solar radio flux at 10.7 cm (commonly referred to as the solar F10.7 index) provides an indicator of solar activity and correlates well with records of UV and visible solar irradiance datasets and sunspot activity. The F10.7 index is provided in 'solar flux units' (s.f.u., equal to $10^{-22} \text{ W m}^{-2} \text{ Hz}^{-1}$) which range from below <50 s.f.u to >300 s.f.u. across a full solar cycle. Consistent daily measurements have been made since 1947 and are now made at the Dominion Radio Astrophysical Observatory in British Columbia, Canada.

The F10.7 index data has been downloaded from the Space Weather Prediction Center (<http://www.swpc.noaa.gov/>) and it is used in Chapter 6.

2.11 Lidar data

The K lidar data used in Chapter 4 is provided for two individual lidar stations; Arecibo (18°N, 293°E) and Kühlungsborn (54°N, 12°E). night-time data from the Arecibo lidar station is kindly provided by Dr. Jonathan Friedman covering the period Jan 2004 to Dec 2009. The data is supplied as individual profiles and requires processing prior to use (e.g. generating monthly profiles and associated mean error). The Kühlungsborn data has be provided by Dr. Josef Höffner, extending from Jan 2004 to Dec 2010. This data has been supplied pre-processed and is only available as night-time monthly mean column densities with associated errors.

3 THE POTASSIUM RETRIEVAL METHODOLOGY

3.1 Introduction

This chapter describes the retrieval technique developed for determining the best fit density profiles for the K radiance profiles measured by the OSIRIS instrument onboard the ODIN satellite. The retrieval scheme used for K is based on a modification of the retrieval scheme developed for Na by Gumbel *et al.* [2007].

In this approach, a forward model is used to simulate a radiance profile that would result from a given K density profile under a particular set of atmospheric and measurement conditions. An optimal estimation method (described by Rodgers [1976, 2000]) is then used with the forward model to determine the best-fit density profile for a given radiance profile. The optimal estimation approach is described in Section 3.2 and the forward model is described in Section 3.3.

The extraction of the K radiance values from the measured OSIRIS limb spectra at 770 nm is a challenging proposition compared with the retrieval of Na. the techniques used to extract these K radiance values are described in Section 3.4.

3.2 Optimal estimation method

3.2.1 Introduction

The problem of inverting measured atmospheric radiance data in order to yield the number density profiles was addressed by Rodgers [1976, 2000]. The starting point for his optimal estimation method was to define a forward model, $F(x,b)$, which relates a set of radiance measurements, y , to the corresponding density profile, x , via:

$$y = F(x,b) + \varepsilon \tag{3.1}$$

In this equation, b includes the set of parameters (e.g. solar zenith angle, albedo, etc) on which the atmospheric radiance values depend, but which are not retrieved in the

inversion process, i.e. are assumed known values. The parameter ϵ represents the set of errors in the measured radiance values.

The numerical technique developed by Rogers inverts the above Equation 3.1 to yield the best estimates of the number density profile, x , based on an assumption of a Gaussian distribution of the measurement errors, ϵ . This inversion method is described below.

3.2.2 *The inversion method*

The inversion of Equation 3.1 is a non-linear problem due to the forward function $F(x, b)$ having a degree of non-linearity. Rogers employed a maximum likelihood condition in order to determine the solution, x , by minimising the following function:

$$\sum [y - F(x, b)]^T \cdot S_e^{-1} \cdot [y - F(x, b)] \quad 3.2$$

where S_e is the measurement error covariance matrix.

The forward function, $F(x, b)$, is assumed to be moderately non-linear and a Gauss-Newton approach is then used to find an iterative solution to the problem. Below, the forward model is expanded about an initial estimate, x_n . The b parameter is omitted from this and subsequent equations for convenience.

$$y = F(x_n) + \frac{\delta F(x_n)}{\delta x} \cdot (x - x_n) + O(x - x_n)^2 \quad 3.3$$

The above equation can be simplified and rewritten as:

$$y = y_n + K_n \cdot (x - x_n) + O(x - x_n)^2 \quad 3.4$$

where K_n is the weighting function given by:

$$K_n = \frac{\delta F(x_n)}{\delta x} \quad 3.5$$

In order to find an iterative solution to the unknown number density profile x , the maximum likelihood estimator given in Equation 3.2 must be minimised by equating its

first derivatives to zero, and then substituting for y from the simplified Equation 3.4. A numerically efficient solution can be found by choosing an initial solution, x_0 , based on *a priori* information. In this way, the iterative solution can be written in the final form:

$$x_{n+1} = x_0 + S_x \cdot K_n^T \cdot (K_n \cdot S_x \cdot K_n^T + S_e)^{-1} \cdot [y - y_n - K_n \cdot (x - x_0)] \quad 3.6$$

The corresponding error covariance is given by:

$$S_{n+1} = S_0 - G(K_n \cdot S_0) \quad 3.7$$

Equation 3.6 can then be rewritten in the simpler form:

$$x_{n+1} = x_0 + G_n \cdot [y - y_n - K_n \cdot (x - x_0)] \quad 3.8$$

where the contribution function G_n is given by:

$$G_n = S_0 \cdot K_n^T \cdot (K_n \cdot S_0 \cdot K_n^T + S_e)^{-1}. \quad 3.9$$

In this equation, S_0 is the covariance of the *a priori* starting profile, and S_e is the covariance of the radiance measurements.

3.3 The forward model

3.3.1 Model Description

The forward model used in this work is a modification of that used for the Na retrieval in Gumbel *et al.* [2007] and first reported in Strong *et al.* [2002]. The forward model simulates a vertical radiance profile for a given input number density profile, as would be measured by the OSIRIS instrument under a specific set of atmospheric conditions.

The following theory for calculating the single-scattered limb radiance $I(\lambda, z_{\text{tan}})$ for wavelength λ and tangent height z_{tan} is reproduced from Strong *et al.* [2002], starting with:

$$I(\lambda, z_{\text{tan}}) = E_0(\lambda) \int_{\text{LOS}} \tau_{\text{in}}(\lambda, \infty : z) \cdot S(\lambda, z, \theta) \cdot \tau_{\text{out}}(\lambda, z : \infty) \cdot dz \quad 3.10$$

This can be rewritten in terms of the incoming and outgoing in the form:

$$I(\lambda, z_{\text{tan}}) = E_0(\lambda) \int_{\text{LOS}}^{\infty} \tau_{\text{in}}(\lambda, \infty : s(z)) \cdot S(\lambda, z, \theta) \cdot \tau_{\text{out}}(\lambda, s(z) : \infty) \cdot ds(z) \quad 3.11$$

$$+ E_0(\lambda) \int_{z_{\text{tan}}}^{\infty} \tau_{\text{in}}(\lambda, \infty : s(z)) \cdot S(\lambda, z, \theta) \cdot \tau_{\text{out}}(\lambda, s(z) : \infty) \cdot ds(z)$$

where $E_0(\lambda)$ is the solar irradiance incident on the top-of-the-atmosphere (TOA) at wavelength λ , $\tau_{\text{in}}(\lambda, \infty : z)$ is the atmospheric transmission in from the TOA to the scattering point at altitude, z , along the OSIRIS LOS. $\tau_{\text{out}}(\lambda, z : \infty)$ is the atmospheric transmission back out from the scattering point at altitude z along the OSIRIS LOS to the TOA, while $s(z)$ denotes the altitude-dependent slant path along the LOS. Finally, $S(\lambda, z, \theta)$ is a scattering term describing the proportion of solar irradiance single-scattered into the instrument LOS, for a forward scattering angle, θ .

In this equation, the integration is divided into two terms, the first corresponding to solar irradiance on the atmosphere beyond the tangent point (far field) and the second between the tangent point and the satellite (near field). This is illustrated in the Figure 3-1 below.

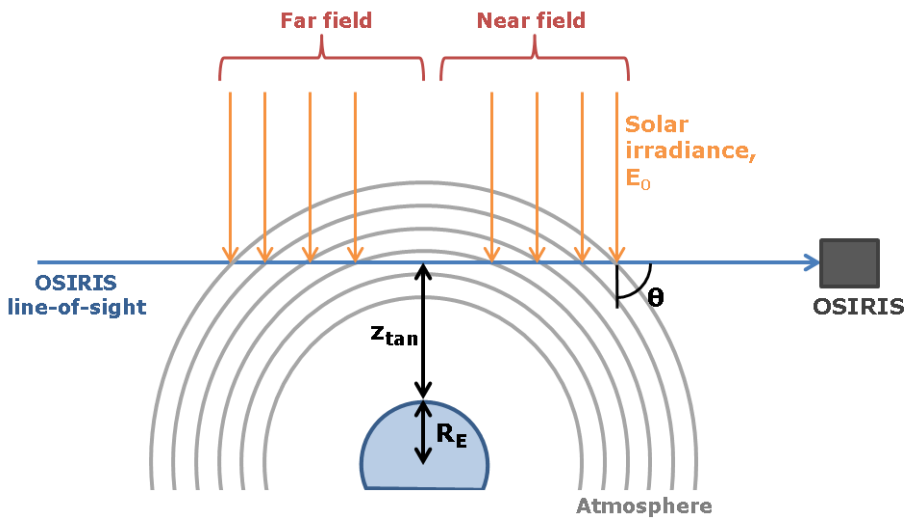


Figure 3-1: Schematic of the limb-viewing geometry in a spherical atmosphere. Adapted from Strong et al. [2002].

The various terms in Equation 3.11 can be individually expanded, so that:

$$\tau_{in}(\lambda, \infty : s(z)) = \exp \int_{\infty}^z k(\lambda, z') . ds(z') \quad 3.12$$

$$S(\lambda, z, \theta) = \frac{1}{4.\pi} P(\theta) . k^{scat}(\lambda, z) \quad 3.13$$

$$\tau_{out}(\lambda, \infty : s(z)) = \exp \int_z^{\infty} k(\lambda, z') . ds(z') \quad 3.14$$

In these equations, $k(\lambda, z)$ is the total volume extinction coefficient as a function of wavelength and altitude, which consists of a combination of Rayleigh and Mie scattering, and absorption by trace gases, such that,

$$k(\lambda, z) = k^{scat}(\lambda, z) + k^{abs}(\lambda, z) = \sigma_{Ray}(\lambda) + \sigma_{Mie}(\lambda) + \sum_i \sigma_i(\lambda) . N_i(z) \quad 3.15$$

where $\sigma_{Ray}(\lambda)$ is the Rayleigh scattering cross-section, $\sigma_{Mie}(\lambda)$ is the Mie scattering cross-section, $\sigma_i(\lambda)$ is the absorption cross-section of trace gas i , and $N_i(z)$ is the atmospheric number density for trace gas species i . $P(\theta)$ is the effective phase function for the scattering which will be defined in the next section .

The K metal layer has a full-width half-maximum of approximately 9 km, and a typical peak atmospheric abundance of only 50 cm^{-3} [e.g. Eska *et al.*, 1998]. This, in conjunction with the fact that the atmosphere is optically thin within the MLT region, results in the mean free path of a scattered photon exceeding 100 km, and the OSIRIS instrument limb-viewing geometry (where the solar scattering angle typically varies between $60\text{-}120^\circ$), means that single-scattering dominates. Thus, in this work, only single elastic scattering is considered, which has the advantage of greatly improving the computational efficiency of the forward model.

3.3.2 Phase function

The phase function $P(\theta)$ for the resonance line scattering is included in Equation 3.13. The phase function is derived from Chandrasekhar [1960] which states that the phase function for angle, θ , for radiation emitted by resonant line emission, is equal to the superposition of both the anisotropic (first term) and isotropic (second term) components, such that:

$$P(\theta) = \frac{3}{4}E_1(\cos^2(\theta) + 1) + E_2 \quad 3.16$$

The constants E_1 and E_2 depend on the angular momentum number, j , of the two energy states for the transition of interest, and are determined using the formulae presented in the table below.

Table 3-1: Calculating the E_1 and E_2 constants. Reproduced from Chandrasekhar [1960].

Δj	E_1	E_2
1	$\frac{(2j+5)(j+2)}{10(j+1)(2j+1)}$	$\frac{3j(6j+7)}{10(j+1)(2j+1)}$
0	$\frac{(2j-1)(2j+3)}{10j(j+1)}$	$\frac{3(2j^2+2j+1)}{10j(j+1)}$
-1	$\frac{(2j-3)(j-1)}{10j(2j+1)}$	$\frac{3(6j^2+5j-1)}{10j(2j+1)}$

For the $K D_1$ transition, there is no change in angular momentum ($\Delta j = 0$), as $j = \frac{1}{2}$ for both the upper and lower energy states [Kramida *et al.*, 2013] and the E_1 and E_2 constants therefore have values of 0 and 1, respectively. This means that the $K D_1$ transition only has an isotropic phase component (i.e. no angular dependence), so that $P(\theta)$ and it can subsequently be ignored.

3.3.3 Spectroscopic properties of K

In order to compute Equation 3.11, the absorption cross-section of K must be known as used in Equation 3.15 which means that individual spectroscopic properties of the K atoms at the resonance transition at 770 nm must be known. The K(D₁) line has an air wavelength of 769.898 nm [von Zahn and Höffner, 1996], and consists of three different isotopes, ³⁹K, ⁴⁰K and ⁴¹K, with respective relative abundances of 93.1%, 0.012% and 6.73%.

The transitions of the K(D₁) and K(D₂) lines are shown below in Figure 3-2. Each D line is subject to further hyperfine split structure lines, such as seen in Figure 3-3. Each of the most abundant isotopes (³⁹K and ⁴¹K) has a slightly different distribution of the four hyperfine split lines. The OSIRIS spectral resolution has insufficient resolution to detect the relative changes in the overall line shape produced by the slightly different hyperfine structure of the different potassium isotopes. As such, no treatment of the hyperfine lines nor the different isotope abundances is considered within the forward model. This is not thought to be a significant approximation, particularly as at mesospheric temperatures (~200 K), the line shape is predominantly Gaussian as shown in Figure 3-3. In the original Na retrieval [Fan *et al.*, 2007; Gumbel *et al.*, 2007], the sodium D line hyperfine structure *was* considered. In this case, it was important to do so because of the proximity of the sodium D lines to one another (0.6 nm), with the relative intensities of both D lines affecting the overall line shape seen by the OSIRIS instrument.

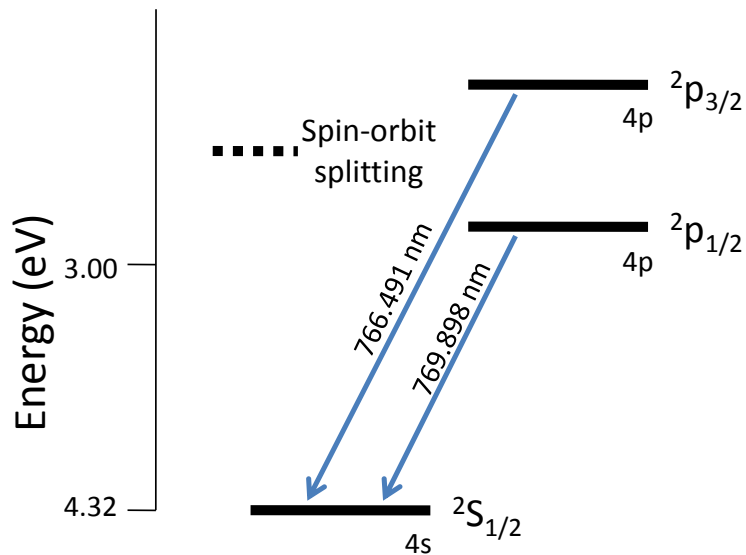


Figure 3-2: Grotrian diagram to show the $K(D_1)$ and $K(D_2)$ line transitions. Note that the $K(D_2)$ (at $\sim 766.5\text{nm}$) cannot be resolved in the OSIRIS spectra due to its proximity to the O_2 A-band (760-765 nm).

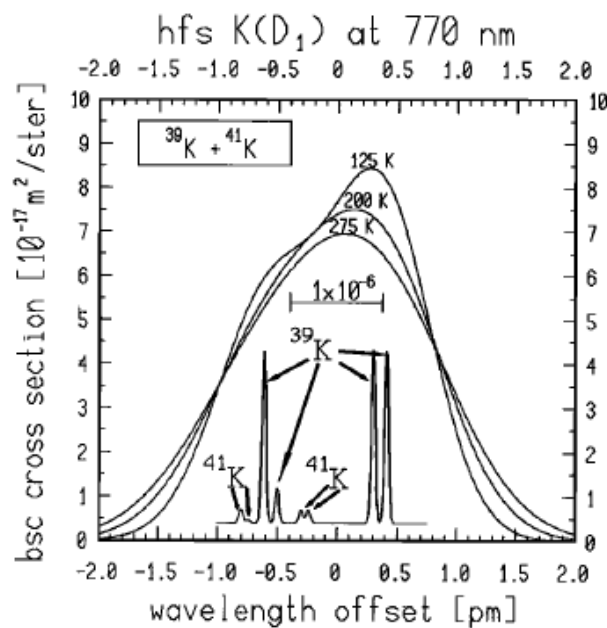


Figure 3-3: The variation of the backscatter cross-section of the $K(D_1)$ transition at $\sim 770 \text{ nm}$ for different temperatures [K]. The positions and relative strengths of the hyperfine split lines is shown for each of the main potassium isotopes (^{39}K and ^{41}K). Reproduced from von Zahn and Höffner [1996].

In order to simulate the correct limb radiance that the OSIRIS instrument would see along its LOS, it is important that the individual K line shapes for each tangent height are modelled (within sufficient resolution) before they are integrated to produce a simulated vertical radiance profile. The spectral resolution used in the forward model is 0.1 pm at the line centre (~770 nm) and 1 pm in the flanks. The K atom cross-section, σ , is calculated using the following formula adapted from the Na retrieval code supplied by Gumbel [personal communication],

$$\sigma = \left(\frac{\left(\frac{\lambda_0 e^2 \sqrt{\pi}}{4\pi\epsilon_0 c^2 (\text{widthFactor}) m_e} f_{K(D_1)} (\lambda_0 - \lambda_{K(D_1)})^2 \right)}{\sqrt{T}} \right) \quad 3.17$$

where λ_0 is the transition wavelength at the line centre, e is the electron charge, ϵ_0 is vacuum permittivity, c is the speed of light, m_e is the mass of an electron and T is the temperature in Kelvin. The `widthFactor` term in further detail below.

The oscillator strength at the $K(D_1)$ transition, $f_{k(D_1)}$, is the probability of absorption or emission by an atom which transitions from one energy state to another. For the $K(D_1)$ transition, $f_{k(D_1)}=0.333$ [Kramida *et al.*, 2013]. The $(\lambda_D - \lambda_{K(D_1)})^2$ term is an expression for the difference between the line centre and a line shifted relative to the line centre. Figure 3-4 shows an example cross-section profile with the line flanks relative to the line centre. At the line centre, the cross-section is $\sim 1.3 \times 10^{-11} \text{ cm}^2$.

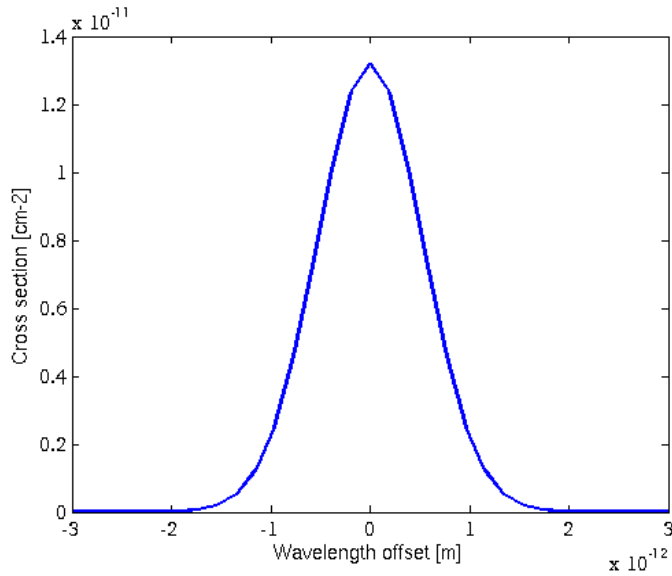


Figure 3-4: $K(D_1)$ line cross-section calculated for $T = 200$ K.

The widthFactor term corresponds to the Doppler line width or the 1/e width and is given by

$$\text{widthFactor} = \frac{1}{c} \sqrt{\frac{2k_b}{m_K}} \sqrt{T} \quad 3.18$$

The Doppler broadening of spectral lines occurs as a function of the temperature T and the mass of the emitting particles - in this case of K, m_K . Constants in the equation include the speed of light, c , and the Boltzmann constant, k_b . A change in temperature causes a change in the distribution of the velocities of the emitting particles which can result in Doppler broadening of the overall line shape. At higher temperatures, there is a larger range of velocities of the emitting particle, which results in a broadening of the spectral line. This effect must be taken into account when considering the changing temperature profile with altitude and determining the total emission signal. At around 85-90 km altitude, Doppler broadening accounts for 0.9 pm of the total line shape as shown in Figure 3-5. This is a relatively small shift compared with the cross-section of the line centre.

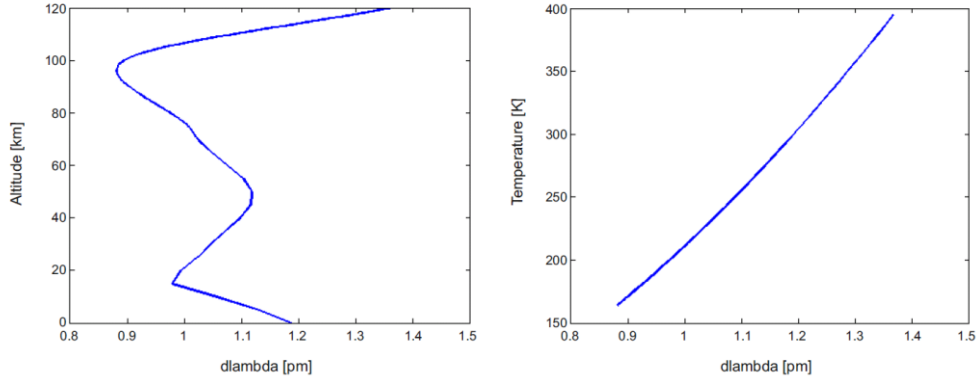


Figure 3-5: [Left] The Doppler broadening (units: pm) as a function of altitude (km) for $T = 200$ K. [Right] The Doppler broadening (pm) as a function of temperature (K).

The mesospheric K layer has a typical full-width half maximum (FWHM) of 10 km [e.g. Eska *et al.*, 1999] and the K atom has a large absorption cross-section of 10^{-12} cm² atom⁻¹. Therefore, the possibility of self-absorption, that is the re-absorption of a photon by a potassium atom, must be considered. If self-absorption occurs, it could result in an error in the retrieved K number density as a consequence of a reduction in the radiance detected along the instrument LOS. In order to estimate the impact of self-absorption for the K(D₁) line, the total absorption α is calculated for a range of path lengths, s , and number densities, N , using the following simplification of the Beer-Lambert law:

$$\alpha(N, s) = \exp(-Ns\sigma) \quad 3.19$$

From Figure 3-6, we can see that self-absorption increases as a function of increasing number density and/or path length. At the observed atmospheric abundances (typically with a peak around 50 atoms cm⁻³) and total LOS path lengths of <1,500 km, self-absorption is 6% or less. This self-absorption is accounted for within the forward model.

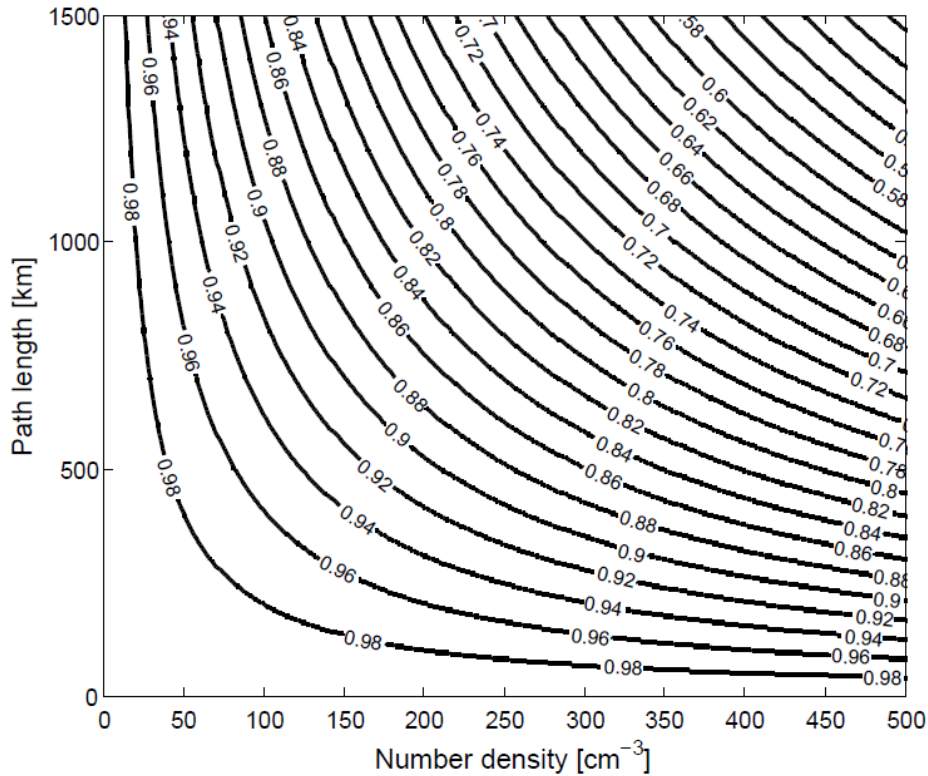


Figure 3-6: Transmission and self-absorption by the K atom as a function of number density and path length. The line values represent the transmission. When there is no absorption, the transmission is equal to 1. N.B. the path lengths used in the calculation are in units of cm. These are converted to units of km in this, for reasons of clarity only.

3.3.4 Determining the solar irradiance

Another key part of solving Equation 3.11 is knowledge of the incident solar radiation $E_0(\lambda)$, at the transition wavelength. In particular, consideration must be made of the Fraunhofer structure lines, which occur as a result of wavelength-specific absorption in the solar photosphere, if the radiative transfer is to be correctly simulated. The Fraunhofer structure relevant to the retrieval of K at 770 nm are shown in Figure 3-7.

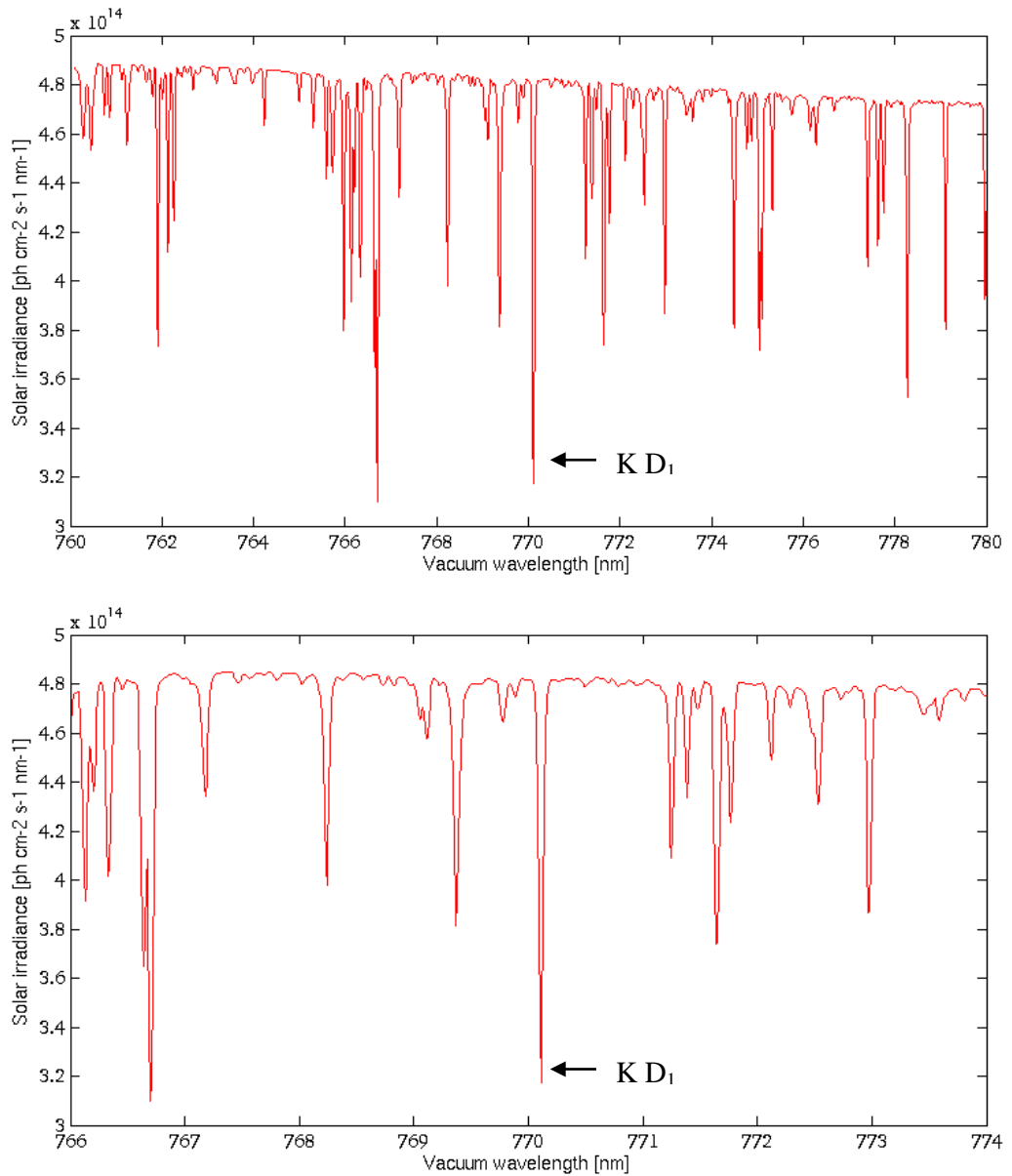


Figure 3-7: The vacuum wavelength solar irradiance spectrum (at 0.01 nm resolution) for wavelength ranges 760-780 nm [top panel] and 760-774 nm [lower panel]. The data is described in Chance and Kurucz [2010] and is available from <http://www.cfa.harvard.edu/atmosphere/links/sao2010.solref.converted>.

The shape of these Fraunhofer structures must be characterised so that the absolute solar irradiance flux at the bottom of the absorption feature is known, along with that at the wings. This is particularly important when considering Doppler shifts and red shifts of the incident solar light relative with respect to the terrestrial atmosphere. In the Gumbel *et al.* [2007] Na retrieval, these descriptive parameters were taken from an experimental

study by McNutt and Mack [1963]. Unfortunately no such experimental data is available for the 770 nm wavelength, nor is a sufficiently high resolution solar spectrum at these wavelengths, capable of resolving the solar spectrum to the equivalent resolution used in McNutt and Mack [1963].

Instead, a new approach is adopted here which estimates the shape of the true 770 nm Fraunhofer line, based on a comparison of the differences between the Na 589 nm Fraunhofer line and that at 770 nm (see Figure 3-8).

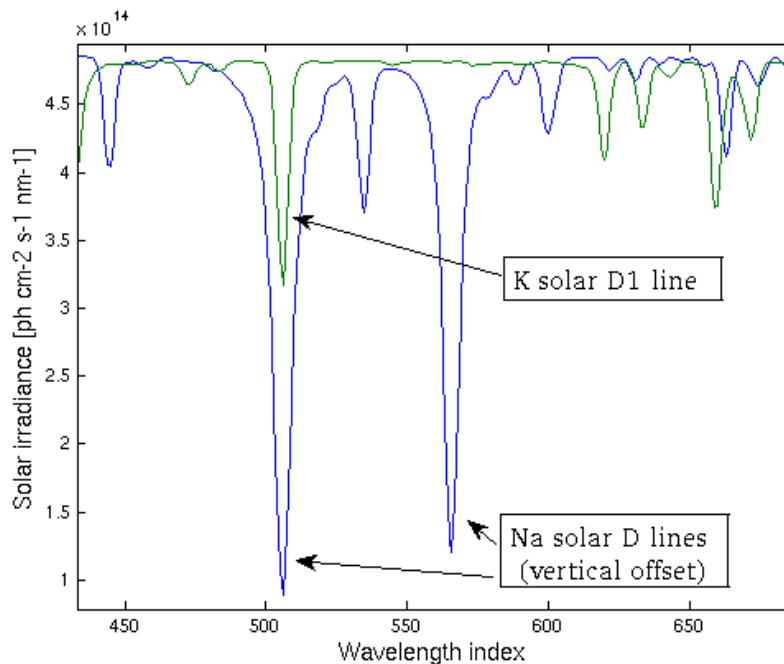


Figure 3-8: Comparison of the $K(D_1)$ Fraunhofer line to the Na solar D lines. The K solar line is much shallower than the Na line, as well as being much narrower. The Na solar D lines have been vertically offset in order for clearer comparison with the K line.

The relative flux at the bottom of the Na(D_1) Fraunhofer line is 0.0495 (here referred to as $I_{ref_{Na}}$), that is, the solar irradiance, is 4.95% of the solar irradiance at the top of the solar spectrum at these wavelengths. An estimate for the equivalent value for the K(D_1) can be found by comparing the depth of the Na and K Fraunhofer lines in a relatively high-resolution solar spectrum (0.01 nm), Chance and Kurucz [2010]) using the relationship

$$I_{ref_K} = \frac{Depthratio_K}{Depthratio_{Na}} I_{ref_{Na}} \quad 3.20$$

By determining the relative depths of the Na and potassium Fraunhofer lines (see Figure 3-9), a value of $I_{ref_K} = 0.11$ is found. After comparison with lidar data, a final value of $I_{ref_K} = 0.13$ is used. The discrepancy between this optimised value and the calculated value (0.11) is likely as a result of the different wavelength resolutions used, both in the Chance and Kurucz spectra, and the empirical spectra described in the McNutt and Mack [1963] paper.

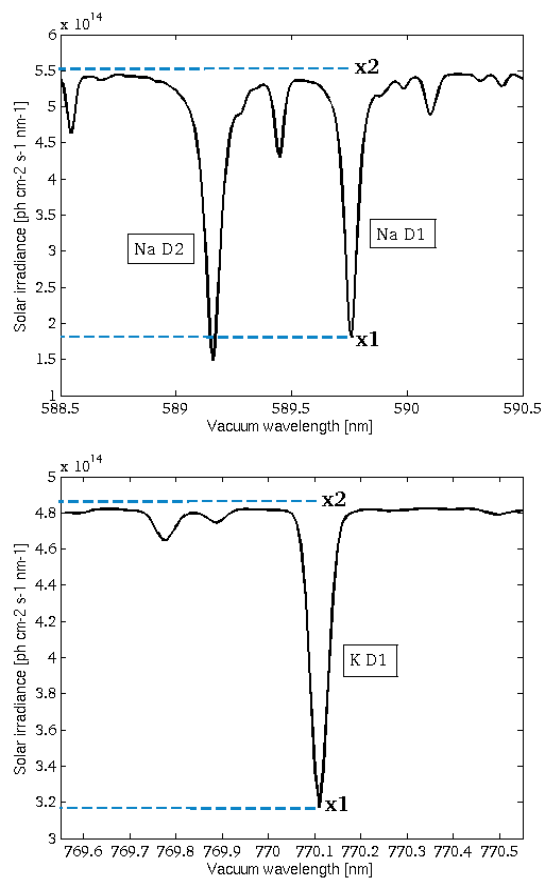


Figure 3-9: The determination of the absolute solar flux at the Fraunhofer line centre for [top panel] Na and [lower panel] K.

The shape of the Na(D₁) Fraunhofer line and the empirical equation that governs it (shown in Figure 3-10) taken from McNutt and Mack [1963] is

$$I_x = I_0 \exp\left(\frac{|x|}{x_e}\right)^A \quad 3.21$$

where x is equal to $(\sigma - \sigma_s)/\sigma_s$, in which σ_s is the wave number of the line centre, and σ is the wavenumber of the position either side of σ_s . I_x is the solar irradiance for position x , relative to the line centre, I_0 . For the Na(D_1) line, the parameter $x_e = 12.8 \times 10^{-6}$ and $A = 2.14$.

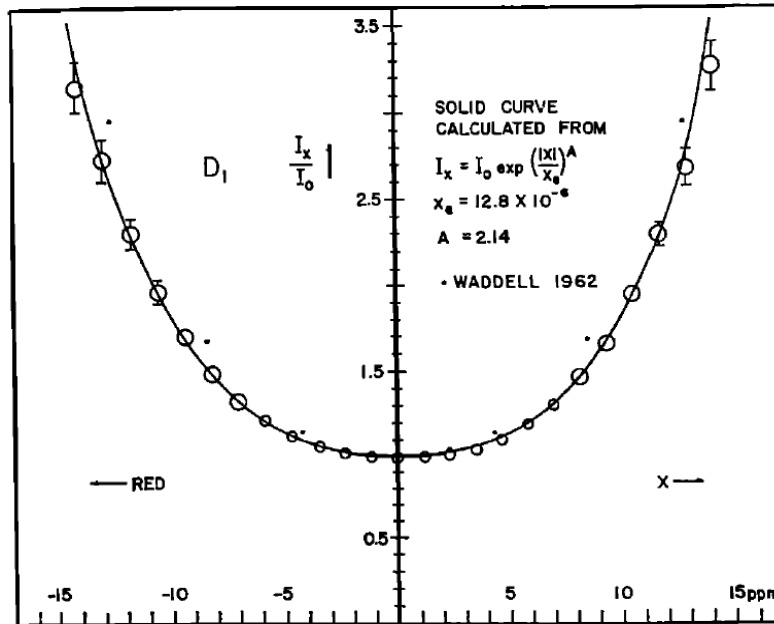


Figure 3-10: Example of the base of the Na(D_1) line at 589 nm. The solid line represents the calculated solar spectrum, with the circles represent empirical data. Reproduced from McNutt and Mack [1963].

For the equivalent K line shape parameters, various values for the x_e and A parameters were chosen in order to accurately model the Chance and Kurucz solar spectrum line (see Figure 3-11). Those which provided the best fit were $x_e = 5.9 \times 10^{-6}$ and $A = 2.10$.

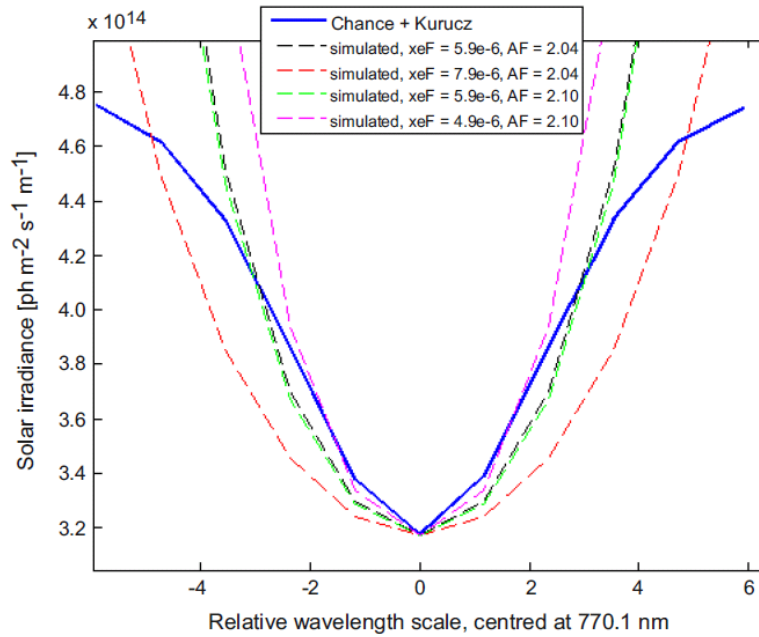


Figure 3-11: Modelling the solar Fraunhofer line at 770 nm. The Chance and Kurucz spectrum is shown versus the simulated spectrum which is calculated from different values for x_e and A parameters (here, labelled xeF and AF , respectively).

The sensitivity of the retrieved density profile to these shape parameters is shown in Figure 3-12. There appears to be a non-linear dependence but, in general, a decrease in either parameters x_0 or A , results in a decreased potassium density profile, whilst an increase in either parameters leads to increased densities.

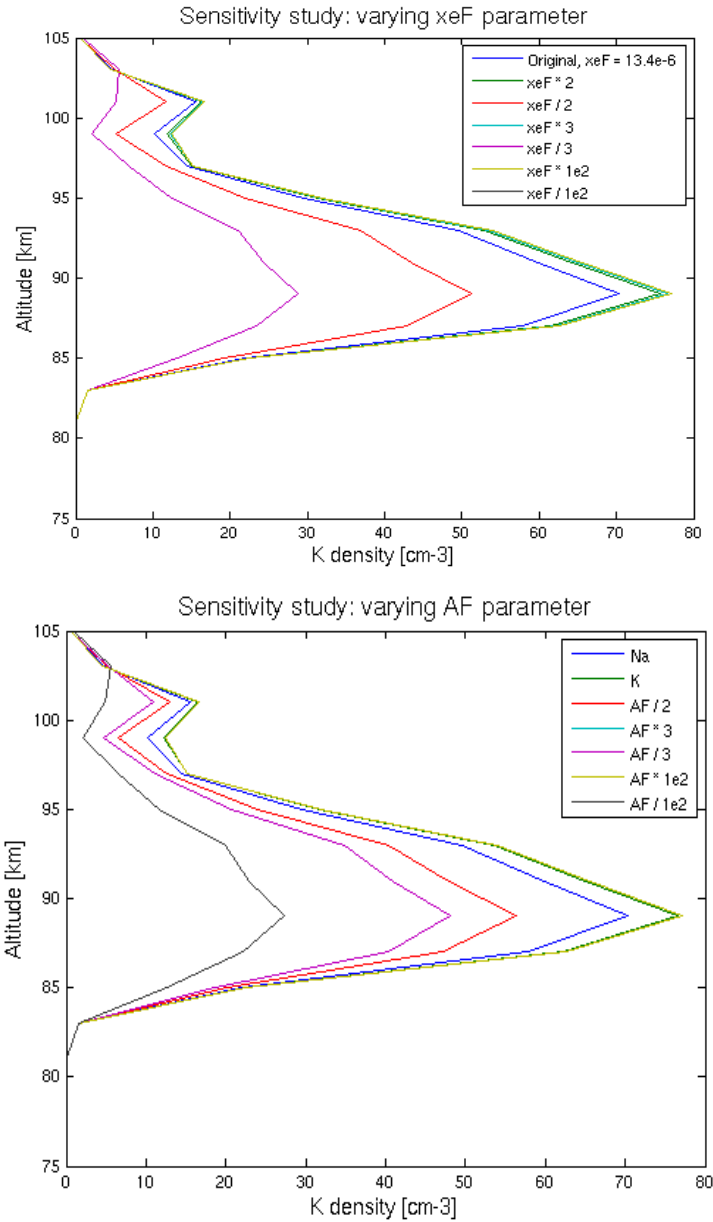


Figure 3-12: Sensitivity of the retrieved K number density profile for choice of x_e [top panel, here labelled xeF] and A parameters [lower panel, labelled AF].

3.3.5 Calculating the local albedo

Due to the limitations of the forward model and processing requirements, only single scattering is considered. The mean free path of a photon in the MLT region is of the order of 100 km. As the FWHM of the potassium layer is <10 km, it is assumed that an emitted photon is unlikely to re-enter the line-of-sight of the instrument. However,

multiple scattering in the lower atmosphere is an important phenomenon and must be considered. Explicit modelling of multiple scattered is outside the scope of this retrieval scheme due to computational expense. Instead, multiple scattering within the lower atmosphere is taken into account as a local albedo effect. It is assumed that scattering from the ground is Lambertian and that there is therefore no angular dependence.

The original Na retrieval [Gumbel *et al.*, 2007] used interpolated albedo information from the Total Ozone Monitoring Satellite (TOMS). This introduced a large uncertainty (~20%) into the retrieval scheme as the albedo derived from TOMS may not have been the exact lower ground scene viewed by OSIRIS, due to the differing temporal sampling of the two instruments. Since that time, however, the following approach has been used which determines an albedo contribution from the OSIRIS limb radiances themselves. In this work, the same new approach has been modified to look at the wavelengths important for the potassium 770 nm transition.

The local albedo is determined from the 40 km limb scan and is derived by comparing the total background radiance to that which would be expected from single Rayleigh scattering only for the equivalent atmospheric conditions. This simulated Rayleigh scattering is derived from ECMWF number density (N₂ and O₂) and temperature profiles. The albedo is then determined as an albedo ratio,

$$albrat = \frac{LB_g}{LSim} \quad 3.22$$

where LB_g is the integrated radiance over the background wavelengths either side of the potassium 770 nm line, and LSim is the simulated background Rayleigh radiance signal. The albrat is usually between 1-2, with a value of albrat = 1 indicating that there is zero net albedo effect. An albrat value < 1 indicates that there is absorption in the measured limb spectrum at these specific wavelengths. Such an albrat value would be expected within the UV part of the spectrum within the ozone absorption wavelengths.

The albrat ratio is included within the forward model as an albedo correction factor, taking into account the contribution from the lower atmosphere into the instrument LOS, E₀,

$$E_0 = E_{dir} \cdot albrat \quad 3.23$$

Here E_{dir} is the incoming solar radiation, and $albrat$ is the contribution from the lower atmosphere. Thus, we can see that the larger the albedo, and thus the $albrat$ value, the larger the incident light in the OSIRIS instrument LOS.

3.3.6 Polarisation

An important issue in the inversion of the OSIRIS data, is the polarisation state of the radiation received by the instrument. The solar radiation incident on the Earth's atmosphere is unpolarised but, after scattering from air molecules and aerosols, becomes polarised. The degree of polarisation of the scattered radiation depends on both the solar zenith angle (SZA) and the azimuth angle (AZ) of the Sun relative to the instrument LOS. Where $SZA = 90^\circ$ and $AZ = 90^\circ$, this is typically $\gg 90\%$ and the radiation is mostly polarised in the plane of the local vertical.

The diffraction grating used by the OSIRIS instrument shows significantly different responses to different states of polarisation of the incoming radiation. Following the approach in McLinden *et al.* [2002], the polarisation state of the incoming radiation is described in terms of a Stokes vector given by $\mathbf{I} = [I \ Q \ U \ V]^T$. Each component of the Stokes vector has the units of radiance. The first term I represents the total radiance; Q represents the radiance polarised parallel and perpendicular to a reference plane; U represents the radiance polarised at 45° and 135° to the reference plane; and V represents circularly polarised radiance. The reference plane is taken to be the plane containing the local vertical and the direction of propagation.

For the OSIRIS instrument, the diffraction grating grooves are aligned horizontal relative to the local vertical. The response of the instrument, I_{diff} , can be written according to McLinden *et al.* [2002] in the form:

$$I_{dif} = f(\lambda) \cdot [I + g_{12}(\lambda) \cdot Q + g_{13}(\lambda) \cdot U] \quad 3.24$$

In this equation, the first term represents the response to un-polarised radiation; the second term is the response to linearly polarised light given by Q; and the third term, the response to polarised radiation U. Note: in this equation, it is assumed that the circularly polarised radiation scattered from the atmosphere is negligible. At 770 nm, the wavelength of the K emission line considered in the present work, the values of the diffraction grating response parameters measured during the OSIRIS flight model characterisation are given by McLinden *et al.* as approximately $g_{12} = 0.05$ and $g_{13} = 0.01$.

Oikarinen [2001] discusses the problem of polarisation for the OSIRIS instrument and identifies two possible simple correction techniques. In the more elaborate approach, a single-scattering radiative transfer model is used to calculate the degree of polarisation of the incoming radiation and then a correction is applied based on the response characterisation of the OSIRIS instrument measured in pre-flight testing (g_{12} and g_{13}). However, a limitation with this approach is that there can be a relatively large error produced between a single-scattering model approach and the full multiple-scattering model approach which correctly calculates the polarisation state of the scattered radiation.

The second correction approach discussed by Oikarinen [2001] is to rely on the fact that at tangent heights above ~30 km, the degree of polarisation is relatively constant with altitude. Therefore, if the spectrum at the required tangent altitude is normalised by the spectrum from an altitude above ~30 km in which the required atmospheric constituent is absent then the effect of the state of polarisation on the instrument response will be cancelled. This is effectively the approach taken in the present work as discussed in Section 3.4 below.

3.3.7 The forward model resolution

The forward model must have a vertical resolution sufficient so that the radiance near the tangent point can be accurately calculated. In this work, the vertical resolution of the

forward model is 0.5 km, extending from the ground to the top-of-the-atmosphere at 120 km, as in Strong *et al.* [2002] and Gumbel *et al.* [2007].

3.3.8 Choice of retrieval grid resolution

The choice of retrieval grid resolution can have a large effect on the final retrieved profile, and this sensitivity is illustrated in Figure 3-13. A vertical retrieval grid resolution of 1 km results in an oscillating retrieved profile and must be avoided. Vertical grid resolutions of 2 km and 4 km result in stable solutions and very similar vertical profiles. This is likely to be due to the 2 km vertical resolution of the OSIRIS radiance profiles. A vertical grid resolution of 2 km was therefore chosen in the present work due to its stability and ability to match the vertical resolution of the radiance profiles, which have been interpolated to a consistent 2 km vertical resolution.

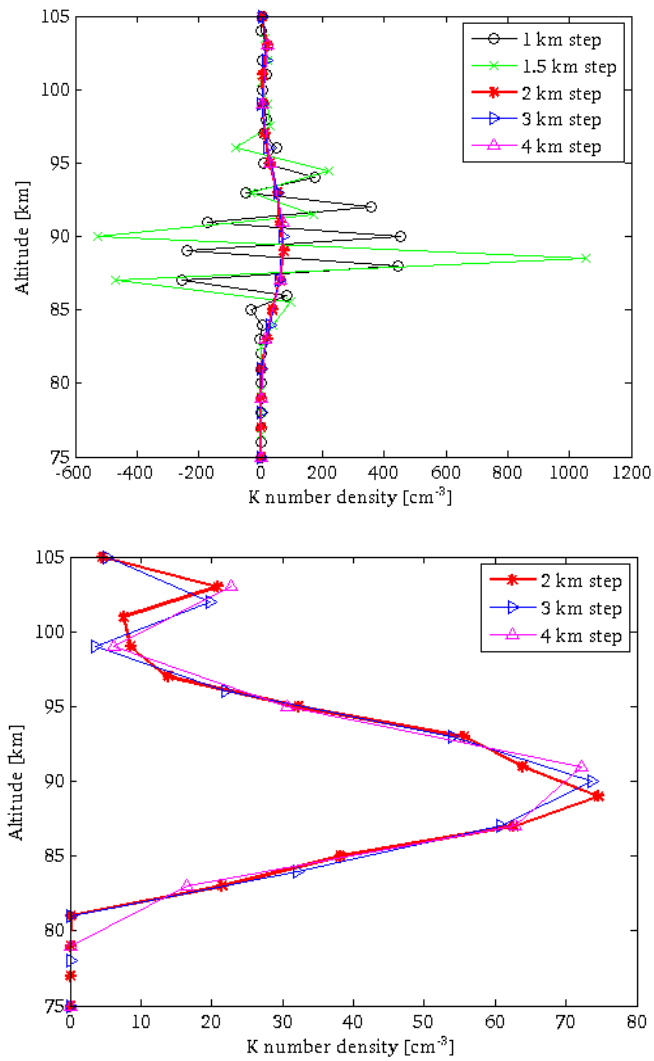


Figure 3-13: Effect of changing the retrieval grid resolution on the final retrieved K number density profiles for [left] vertical grid resolutions of 1, 1.5, 2, 3 and 4 km and [right] for resolutions of 2, 3 and 4 km only (omitting profiles for 1 and 1.5 km for clarity).

3.3.9 The *a priori* profile

In this work, the *a priori* number density profile (x_a) represents a first guess as to what the true number density profile might be and serves simply as a starting point for the retrieval as described in Section 3.3. Additionally, as the retrieval does not have a unique solution (i.e. it is formally ill-posed), the *a priori* and its associated covariance is

required to regularise the solution, and guard against the amplification of measurement errors.

A mean K number density profile derived from a single annual mean mid-latitude K lidar profile (from Kühlungsborn, 54°N) is used as the *a priori* profile, having been interpolated to the vertical retrieval grid resolution of 75-105 km with 2 km vertical resolution. The covariance (shown in Figure 3-14, along with the *a priori* profile) was chosen to reflect the large amount of natural variation seen within both the Arecibo and Kühlungsborn lidar datasets).

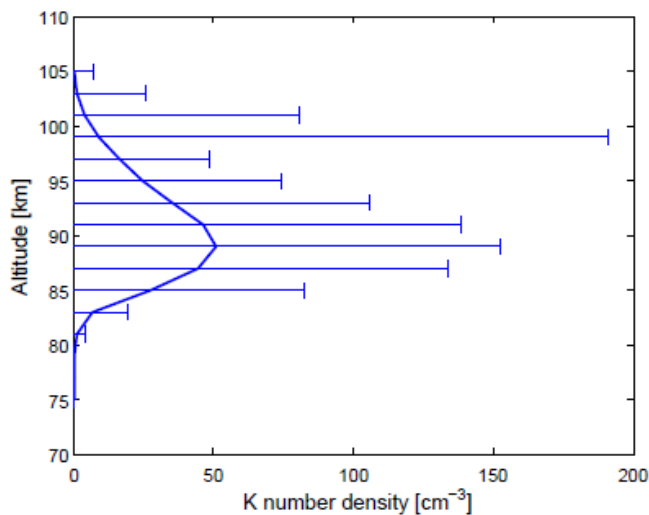


Figure 3-14: The *a priori* and its associated covariance.

Used as a first guess, it is important that the retrieval solution is not too sensitive to the choice of *a priori* profile; it would render the retrieved profile relatively useless. The effect of choosing different *a priori* profiles is shown in Figure 3-15. Increasing or decreasing the *a priori* density profile by 50% has only a limited effect on the retrieved density within the peak region (between 85-100 km) demonstrating a limited dependence on the *a priori* input profile. It is likely that this lack of dependence is due to the selection of appropriate retrieval grid altitude steps. There is some effect on the top (>100 km) and bottom (<85 km) of the layer; the reasons for this will be discussed in Section 4.2.4

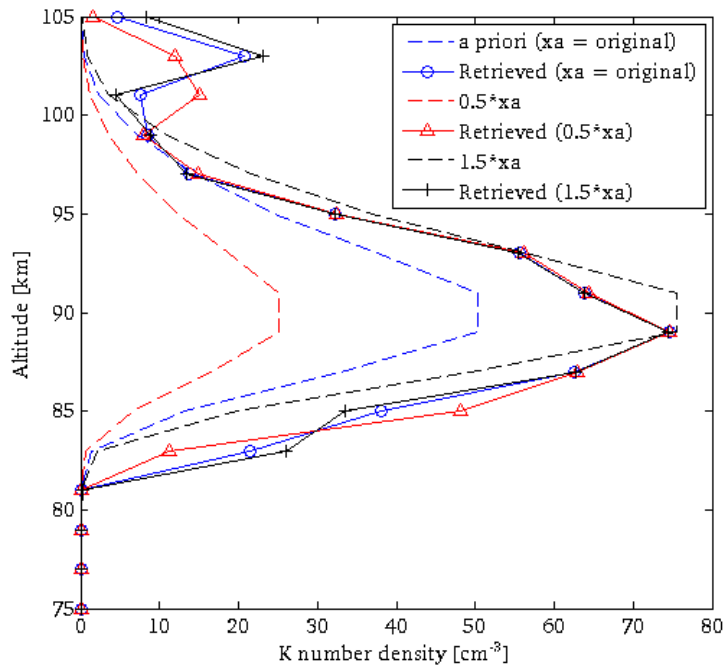


Figure 3-15: *Illustrating the effect of different a priori (here, referred to as x_a) profiles on final retrieved K number density profiles.*

3.3.10 Consideration of limb geometry

As the Odin spacecraft operates in a dusk/dawn orbit, the orbit is close to the terminator and so the majority of observations are made at a solar zenith angle (SZA) near 90° . The exception to this is during the summer polar regions where this SZA can decrease to around 70° . As a result, the local variation of the SZA along the line-of-sight must be taken into account and is determined for both the near- and far-fields, as in Equation 3-11.

3.3.11 Forward model input parameters

The forward model requires a number of additional input parameters for simulating the limb radiance. To summarise, it includes:

- The solar irradiance characteristics and Fraunhofer structure used in the radiative transfer model are originally based on the solar spectrum from Chance and Kurucz [2010].
- The temperature profiles (up to 120 km) used to determining the K cross-sections are taken from the Extension of Mass Spectrometer Incoherent Scatter (MSISE-00) model with a 0.5 km vertical resolution.
- Air density profiles (N_2 and O_2) (0-120 km, with 0.5 km vertical resolution) taken from MSISE-00 are also used for the forward model atmosphere.
- Air density and temperature profiles from the European Centre for Medium Range Forecasts (ECMWF) ERA-Interim model are used for determining the Rayleigh scattering component in the albedo contribution calculation.

3.4 Measurement of potassium radiance values

The retrieval of K represents a much greater challenge than that of Na. Whilst both Na and K have very similar, large absorption cross-sections (around 10^{-12} cm²), the atmospheric abundance of K in the MLT is roughly a factor 50 smaller than Na and the peak K radiance measured by the OSIRIS instrument is an order of magnitude smaller, which makes the retrieval of K number density profiles more sensitive to the sources of error [see Chapter 4 for discussion of errors].

Similar to Na at 589 nm, K has two D lines at 769.90 nm (D_1 line) and 766.49 nm (D_2 line). However, whilst the sodium D lines are separated by about 0.6 nm, the K D lines are considerably further apart with over 3 nm distance between the D_1 and D_2 lines. The $K(D_2)$ line, although stronger than the D_1 line, is overlapped by the oxygen A-band at 760-765 nm, making it very difficult to observe.

The K 770 nm line is also in the near-IR where solar irradiance is smaller, which, in conjunction with K having a smaller atmospheric abundance, means that this resonance line has a much poorer signal-to-background ratio than that of Na at 589 nm. One final consideration is that it is likely that the response function of the spectrometer CCD (charge coupled device) detector has degraded preferentially at these longer wavelengths

in accordance with quantum efficiency [Llewellyn *et al.*, 2004], reducing the instrument sensitivity. All of these combine to make the retrieval of K very much more challenging than that of Na.

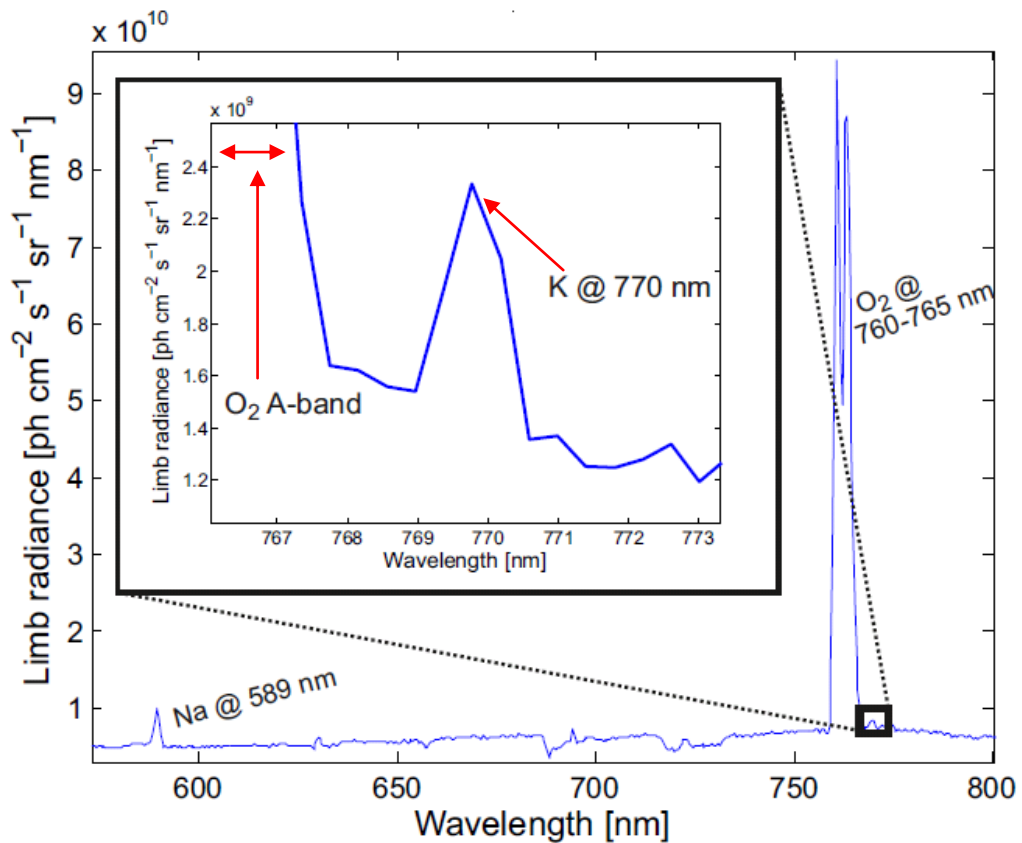


Figure 3-16: An OSIRIS limb radiance spectrum at 90 km the relative levels of K at 770 nm and Na at 589 nm.

3.4.1 Extracting K radiance values

The limb radiance detected by the OSIRIS instrument consists of discrete emission and absorption features superimposed over broader Rayleigh and Mie scattering features. An example set of OSIRIS limb radiance spectra for tangent heights between 40-100 km is shown in Figure 3-17. In this spectrum, the O₂ A-band can be clearly seen between 760-765 nm. The K(D₂) line can be faintly seen at 766.5 nm and the K(D₁) line at 770 nm can be seen at tangent heights of approximately 70-100 km.

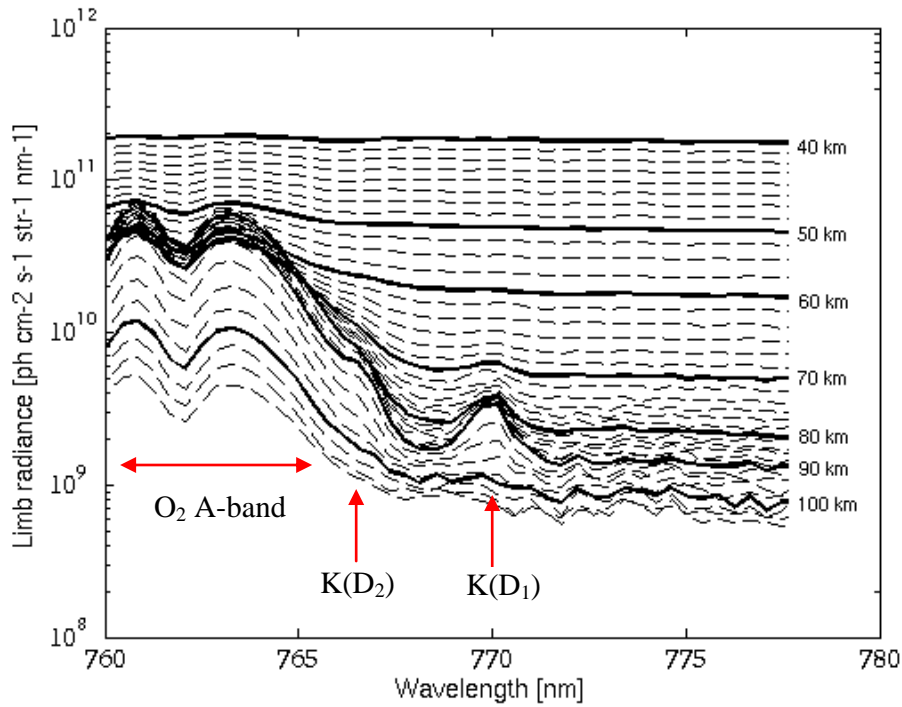


Figure 3-17: OSIRIS limb spectra at tangent heights between 40-104 km at a solar zenith angle of 88.0°.

The smaller signal-to background of K at 770 nm requires careful consideration when determining the true K resonance emission and deriving vertical radiance profiles from OSIRIS. Solar radiation contains a large number of characteristic absorption features, known as Fraunhofer structure, that exist as a result of wavelength-specific absorption by species present in the solar photosphere. It is important that these are taken into account when removing the background radiance from a specific limb radiance spectrum.

Unlike some other instruments, OSIRIS does not provide a Sun reference limb measurement. This means that the solar Fraunhofer features present in the solar spectra must be accounted for in some other way. A typical way of doing this is to take a ratio of two limb radiance spectra from different tangent heights, one of which is used as a reference. In this work, the 40 km tangent height limb spectrum has been used as the reference. This was chosen as it was assumed that the K signal in it would be very small

and that it was also sufficiently high so as to avoid the issues of highly variable Mie scattering and albedo effects prevalent at lower altitudes.

For any given full set of OSIRIS scans, the 40 km spectrum was normalised to unity at 770 nm. This normalised 40 km spectrum was then used to normalise all other limb scans within the set in order to account for the shape of the background, such as Fraunhofer structure and spectral features present at both MLT heights and in the lower atmosphere. This has the additional benefits of eliminating the need for an absolute instrument calibration and consideration of the instrument response function.

In order to derive the amplitude of the K emission line, the background limb radiance must first be removed. A first-order polynomial (green) is fitted to the background regions either side (768.15-768.96 nm and 770.58-771.80 nm). A second-order polynomial (red) is fitted to the peak region (769.96-770.58 nm). These wavelength ranges were chosen as they were clear of any significant oxygen A-band signal contamination and known emission line features of other species. The area bounded between the signal curve and background baseline is then integrated to produce the total K emission [units: $\text{ph cm}^{-2} \text{s}^{-1} \text{sr}^{-1}$]. The fitting of the baseline to the background regions either side of the K peak accounts for any broadband changes in the background, during the deconvolution of the spectrum. An example of this fitting process is shown in Figure 3-18. These integrated radiances are subsequently used to produce a pure K radiance profile as a function of height as seen in Figure 3-19.

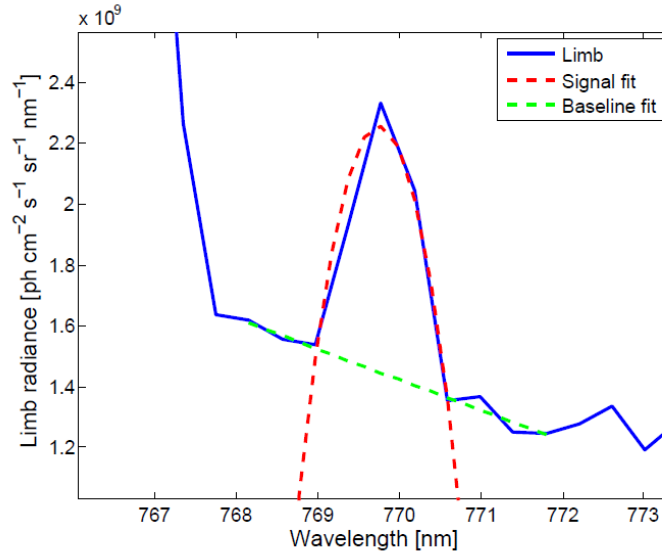


Figure 3-18: *Extracting the K emission signal. An example normalised 90 km limb radiance spectrum is presented showing the $K(D_1)$ line at ~ 770 nm.*

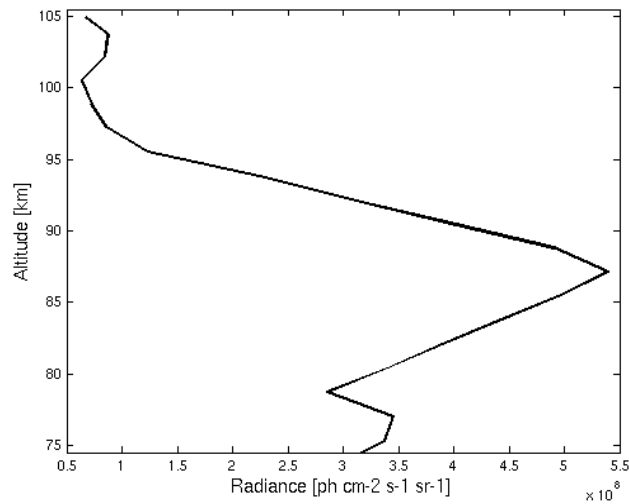


Figure 3-19: *Example vertical radiance profile derived from OSIRIS limb spectra.*

3.4.2 Quality-control of radiance profiles

Quality-control of the OSIRIS limb radiance spectra is an essential part in producing vertical radiance profiles of sufficient quality for use in the potassium retrieval. Due to the weaker signal-to-background of the $K(D_1)$ line relative to the Na lines at 589 nm,

extensive quality-control (QC) measures were performed in order that only the 'best' spectra with the lowest associated errors were using in the retrieval.

Each Level 1 radiance spectrum has an associated measurement error provided with the data. This includes error contributions from the CCD dark current and detector readout noise. Within the 770 nm region, the measurement errors are very small often comprising only 5% of the absolute radiance per pixel. However, occasionally, random shot noise (such as those caused by cosmic rays falling on the CCD), can result in the measurement error increasing to at least an order of magnitude greater than the corresponding radiance. Such radiance spectra are filtered out prior to being used in the retrieval. Pre-processing of the Level 1 spectra is performed for each year individually. A mean error limb spectrum is constructed from all available associated measurement error spectrum at 40 km for all scans. The spectra at approximately $40(\pm 1.5)$ km are used because of their importance in the normalisation of all other limb scans (see Section 3.4.1). If the 40 km limb spectrum has a large associated error, it is likely that all other tangent height limb spectra within the same scan are compromised too. For each full scan, each individual 40 km measurement error spectrum is compared to this mean error spectrum, pixel by pixel. If the individual error spectrum exceeds $\pm 1.5\sigma$ of the mean error at any pixel, the whole scan (at all tangent heights) is discarded.

Another QC test is performed following the fitting process and extraction of the vertical K radiance profiles described in Section 3.4.1 . The vertical radiance profile has associated error, which now consists of both the original measurement error plus the error introduced by the fitting process. Using a similar approach as above, a mean vertical error profile is constructed, using all available data for the particular year being processed. If the total error (for any altitude) within an individual radiance profiles lies outside of $\pm 1.5\sigma$ of the mean error profile, it is discarded. This process is designed to eliminate vertical radiance profiles which are the product of poor-quality fits alone, or where the fitting error and original measurement error combine to produce an unacceptably high total error.

Other additional quality-control criteria include excluding scans where the Sun is below the horizon (e.g. where $SZA > 92^\circ$), scans in which the Moon is within the field-of-view, or where the Odin spacecraft is located within the South Atlantic Anomaly region (and thus may be subject to high levels of radiation).

As a result of the stringent quality-control checks, a large amount of K profiles are discarded. For any given year, the total number of vertical K radiance profiles typically represents <35% of the total number of Na profiles (they should be identical, as the same limb radiance spectra are used for both retrievals). The retrieval of the $K(D_1)$ at 770 nm is an challenging problem. While being an obvious limitation, it is felt that this is an appropriate and acceptable quality-control check so that only the highest quality data (i.e. those with associated errors below a certain threshold) are used in the K retrieval. Future improvements may include relaxing these criteria which will result in a larger dataset.

Despite the Odin spacecraft being launched in Feb 2001, only relatively limited data exists for the first few years of operation up until 2004, in part due to the instrument undergoing significant calibration tests [J. Gumbel, pers. communication] and partly due to the split-mission commitments (50% astronomy, 50% aeronomy). Following application of the described QC criteria, the number of vertical K radiance profiles available for 2001-2003 is very limited, with only a couple of months coverage at certain latitudes). It was therefore decided to focus on data for 2004 onwards only. Future work may allow these earlier years to be revisited.

3.4.3 The Ring effect

The Ring effect was first reported by Grainger and Ring in 1962, and concerns the increase of the photon flux in the solar Fraunhofer minima, as a result of inelastic rotational Raman scattering (RRS, predominantly by O_2 and N_2) [e.g. Chance and Spurr, 1997; Sioris and Evans, 1999]. This acts to reduce the depth of the absorption features (via a so-called 'filling-in') and contributes to additional illumination of the K layer. The neglect of the Ring effect introduces a systematic error into any retrieval scheme.

However a strong relationship exists between wavelength and the extent of the filling-in, with longer wavelengths exhibiting a weaker Ring effect [Sioris and Evans, 1999].

The impact of the Ring effect at 770 nm is estimated using the box-car approach outlined in Langowski *et al.* [2014a]. The spectral redistribution from rotational Raman scattering is relatively small in comparison to that resonantly Rayleigh scattered (i.e. <10%). As such, the Ring effect can effectively be linearised in terms of its impact on the limb emission radiances. A boxcar function of 3.3 nm is used to simulate, and correct for the Ring effect in the SCIAMACHY solar spectrum (which is subsequently used to normalise the SCIAMACHY limb radiance spectrum). The OSIRIS K retrieval uses a modification of this approach; the 40 km limb radiance is used to normalisation, instead of a solar spectrum (see Section 3.4.1).

An example of normalised OSIRIS limb radiance spectrum at 90 km is presented in Figure 3-20, along with corresponding corrected spectra for a range of different RRS contributions (2, 4, 6 and 8% of the total scattering, with the remainder due to resonant Rayleigh scattering). A higher RRS percentage results in a larger reduction in the depth of the solar Fraunhofer line, or in this case, the shape of the any solar absorption feature present in the 40 km limb radiance. Normalising the 90 km limb radiance with this corrected 40 km spectrum results in an enhancement of the radiance at 770 nm, and an increase in the integrated vertical radiance profile (also shown in Figure 3-20).

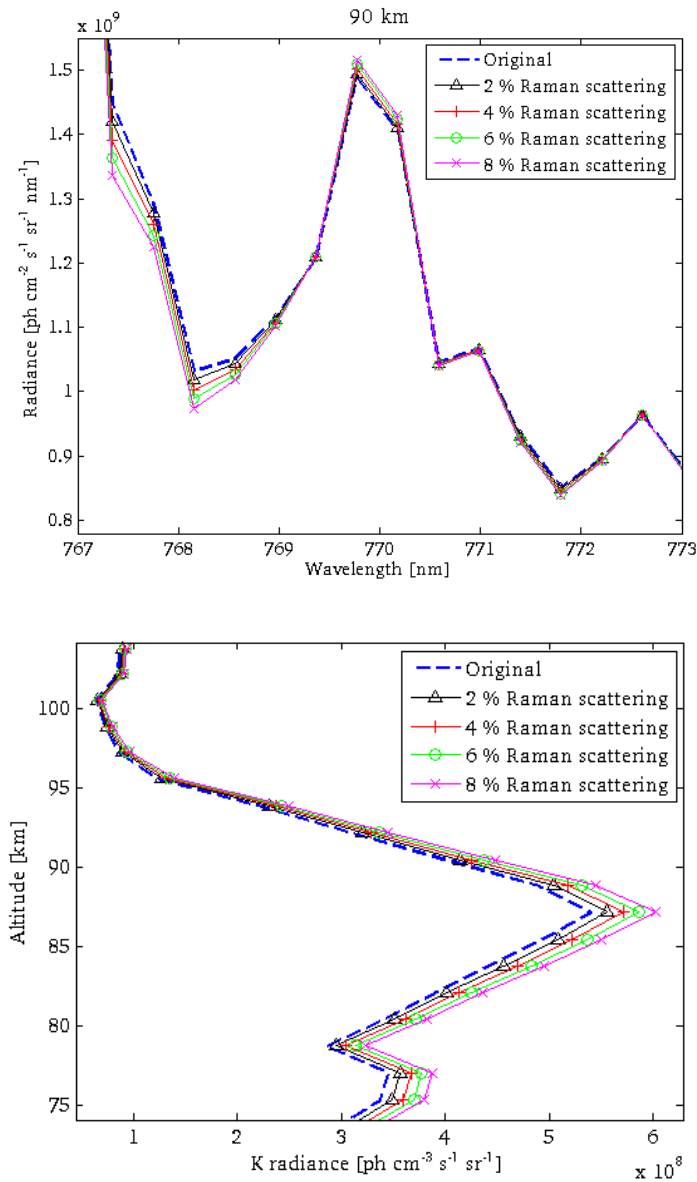


Figure 3-20: Correcting for the Ring effect. Left panel: A example limb radiance for 90 km, which has been normalised by a 40 km, corrected for a variety of RRS contributions (2%, 4%, 6% and 8%). Right panel: The vertical radiance profiles which result from different Ring effect correction values.

The true percentage of Raman scattered light likely lies between 3-6% [Langowski *et al.*, 2014a]. The maximum increases in the resulting K number densities are <5%, even assuming a 6% RRS contribution. Thus, due to the additional computational expense that employing a boxcar approach would necessitate, the decision is made to neglect the Ring effect treatment. Instead, it is included as an additional source of systematic uncertainty within the retrieval (discussed in Chapter 4).

3.4.4 The weighting and contribution functions

The weighting function given in Equation 3.5 represents the forward model response to changes in the atmospheric state. An example typical final weighting function is shown in Figure 3-21. Each curve shows the sensitivity of the forward model to the state vector for a particular altitude, and the retrieved K number density is derived from a combination of all the weighting function curves at this retrieval altitude. From this figure, it can be seen that in general, the forward model is most sensitive to number densities at the corresponding retrieval altitude, i.e. the 87 km curve peaks at 87 km on the y-axis. The exception to this is at the lowest altitudes (71 and 73 km) where the forward model is sensitive to number densities at higher altitudes.

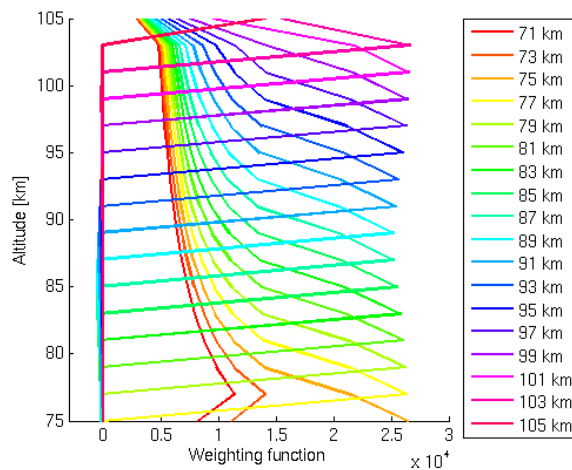


Figure 3-21: A typical calculated weighting function.

An example contribution matrix (where $G_i = \delta x / \delta y$) is shown in Figure 3-22, with each curve representing the sensitivity of the final retrieved density to the original radiance measurement. In general, the final retrieved density is most sensitive to the radiance measurement at the same altitude and there is a positive relationship where an increase in the observed radiance is related to an increased retrieved number density. Below this altitude, the retrieved density profile is negatively sensitive to the original radiance measurement; a positive increase in the radiance profile produces a decrease in the

retrieval at the above altitude step. Below 83 km, the retrieved density profile is sensitive to changes in the observed radiance at a range of tangent heights.

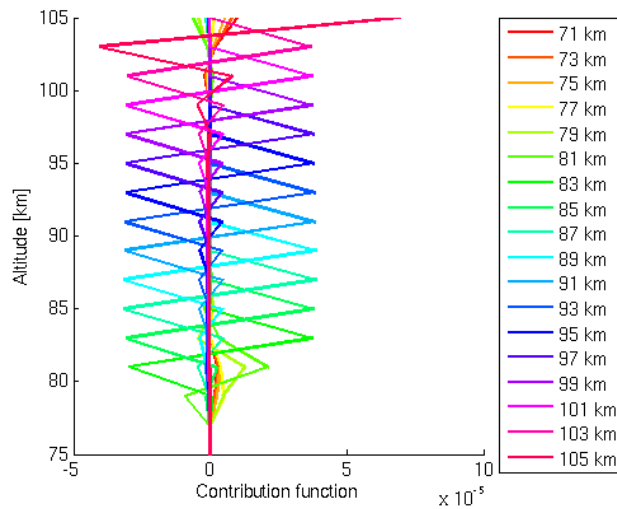


Figure 3-22: A typical contribution function.

3.5 Summary

In this chapter, the first retrieval algorithm for retrieving mesospheric K has been described which uses radiance profiles from the OSIRIS instrument. This K retrieval scheme has been developed from an existing Na retrieval scheme first developed by Gumbel *et al.* [2007].

The K emission characteristics are significantly harder to extract from the OSIRIS limb spectra due to the reduced atmospheric abundance of K relative to Na, and also due to the fact that the 770 nm K(D₁) line is to the right of the prominent 760-765 nm O₂ A-band, with the K(D₂) line overlapped by the right-hand flank of this band at the OSIRIS spectral resolution.

A new way of extracting this K emission information has been described. In addition, a new approach has also been made to estimate the background solar irradiance flux incident at 770 nm, whereas in the sodium retrieval, empirical experimental parameters were used to describe this solar flux.

A full characterisation of the error source relevant to the K retrieval are presented in the subsequent Chapter 4, along with a comparison of retrieved K profiles to available K lidar data for ground-truthing purposes.

4 ERROR ANALYSIS AND VALIDATION

4.1 Introduction

A key part of any retrieval scheme is a comprehensive analysis of contributing error sources. A full characterisation of the error sources relevant to the K retrieval is presented in Section 4.2. A further vital component is the validation of the retrieved product. In this case, the retrieved K number density profiles are ground-truthed via comparison with available lidar data, presented in Section 4.3.

4.2 Characterisation of error

For correct interpretation of retrieval results, a comprehensive characterisation of contributing error sources is important. If the uncertainty is too large, the retrieval results will be of insufficient accuracy for subsequent analyses, such as comparing with model simulations. A better understanding of error sources can also ultimately help to further improve the retrieval algorithm as a whole.

The error analysis as presented in Rodgers [1990, 2000] identifies four distinct categories of errors relevant to atmospheric remote sensing applications:

$$\mathcal{E}_{total} = \mathcal{E}_m + \mathcal{E}_s + \mathcal{E}_f + \mathcal{E}_b \quad 4.1$$

The total error \mathcal{E}_{total} includes the errors associated with the measurements themselves \mathcal{E}_m , the smoothing error \mathcal{E}_s , forward model error \mathcal{E}_f , and forward model parameter error \mathcal{E}_b . The total retrieval error \mathcal{E}_{total} can then be calculated by adding these individual error sources in quadrature, such that:

$$\mathcal{E}_{total} = \sqrt{\mathcal{E}_m^2 + \mathcal{E}_s^2 + \mathcal{E}_f^2 + \mathcal{E}_{mb}^2} \quad 4.2$$

Each of these error categories will be discussed separately in more detail in the following sub-sections.

4.2.1 Measurement noise

The error in the retrieval which arises as a result of errors in the OSIRIS measurements and the derivation of the vertical radiance profile in Section 3.4 is represented by,

$$\varepsilon_m = G(\Delta_y) \cdot S_\varepsilon \quad 4.3$$

where $G(\Delta_y)$ is the contribution function and S_ε is the error covariance matrix of the measurements.

Instrument noise consists of random errors from the detector, which include photon shot noise from the source, the dark shot noise due to fluctuations in the dark current of the detector, and the detector readout noise, and the uncertainty in the altitude registration of each exposure (also known as the pointing error). The pointing error is such that there is a reported accuracy of <500 m to the tangent height [Haley *et al.*, 2004; McLinden *et al.*, 2012].

Additional terms which are included in the measurement error budget include the systematic error introduced by neglecting any treatment of the Ring effect. This is thought to contribute an additional 5% uncertainty. Finally, a key source of error is that introduced as a result of the fitting routine described in Section 3.4 when extracting the K emission radiance. The RMS-error of the fit between the OSIRIS measurement and the fitted second-order polynomial is computed and combined on an RMS basis with both the instrument noise, and polarization and Ring effect uncertainties.

An example limb radiance profile with associated measurement errors is presented in Figure 4-1. The largest measurement error occurs above and below the peak layer altitudes, typically exceeding 13%, compared to the 5-10% error seen in the peak layer region. This makes sense in that the signal-to-noise is likely to be reduced outside of the peak region.

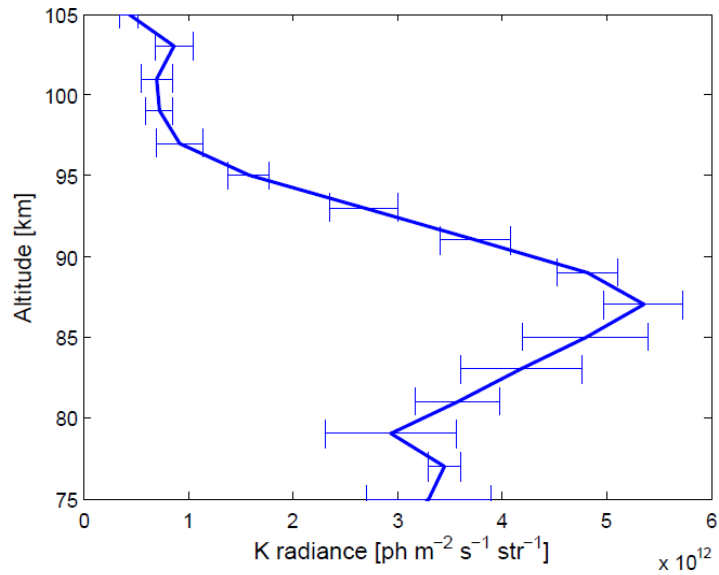


Figure 4-1: Example retrieved number density profile with associated measurement error contribution indicated by horizontal bars.

The sensitivity of the retrieved profile to changes in the measurement error is shown in Figure 4-2. Even with changes of $\pm 50\%$, the retrieval result is very stable for the peak region between 85-95 km, with no change in the peak layer height of the retrieved profile nor the absolute number densities. However, above and below these altitudes, there is a degree of sensitivity to the measurement error. Again, this is intuitive, as the signal-to-noise of the limb radiances is poorer above and below the peak layer, such that there is increased relative noise at these altitudes.

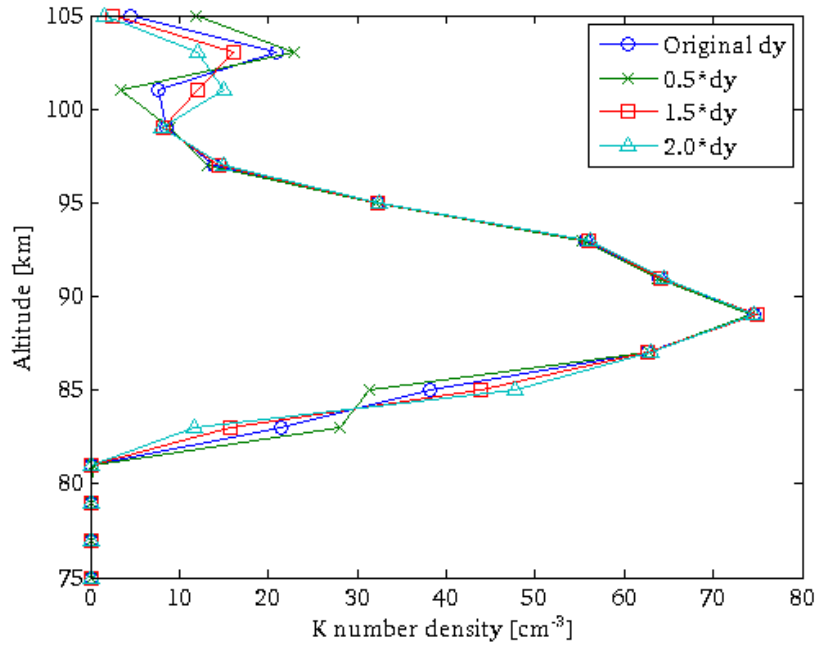


Figure 4-2: Sensitivity of retrieved profile to measurement error, Δy (referred to as dy in plot).

4.2.2 Forward model error

The forward model error, ε_f , consists of systematic errors that occur due to approximations and deficiencies within the forward model. Such approximations include the consideration of single scattering only within a spherical and horizontally homogenous atmosphere, and that resonant scattering is assumed to lead to a loss of a photon (thus removing it from the instrument LOS). Additional uncertainties arise due to the relatively limited vertical resolutions of the forward model and retrieval grid.

The forward model error is extremely difficult to estimate as a full characterisation would require comparison to an exact model with full and perfect representation of the physics. As a result, this error source is not considered further. However, it is likely to be systematic in nature, and comparisons with lidar data [Section 4.3] suggest that the forward model error is likely to be small.

4.2.3 Forward model parameter error

The retrieval model parameter error includes the uncertainties associated with all physical parameters, b , related to the forward model, with

$$\varepsilon_b = G(\Delta_F) = G_y \cdot K_b (b - \hat{b}) \quad 4.4$$

The term $(b - \hat{b})$ is the difference between the unknown true parameters and the parameters used in the forward model. The sensitivity of the retrieval result to each parameter error source is K_b , where

$$K_b = \frac{\partial F(x, b)}{\partial b} = \frac{\partial y}{\partial x} \quad 4.5$$

Similar to the forward model error, the forward model parameter errors are difficult to accurately estimate as it requires some knowledge of the true value of the parameter. The key sources for the forward model parameter error include the albedo, the estimation of the solar photon flux at the transition wavelength (the absolute solar irradiance at 770 nm, and the x_e and A parameters), and temperature, and these are all likely to be systematic in nature.

To estimate K_b , each parameter was perturbed by a specific amount commensurate with the estimated uncertainty of this value, such as one standard deviation if applicable. The temperature profile is taken from MSISE-00 and is used in the calculation of the K cross-section. A temperature profile was perturbed by $\pm 5\%$ which equates to around $\pm 4 \times 10^{10}$ ph m⁻² s⁻¹ sr⁻¹ K⁻¹ change at MLT altitudes, and the response of the retrieval is assessed in Figure 4-3.

The temperature profile plays an important role in the calculation of the potassium cross-section. There is a very slight non-linearity in the simulated radiance profile in response to this perturbation in the peak region. This is likely to be as a result of the $1/\sqrt{T}$ term dependency of the cross-section in Equation 3.17.

The albedo represents another source of uncertainty. The albedo is derived using the 40 km OSIRIS limb radiance and is therefore dependent on the absolute calibration of the instrument. Since the work of Gumbel *et al.* [2007], improvements have been made to the calibration of the instrument spectra and it is generally believed to be accurate to within 5% for the longer wave measurements [N. Lloyd, pers. comm.]. To be conservative, the albedo was perturbed by $\pm 10\%$ and the response of the retrieval is also shown in Figure 4-3. For an albedo of 1.3, this equates to an uncertainty of $\pm 1.3 \times 10^{12}$ $\text{ph m}^{-2} \text{s}^{-1} \text{sr}^{-1}$. The retrieval is equally sensitive to an equivalent increase or decrease in the amount of albedo used.

The final sensitivity studies looked at the retrieval response to changes in the parameters used for the determination of the solar reference flux ~ 770 nm. The absolute solar irradiance at 770 nm was perturbed by $\pm 5\%$ to both reflect the uncertainty in calculating determining the flux at the bottom of the Fraunhofer line, and also to account for the approximate 0.1% total variation in the solar flux across a solar cycle [e.g. Willson and Hudson, 1991; Fröhlich and Lean, 1998; Willson, 2014]. The effect of changing the x_e and A parameters by $\pm 3\%$ on the modelled solar irradiance is shown in Figure 4-4. Again, the retrieval sensitivity to these changes are shown in Figure 4-5.

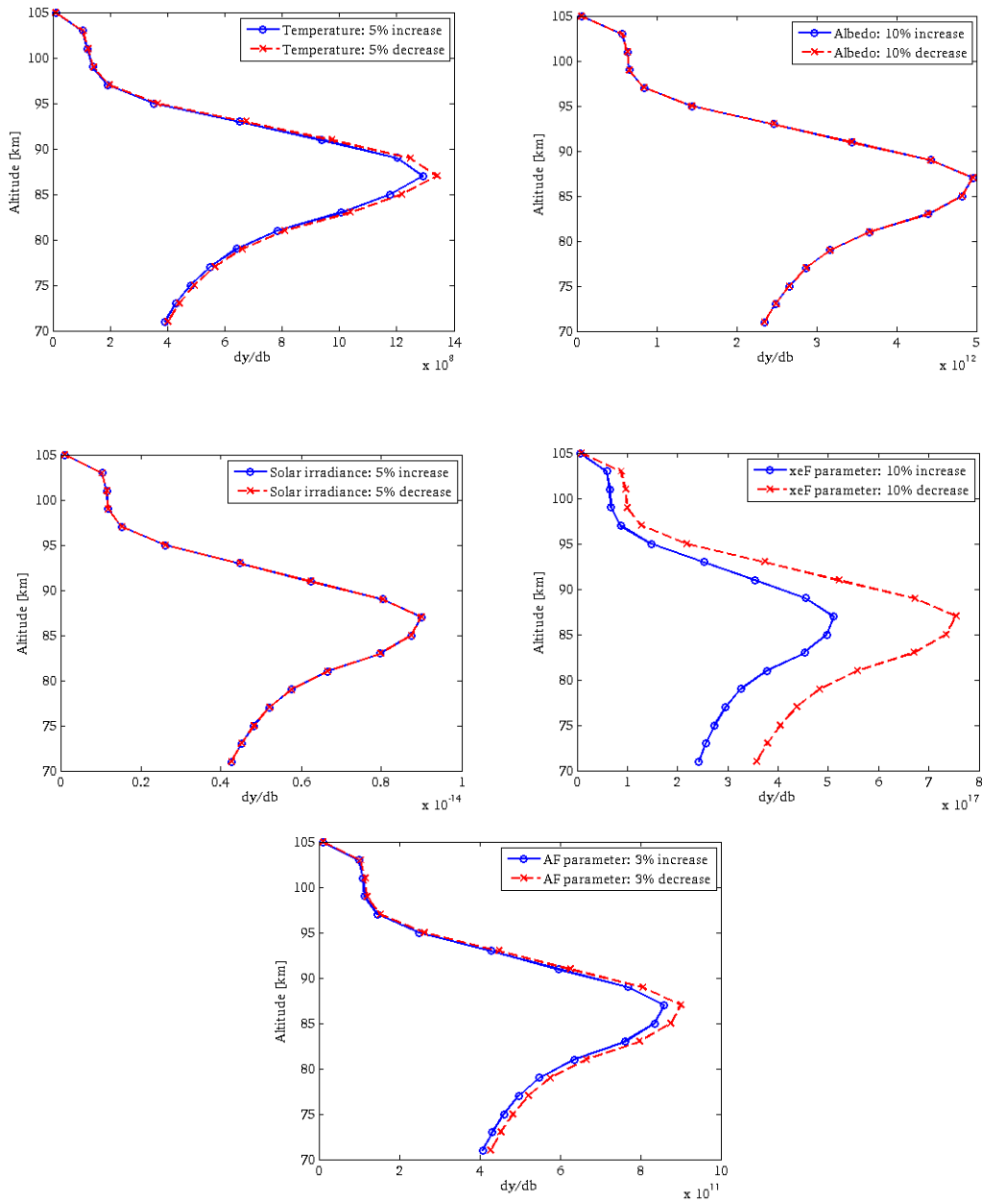


Figure 4-3: Sensitivity of the retrieval to a change in the forward model parameters.

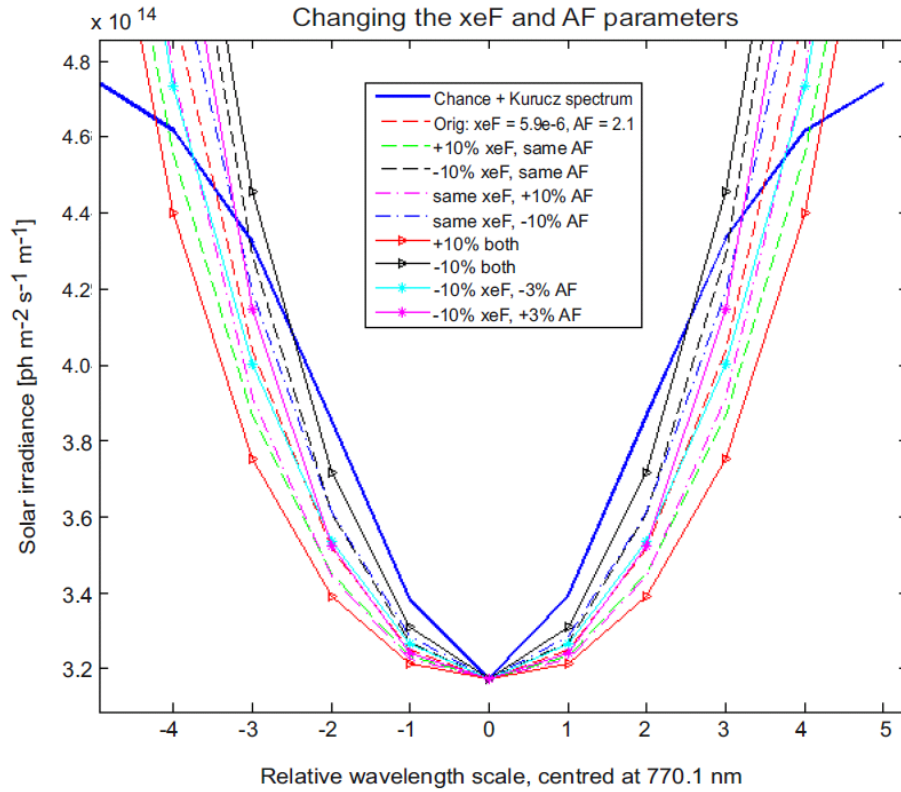


Figure 4-4: Effect of changing the x_e and A parameters (referred to in plot as xeF and AF , respectively).

The error contribution from each of these parameters can now be calculated using Equation 4.2, and the total forward model parameter error can then be determined by adding these individual errors on a RMS basis. The resulting error contributions, along with the total forward model parameter error, are shown in Figure 4-5. By far, the largest error contribution comes from the albedo parameter. In all cases, the contributions from each of the model parameters is greatest within the peak region.

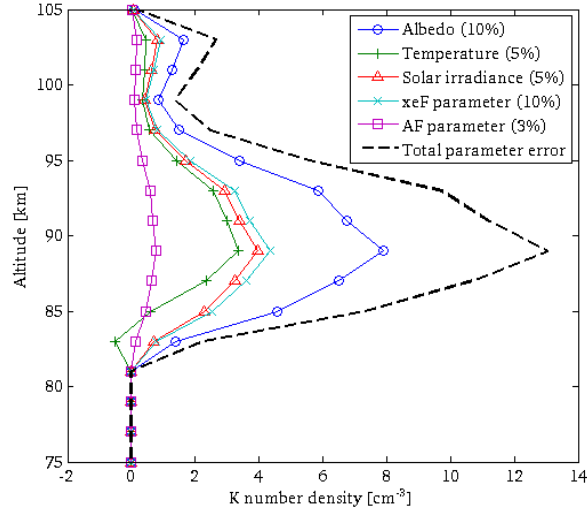


Figure 4-5: Contributions to the forward model parameter error. Need to understand why temperature results in a negative profile at 83 km.

4.2.4 Smoothing error

The smoothing error in Equation 4.2 represents the uncertainty in the observed vertical structure of the retrieval as a result of the instrument making a series of discrete measurements at specific altitude intervals rather than a continuous series of measurements. As a result, the retrieval results are smoothed and this smoothing error must be considered when interpreting the results

$$\varepsilon_s = (A - I).(x - x_a) \quad 4.6$$

Where A is the averaging kernel ($A=G.K$), and I is an identity matrix. The averaging kernel reflects the influence of the true state x_t on the retrieved result \hat{x} , such that

$$A = \frac{\delta \hat{x}}{\delta x_t} \quad 4.7$$

As the true state is unknown, the averaging kernel can instead be estimated statistically using via

$$A = G.K$$

4.8

An example averaging kernel is shown in Figure: 4-6. The retrieval at any altitude is an average of the whole profile weighted by this row. For an ‘ideal’ retrieval, this averaging kernel should be a unity matrix. However, this is often not the case due to the limited vertical resolution of the limb instrument, and thus the retrieval is usually smoothed with information from multiple observation altitudes contributing to the final retrieved density at any given altitude. At a retrieval altitude of 91 km (curve for 91 km), the retrieval is most sensitive to a change in the true state at the same altitude (at 91 km on y-axis), which is close to ideal. The lowest altitude curves (75, 77 and 79 km) are sensitive to perturbations in the true state between 77-83 km and 99-105 km; this is most likely as a result of there being little information in the measurements within these region and results in the retrieval smoothing the true state below 83 km.

The vertical resolution of the retrieval can be estimated by the FWHM of the elements of the averaging kernel matrix. For this work, the vertical resolution is approximately 2 km within the peak region, decreasing to 4 km above and below the peak layer.

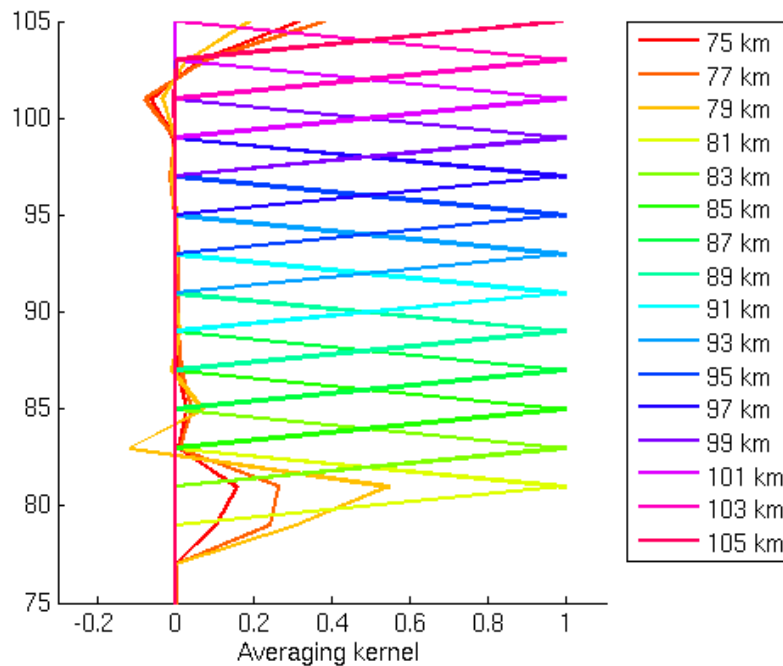


Figure: 4-6: Example averaging kernel.

An example smoothing error profile is shown in Figure 4-7. As can be seen, while there is almost no smoothing of the true profile within the peak region (87-95 km), the smoothing error increases outside of this region. At around 80 km, the smoothing error approaches 50% of the retrieved profile and above 100 km, this increases to 60-70 km. This is not ideal but is to be expected as a result of the lack of information in the measurements in these region outside of the peak layer.

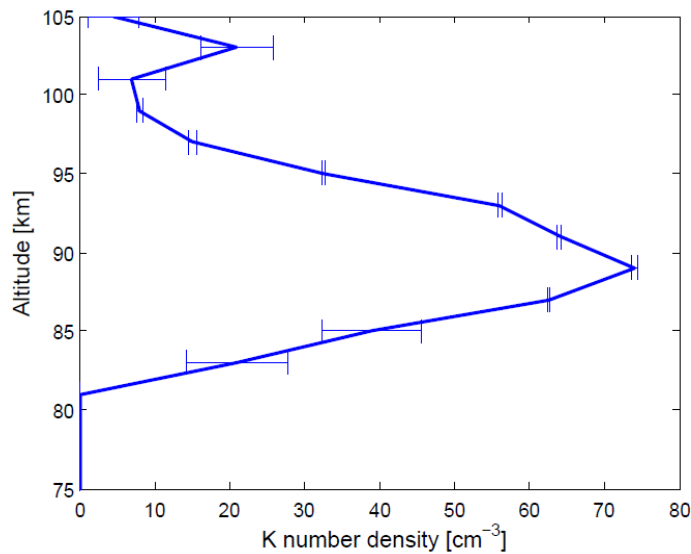


Figure 4-7: Retrieved *K* number density profile with associated smoothing error contribution indicated by horizontal bars.

4.2.5 Total retrieval error

The total error and the different error source contributions for an example retrieved profile is shown in Figure 4-8. Here, the total error consists of the measurement error, smoothing error and model parameter error with the largest absolute total error occurring within the peak region of the layer.

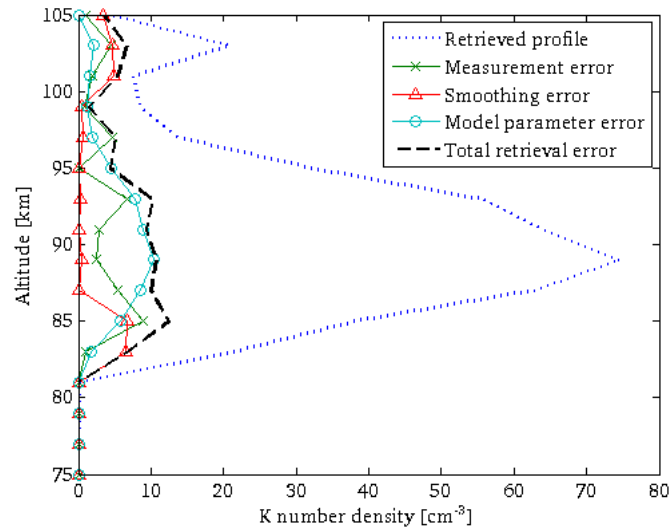


Figure 4-8: Contributions from different error sources to the final retrieved profile.

However, the largest absolute error may of course naturally arise as a result of the retrieved profile being the largest at this point, and it is important not to confuse this as being the region where there is the *most* error. Instead, it is important to consider a breakdown of the relative error contributions normalised by the retrieved profile (shown in Figure 4-9). It can now be seen that the relative error contribution is lowest in the peak region (around 15%) and increases to a maximum at 80 km (50%) and 101 km (70%), with the largest contribution coming from the smoothing error.

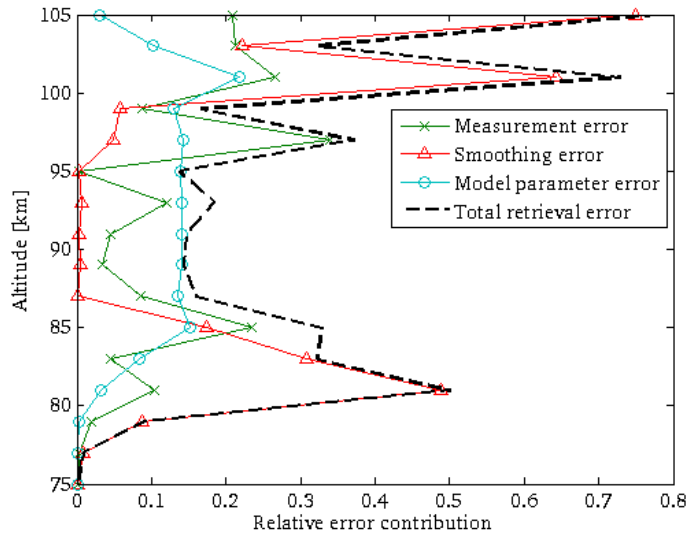


Figure 4-9: *Relative contributions from the different error sources to the final retrieved profile.*

4.3 Ground-truth for K retrievals

The comparison of the retrieved K metal layers with available lidar station data presents the most comprehensive way to ground-truth the retrieval results. This is typically done by comparing the retrieved profile (plus total error) with the corresponding lidar profile (with associated total error) during a satellite overpass of that particular lidar station. Whilst there are a number of Na and Fe lidar stations at a variety of global latitudes, the K lidar dataset record is very sparse, with only two stations at Arecibo and Kühlungsborn providing relatively long-term records (indicated by the blue stars in Figure 4-10). These K lidars are capable of retrieving information about the K layer with very high vertical resolution (~ 0.15 km) and have excellent temporal sampling during operation periods.

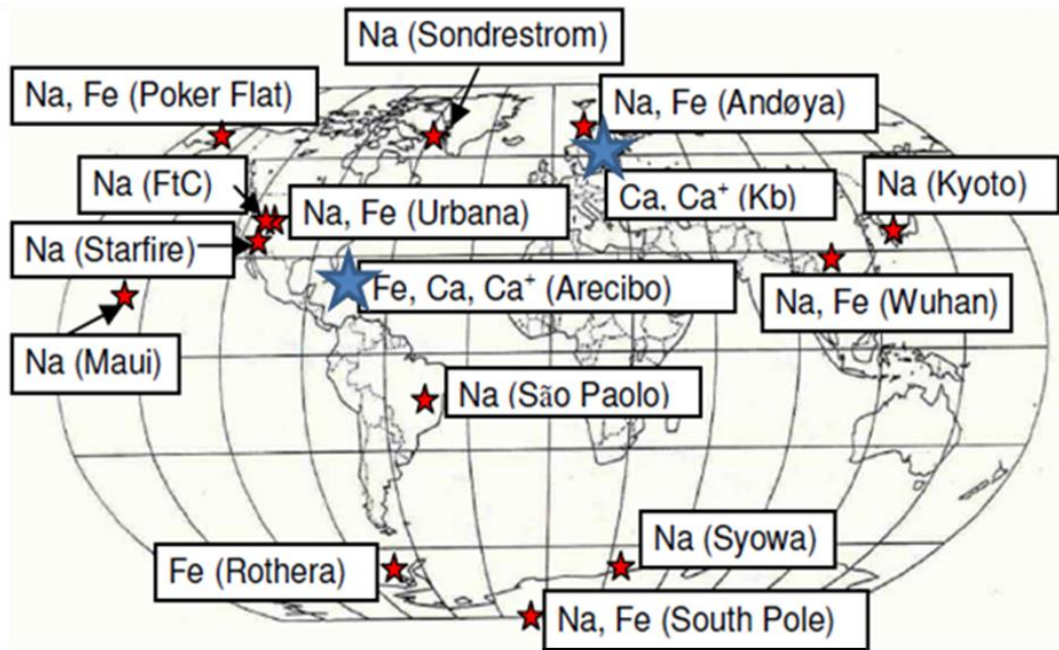


Figure 4-10: *The global lidar network. The K lidars at Arecibo and Kühlungsborn (Kb) are indicated by blue stars. Reproduced from the 4M proposal [J. Plane, pers. comm.].*

4.3.1 Comparison with Arecibo (18°N)

The Arecibo lidar station is located in Puerto Rico at 18.35°N, 293.25°E. Whilst the data record covers a large number of years (data available across the period 2001-2009), the data record is intermittent with large periods of time in which no observations take place. This presents a problem in terms of delivering a robust ground-truth plan. Nevertheless, all available K data must be used to best advantage.

There are only a small number of Odin satellite overpasses within the vicinity ($\pm 5^\circ$ lat and $\pm 10^\circ$ lon, within the range of $\pm 1-2$ days) of Arecibo during the periods the lidar is in operation. The date and latitude/longitude information for these instances are listed in Table 4-1.

Table 4-1: List of simultaneous OSIRIS and Arecibo lidar measurements.

Period	OSIRIS	Arecibo lidar
May 2004	16 th May 16.86°N, 286.09°E	15 th May 18.35°N, 293.25°E
Aug 2007	15 th Aug 16.63°N, 297.95°E	15 th May 18.35°N, 293.25°E
Jan 2008	25 th Jan 16.91°N, 300.31°E	23 rd Jan 18.35°N, 293.25°E
Jan 2008	25 th Jan 16.91°N, 300.31°E	24 th Jan 18.35°N, 293.25°E

These case studies are presented in Figure 4-11 to Figure 4-14. In each Figure, the left-hand side plot shows all the lidar profiles for that day in red, with the satellite profile shown in red. It is easy to see that there is a large amount of variation in the Arecibo K layer profile even over a short period of a day. Indeed the variation is so large that individual K profiles cannot be picked out. Because of this variation, it is very difficult to draw any conclusions by comparing a single OSIRIS profile with a lidar profile, particularly as the OSIRIS profile is not necessarily at the same exact latitude-longitude position as the lidar station.

The right-hand side plots show the same OSIRIS profiles, but this time the mean OSIRIS profile is shown along with ± 1 standard deviation. The mean Arecibo profile in Figure 4-11 and the single OSIRIS profile show very similar features, namely a relatively small peak at 85 km and a much larger peak near 95 km. The absolute number densities of the OSIRIS profile differ on the top side (>100 km) and bottom side (<89 km) when compared to the Arecibo mean profile and the associated standard deviation. This could be attributed to the reduced sensitivity of the retrieval above and below the peak layer height. However, the OSIRIS is still perfectly within the range of the lidar

measurements in the left-hand side plot of Figure 4-13. This draws attention to a caveat that one must be careful when comparing data of this nature.

The following day (24th Jan, Figure 4-14) this layer then appears to have split into two layers, one peaking at around 85-90 km and the other around 95-98 km. The OSIRIS profile, which corresponds to a day later still (25th Jan), could be a continuation of this layer split and shows a distinct layer between 87-91 km and another centred around 95 km.

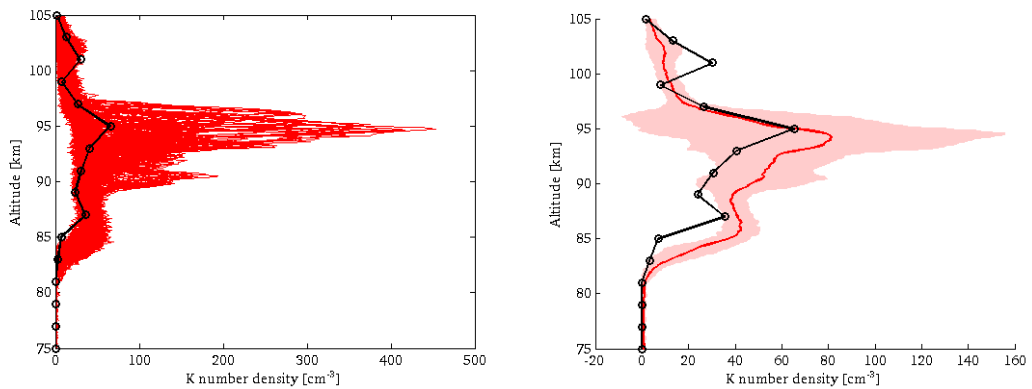


Figure 4-11: OSIRIS K profile (16.86°N, 286.09°E, 16th May 2004) versus Arcicbo lidar (15th May 2004). [Left panel] OSIRIS single profile in black, all Arcicbo lidar profiles in red. [Right panel] OSIRIS single profile in black, mean Arcicbo lidar profile in red (± 1 standard deviation, shaded area).

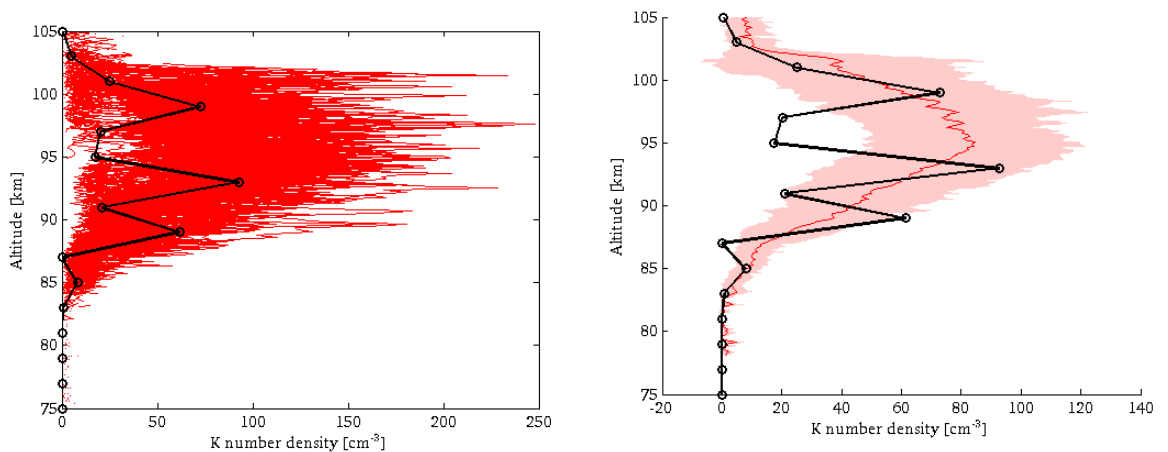


Figure 4-12: OSIRIS K profile (16.63°N, 297.95°E, 15th Aug 2007) versus Arcicbo lidar (15th Aug 2007). [Left panel] As in figure above (OSIRIS single profile in black, all Arcicbo lidar profiles in red). [Right panel] As above (OSIRIS

single profile in black, mean Arecibo lidar profile in red (± 1 standard deviation, shaded area).

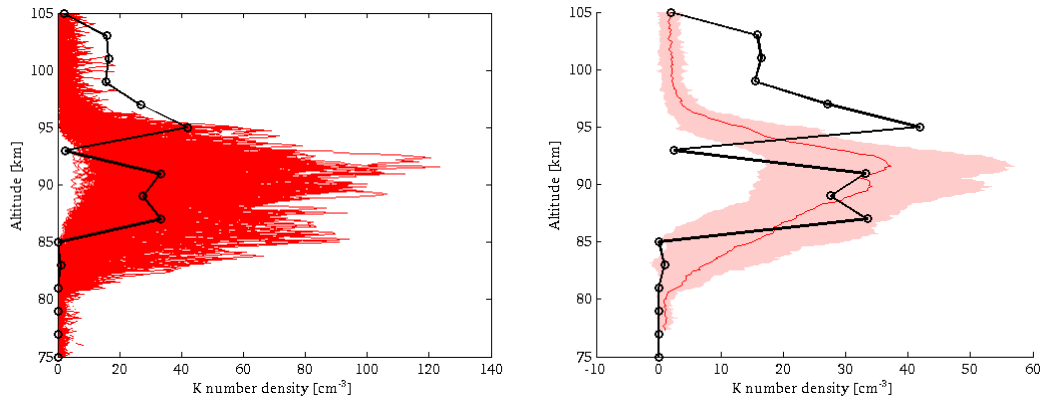


Figure 4-13: OSIRIS K profile (16.91°N , 300.31°E , 25^{th} Jan 2008) versus Arecibo lidar (23^{rd} Jan 2008). [Left and right panels] As above.

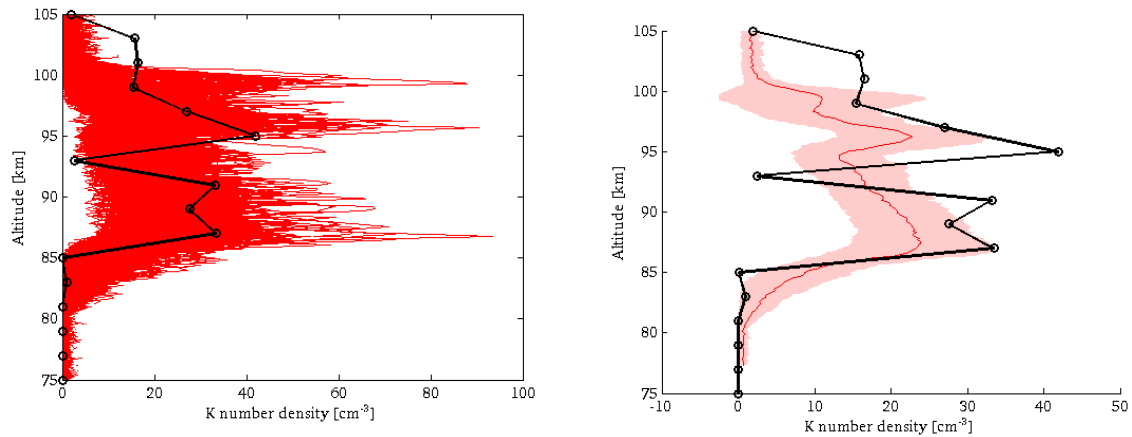


Figure 4-14: OSIRIS K profile (16.91°N , 300.31°E , 25^{th} Jan 2008) versus Arecibo lidar (24^{th} Jan 2008). [Left and right panels] As above.

As can be seen from the above simultaneous plots, there is a huge amount of variation within the K number density layer even over a very short period, and unless an exact overpass is achieved during a period when the Arecibo lidar is in operation, any robust comparison is difficult.

Another approach is to compare monthly mean profiles for OSIRIS and Arecibo. Here, a test year of 2004 was chosen due to the relatively large occurrence of measuring days at Arecibo. For each month, the mean monthly OSIRIS profile (zonally averaged in a 10° latitude band centred about Arecibo) ($\pm 1\sigma$) is compared to the mean monthly Arecibo profile ($\pm 1\sigma$) and these are shown in Figure 4-15 to Figure 4-22. The OSIRIS mean is the mean of all available measurements within this latitude band for the specific month. The Arecibo monthly mean consists of the mean of the daily mean profiles within each month. The number of OSIRIS and Arecibo profiles used to produce each respective mean is indicated in the figure captions.

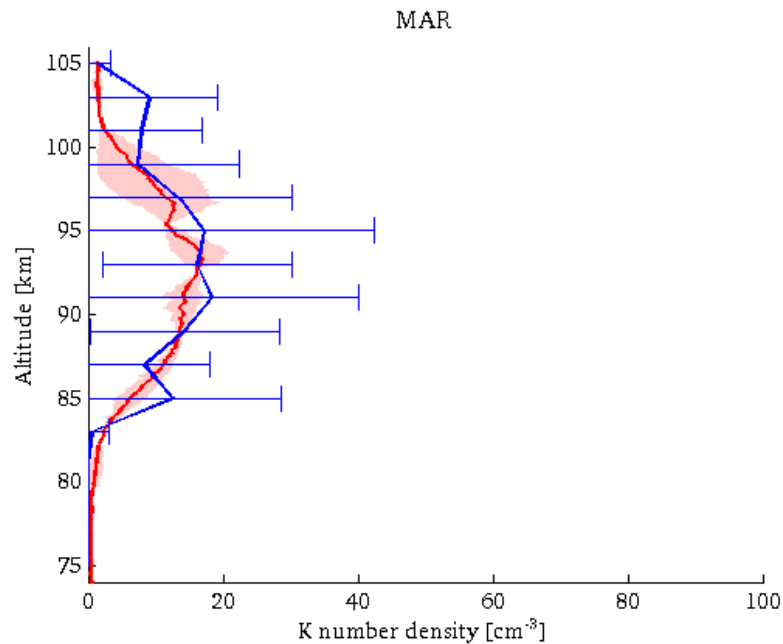


Figure 4-15: March 2004. OSIRIS zonal (13-23°N) mean profile (blue, ± 1 standard deviation) [17 profiles] versus Arecibo (18°N) (red, ± 1 standard deviation) [2 profiles].

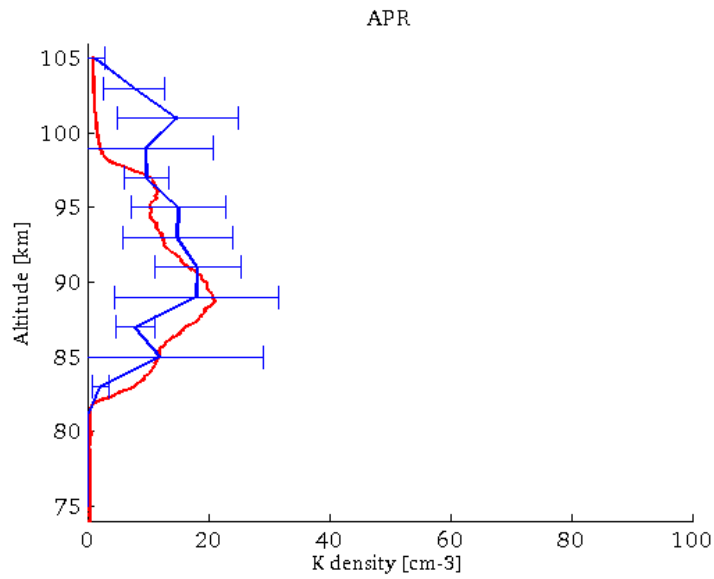


Figure 4-16: April 2004. As Figure 4-15, but OSIRIS profile [4 profiles] versus Arecibo. [1 profile].

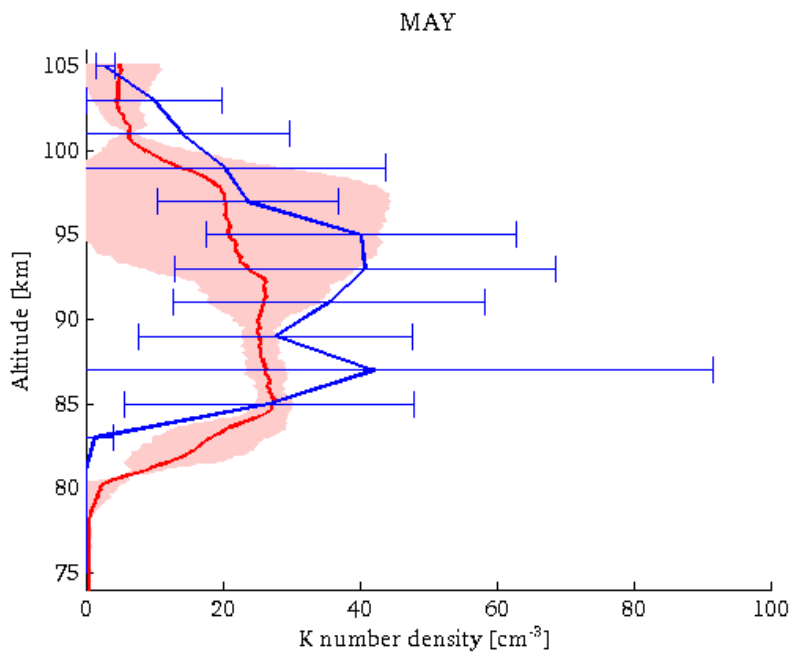


Figure 4-17: May 2004. As before, but OSIRIS [15 profiles] versus Arecibo [2 profiles].

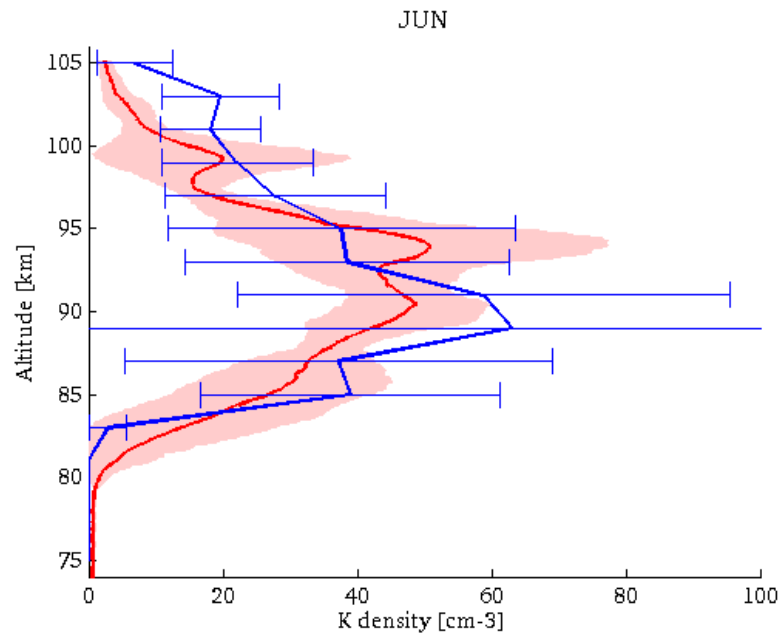


Figure 4-18: June 2004. As before, but OSIRIS [22 profiles] versus Arcibo [3 profiles].

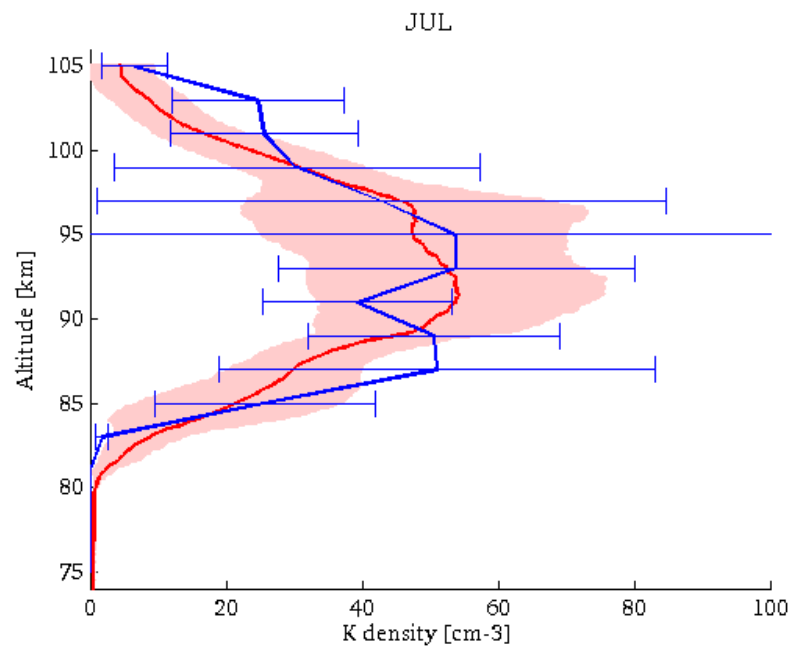


Figure 4-19: July 2004. As before, but OSIRIS [12 profiles] versus OSIRIS [6 profiles].

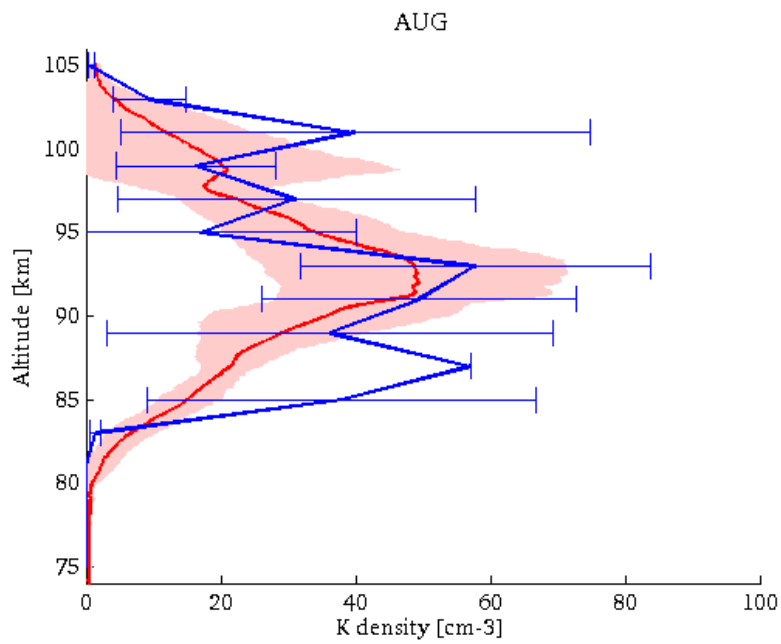


Figure 4-20: August 2004. As before, but OSIRIS [4 profiles] versus Arecibo [7 profiles].

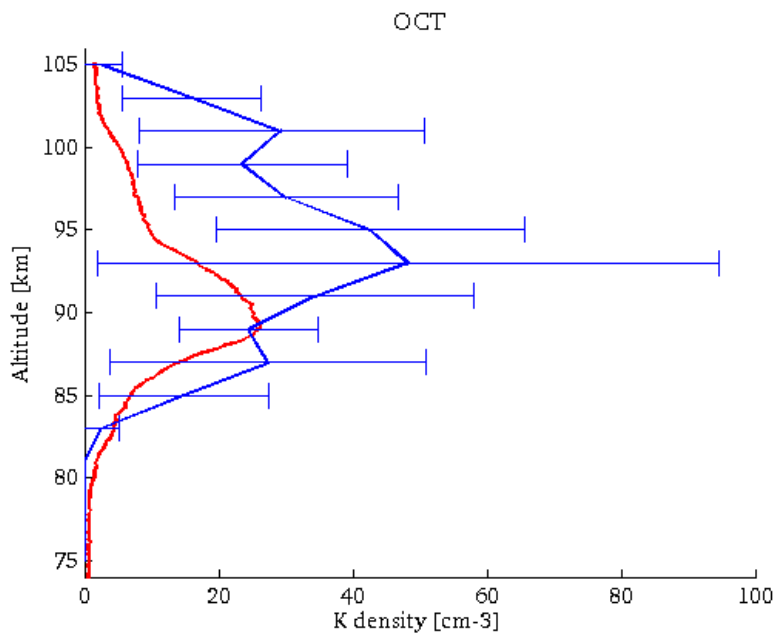


Figure 4-21: October 2004. As before, but OSIRIS [9 profiles] versus Arecibo [1 profile].

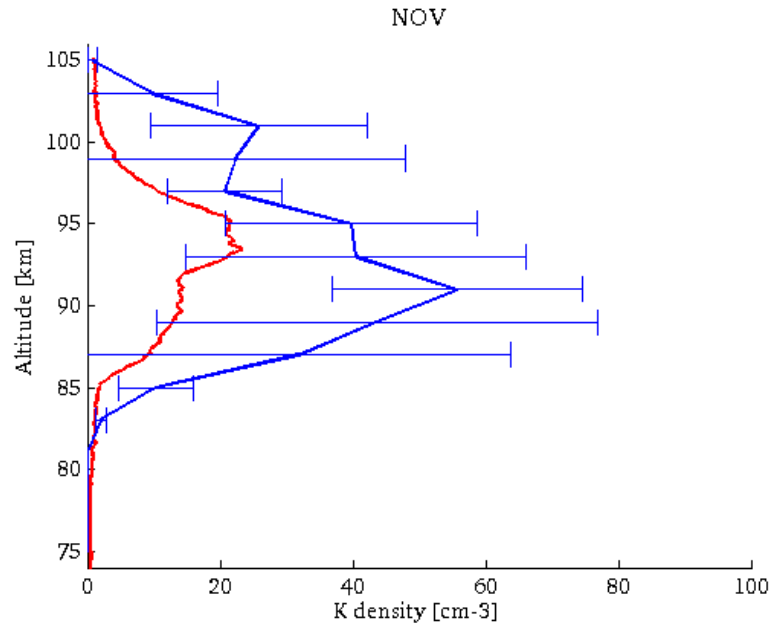


Figure 4-22: November 2004. As before, OSIRIS [4 profiles] versus Arecibo [1 profile].

Overall, the OSIRIS monthly means compare well to the Arecibo lidar means with the overall absolute densities being similar. In many cases, the variation (indicated by the error bars) is similar for both the OSIRIS and Arecibo profiles. The OSIRIS data variation is occasionally larger, but this should be expected as a result of the wider latitude band that the data is taken from, compared to the single latitude-longitude location of the lidar station.

The closest agreement occurs when the greatest number of profiles are used for deriving the OSIRIS and Arecibo means. One such example is for July, where the OSIRIS profile consists of 12 individual profiles and the Arecibo profile consists of 6 days worth of measurements. The worst agreement can be seen for months where there is only one day's worth of measurements used for the monthly Arecibo mean, i.e. for October and November. April is the exception to this with good general agreement between the OSIRIS and Arecibo means. The Arecibo mean is produced solely from measurements made on the 17th April 2004. The OSIRIS mean consists of scans made on the 19th, 20th, 3 x 27th and 28th April 2004, but these are zonal measurements made within a 10°

latitude band centred over the Arecibo latitude. Whether or not the OSIRIS profile measured the same layer as seen at Arecibo on the 17th April is unclear.

Discrepancies between the OSIRIS and Arecibo profiles can be caused by a variety of factors. Firstly, a lack of data can contribute to misleading comparisons. The example year of 2004 was chosen because this is the period with the most number of Arecibo measuring days. However, as can be seen by the number of daily mean profiles averaged to produce the monthly mean, this is still a sparse record. Additionally, due to the dual astronomy and aeronomy objectives of the Odin mission, the number of OSIRIS observing days is relatively limited in 2004. In later years, the aeronomy part of the mission was prioritized and the number of scans dedicated to this purpose became a majority.

Another source of difference is that the OSIRIS mean profiles are zonal means centred around the Arecibo station (18°N) $\pm 5^{\circ}$ latitude. Additionally both morning and evening scans are used, and all available Arecibo data is used regardless of the time that it was observed. The reason for this is to maximize the number of scans available for each monthly mean. Nevertheless, as a result of the large K layer variation indicated in the simultaneous measurement plots, these factors can result in discrepancies between the OSIRIS and Arecibo measurements. Despite all of these differences, overall the OSIRIS data appears to be agree comparably to the available lidar data.

A final method of comparison is to compare the monthly column density profiles for 2004 (see Figure 4-23). Column densities generally represent a more robust retrieval product than individual retrieval profiles. Only data between altitudes of 75-97 km is used in order to minimise the impact of the highly variable sporadic K layers (see Section 5.8) which predominantly occur above this altitude. A similar exclusion approach is acknowledged or used in other studies [e.g. Eska *et al.*, 1998; 1999; Friedman *et al.*, 2002; Fricke-Begemann *et al.*, 2002]. The OSIRIS measurements are largely spatio-temporally independent. Thus the error of the mean (2σ) is used as the error range for the OSIRIS data; this consists of $2\sigma/\sqrt{N}$, where N is the number of individual profiles used to calculate the mean. In contrast, due to the nature of lidar

measurements (i.e. many continuous measurements may be made over a short period of time, but intermittently thereafter), the error of the mean does not represent an appropriate choice of error range. In this case, the standard deviation of the mean (1σ) is used instead to represent the error of the lidar data, and provide an estimate of the strong temporal variation within the layer.

Both the OSIRIS and Arecibo datasets clearly show a summertime maxima and there is a very good overall agreement across the March-August period. No Arecibo data is available in September 2004, but it can clearly be seen that the OSIRIS October and November column densities are considerably larger than those for Arecibo. Referring back to Figure 4-21 and Figure 4-22, this is most likely due to only one day's measuring period at the Arecibo lidar station during these months.

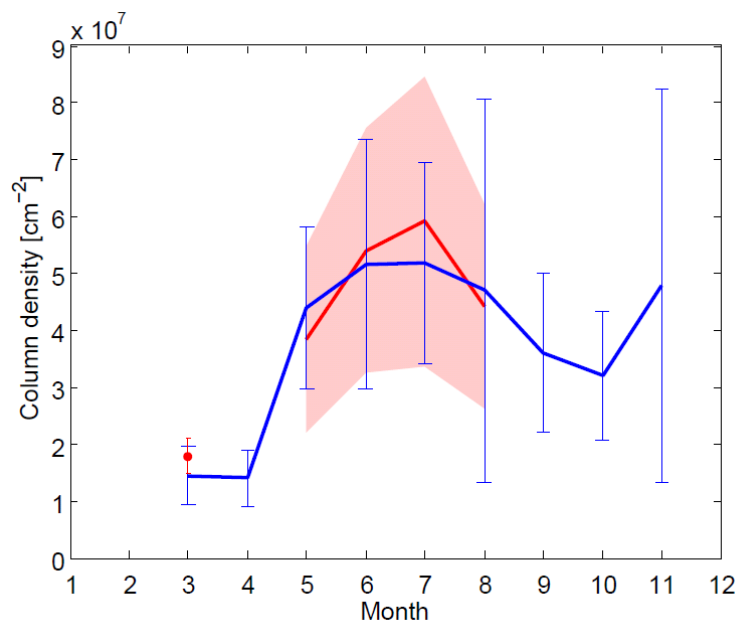


Figure 4-23: Comparison of OSIRIS versus Arecibo monthly mean column densities for 2004. The OSIRIS monthly mean column density for $18\pm 5^\circ\text{N}$ is shown in blue, along with the corresponding error of the mean (2σ , vertical bars), while the Arecibo monthly mean column density along with the associated variation (1σ , shaded area) is shown in red.

4.3.2 Comparison with Kühlungsborn lidar (54°N)

The Kühlungsborn lidar station is located in northeast Germany at 54.1°N, 11.8°E. A comparison of the OSIRIS versus Kühlungsborn monthly mean column densities for 2005 (chosen due to the largest availability of lidar data being present in this year) is presented in Figure 4-24. Overall there is largely very good agreement between April to November, with a summertime maximum and equinoctial minima being observed in both the OSIRIS and lidar datasets. Additionally, a local midsummer minimum exists in both datasets, although the OSIRIS minimum occurs one month later (July) than in the lidar data (June). The OSIRIS data lies within the range of variation of the Kühlungsborn lidar data.

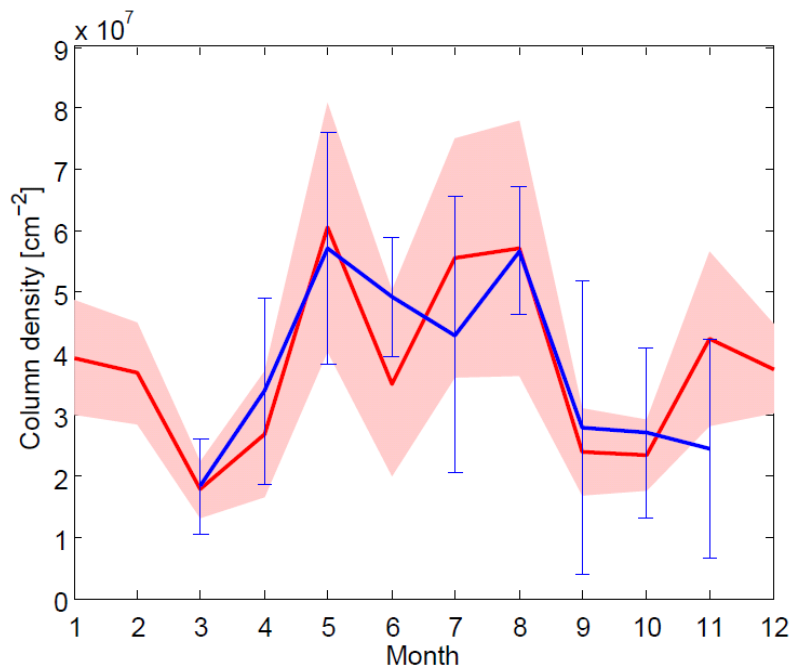


Figure 4-24: Comparison of OSIRIS versus Kühlungsborn monthly mean column densities for 2005. The OSIRIS monthly mean column density for $54 \pm 5^\circ\text{N}$ is shown in blue, along with the corresponding error of the mean (2σ , vertical bars), while the Kühlungsborn monthly mean column density along with the associated variation (1σ , shaded area) is shown in red. Only data between 75-97 km is used in order to minimise the impact of sporadic K layers on the analysis.

4.3.3 Comparison with Tenerife lidar data (28°N)

A comparison of the OSIRIS versus Tenerife monthly mean column densities is presented in Figure 4-25. This comparison uses data presented in Fricke-Begemann *et al.* [2002], who made lidar measurements across 55 nights between 27th March-29th November 1999, at the Observatorio del Teide, Tenerife (28.2°N, 17.3°W). As no direct comparison of OSIRIS data can be made for this period, a multi-year mean monthly mean column density set for 2004-2011 is used instead. Overall, there is satisfactory agreement between both the OSIRIS and lidar dataset, with both showing a summertime K column density maximum of comparable magnitude.

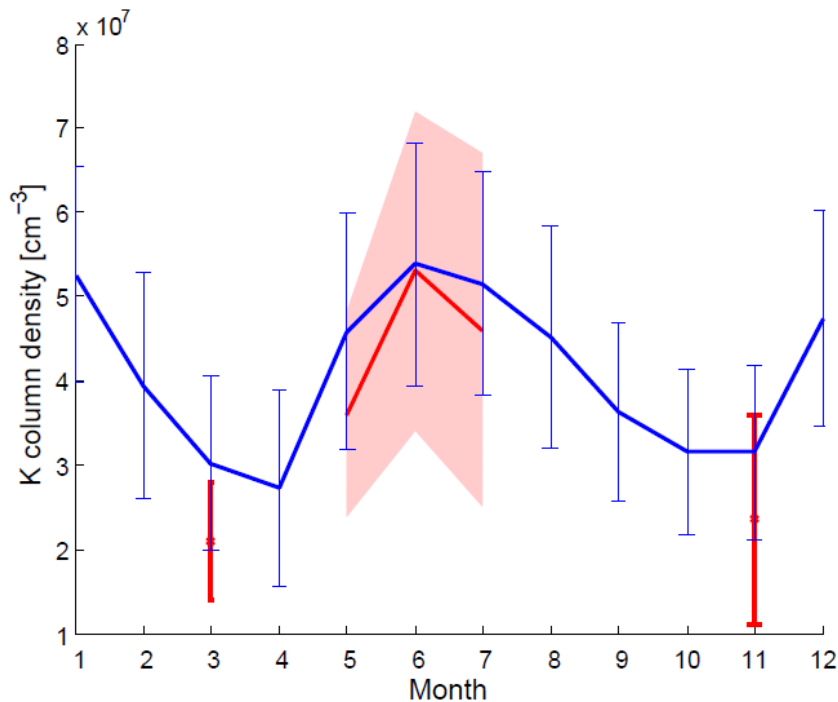


Figure 4-25: Comparison of OSIRIS versus Tenerife [Fricke-Begemann *et al.*, 2002] monthly mean column densities. The OSIRIS multi-year mean (2004-2011) monthly mean column density for $28 \pm 5^\circ\text{N}$ is shown in blue, along with the corresponding error of the mean (2σ , vertical bars). The Tenerife data consists of 55 nights of measurements made during Mar-Nov 1999; the monthly mean column density is determined and is shown, along with associated variation (1σ , shaded area), in red. Only OSIRIS data between 75-97 km is used in order to minimise the impact of sporadic K layers on the analysis.

4.4 Summary

Error-characterisation and ground-truthing are important steps in developing and testing any new satellite dataset. The error sources and contributions to the retrieval have been discussed with the largest contribution coming from the model parameter error within the peak region and both the smoothing error and measurement error outside of the peak region.

Finally, the OSIRIS K retrieved data are compared with ground-truth lidar data from Arecibo, Kühlungsborn and Tenerife, and are shown to compare reasonably well. Reasons for discrepancies include the fact that the OSIRIS data is taken for a 10 degree latitude band centred around the lidar station. In addition, observations from all longitudes are used, whereas the data from the lidar station are for a specific latitude-longitude position. Both the OSIRIS and lidar profiles indicate that there is a lot of variation within the layer. Thus, the intermittent nature of the lidar operation periods, as well as the need to produce mean OSIRIS profiles for large latitude bands will account for a certain and unknown degree of discrepancy between the datasets.

The following Chapter 5 will now use the new OSIRIS K dataset to present the first look at the near-global behaviour of K, use it to validate a global model, and use it for a number of applications.

5 THE GLOBAL POTASSIUM LAYER

5.1 Introduction

Lidar studies from Arecibo (18°N) and Kühlingsborn (54°N) have shown that the K layer has an unusual semi-annual seasonality (winter and summer maxima) in contrast with the annual seasonality (winter maximum only) seen in the Na and Fe layers. However, due to the very limited horizontal coverage of the two K lidar stations, a global view of the layer and its seasonality can only be determined from satellite observations. Results from the previous chapter have shown that the OSIRIS data compares well to the existing available lidar data. As part of this thesis, the OSIRIS K and Na datasets have now been extended to continuously cover the period 2004 to summer 2013. In this chapter, the first near-global results from the retrieved K dataset will be presented, and the seasonal and latitudinal characteristics of the layer (e.g. K column abundance, absolute number density height profile, and the layer height and width) will be described.

Specific emphasis will be placed on the stark contrast between the K and Na seasonality (Section 5.3), and the chemistry which determines this unusual K behaviour will be introduced (Section 5.4). In the subsequent subsections, the K layer will be explored in more detail, specifically looking at diurnal changes within the K layer (5.6), examination of the interaction of the K layer with polar mesospheric clouds in Section 5.7, and finally, the horizontal and temporal occurrence of sporadic layers is presented in Section 5.8 In each section, where applicable, the relevant literature will be reviewed in the prefacing introduction.

5.2 A first look at the near-global K layer

5.2.1 Column abundance

A near-global view of the zonally-averaged OSIRIS K layer column densities is shown in Figure 5-1. Each grid box represents the mean monthly column integrated density

binned into 10° latitude bands (for 75-97 km only, as discussed in Section 4.3). The blank grid boxes indicate where no OSIRIS K profiles are available. At very high winter latitudes, this results from a lack of OSIRIS measurements during the polar night. For the mid-high winter latitudes, these boxes are as a result of the OSIRIS solar zenith angles always exceeding 93° , and thus these measurements are excluded. Additionally, further profiles have been excluded due to quality-control processes described in Chapter 3.

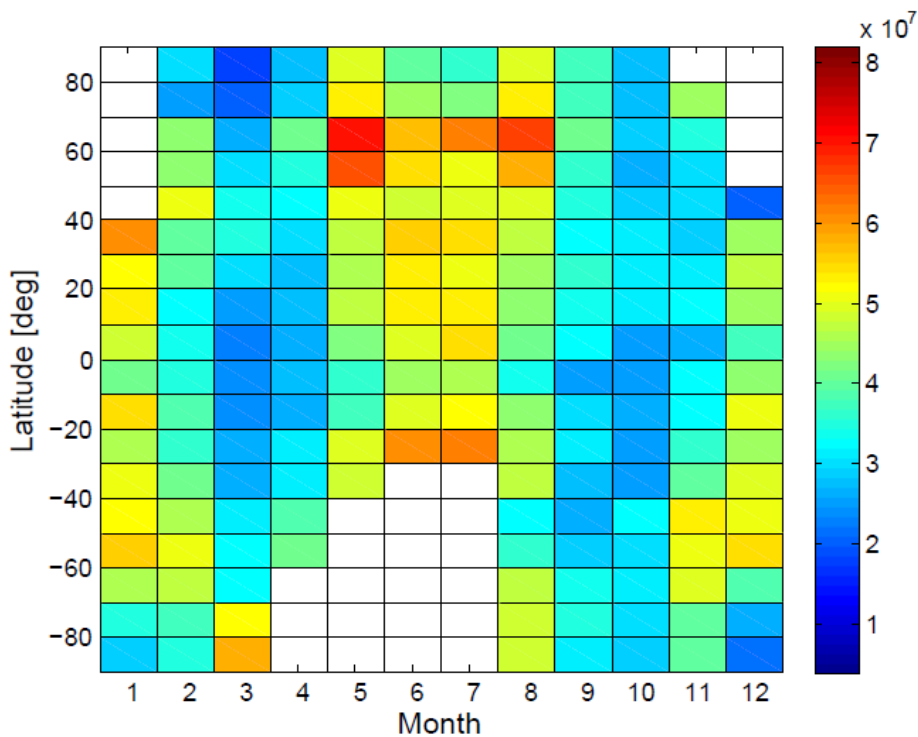


Figure 5-1: Grid plot of the monthly averaged total OSIRIS K column density zonally averaged in 10° latitude bins for 2004-2013. [Units: $K \text{ atoms cm}^{-2}$].

As described in Chapter 4, other studies have shown that the K layer is semi-annual in extent with summer- and winter-time maxima, and the OSIRIS data shows good agreement with these lidar data. For the first time, the different latitudinal variation can be seen at latitudes without lidar coverage.

The seasonal variation can be seen at northern latitudes above 50°N , with the variation less pronounced between $30\text{-}50^\circ\text{N}$. Additionally, there appears to be hemispheric

asymmetry, with the northern hemisphere (NH) variation larger than that of the southern hemisphere (SH). Within the high summer latitudes, a local summer minimum is apparent. In general, the NH spring minimum is deeper than that of the autumn minima. This spring/autumn difference is most likely a result of the seasonal dependence of the K injection flux, as shown in Figure 5-2. This occurs as a result of the peak input of meteoroids in the autumn period and hence an increase in the amount of ablated metals within the MLT region.

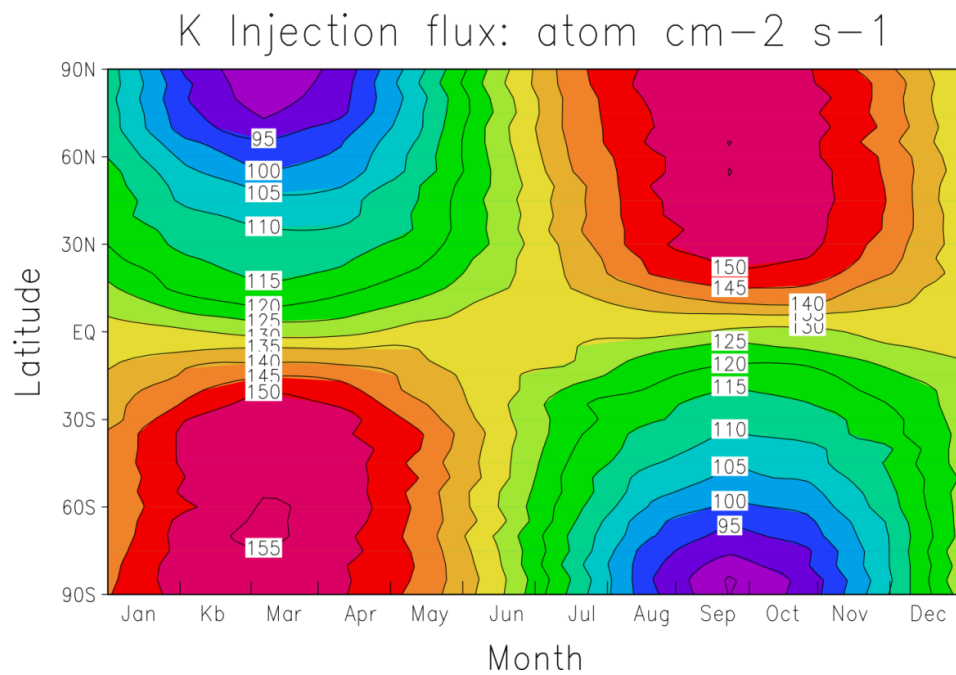


Figure 5-2: The K injection flux [units: K atoms cm⁻² s⁻¹]. From W. Feng (pers. communication).

Column density profiles for individual latitudes are shown in Figure 5-3. Within both hemispheres, the strongest annual variation is generally seen at higher latitudes. The exception to this is for 0-30°S where there is a very large summer-winter variation; this likely results from the relatively high June and July column densities between 20-30°S. Both the NH and SH 60-82° profiles show local summertime minima between May to August, and November to March, respectively; this is likely as a result of polar depletion by polar mesospheric clouds, and is discussed in Section 5.7.

As shown in Chapter 4, there is good agreement between the OSIRIS and lidar K column densities despite spatio-temporal differences. This agreement serves as the basis for using the OSIRIS dataset to investigate the chemical and dynamical processes relevant to the global K densities discussed further in this chapter.

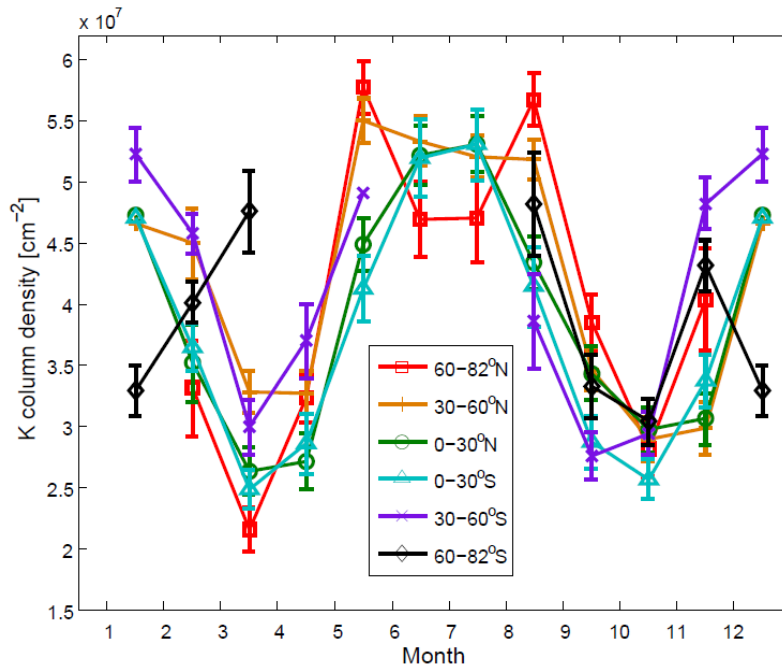


Figure 5-3: OSIRIS K zonal mean monthly mean column density profiles (2004-2013), binned into 30° latitude bands. NB: the OSIRIS latitude coverage only extends up to 82°N and 82°S. Vertical error bars represent the error of the mean ($2\sigma/\sqrt{N}$, where N = no. of observations within the month). Only data from profiles <97 km is considered. [Units: K atoms cm^{-2}].

5.2.2 Monthly mean density profiles

The seasonal variation in the absolute K densities is shown in Figure 5-4. The largest seasonal variation occurs at latitudes $>60^\circ$ in both hemispheres. This is in agreement with satellite observations of Na [Fussen *et al.*, 2004; Fan *et al.*, 2007a; Fussen *et al.*, 2010; Hedin and Gumbel, 2011] and modelling studies of Na [Marsh *et al.*, 2013] and Fe [Feng *et al.*, 2013]. This may be as a result of transport of K atoms poleward away from low latitudes as a result of the meridional circulation, as first identified by Gardner *et al.* [2005] who sought to explain the unusually high wintertime densities of Na and Fe

at the South Pole. There is also a large amount of seasonal variation in the 0-30°S profile (predominantly due to the influence of the layer between 20-30°S), which could possibly be related to South Atlantic anomaly region activity and the impact of sporadic *E* on the K metal layer (see Section 5.8). In many profiles, there is a pronounced secondary layer at 95 km and above. These are likely to be sporadic K layers (also, Section 5.8) which are of sufficiently high concentrations that they are not fully removed with averaging and show up in the monthly layer. Alternatively, it is also possible that they may be an artefact from the large retrieval errors (between 15-70%) associated with the OSIRIS K profiles at these altitudes.

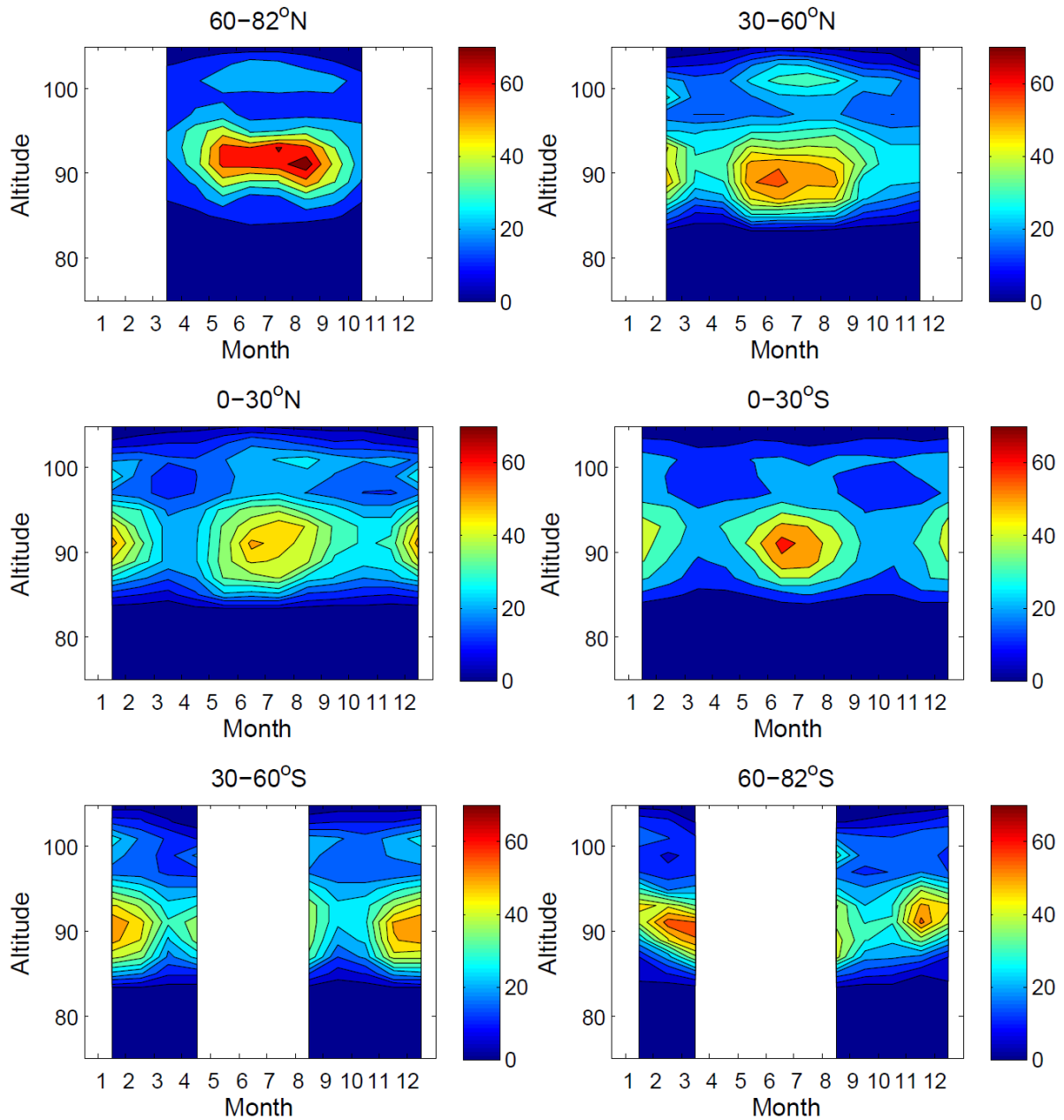


Figure 5-4: Seasonal variation of the OSIRIS mean monthly K layer, as a function of month and altitude, in 30° latitude bins (with the exception of 60-82° profiles). White gaps indicate either no OSIRIS coverage, or no available data. [Colour bar units: K atoms cm⁻³].

5.2.3 Peak layer height plots

A comparison of the mean centroid altitudes of the zonal mean OSIRIS K layer profiles is shown in Figure 5-5. The mean global centroid height is approximately 91.2 km, with a mean variation of ± 0.6 km throughout the year. The centroid altitude variation is

typically greatest at high latitudes (91.9 ± 1.2 km for $60\text{-}82^\circ\text{N}$, 91.3 ± 0.7 km for $60\text{-}82^\circ\text{S}$), and linearly decreases towards the low latitudes (91.2 ± 0.4 km for both the $0\text{-}30^\circ\text{N}$ and $0\text{-}30^\circ\text{S}$ profiles).

Due to the limited vertical resolution of the K retrieval (approximately 2 km), the centroid altitude cannot be resolved to the same resolution and precision as a ground-based lidar. Indeed, the variability of the mean OSIRIS centroid altitude is typically smaller than the vertical resolution of the retrieval. Despite this, the semi-annual variation (highest centroid altitudes during the equinoxes) is largely consistent with lidar measurements of the K layer at Arecibo and Kühlungsborn [Eska *et al.*, 1998; Friedman *et al.*, 2002; Höffner and Lübken, 2007].

Although there is a relatively small annual variation in the centroid height ($<1\%$ of the mean centroid height), the largest variation occurs at low- and high-latitudes (with means of 91.2 ± 0.4 km and 91.6 ± 0.9 km, respectively, versus 90.9 ± 0.5 km for mid-latitudes). The solstitial centroid minima are likely as a result of dynamical downwelling in the winter mesopause area (shifting the whole metal layer downwards) and layer changes resulting from polar mesospheric cloud (PMC) depletion within the summer polar regions (both depletion on the underside of the K layer, and the corresponding downward vertical eddy flux which results in depletion on the topside of the layer (discussed further in Section 5.8). The lack of PMCs outside of the polar regions, and the reduced vertical dynamical changes within the low latitudes likely results in the reduced centroid variation seen within these profiles.

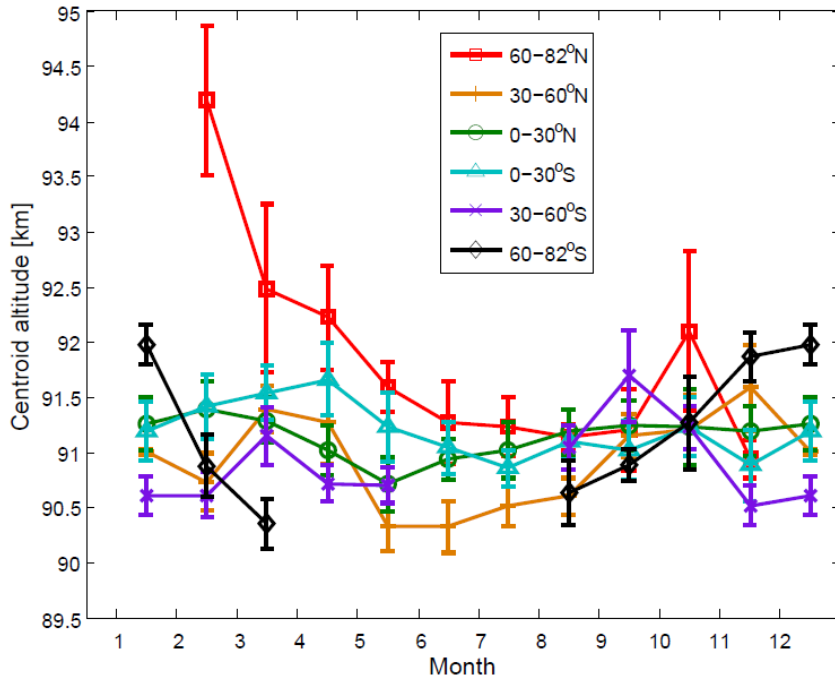


Figure 5-5: Centroid altitude profiles of the OSIRIS zonal mean monthly mean K layer (2004-2013), binned into 30° latitude bands. NB: the OSIRIS latitude coverage only extends up to 82°N and 82°S. Vertical error bars represent the error of the mean.

5.2.4 Layer width variations

The root-mean square (RMS) layer width profiles for different latitude bands are shown in Figure 5-6. The mean global OSIRIS RMS-width is 3.4 km with an absolute mean variation of ± 0.6 km (derived from an approximate range of 2.6-3.8 km). This lies within the 2.3-5.8 km range (mean = 4.0 km) recorded during the Polarstern ship-borne campaign [Eska *et al.*, 1999], which consisted of 66 nights of lidar measurements made between Mar-Jul 1996 across a latitude transect of 71°S and 54°N.

As before, the OSIRIS K retrieval has a limited sensitivity to changes in the RMS-width. However, generally, the global OSIRIS RMS-widths compare well to the available lidar observations and show latitudinal variation in terms of the seasonality of the RMS-width in both hemispheres. The largest annual variation is seen at high-latitudes (± 0.5 km and ± 0.3 km, for 60-82°N and 60-82°S, respectively, compared to approximately ± 0.2 km for the other latitude bands). For latitudes between 0-30°, the early summer RMS-width is

typically ~ 0.3 km higher than during winter. The reverse is seen for latitudes between 60 - 82° where the RMS-width exhibits a winter time maxima and a summer time minima. This is in general agreement with Friedman *et al.* [2002] and Fricke-Begemann *et al.* [2002] who reported low seasonal variation at Arecibo (18°N) and Tenerife (28°N) and early summer RMS layer with maxima, respectively, while Eska *et al.* [1998] found that the RMS-width was higher in winter than during summer for K hlungsborn at 54°N . The sensitivity of the RMS-width to the top- and bottom-sides of the mean profiles (where the OSIRIS retrieved profiles typically have the greatest associated errors) can make the identification of causal mechanisms difficult. The wintertime dynamical downwelling acts to compress the K layer which can result in reduced wintertime RMS-widths. The RMS-width is also particularly sensitive to the occurrence of sporadic K layers which exhibit a semi-annual variation (summer and wintertime maxima, see Section 5.7). Both of these may result in the summertime RMS-width maxima (and wintertime minima) seen within the low latitude bands. The general summertime RMS-width minima at high-latitudes can perhaps be explained as a result of interaction with PMC particles (see Section 5.8); removal of K atoms by uptake on PMCs results in a summertime reduction of the RMS-width.

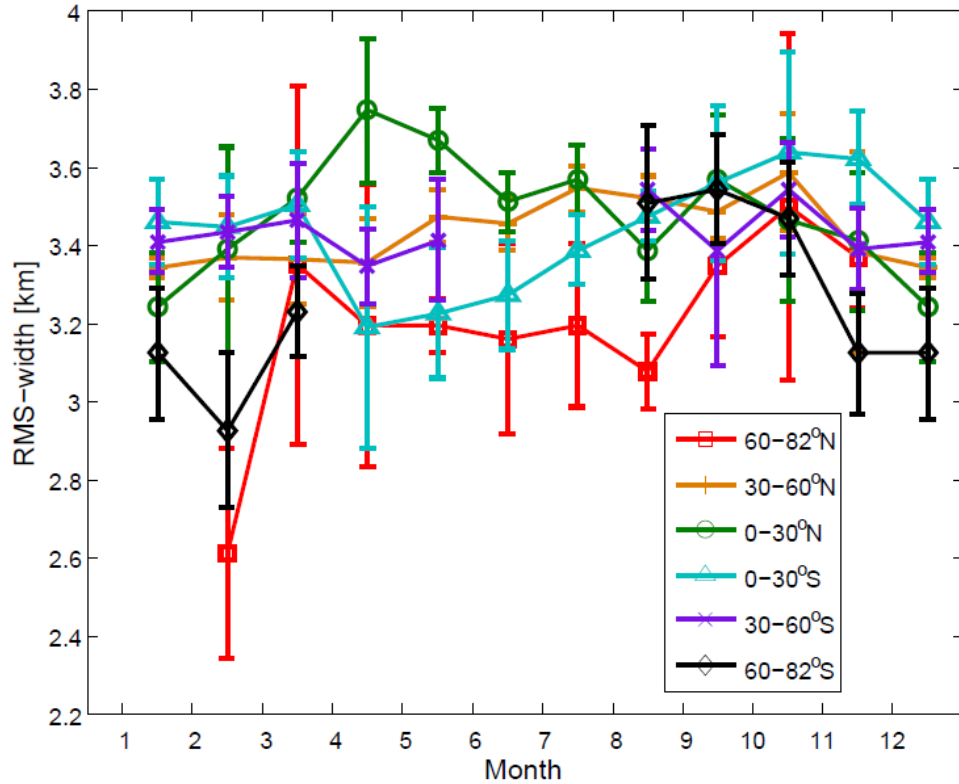


Figure 5-6: RMS-width profiles of the OSIRIS zonal mean monthly mean K layer (2004-2013), binned into 30° latitude bands (with the exception of the $60\text{-}82^\circ$ bands). Vertical error bars represent the error of the mean. [Units: km].

5.3 The different behaviours of K and Na

Figure 5-7 presents the global OSIRIS K layer (top panel) contrasted with the Na layer (also retrieved from OSIRIS) (bottom panel). It can be seen that the metals exhibit two quite different seasonal behaviours; Na has a marked annual seasonality with a wintertime maximum and a summertime minimum. In contrast, K also displays a summertime maximum in addition to the wintertime maximum. This behaviour is very surprising as both Na and K are Group I alkali metals and therefore would be expected to behave in the same way.

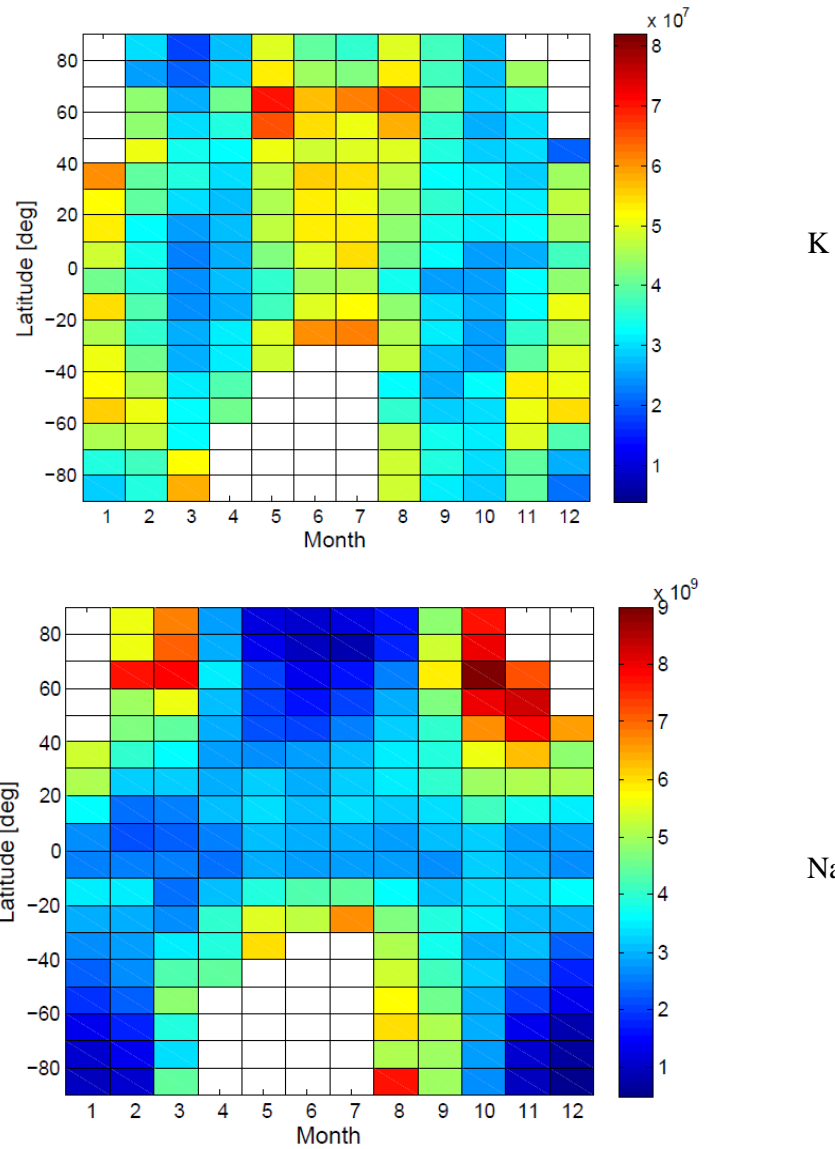


Figure 5-7: Global gridded column density retrieved from OSIRIS (2004-2013) binned into 10° latitude bands for, [top panel] K and [lower panel] Na. [Units: metal atoms cm^{-2}].

5.4 Explanation for the unusual behaviour of K

Both K and Na exhibit wintertime layer maxima as a result of both the hemispheric autumn/winter maximum in the meteor input function (Figure 5-2) and the wintertime downwelling associated with the meridional circulation which compresses and enhances the metal layers.

The observation of the near-global semi-annual seasonality seen in the OSIRIS K data served as an impetus to determine an explanation for the different summertime

behaviour of K and Na. A new chemistry scheme for K, shown in schematically in Figure 5-8, was derived using electronic structure theory and statistical rate theory (Plane *et al.*, 2014).

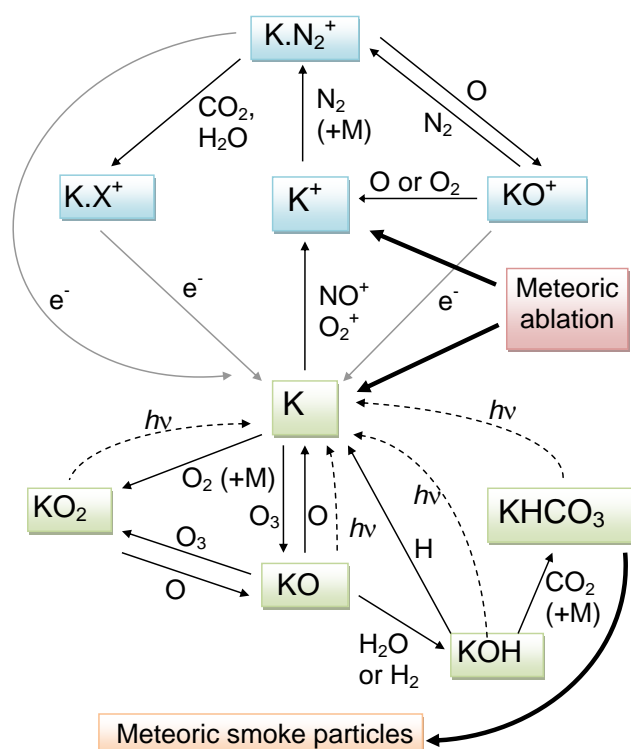


Figure 5-8: Schematic of the main K layer chemistry [reproduced from Plane *et al.*, (2014a)]. Pink boxes indicate the ultimate sources and sinks of the K atoms; meteoric ablation being the original source of the K atoms, and polymerisation of K compounds into meteoric smoke particles resulting in removal. The blue boxes indicate reservoir species on the topside of the neutral K layer, green boxes indicate metallic reservoir compounds on the bottom side of the layer. Solid lines indicate chemical reactions and broken lines indicate photochemical reactions.

The topside of the layer is dominated by ion chemistry with K^+ ions formed as a result of photo-ionisation and charge transfer with ambient ions (Reactions R5.1-R5.3).



The K^+ ions form clusters with an available ligand, before being neutralised and converted back to K via dissociative electron recombination (R5.4):



As the K^+ ion is a relatively large singly-charged ion, it forms only weakly bound clusters with low binding energies of $<20 \text{ kJ mol}^{-1}$. Reaction R5.4 only becomes significant during the colder temperatures of the summertime MLT, which results in a relatively higher ratio of $K:K^+$ and an associated K summertime maximum. In contrast, the relatively smaller Na^+ ion has a much larger binding energy (approximately 30 kJ mol^{-1}) [Daire *et al.*, 2002] and the analogous dissociative electron recombination reaction is inefficient during the summertime.

The underside of the K layer is governed by neutral chemistry, with K being cycled between various reservoir compounds. The predominant reactions relevant to this work are summarised in Reactions R5.5 to R5.11.

Neutral K can react with both O_3 [R5.5] and O_2 [R5.6] to form KO and KO_2 , respectively.



However, as reaction R5.6 is pressure-dependent, it only competes with reaction R5.5 at altitudes below 85 km.

KO is converted back to neutral K via:



Alternatively, both KO and KO_2 may be further oxidised by O_3 :





While both of these K species may be destroyed by atomic O (not shown in Figure 5-8), the most stable reservoir compounds are formed via reaction with H₂O to form hydroxide species:



and the subsequent addition of CO₂ to form the bicarbonate species:



All of the main K reservoir species can be converted back to neutral K via photolysis:



The main reservoir of both Na and K is the metal bicarbonate, NaHCO₃ and KHCO₃ respectively. However, a crucial difference in the available mechanisms for the conversion of this metal bicarbonate back to the neutral metal exists between Na and K. It is this which further contributes to the differential seasonal behaviours of the two metals.

For Na, two pathways exist for the conversion of the metal bicarbonate to the atomic metal (see Figure 5-9); photolysis via the analogous reaction to R5.12, and via reaction with H shown below,



The photolysis reaction is essentially temperature independent, but the reaction with H has a strong positive temperature dependence; R5.13 has an activation energy of approximately 10 kJ mol⁻¹ [Cox *et al.*, 2001]. During the colder temperatures of the summertime MLT, this reaction becomes very slow, resulting in a build-up of NaHCO₃ relative to atomic Na (hence a summertime minimum in the observed Na layer).

5.4.1 Comparison of OSIRIS versus WACCM K column densities

The new K chemistry scheme was added to WACCM (by Wuhu Feng, University of Leeds). The WACCM modelled K data has only previously been compared to K lidar data from Kühlungsborn at 54°N [Plane *et al.*, 2014a]. Via comparison with the WACCM K output, the OSIRIS K data provides an excellent opportunity to test the performance of this new chemistry scheme on a near-global scale for the first time.

A comparison of the OSIRIS and WACCM K data for 2004 is presented in Figure 5-10. Here it can be seen that the model is now able to simulate the semi-annual behaviour of K, although it cannot fully reproduce the variation seen in the OSIRIS K column densities. Interestingly, the model is able to reproduce the spring/autumn hemispheric differences. In the northern hemisphere, the spring K minimum is stronger than the autumn minimum in both the OSIRIS and WACCM plots and is thought to be related to the autumn MIF maxima. Hemispheric asymmetry is also seen in both the satellite and model datasets; similar results have also been seen in the long-term OSIRIS Na dataset reported in Hedin and Gumbel [2011] and is likely attributed to the hemispheric differences in the relative sizes of the Arctic and Antarctic polar vortices and the impact that these have on global circulation. The good general agreement of the WACCM modelled K layer with the OSIRIS data, at all latitudes, supports the K chemistry scheme outlined in Plane *et al.* [2014a] and documented earlier in Section 5.4.

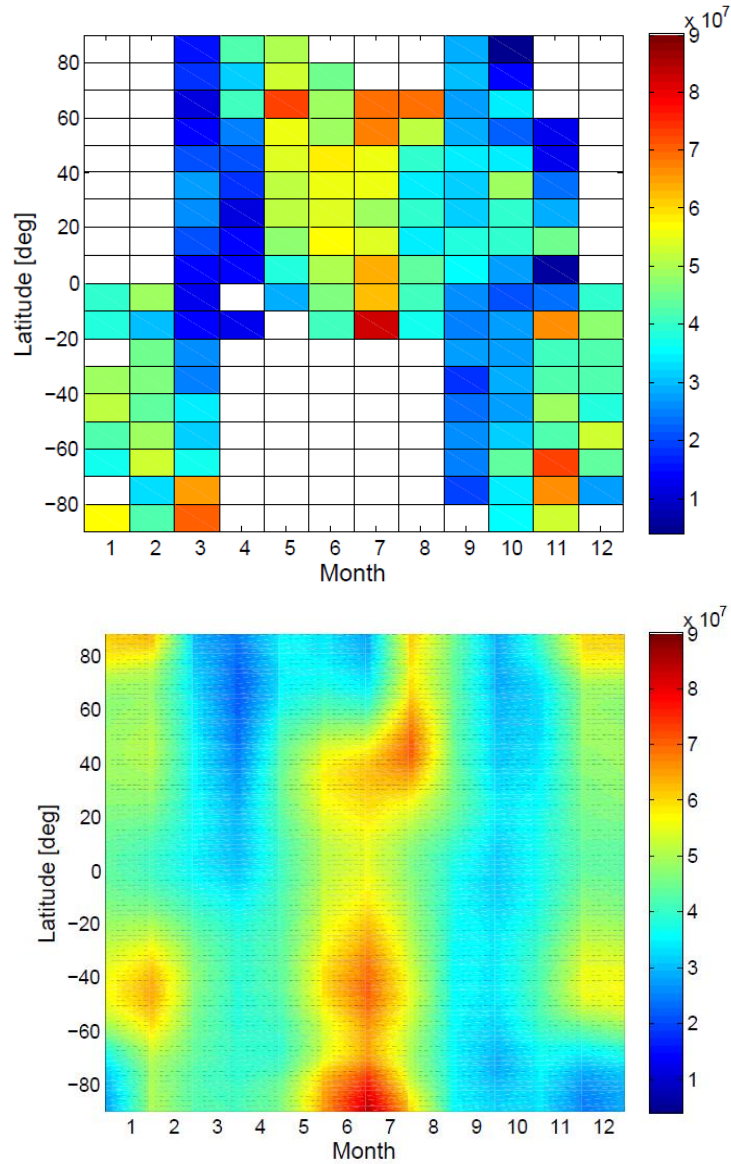


Figure 5-10: Comparison of OSIRIS (top panel) and WACCM (lower panel) K column densities, as a function of month and latitude for 2004. [Units: K atoms cm^{-2}].

5.5 The relationship between temperature and K

5.5.1 MLT temperature: how well does WACCM compare to SABER?

A key question is whether the latitudinal differences in the K layer are due to the temperature variations. In order to investigate this relationship, WACCM model data is used. However, it is first important to ascertain whether WACCM is capable of

producing a sensible temperature distribution relative to observed temperatures. Figure 5-11 shows the mean global temperatures at 90 km over a 6-year period (2004-2009) for both the WACCM-ERA (top panel) and SABER (lower panel) datasets. The temperature fields for 90 km were chosen as this is the approximate altitude of the peak K density. As can be seen, both the model and satellite show a summertime temperature minimum and wintertime maximum, in both hemispheres. This results from the increased gravity and planetary wave activity which originates in the summer troposphere, as outlined in Chapter 1.

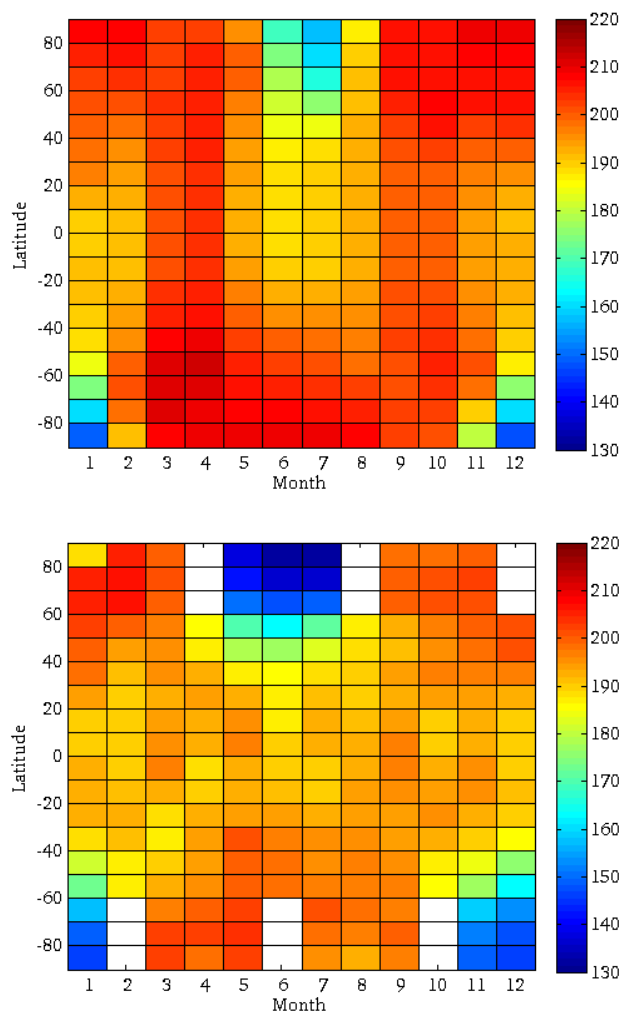


Figure 5-11: Mean temperature at 90 km for a 6-year period (2004-2009) derived from WACCM-ERA (top panel) and SABER (lower panel) data. [Units: K].

The temperature difference between the two datasets (WACCM-ERA minus SABER) is shown in Figure 5-12. WACCM-ERA currently over-estimates the 90 km temperature, relative to the SABER measurements, particularly during the summer months at high latitudes and the equinox months at most latitudes. This lower (2-3 km) and warmer summer mesopause has also been documented in a climatological WACCM (1960-2006) versus SABER (2002-2011) comparison for January and July zonal profiles [Smith *et al.*, 2012]. In addition, this mesopause issue is also highlighted in Feng *et al.* [2013] through comparisons with another version of WACCM (SD-WACCM) and the COSPAR International Reference Atmosphere (CIRA) [for further details of CIRA, see Fleming *et al.*, 1990]. It is thought that this model-observations discrepancy is likely as a result of a meridional circulation which is too strong in the model.

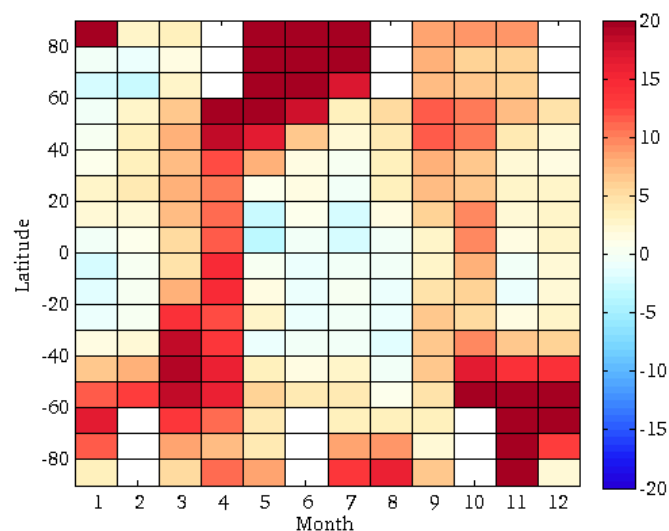


Figure 5-12: Temperature difference between WACCM-ERA and SABER (WACCM-ERA minus SABER) at 90 km. [Units: K].

To better understand the latitudinal temperature differences, vertical profiles for both WACCM-ERA and SABER are shown in Figure 5-13 and Figure 5-14. The SABER data shows a clear decrease of the height of the mesopause during the summer months, most pronounced at mid- and high-latitudes, with a pronounced decrease in temperatures below 95 km. During the winter months, much warmer temperatures occur between 75-

90 km at these latitudes. In comparison to the SABER profiles, the WACCM summer mesopause is 1-2 km lower at all latitudes. As a result the temperatures around 90 km are generally warmer (>20 K at high summer latitudes) than the corresponding SABER temperatures (as depicted in Figure 5-12).

Despite these summertime temperature differences, WACCM is generally doing a reasonable job at simulating the correct latitudinal temperature field. Thus, the WACCM-ERA output will be used to better understand the global K layer, but the importance of the simulated mesopause height must be considered when analysing model output with respect to its influence on the summertime chemistry.

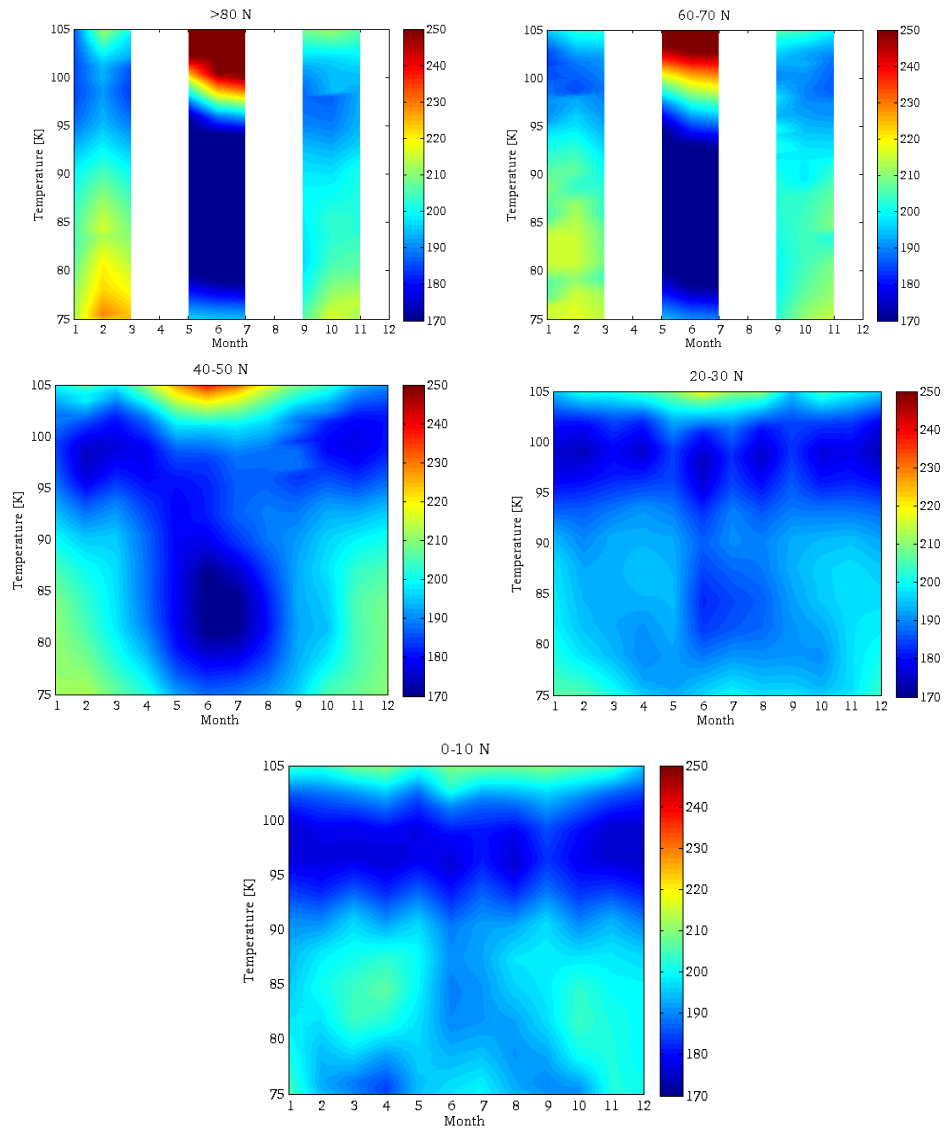


Figure 5-13: SABER observed mean vertical temperature profiles (2004-2009) for selected latitude bands. White gaps indicate no data is available due to a lack of satellite coverage as a result of the alternating yaw cycles outlined in Chapter 2. [Units: K].

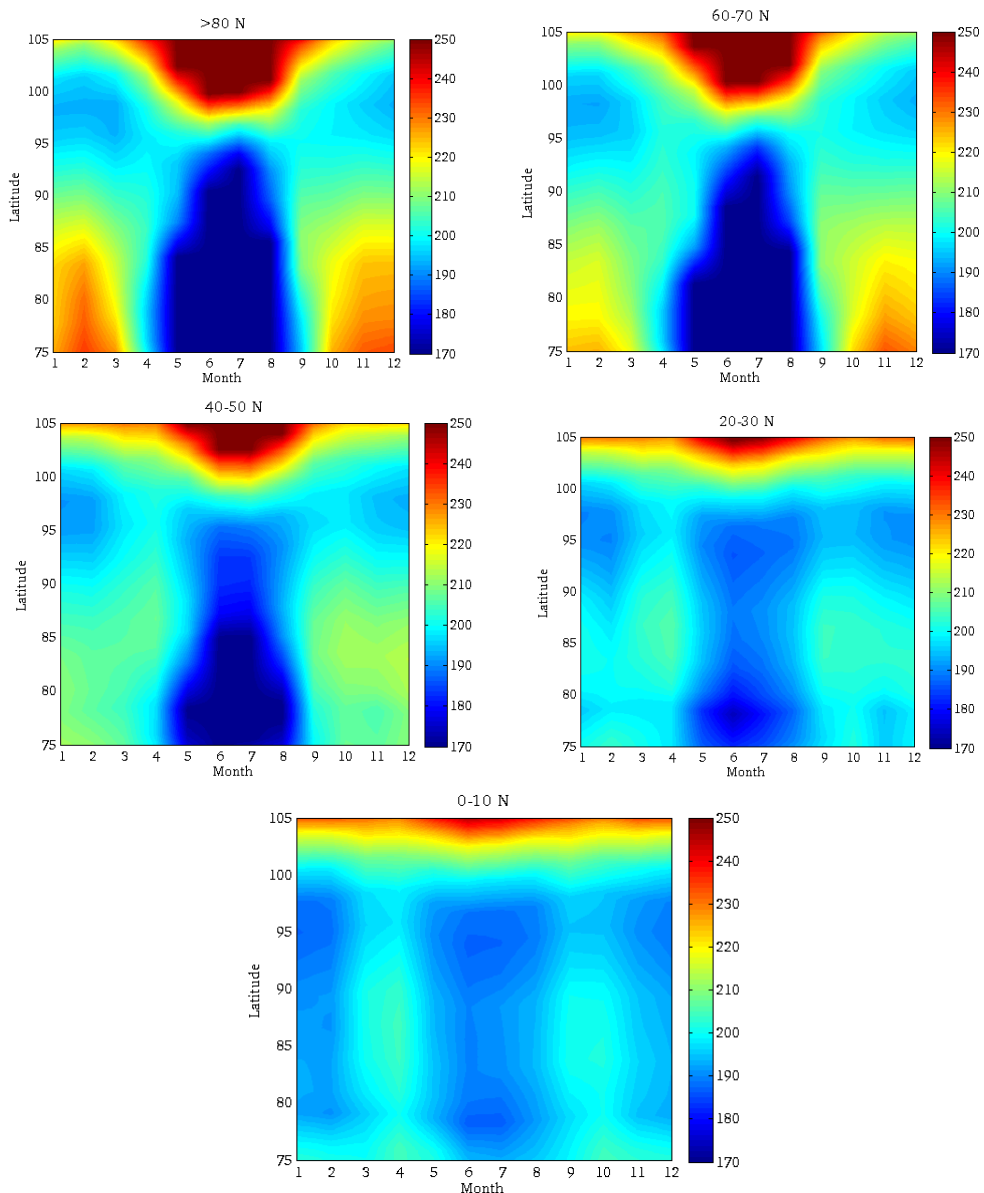


Figure 5-14: WACCM-ERA simulated mean vertical temperature profiles (2004-2009) for selected latitude bands. [Units: K].

5.5.2 Relationship between temperature & K column density versus latitude

The summertime K column density maxima (shown in Figure 5-10) correspond with the low summer temperatures shown in the previous figures. This supports the K chemistry outlined in Section 5.4, with respect to the efficiency of the K^+ ion conversion back to atomic K during the cold summertime MLT.

The summertime dynamical upwelling and corresponding wintertime downwelling lead to the greatest seasonal temperature variation occurring predominantly at high latitudes, and to a lesser extent at the mid-latitudes. It is at these latitudes that the K layer column density also exhibits the largest seasonal variation. Firstly, the wintertime downwelling compresses the metal layer; this effect is strongest close to the wintertime pole. Secondly, colder temperatures promote the increased conversion of the weakly bonded K^+ clusters back to atomic K. Both of these factors result in a more pronounced semi-annual K column density amplitude at these mid- and high latitudes compared to the lower latitudes, and provide support to new K chemistry scheme.

5.5.3 The differential response of modelled Na and K to temperature

The differences between the WACCM modelled Na and K seasonal variations are examined further in Figure 5-15 with the corresponding WACCM temperature profiles shown in Figure 5-16. During the solstice months (June and December), the Na density displays a maximum in the winter hemisphere only, with the largest densities at mid- and high latitudes which correspond with the occurrence of the warmest MLT temperatures. Within the summer hemisphere, where the MLT is at its coldest, the Na layer is depleted (more Na remains as $NaHCO_3$ due to the temperature dependence of Reaction R5.13). In contrast the K layer exhibits maxima in both the summer and winter hemispheres, even during the very cold summer polar region. Both the Na and K layer experience depletion on the underside of the layers at high polar latitudes during the summer hemisphere and this is related to the uptake of the metal atoms on the surface of polar mesospheric cloud droplets.

In the spring/autumn months (March and October), the behaviour of the Na and K layers is reasonably similar, with both metals exhibiting greater abundances within the southern hemisphere, regardless of month. This hemispheric asymmetry may be related to the differences between the relative size and strengths of the polar vortices; PMCs are less pronounced over Antarctica because the Arctic vortex is weaker so there is less upwelling/cooling in the SH.

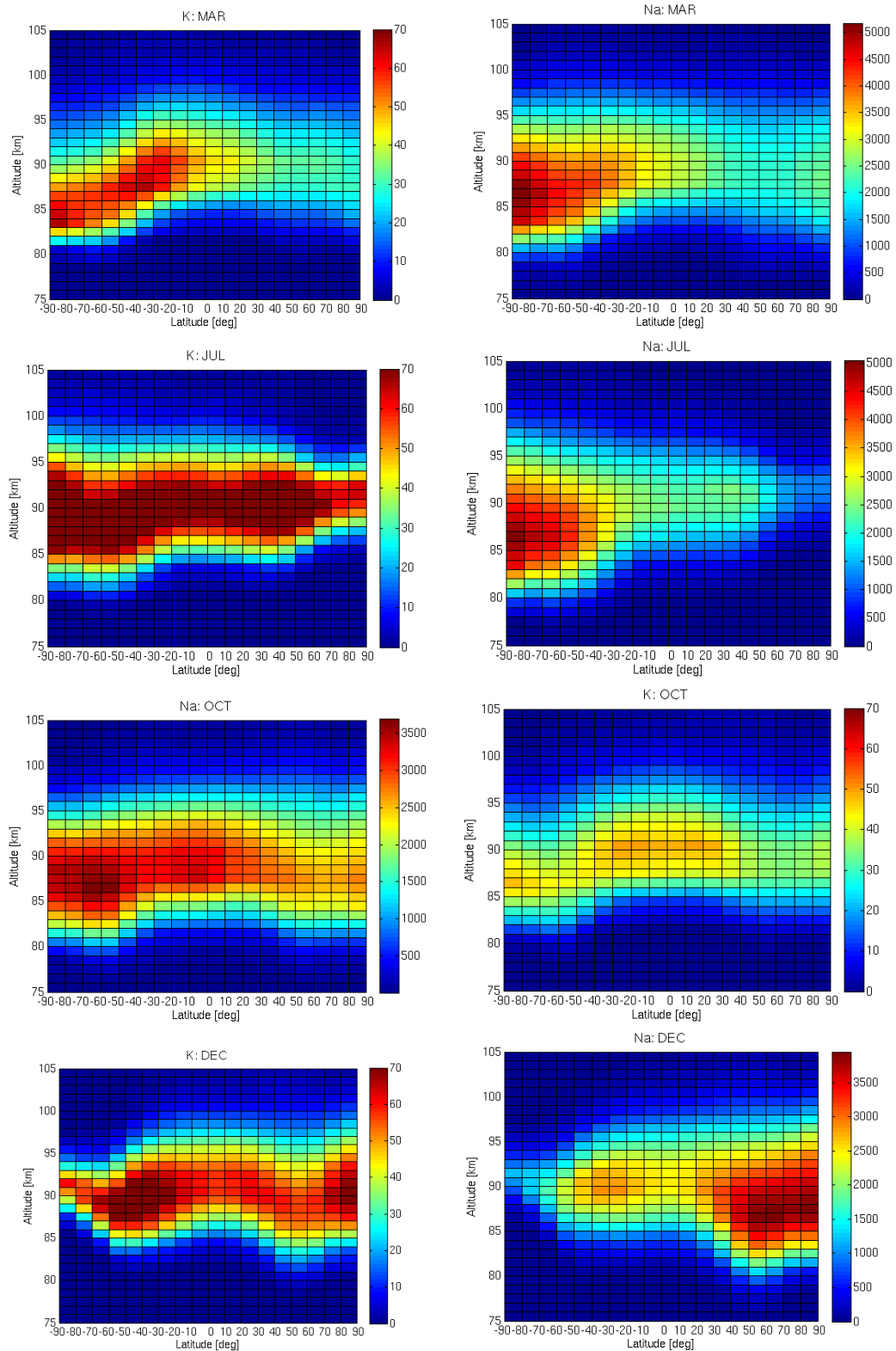


Figure 5-15: Comparison of the K versus Na zonal mean monthly mean profiles, using WACCM-ERA data (2004-2009) as a function of altitude and latitude. [Units: metal atoms cm^{-3}].

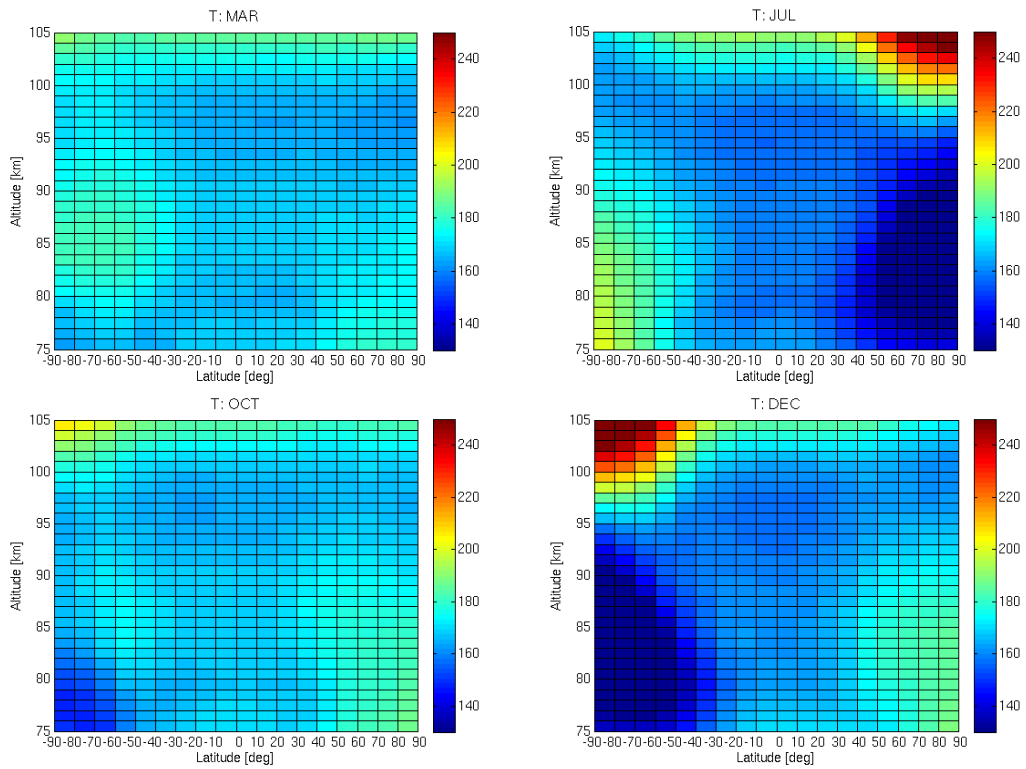


Figure 5-16: WACCM-ERA zonal mean monthly mean temperature profiles (2004-2009) as a function of altitude and latitude. [Units: K].

A correlation analysis between both WACCM metal datasets and temperature has been performed across the 6-year (2004-2009) period, as a function of latitude and altitude, and is shown in Figure 5-17. Na shows a clear positive correlation with temperature at all latitudes, particularly under 95 km. As the temperature increases, more NaHCO_3 is converted back to the neutral Na layer. At colder temperatures, this reaction becomes too slow (because of the large activation energy for the reaction $\text{NaHCO}_3 + \text{H} \rightarrow \text{Na} + \text{H}_2\text{CO}_3$) and thus a higher proportion of Na resides in this reservoir species. This positive temperature dependence has been well-documented in other studies, such as Plane *et al.* [1999] and Fan *et al.* [2007a].

K demonstrates a rather more complicated relationship with temperature. For the most part, there is a negative correlation between K density and temperature above 85 km. There is no temperature dependence of the neutral K chemistry. However, as

temperatures decrease, more of the weakly clustered K^+ ions convert back to the neutral layer.

At high latitudes, there is a positive correlation between temperature and K density below 90 km, and a weak mixed correlation (both positive and negative) between 90-95 km. This is likely as a result of indirect impacts on the K layer, rather than a direct effect of temperature. Dynamical wintertime downwelling results in a compression of the layer. This, along with the autumn/winter peak in the MIF result in a K maximum and an apparent positive correlation between K density and temperature at high latitudes where the wintertime downwelling is strongest. Although K density is anti-correlated with temperature during the summertime, an additional confounding factor may be the removal of K by uptake on PMCs at high latitudes; more PMC activity during the colder summertime may result in less K. Thus, this acts as another indirect temperature-related effect on the K layer. All of these indirect effects average out to produce the variable, but typically weak, positive correlation between K and temperature at the mid- to high latitudes in both hemispheres.

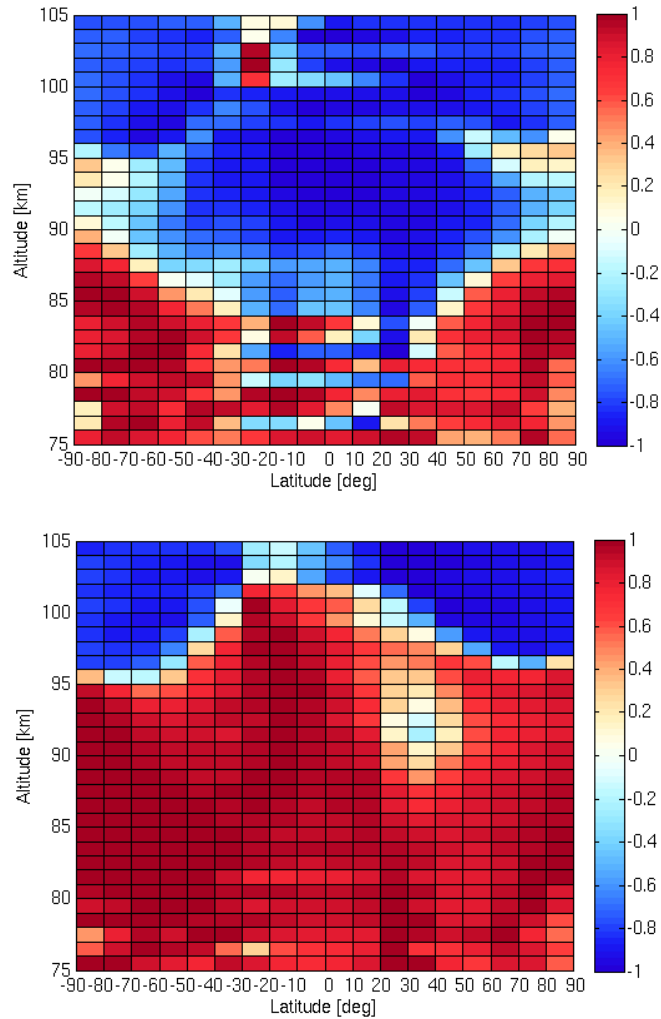


Figure 5-17: Correlation analysis between WACCM K (top panel) and Na (lower panel) number densities, and temperature, for all months between 2004-2009, as a function of latitude and altitude. The independent variable is time.

5.6 The diurnal behaviour of K

The OSIRIS instrument has two equator crossing times: 0600 LT on the descending node and 1800 LT on the ascending node. This allows diurnal effects in the K layer to be detected in the measurements. Figure 5-18 shows the difference between the morning and evening OSIRIS K densities as a function of latitude and altitude for a 2004-2009 mean profile, for March, July, October and December. Above 85 km, the morning densities generally tend to be greater than the evening density profiles, for all four monthly profiles. This is in agreement with the findings of Lautenbach *et al.* [2014] who observed the tidal patterns in K densities at Kühlingsborn. Figure 5-19 shows the

equivalent plots using WACCM output for four selected available latitudes (78°N, 54°N, 18°N and 78°S); in all cases, K number densities at 0600 LT exceed those of 1800 LT at altitudes >85 km. Given that the model can reproduce what is seen in the satellite and lidar observations, it serves as an excellent tool to elucidate the processes which result in this diurnal difference.

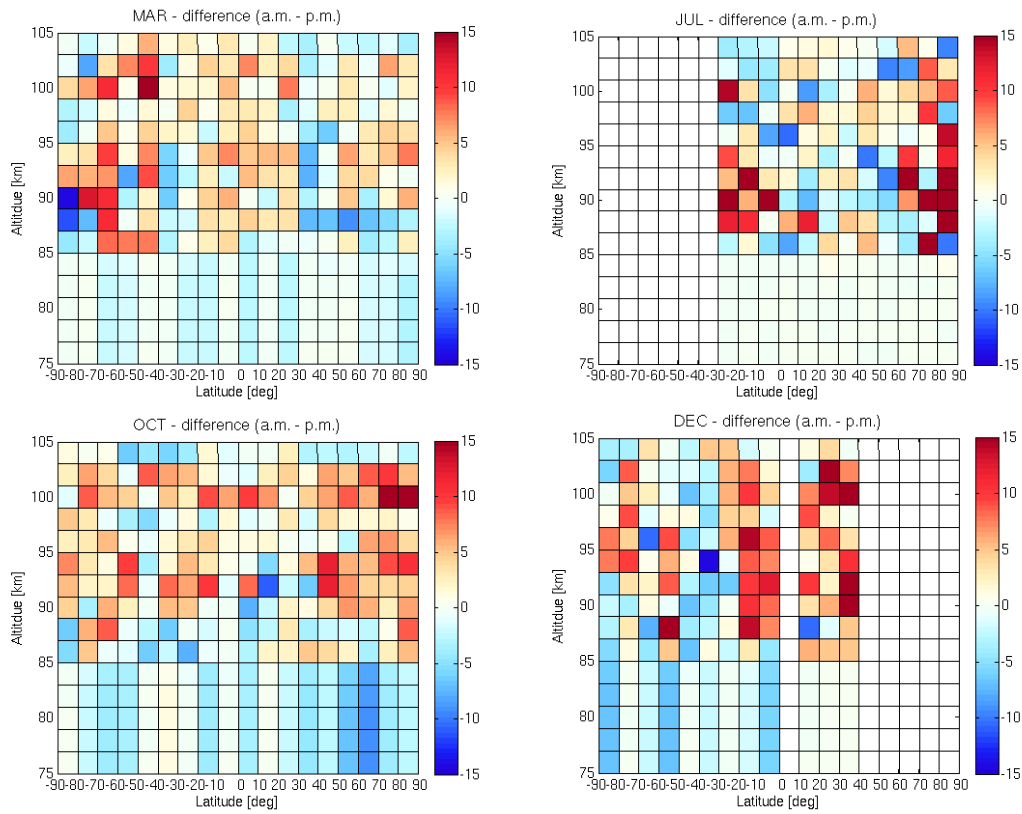


Figure 5-18: OSIRIS diurnal difference (a.m. minus p.m.) in the K number density as a function of altitude and latitude, for March, July, October and December. Multi-year mean over 2004-2009 period. [Units: $K \text{ atoms cm}^{-3}$].

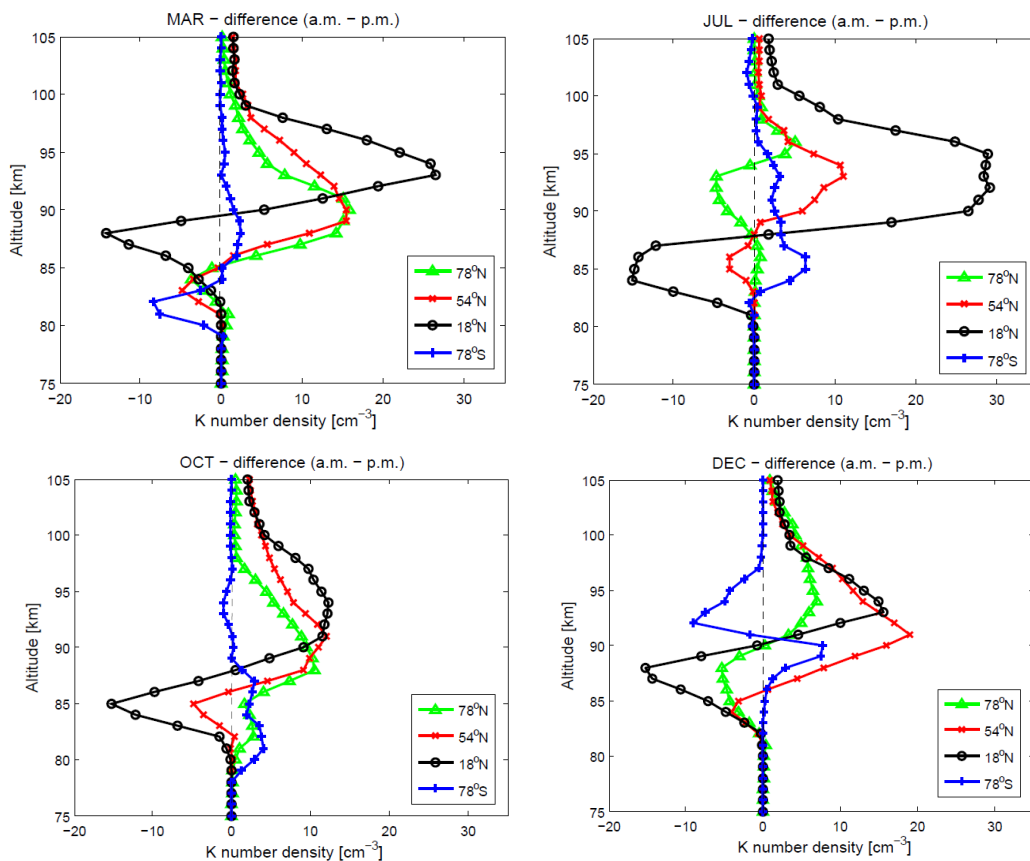


Figure 5-19: WACCM diurnal difference (a.m. minus p.m.) in the K number density as a function of altitude, for a selection of available latitudes (78°N , 54°N , 18°N and 78°S), for March, July, October and December 2004. [Units: K atoms cm^{-3}].

Figure 5-20 shows the diurnal cycles of K and the main species relevant to its chemistry. The photochemistry has a dominant effect on the evolution of the K layer throughout the day. The K^+ layer is dominant during the daytime as it is produced through the ionisation of the atomic K layer (hence there is a corresponding K minimum during the majority of the daylight hours). The atomic oxygen layer is at a maximum during daylight hours formed predominantly from the photolysis of O_3 . Both atomic O and H are the dominant reactive species relevant to the K chemistry, and both are at a maximum at 1800 local time rather than 0600 LT. The build-up of atomic H during the daytime is another key difference between Na and K; whilst K experiences a morning maximum, Na shows a clear evening maximum [e.g. see Simonich *et al.*, 1979; Clemesha *et al.*, 1982; Fan *et al.*, 2007; Hedin and Gumbel, 2011]. Again, this occurs as a result of the activation

energy of the major metal bicarbonate reservoir species and its reaction with atomic H (R5.13). This reaction is important for Na and results in an increase in the number of neutral Na atoms. Thus, as the evening atomic H layer is larger than the morning, the neutral Na layer will be at a maximum also in the evening.

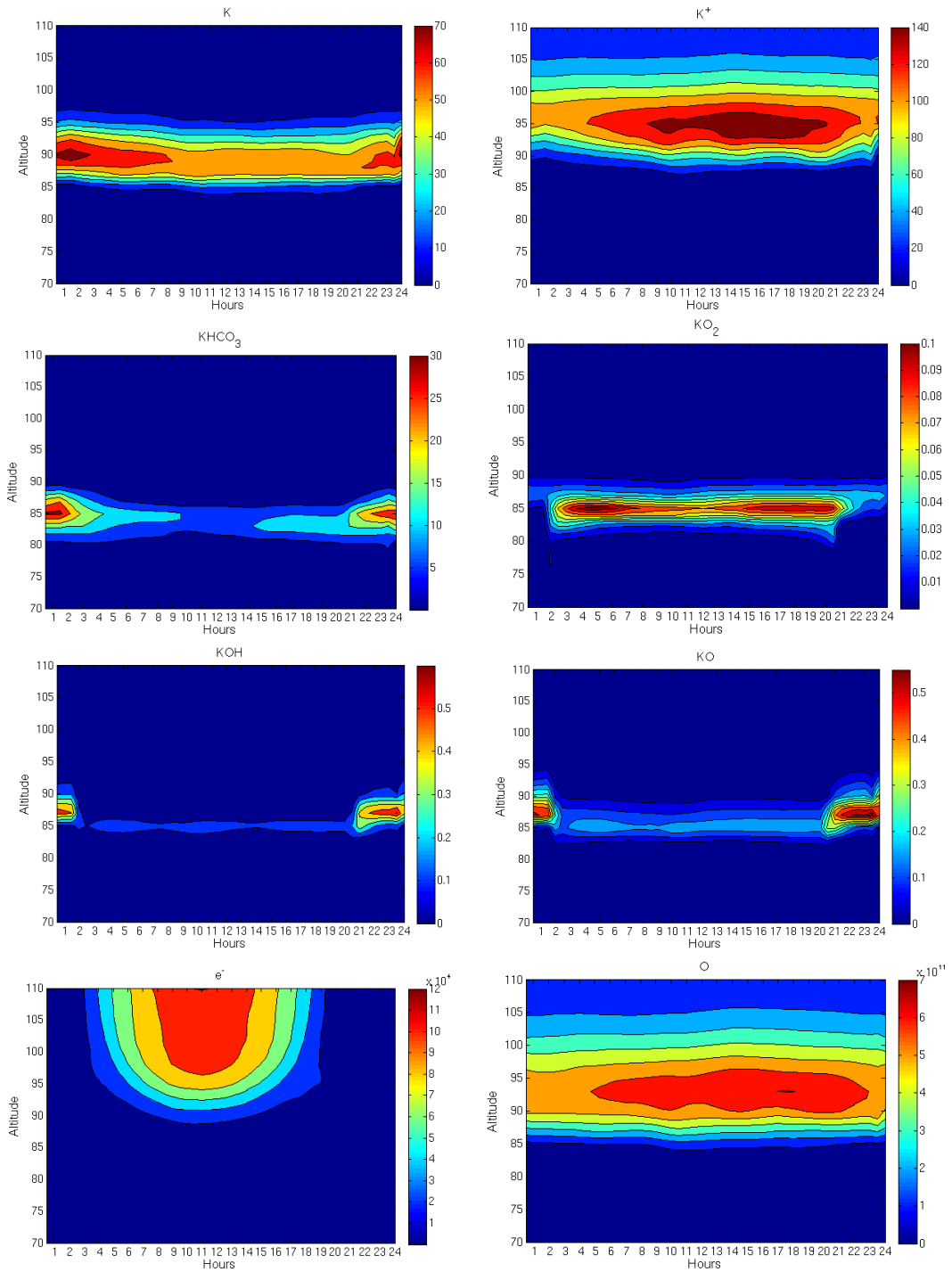


Figure 5-20: Diurnal mean profiles of various WACCM chemical species related to K chemistry as a function of altitude and local time. All profiles are for a low latitude (18°N) location and for 2004.

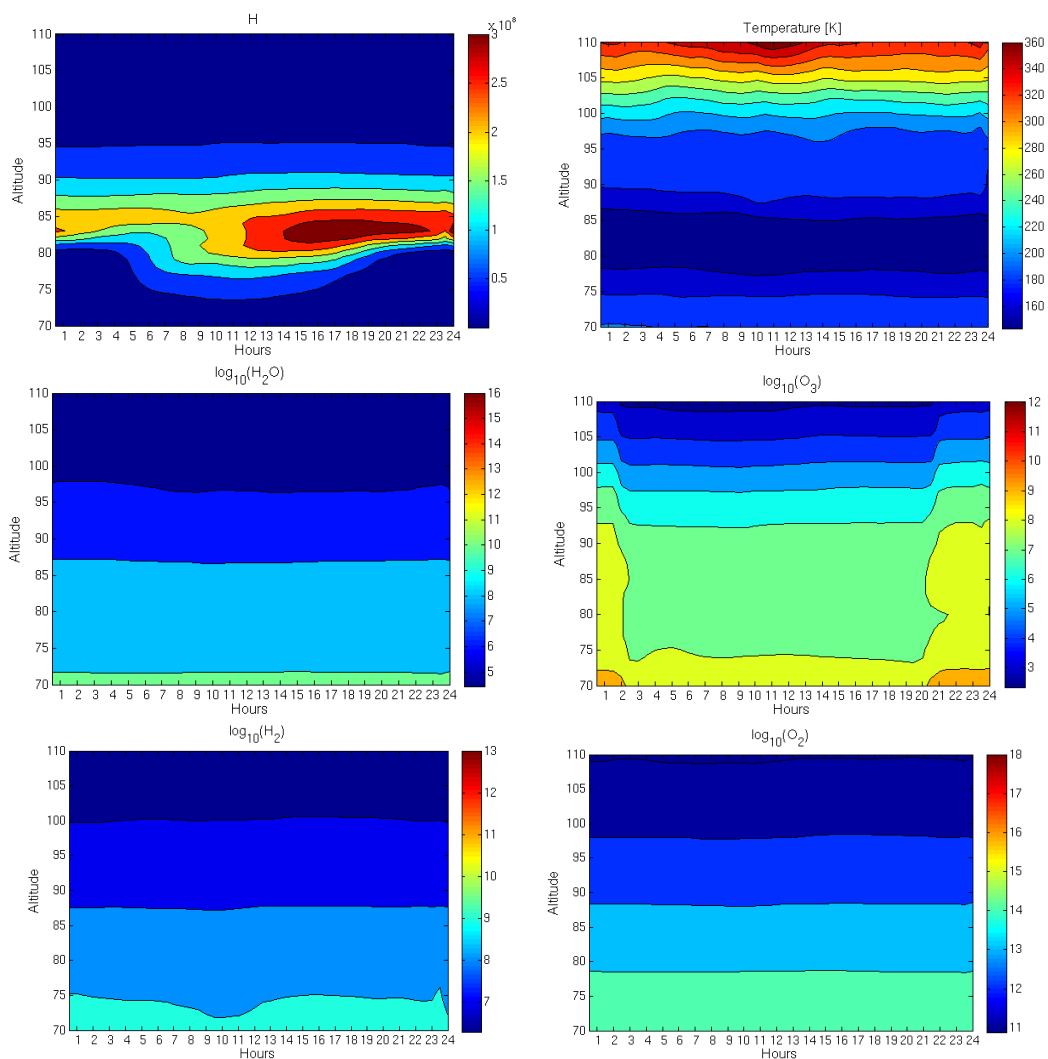


Figure 5-20: *continued.*

In order to explain why there is an altitudinal difference in the morning and evening profiles as shown in Figure 5-18 and Figure 5-19, it is important to look at the diurnal variation of the main individual species concentration profiles relevant to K chemistry. Figure 5-21 shows the major relevant K species (K, K^+ , and $KHCO_3$) on a logarithmic scale for clearer comparison, and depicts the morning K density profile exceeding the evening profile at altitudes above 87 km. As shown in the WACCM output, the predominant mechanism for this is photo-ionisation (directly and indirectly through charge transfer with NO^+ and O_2^+) of the neutral K layer during the day, which results in a higher proportion of K^+ in the evening versus the morning profile. At altitudes below 86 km, the evening K density profile generally exceeds that of the morning profile, as

also seen in the OSIRIS data. Below this altitude, the reasons for the evening K maximum are more complex, and appear to be as a result of more subtle changes in the diurnal changes of both K^+ and the main K reservoir, $KHCO_3$.

On diurnal timescales, photochemistry appears to be a more dominant effect on the diurnal cycle of the K layer, rather than the temperature and dynamical effects which are more important on seasonal timescales.

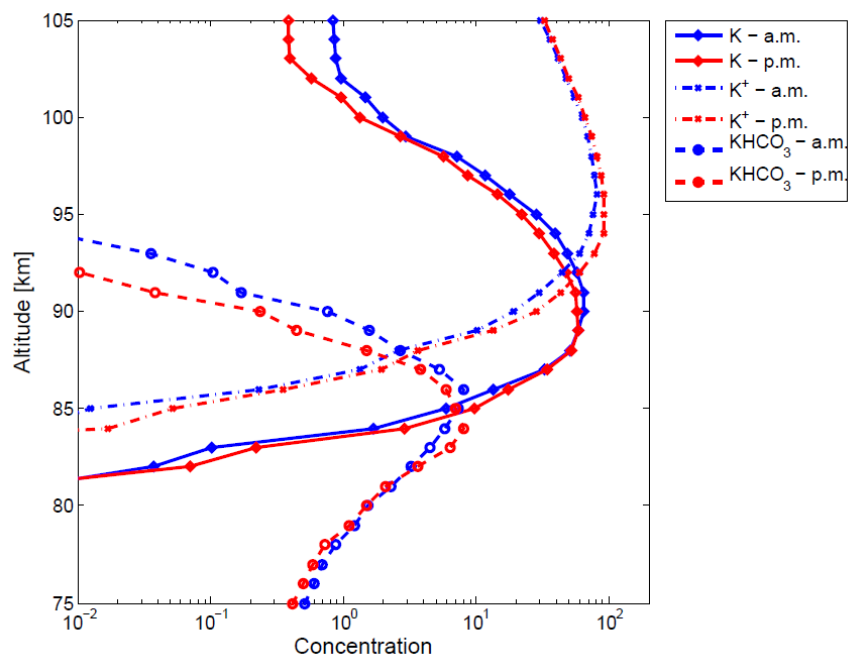


Figure 5-21: Comparison of WACCM-simulated morning (0600 LT) and evening (1800 LT) profiles of the main chemistry species relevant to the neutral K layer chemistry. The concentration is on a log scale for a clear comparison.

5.7 Polar depletion of the K layer

Within the upper mesosphere, water vapour is a minor constituent, with a typical volume mixing ratio of only a few parts per million. Despite this, the very low temperatures (<150 K) within the summer polar mesosphere support the growth of polar mesospheric clouds (PMCs) [Lübken, 1999] over a wide latitude band (>55°) at altitudes between 82-88 km [e.g. von Zahn, 2003; Lübken and Höffner, 2004; DeLand *et al.*, 2006], and with a mean PMC altitude of ~83 km [von Cossart *et al.*, 1996; Alpers *et al.*, 2001; Wickwar

et al., 2002; Fiedler *et al.*, 2003; Höffner *et al.*, 2003; Thayer *et al.*, 2003; 2006]. PMCs typically appear from May to late August/early September, with a concentration maximum approximately 20 days after the summer solstice [Olivero and Thomas, 1986; DeLand *et al.*, 2006].

The PMC ice surfaces efficiently remove metal atoms at very low temperatures [Plane *et al.* 2004; Murray and Plane, 2005] and this removal leads to summertime minima as documented in the Na and Fe metal layers [e.g. see Gardner *et al.*, 1988; Gardner *et al.*, 2005; She *et al.*, 2006]. Although the K^+ chemistry (described in Section 5.4) results in a summertime maximum unique to this metal, lidar observations at Spitsbergen ($78^\circ N$) have demonstrated that the K layer exhibits a local minimum during PMC season [Lübken and Höffner, 2004; Raizada *et al.*, 2007].

Satellite observations of the K layer provide a means for detection the occurrence of PMCs and their impact on the K layers, globally. This subsection aims to demonstrate the impact of PMCs on the global K layer at a variety of locations using the OSIRIS observations. The seasonal variation of the K layer for the four different latitude bands is shown in Figure 5-22. At $78^\circ N$, the summertime K layer exhibits depletion on the underside between May and August, that is not apparent in the layers at $28^\circ N$ and $18^\circ N$. The maximum K depletion occurs within June/July when polar mesospheric temperatures are coldest and the atmospheric upwelling is strongest, transporting water vapour up to these altitudes. Along with the increased rate of ionisation during the summer (which results in a greater number of neutral K being converted to K^+ via charge transfer with NO^+ and O_2^+), depletion by PMCs can also affect the topside of the K layer. The removal of K atoms below 88-90 km as a result of PMC depletion drives the downward transport of K atoms from higher altitudes as a result of vertical eddy diffusion [Raizada *et al.*, 2007]. This effect can be seen in the $78^\circ N$ profile, with a reduction of K atoms on both the top- and bottom-sides of the layer.

The impact of PMCs on the K layer is investigated in further detail in Figure 5-23. Both the $78^\circ N$ profile and to a lesser extent, the $54^\circ N$ profile exhibits local minima in the

column density during May-August, which is consistent with removal of metal atoms by PMCs on the underside.

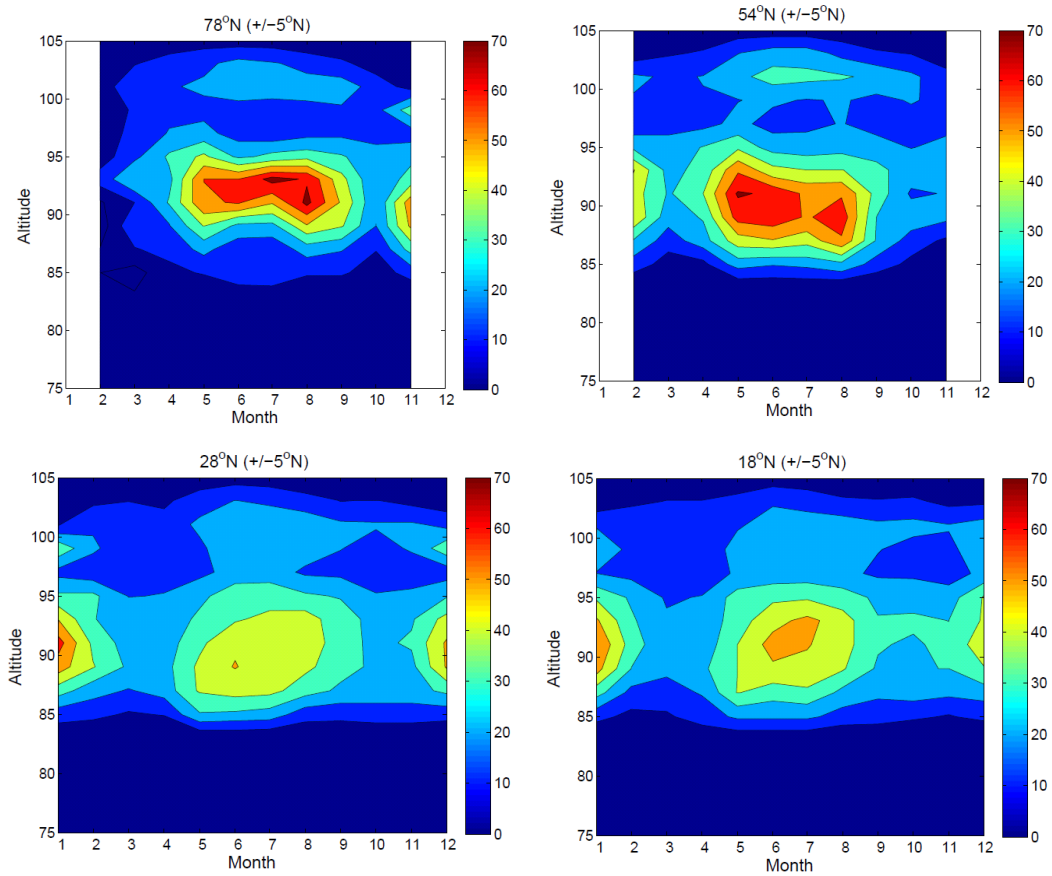


Figure 5-22: The seasonal mean OSIRIS K layer at latitudes corresponding with the Spitsbergen (78°N), Kuhlungsborn (54°N), Tenerife (28°N) and Arcibo (18°N) lidar stations, all $\pm 5^\circ$

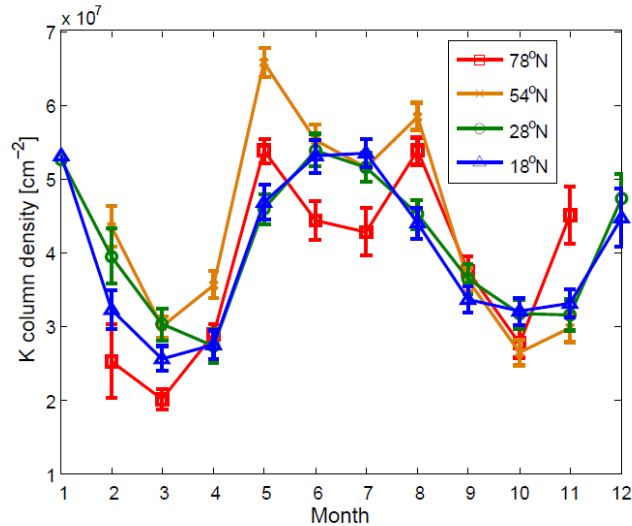


Figure 5-23: Comparison of zonal mean OSIRIS K layer column density centred about Spitsbergen (78°N), Kuhlungsborn (54°N), Tenerife (28°N) and Arecibo (18°N), all $\pm 5^\circ$. Vertical bars indicate the error of the mean (2σ). [Units: $K \text{ cm}^{-2}$].

5.8 Sporadic layer activity of K

5.8.1 Overview

Sporadic metal layers were first reported by Clemesha *et al.* [1978] who detected thin sodium layers which appeared overhead the lidar at São José dos Campos (23°S, 46°W). These layers exhibited peak densities 2.5 to 3 times larger than the typical Na layer and after appearing suddenly, the events lasted from a few minutes to several hours.

The occurrence of sporadic metal layers have previously been attributed to various mechanisms, including a possible link to meteor showers [Clemesha *et al.*, 1978], the sputtering of metal atoms from cosmic dust particles [von Zahn *et al.*, 1987; Beatty *et al.*, 1989], the redistribution of the typical metal layer by gravity waves [Kirkwood and Collis, 1989; Delgado *et al.*, 2012], the dissociation of the metal reservoir species (in this case, NaHCO_3) [von Zahn and Murad, 1990], temperature fluctuations which produce an enhancement from some unknown metal source [Zhou *et al.*, 1993] and finally the neutralisation of metal ions via interaction with a sporadic E layer [Cox and

Plane, 1998; von Zahn and Hansen, 1988; Hansen and von Zahn, 1990; Kane and Gardner, 1993]. Due to the correlation between the occurrence of sporadic *E* layers with sporadic metal events, the latter theory is now widely accepted as being the major mechanism (although other mechanisms may contribute) involved in the formation of sporadic metal layers [von Zahn and Hansen, 1988; Batista *et al.*, 1989; Mathews *et al.*, 1993; Collins *et al.*, 2002; Fan *et al.*, 2007]. This theory has also been supported by a combination of laboratory [Cox and Plane, 1997] and modelling studies [Cox and Plane, 1998; Heinselman, 2000; Collins *et al.*, 2002].

Na remains the most observed sporadic metal layer with lidar observations made at northern hemisphere high and low latitudes [Kwon *et al.*, 1988; Hansen and von Zahn, 1990; Kane *et al.*, 1993] and at southern hemisphere low latitudes [Batista *et al.*, 1989]. The middle latitude occurrence of sporadic Na layers (hereafter referred to as Na_s) in both hemispheres appears to be highly geographically variable. Observations over the Urbana lidar station (40°N) [Gardner *et al.*, 1986] and Europe [Gibson and Sandford, 1971; Megie and Blamont, 1977; Gardner *et al.*, 1993] show low Na_s occurrence, whereas observations from Japan [Nagasawa and Abo, 1995] show a locally high Na_s, which is thought to be related to its low geomagnetic latitude. These differences may be related to the magnetic latitude as reported in Gong *et al.* [2002]. The first global study of Na_s was performed by Fan *et al.* [2007] using OSIRIS retrieved Na data for the period 2003-2004, who found a global Na_s occurrence ~5%. Additionally, they found that Na_s were more prevalent in the Southern hemisphere, with a particularly active Na_s region extending from South America (at latitudes >40°S) to the Antarctic peninsula. This is likely related to the gravity wave momentum flux which occurs between Rothera and the lower trip of Argentina [e.g. Ern *et al.*, 2004].

5.8.2 Sporadic K Layers

Although a number of studies [e.g. Eska *et al.*, 1998; Fricke-Begemann *et al.*, 2002; Friedman *et al.*, 2002; Delgado *et al.*, 2012] have observed sporadic K layers (hereafter referred to as K_s), occurrence statistics have only been reported in Ruben Delgado's PhD

thesis [2011], which examined the Fe and K sporadic layers above the Arecibo lidar station. He found that the mean annual occurrence probability of a K_s was 18.5% as viewed by the Arecibo lidar (with K_s observed for 223 hours out of the total 1312 hour observation period), and also found that K_s exhibited a semi-annual behaviour with winter and summer time occurrence probability maxima (reproduced in Figure 5-24). This work is supported by earlier observations from Friedman *et al.* [2002] showing that the K_s occurred with the highest frequency from April onwards.

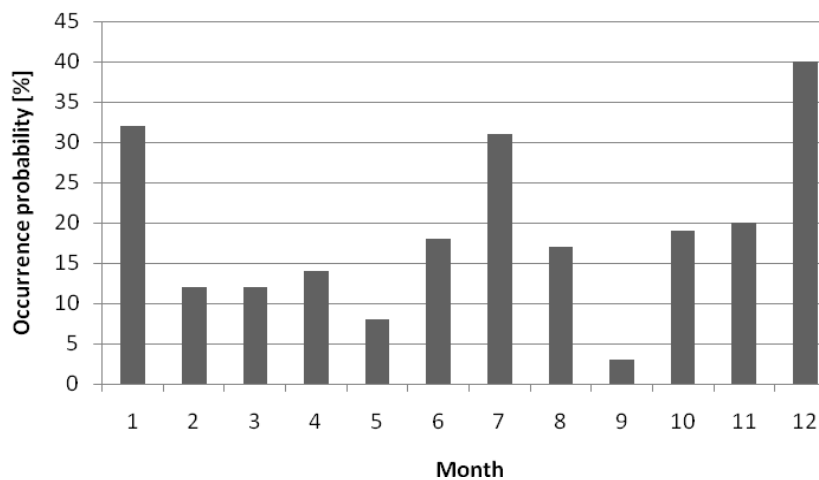


Figure 5-24: Frequency occurrences of sporadic K layers at Arecibo for a total of 1312 hours of measurements across 147 different nights between Feb 2002 and Dec 2005. Adapted from Delgado [2011].

To assess the global K_s occurrence probabilities using the OSIRIS near-global data, it is important to first choose appropriate sporadic layer detection criteria. Detection criteria used differs between different studies which make cross-comparison of datasets difficult. The detection criteria used here follows that defined by Fan *et al.* [2007], which themselves are derived from Clemesha [1995]. A K_s layer is identified if it fulfils the following criteria;

- the density of the possible sporadic layer exceeds three times the density of a standard mean K density layer at the same given altitude,

- and the peak density of the possible sporadic layer is equal to or greater than half of the peak density of the standard mean K layer (for the same latitude band), and,
- the FWHM of the possible sporadic layer is smaller than 4 km.

This final criterion was chosen to be compatible with the vertical resolution of the retrieved data, and ensures that only possible sporadic layers with the required narrow FWHM are identified. Example sporadic layers from OSIRIS profiles which fit these criteria are presented in Figure 5-25.

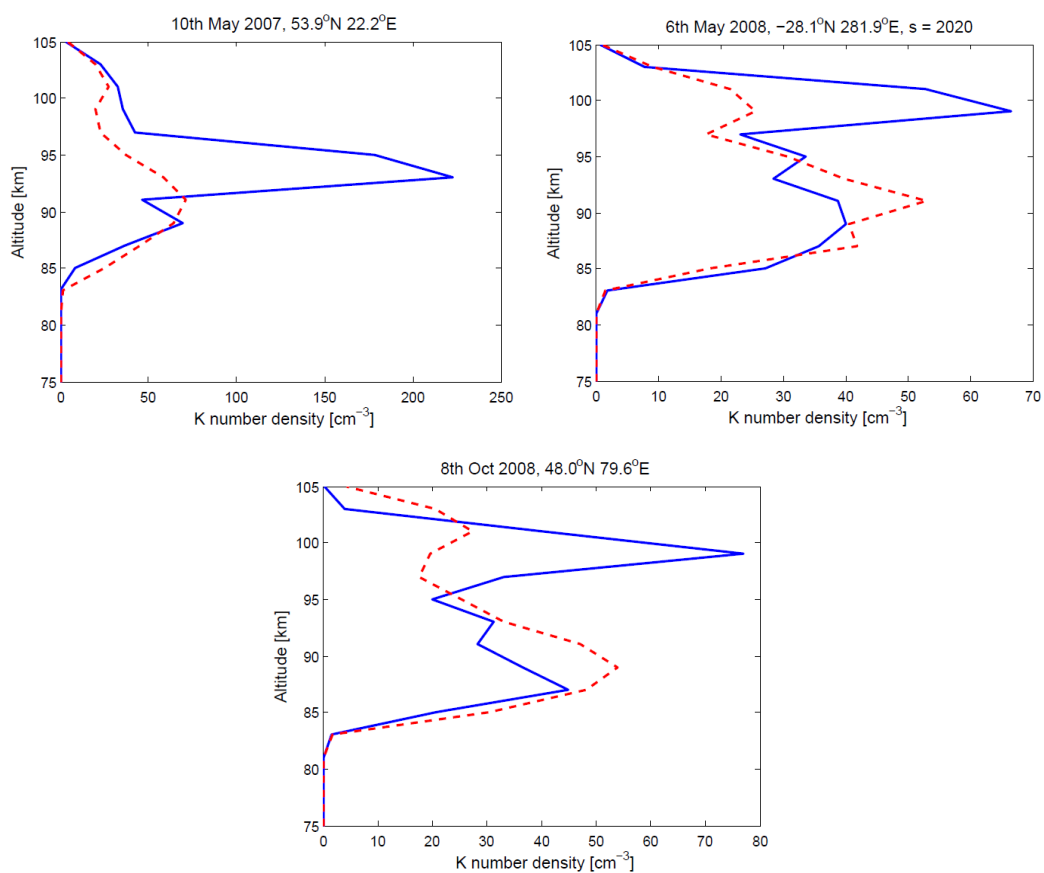


Figure 5-25: Example sporadic K layers as detected by OSIRIS (blue, solid line). The standard mean K layer is derived from the associated mean monthly zonal mean ($\pm 5^\circ$ either side of the possible sporadic K layer) profile (red, broken). [Units: K atoms cm^{-3}].

Delgado [2011] reported K_s frequency occurrences of roughly between 10-15% during spring/autumn (with the exception of the very low 2.5% occurrence during September),

and typical occurrences of 20-40% during summer/winter (see Figure 5-26). The OSIRIS results show a similar frequency occurrence at the 10° zonal band centred around Arecibo, with a summer maximum K_s occurrence in July and equinoctial minima. However, whilst the Delgado results point to the highest annual frequency occurrences during Dec/Jan (>30%), there is no such pronounced maximum evident in the OSIRIS data. A possible reason for this is the different local sampling observation periods of the two datasets; the OSIRIS data is a multi-year K_s occurrence (for 2004-2011), whilst the Delgado period only covers a total of 1312 hours of measurements on 147 different nights between February 2002 and December 2005. Additionally, the local times are also different; the lidar measurements are performed during night-time only, versus the daylight measurements made by OSIRIS. This may mean that the Arecibo lidar detected a small number of K_s events which the Odin spacecraft missed. The OSIRIS annual mean occurrence of ~13% is also lower than the 18.5% occurrence detected by Delgado [2011], which may also be as a result of the different spatio-temporal sampling of the satellite and lidar datasets, making specific cross-comparison difficult.

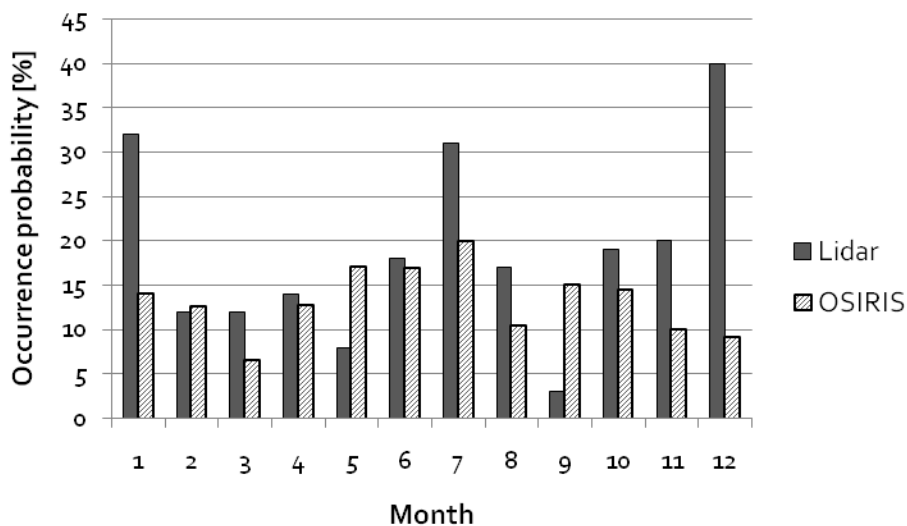


Figure 5-26: Comparison of sporadic K layer occurrence probability observed at Arecibo [Delgado, 2011] and by OSIRIS.

Figure 5-27 presents a global map of the probability of K_s occurrence as a function of month and latitude (in 10° bins). The data in each grid box represents the percentage occurrence of possible sporadic layers between 2004-2011, as a function of the total number of OSIRIS profiles used. Similar to those observations reported in Friedman *et al.* [2002] and Delgado [2011], the highest K_s occurrence frequencies occur in summer and winter, with spring/summer minima. There appear to be very high K_s frequency occurrences ($>50\%$) at northern hemisphere mid-latitudes ($40-70^\circ\text{N}$) during February. Additionally, very high occurrences ($>60\%$) are present in January between $0-10^\circ\text{N}$, and December between $40-50^\circ\text{N}$. As the data in the grid boxes represents monthly mean K_s frequency occurrences binned into 10° zonal bands, it is unclear whether there are any geographic effects as a function of longitude.

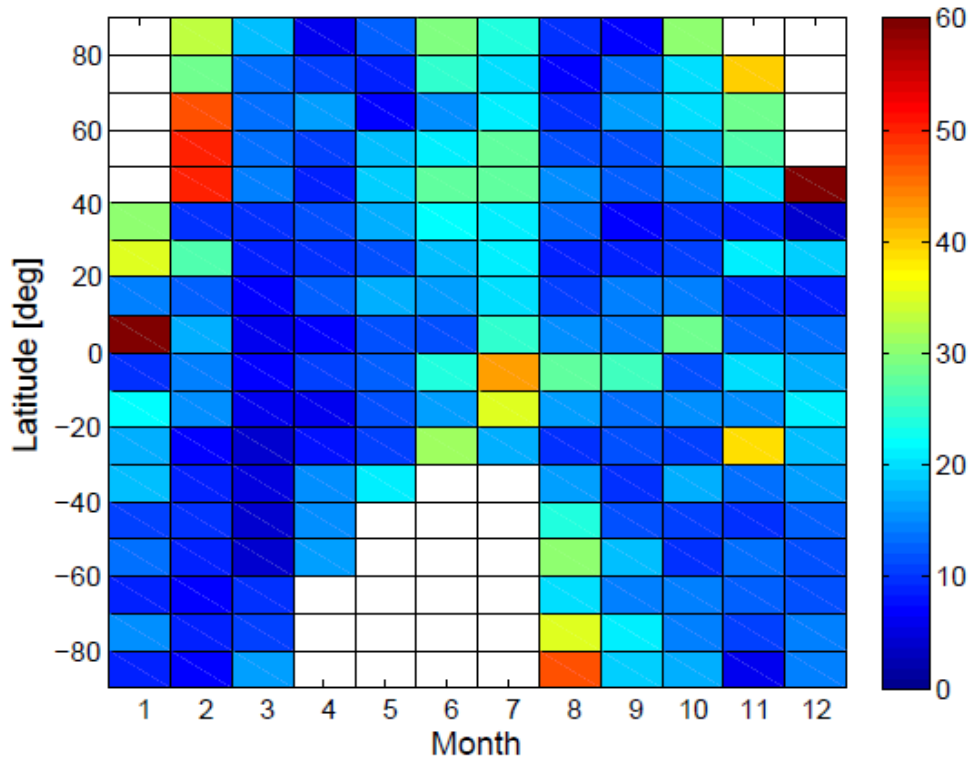


Figure 5-27: Percentage occurrence of OSIRIS-detected sporadic K layers as a function of month and latitude (10° bins). The data comprises of the mean percentage occurrence for all years 2004-2011.

In order to further investigate the global occurrence of K_s , it is useful to examine the geographic variation of such events. Figure 5-28 shows the mean percentage occurrence of K_s as a function of latitude (in 10° bins) and longitude (in 30° bins) for the period 2004-2011. The data show geographically very variable percentage K_s occurrences, with an apparent slight northern hemisphere bias in the number of K_s events, particularly in the region $40\text{-}70^\circ\text{N}$. Additionally, there are also regions of high percentage occurrence around the lower half of South America and the Atlantic and Pacific regions either side, consistent with the South Atlantic Anomaly region, and gravity waves generated by the Andes. This enhancement effect was also seen in the Na_s results of Fan *et al.* [2007], who also noted that there was a particularly high Na_s occurrence in the Southern China and Japan regions. Whilst the OSIRIS K_s data does not show relatively high enhancements at latitudes as Japan and South China, there is a region of locally very high ($>22\%$) occurrence northeast of Japan, confined to $40\text{-}60^\circ\text{N}$ and $150\text{-}180^\circ\text{E}$.

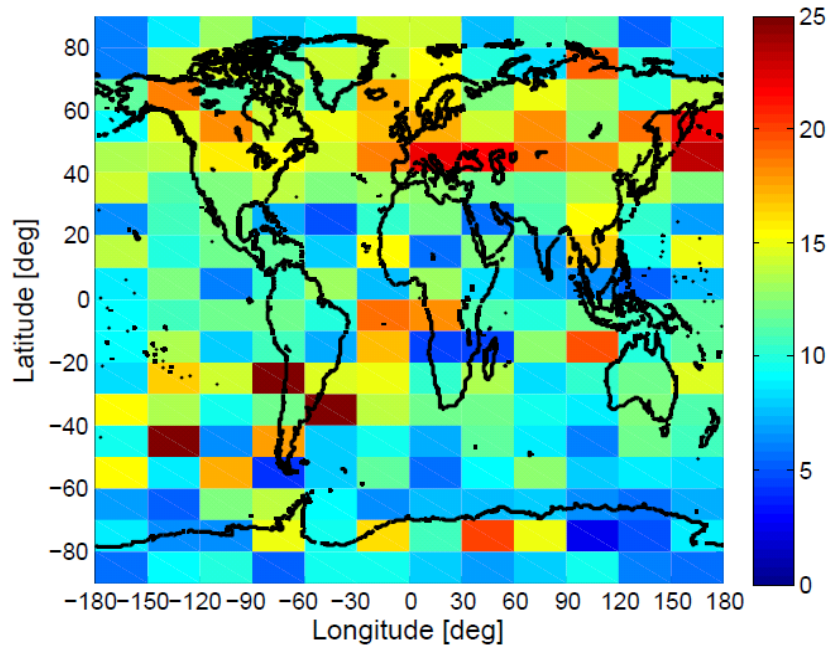


Figure 5-28: Percentage occurrence of OSIRIS-detected sporadic K layers as a function of latitude (10° bins) and longitude (30° bins). The data comprises of the mean percentage occurrence for all years 2004-2011.

As discussed earlier, the occurrence of sporadic E layers (E_s) represents the most probable cause of the occurrence of sporadic metal layers, neutralising metal ion species via reaction R5.4 (in Section 5.4). Fan *et al.* [2007b] compared the occurrence of OSIRIS detected Na_s with E_s occurrence data taken from Leighton *et al.* [1962], finding a good general agreement between regions of high E_s activity and high Na_s occurrences. Figure 5-29 shows the percentage E_s occurrence maps, reproduced from Chu *et al.* [2014] for at three-monthly means across the period 2006-2010 using data from the Constellation Observing System for Meteorology, Ionosphere and Climate (COSMIC) GPS radio occultation measurements.

For Dec-May, a prominent percentage occurrence of E_s occurs over South America, extending across both the southern Atlantic and Pacific regions. This corresponds well to the region of relatively enhanced K_s activity as shown in Figure 5-28. In the Mar-Jun E_s mean profiles, there is a region of relatively high E_s occurrence centred over eastern Asia (encompassing Japan, extending up to approximately $50^\circ N$), mainland Europe and

North Africa (10-50/60°N) and over North America/Canada (>50°N). Each of these corresponds to 'hot spot' regions of relatively high K_s occurrence within the OSIRIS data. This provides support to the leading theory that sporadic metal layers occur as a result of neutralisation of metal ions by sporadic E layers.

Within the solstice profiles (Jun-Aug and Dec-Feb), the E_s occurrence rate is at a maximum within the summer hemisphere. Whilst this would explain the summertime maximum in the northern hemisphere OSIRIS K_s occurrence data relative to the equinoxes, the equivalent southern hemisphere summer maximum is not seen. Additionally, at the majority of latitudes, the OSIRIS data show a stronger winter maximum in K_s occurrence than in summer. The available K_s occurrence measurements reported in Delgado [2011] also show a semi-annual seasonality in K_s occurrence with a pronounced wintertime maximum (although this is not seen in the OSIRIS data at this particular zonal band).

While geographically, the occurrence of K_s appear to positively correlate with the occurrence of sporadic E layers, the seasonal occurrence of both seems to show a disconnect. Further investigation is required into the spatio-temporal of individual sporadic K layers, although this is beyond the scope of this work. It is likely that the relationship between K_s and E_s is quite complex: since the metallic ions convert into neutral atoms, in principle there should be little spatio-temporal correlation. However, in practice, an E_s layer has to descend to approximately 100-105 km in order to neutralise these metallic ions. Since tidal descent rates are typically 4 km hr^{-1} , there can often be a close correspondence as one turns into the other. However, time-of-day is important; the OSIRIS instrument can only view the K_s layers at two local times, whereas the E_s often descend to the critical altitude around local midnight. This means that the seasonal variation is probably linked to the strength of the tides, as well as to concentrations of other species relevant to the metal chemistry, such as atomic O, etc.

A lack of K lidar observations make it difficult to verify the K_s occurrences seen by OSIRIS. The data presented here is the first look at the global K_s occurrences. Whilst it represents the 'best look' so far, there are limitations to the dataset. Namely, the OSIRIS

instrument just takes a 'snapshot' of the metal layer at 6 a.m./6 p.m. and may not give a representative view of the general layer as might be seen in the lidar data (although these themselves are subject to different limitations). Additionally, as in all measurements, there may be some errors in the detection criteria; a K_s may be developing as the Odin spacecraft makes an overpass, but the detection criteria and the retrieval resolution is not sufficient so as to positively identify such an event. Further, the OSIRIS data is not immune to statistical errors or under-sampling; the K measurements are limited and any positively identified K_s events which occur during an overpass may not be representative of the true K_s frequency occurrence.

Overall, the OSIRIS K_s data agrees satisfactorily with data from both Friedman *et al.* [2002] and Delgado [2011]. Beyond this, a lack of lidar observations make the verification of the satellite data impossible at present. Whilst there are differences in the winter/summer occurrences, there appears to be a strong positive correlation between the geographic occurrence of both sporadic K and sporadic E layers, which provides support to the neutralisation of metal ions by sporadic E as being the predominant cause of sporadic metal layers.

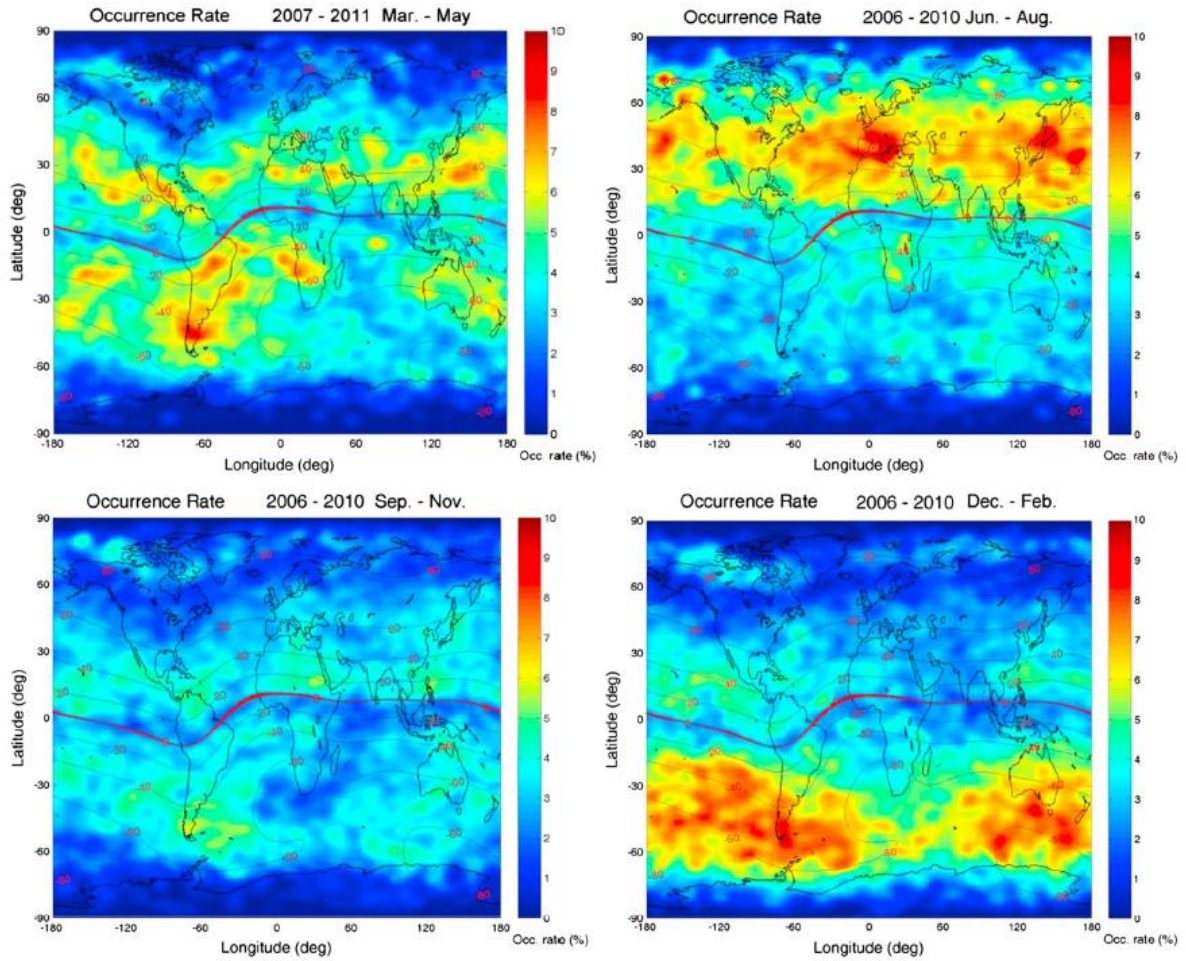


Figure 5-29: Percentage occurrence of sporadic E layers. Reproduced from Chu *et al.* [2014].

5.9 Chapter summary

The unusual behaviour of K, compared with the other metals, has been a long-standing problem, since the early observations of K by Sullivan and Hunten [1964]. A new theoretical basis developed by Plane *et al.* [2014a] for this behaviour produces a modelled response which compares well to the K observations. The work in this chapter has helped to confirm this theory using satellite data, and established that this semi-annual seasonality is global in extent for the first time, with the strongest variation in the mid-latitude and polar regions.

The neutral chemistry of K is shown to be temperature-independent in contrast with that of Na. The late autumn maximum in the MIF, along with wintertime convergence, act to enhance the layers of all metals within the winter hemisphere. In addition, the positive temperature-dependence of the Na neutral chemistry results in additional enhancement (conversion from the NaHCO_3 reservoir to the neutral Na layer) during the period of warmer temperatures. In summertime, the Na neutral chemistry slows down so that there is no such maxima during the cold summertime temperatures. However, the K ion chemistry remains active during these cool temperatures, with dissociative electron recombination of weakly-bound K^+ ion clusters acting to enhance the summertime atomic K layer, producing a summertime K maximum. The column and absolute abundance, centroid layer height and RMS-width of the K layer have been examined with the satellite data, and these responses have been shown to be consistent with the theoretical chemistry.

It has been shown that there is a clear diurnal response within both the OSIRIS observed and WACCM modelled K layers, with a morning maximum and evening minima at altitudes above 86 km related to the photo-ionisation of neutral K throughout the day. In contrast, below this altitude, the evening profile K densities exceed the morning densities as a result of the build up of atomic O and H which, together with direct photochemistry, release K from its reservoir species.

The ability to detect polar mesospheric clouds via depletion of K atoms on the underside of the OSIRIS retrieved metal layers has been demonstrated. This will allow both the global response of the K layers to PMC depletion to be better examined, and will also provide an indirect measure of PMC activity and extent which can be used as a complementary dataset to other PMC measurements.

Finally, the occurrence of sporadic K layers as detected by the OSIRIS instrument has been described. The OSIRIS K_s data compares well with available lidar statistics at Arecibo (18°N), and the near-global data shows a semi-annual seasonality in their occurrence. The positive correlation between the geographic occurrence of the sporadic

K and sporadic *E* layers supports the leading theory that such sporadic metal layers occur as a result of neutralisation of metal ions by sporadic *E* to form neutral atoms.

Finally, the ability to detect polar mesospheric clouds via depletion of K atoms on the underside of the OSIRIS retrieved metal layers has been demonstrated. This will allow both the global response of the K layers to PMC depletion to be better examined, and will also provide an indirect measure of PMC activity and extent which can be used as a complementary dataset to other PMC measurements.

6 SOLAR CYCLE EFFECTS AND LONG-TERM TRENDS

6.1 Overview

The work in Chapter 5 presented the first near-global look at the K layer and examined the underlying mechanisms behind the mean seasonal and diurnal differences in the observed and modelled K and Na layers. The unusual behaviour of K results from two key factors: the temperature independence on the underside of the K layer (the $\text{KHCO}_3 + \text{H} \rightarrow \text{K} + \text{H}_2\text{CO}_3$ reaction has too large an activation energy to be viable at MLT temperatures) and the ability of the K^+ ion to form clusters which undergo dissociative recombination back to neutral K, at the very low temperatures that occur within the summer MLT. These mechanisms produce both a summertime and a wintertime maximum in the K layer. This chapter seeks to examine whether the differences in the metal chemistries cause differential responses to the changes associated with the solar cycle, and longer-term trends within the atmosphere.

The first half of this chapter (Section 6.2) focuses on the observed and modelled K and Na response to the 11-yr solar cycle. The 11-yr solar cycle is a major source of natural variation in the climate system and its impacts on the whole atmosphere are reviewed first. The OSIRIS K dataset extends from 2004 onwards, which encompasses the second half of solar cycle 23 (1996-2008), and the current solar cycle 24 (2009-present). This relatively short dataset means that only a preliminary analysis of the solar cycle impact on the OSIRIS and WACCM K and Na metal layers is presented.

The second half of the chapter (Section 6.3) concerns the longer-term changes in the WACCM modelled Na, K and Fe metal layers in response to a changing climate. A review of the long-term trends in the MLT region is presented first. The suitability of the WACCM data to detect long-term trends is then demonstrated and the technique used for deriving long-term linear trends is outlined. The relationship between the long-term trends in the modelled metal layer column densities and other atmospheric variables

relevant to their chemistry, is explored. Finally, the long-term linear trends of the metal layer centroid altitudes and RMS widths is then explored.

6.2 Response of the metal layers to the solar cycle

6.2.1 *The solar cycle and the response of the MLT region*

The 11-yr solar cycle (hereafter just referred to as SC) concerns the periodic changes in sun spot and flare activity on the surface of the Sun, and it is an important source of variation within the whole atmosphere. These SC effects are caused by changes in temperature, and rates of photo-ionisation and photo-dissociation. The impacts of the SC within the MLT region have previously been reviewed in Laštovička [2005], Beig [2011] and Plane *et al.* [2014b]. In general, a positive correlation is found between MLT temperature trends and SC activity [e.g. Laštovička, 2005; Marsh *et al.*, 2007; Xu *et al.*, 2007]. The SC influence is not constant with altitude, with a larger SC response with increasing altitude [e.g. Laštovička *et al.*, 2008; Beig, 2011; Forbes *et al.*, 2014].

Determining SC trends within MLT dynamics is challenging due to the high spatio-temporal variation and very limited observations, and overall trends are unclear. The choice of analysis period greatly affects the observed response and various studies have found either no clear SC influence on prevailing zonal winds [e.g. Fraser, 1990], a negative correlation [e.g. Bremer, 1997], or a positive correlation [e.g. Sprenger and Schminder, 1969; Namboothiri *et al.*, 1993; 1994; Fahrutdinova *et al.*, 1997; Jacobi, 2014]. A mixed relationship appears to exist between gravity wave (GW) activity and SC with both positive and negative trends apparent in Gavrilov *et al.* [1999] depending on location. Jacobi [2014] found a possible positive SC influence on GW activity and found that the SC-induced variation in both GWs and the mesospheric zonal jet was greater than observed long-term changes.

Thermospheric density is anti-correlated with solar activity [e.g. Mlynchzak *et al.*, 2010; Qian *et al.*, 2011] and this is proposed as being due to the relative radiative cooling roles of CO₂ versus nitric oxide (NO). Beig *et al.* [2012] found no significant solar signal in

O₃ within the HALOE data for 1992-2005. However, within the upper mesosphere they found that the solar response is ~5%/100 solar flux units (s.f.u.) for both low- and mid-latitudes. Merkel *et al.* [2011] found a 4% reduction in O₃ concentration at altitudes above 40 km during solar active conditions.

There are relatively few studies on the SC influence on mesospheric H₂O. Remsberg [2010] used HALOE observations and found an anti-correlation between the solar cycle and water vapour, with solar max-min differences of ~4% at 0.2 hPa increasing to ~23% at 0.01 hPa. The SC response in water vapour at 20°N was found to be in good agreement with the ground-based observations of Nedoluha *et al.* [2009] made at Mauna Loa, Hawaii (19.5°N). Hartogh *et al.* [2010] and Hartogh *et al.* [2013] also found an anti-correlation between solar activity and upper mesospheric water vapour during winter. Related to water vapour, an anti-correlation is seen within both the occurrence frequency [Shettle *et al.*, 2009] and brightness [DeLand *et al.*, 2007] of PMCs, and the occurrence frequency of polar mesospheric summertime echoes (PMSEs) [Smirnova *et al.*, 2010] related to solar activity. In contrast, Latteck and Bremer [2013] found that PMSE occurrence rates were positively correlated with solar activity.

6.2.2 Solar cycles 23 and 24

The solar F10.7 radio flux for the last 3-4 solar cycles (1986-2012) is shown in Figure 6-1 while the long-term time series of sunspot activity is shown in Figure 6-2. In both datasets, the solar minimum period between solar cycles 23 and 24 has been unusually quiet and the current solar maximum has been considerably weaker than recent cycles. The reasons for this declining solar activity are currently unclear; it may just be natural variation but other possible explanations include that the Sun is nearing a minimum in the approximately 80 to 100-year Gleissberg cycle (which concerns cyclic activity of sunspot formation, e.g. see Gleissberg [1967]; McCracken *et al.* [2013]) or that the declining solar activity may be linked to a new 'Maunder Minimum' type period [e.g. Lockwood *et al.*, 2011], which was a period of very low sunspot activity between 1645 to 1715.

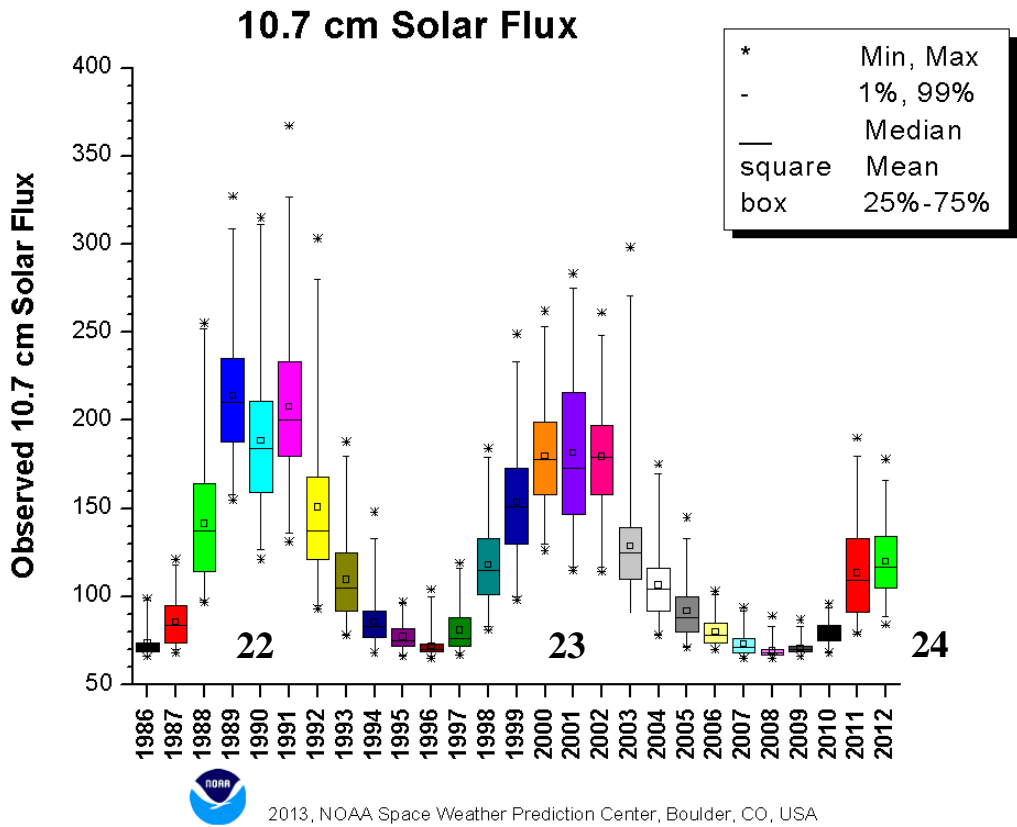
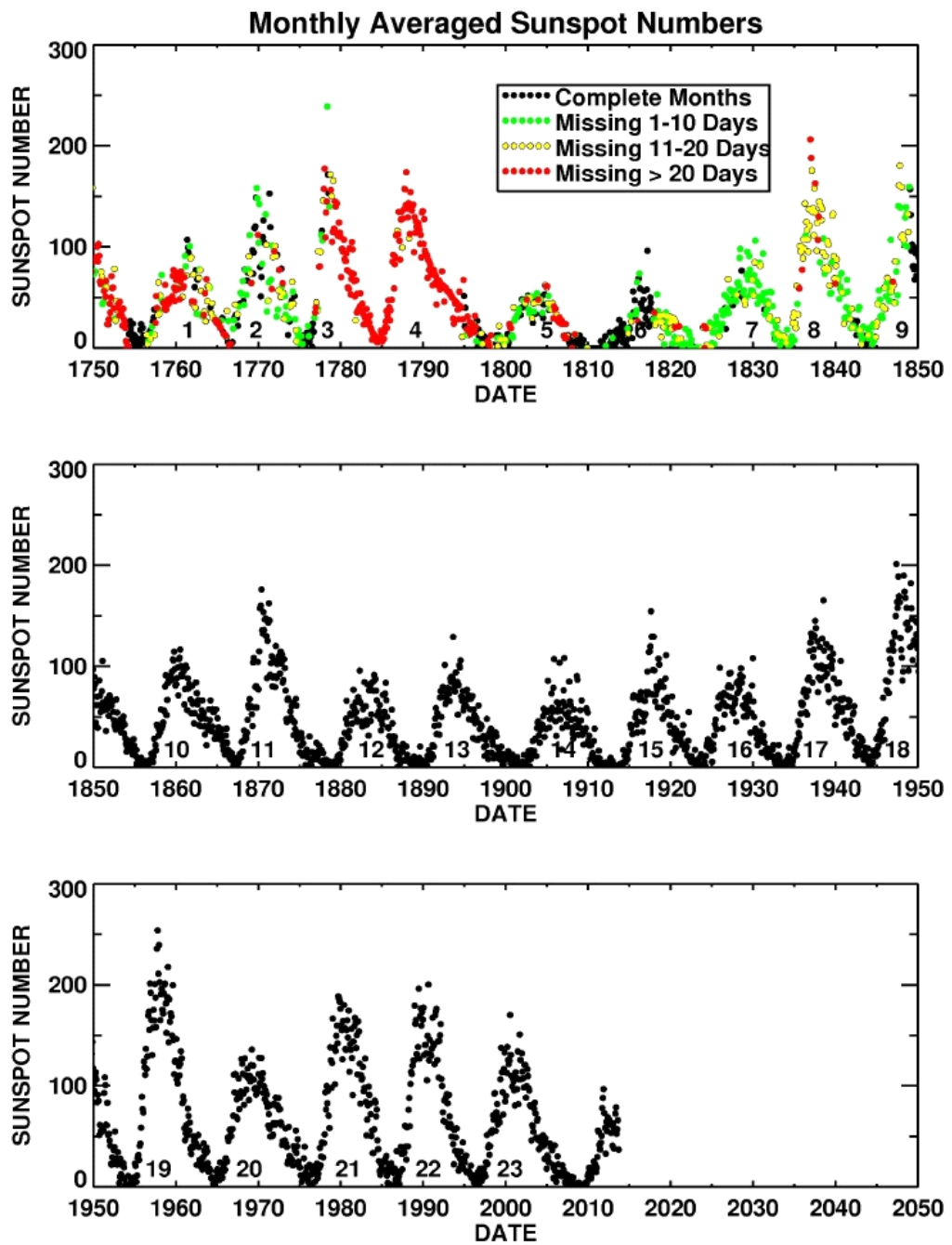


Figure 6-1: The F10.7 solar flux is shown as a function of time. The most recent solar minimum period (2008-2010) is unusually quiet. Reproduced from: www.swpc.noaa.gov/forecast_verification/Assets/F10/F10ObsPlot.html. Annotated to include solar cycle numbers.



HATHAWAY/NASA/MSFC 2013/10

Figure 6-2: Long-term times series of sun spot observations for the period 1750-2014. Reproduced from <http://solarscience.msfc.nasa.gov/>.

6.2.3 *The solar cycle response of the Na and K metal layers: OSIRIS versus WACCM*

A robust solar cycle trend analysis would include data which covers a number of solar cycles, i.e. a dataset of 25-30 years. There are obvious limitations in any SC trend analysis which uses data which covers less than one full cycle (i.e. 10 years, from 2004-2013), as in the case with the OSIRIS dataset. Another potentially significant confounding factor is that the period covered by the OSIRIS data (2004-2013) spans solar cycles 23 and 24, during which there an unusually quiet solar cycle. This may result in any inter-annual variation within the sampled data masking any solar cycle effect. All of these factors contribute to making the following analysis only a tentative look at whether there is a SC response in the observed and modelled Na and K metal layers. Despite these limitations, evidence of a differential response between K and Na to the solar cycle will represent a key test of the underlying chemical behaviours described in Chapter 5.

6.2.3.1 *Comparison of the observed versus modelled K and Na column densities*

The monthly mean global K and Na column densities is determined for both OSIRIS and WACCM across the 2004-2013 period. Although the WACCM data covers this whole period, reliable OSIRIS data is only available up until mid-2013. Beyond this date, there have been issues with the instrument's thermal environment which resulted in the instrument being switched off for periods of time while testing took place.

A comparison of the OSIRIS versus WACCM global K column density time series is presented in Figure 6-3. While the OSIRIS and WACCM output generally compares well with respect to the timing of the summer and winter maxima, the WACCM output does not capture the strong inter-annual variation seen in the OSIRIS data. Also, it cannot reproduce the strong and variable spring/autumn minima seen in the satellite data.

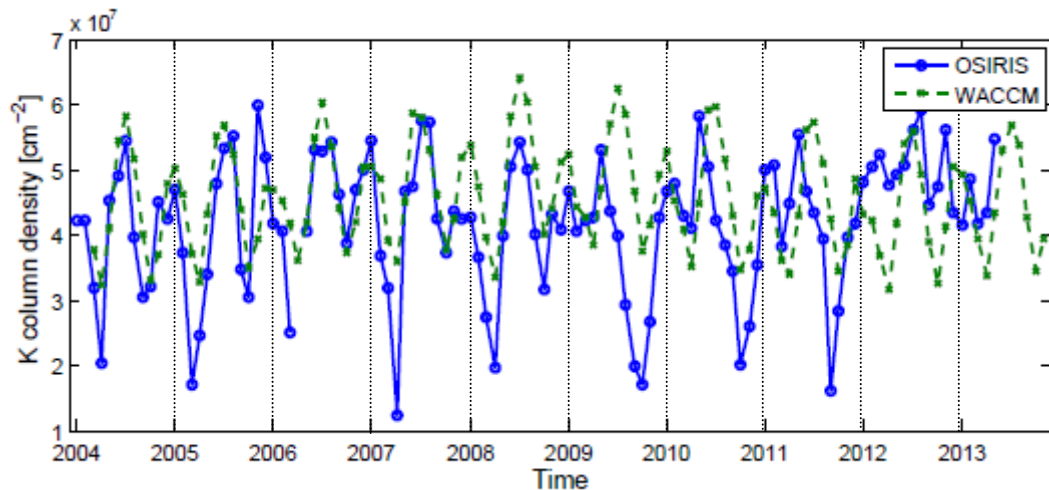


Figure 6-3: Comparison between the OSIRIS versus WACCM monthly mean global K column densities between 2004-2013. Vertical lines added to help guide the eye. [Units: K atoms cm^{-2}].

At first glance, there is no overall trend in the OSIRIS K time series presented here. A slight increase in the WACCM K column densities can be seen during the solar minimum period, peaking between 2008-2009.

The monthly percentage anomalies for both OSIRIS and WACCM K are presented in Figure 6-4. Each monthly anomaly is determined as the percentage deviation from the multi-year monthly mean value. The percentage K anomalies in the OSIRIS dataset are much larger than for WACCM; this would be expected as the model does not capture the high inter-annual variation seen in the OSIRIS data. Additionally, the WACCM data consists of monthly averages which sample the whole diurnal cycle, in contrast to the OSIRIS data which consists of two local times only. The WACCM K anomaly ranges from +10% during the solar minimum years (centred around 2008-2009), to approximately -10% in the surrounding years. In contrast, there is no clear overall anomaly pattern within the OSIRIS data, with the OSIRIS K anomalies ranging from -60% to +40%. The data is much noisier, with some years (e.g. 2004) having large negative anomalies, whilst others display both positive and negative seasonal anomalies depending on month. This is likely as a result of inter-annual differences in the timing of the winter and summer K maxima in the OSIRIS data (see Figure 5-10). For example,

while the timings of the summer/winter K maxima are very uniform in the WACCM data, there is a lot of variation in the OSIRIS data, particularly within the maximum-minimum transition between the latter half of 2009, and again during the latter half of 2010 and 2011. In general, the equinoctial minima are not as pronounced in 2012 with a much higher relative annual K column density persistent throughout the year, which manifests itself in Figure 6-4 as a strong positive K anomaly.

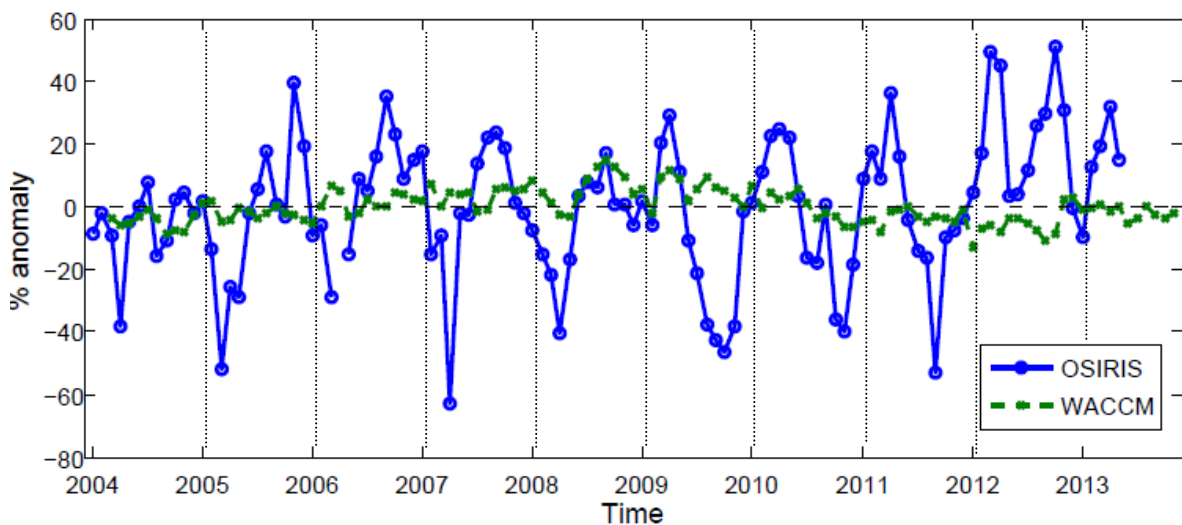


Figure 6-4: Comparison between the OSIRIS versus WACCM monthly global K anomalies between 2004-2013. [%, relative to the multi-year monthly mean K column density]. Vertical lines added to guide the eye.

Figure 6-5 presents a similar OSIRIS-WACCM comparison between the monthly mean global Na column densities. Again, while the Na seasonality is generally captured well in WACCM relative to the OSIRIS data, WACCM does not capture the full inter-annual variation seen in the satellite data. No overall change is apparent in the WACCM Na output. The OSIRIS Na data may show a slight minimum during the solar minimum years, with the winter maxima not as pronounced as in other years. However, any trends in the OSIRIS and WACCM Na datasets appear very weak.

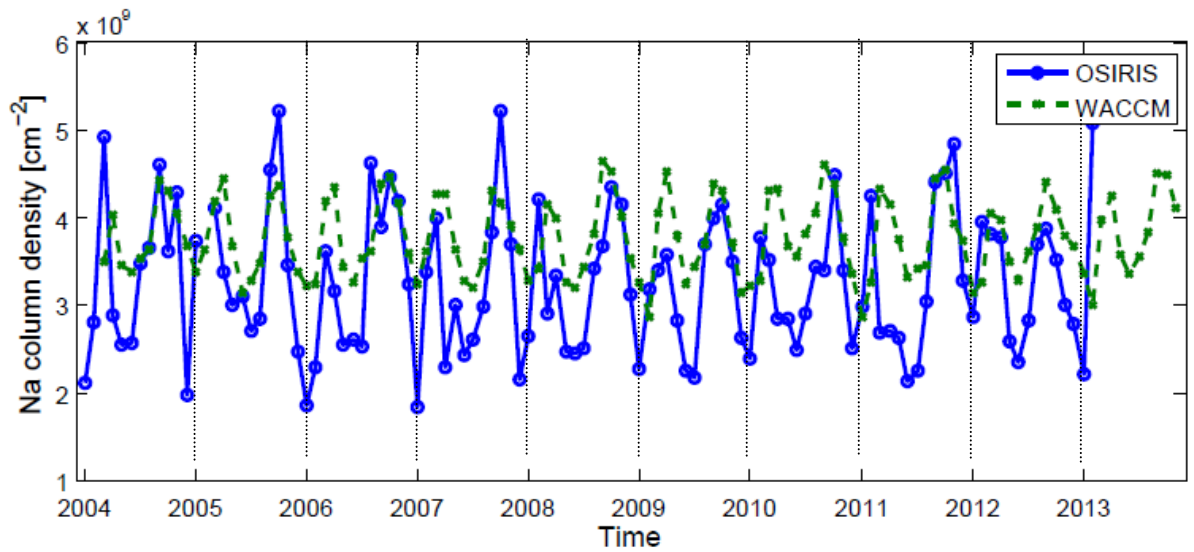


Figure 6-5: Comparison between the OSIRIS versus WACCM monthly mean global Na column densities between 2004-2013. [Units: Na atoms cm^{-2}].

Figure 6-6 presents the percentage anomalies in the monthly mean global Na column densities for both OSIRIS and WACCM datasets. While there is no obvious trend in the WACCM output, a slight positive correlation may be seen between the OSIRIS Na column density and the solar cycle; a minimum during the solar minimum years, with a positive anomaly during the years outside of this time period. A quantitative approach is presented in the following section.

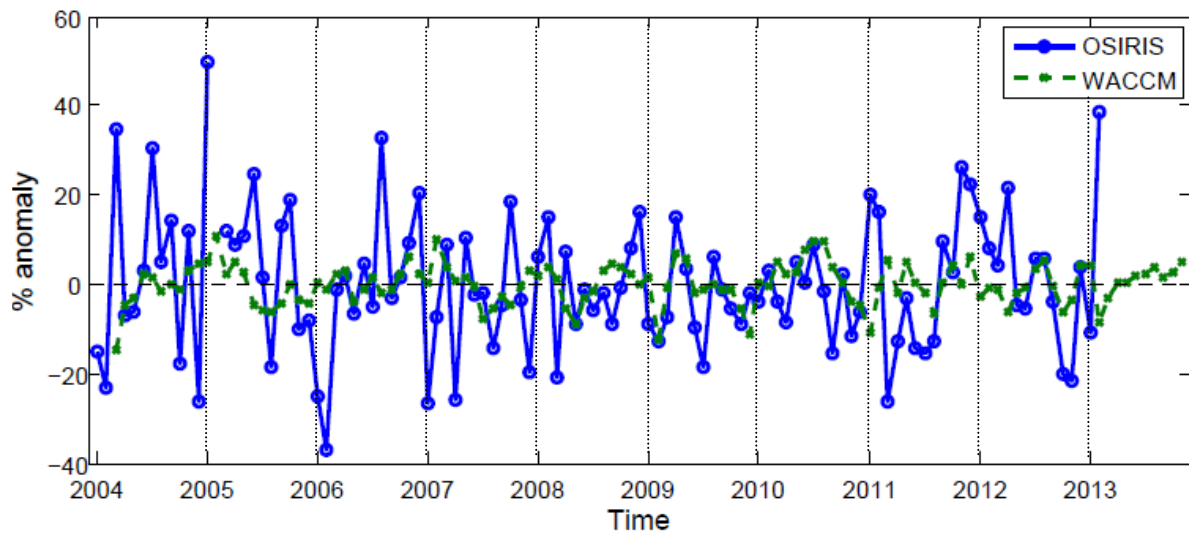


Figure 6-6: Comparison between the OSIRIS versus WACCM monthly global Na anomalies between 2004-2013 [% , relative to the multi-year monthly mean Na column density].

6.2.3.2 Correlation analysis between metal datasets and solar cycle indices

This section examines whether there is any quantitative evidence of a solar cycle effect in the metal layers, in light of the caveats provided in the introduction to this section. The solar F10.7 radio flux and temperature data from SABER are used to represent the solar cycle. The solar F10.7 radio flux for the period 2004-2013 is presented in Figure 6-7; a clear peak in the radio flux is seen during the solar maximum period (2012-2013) and a minimum is seen during the solar minimum period (approximately 2008-2009).

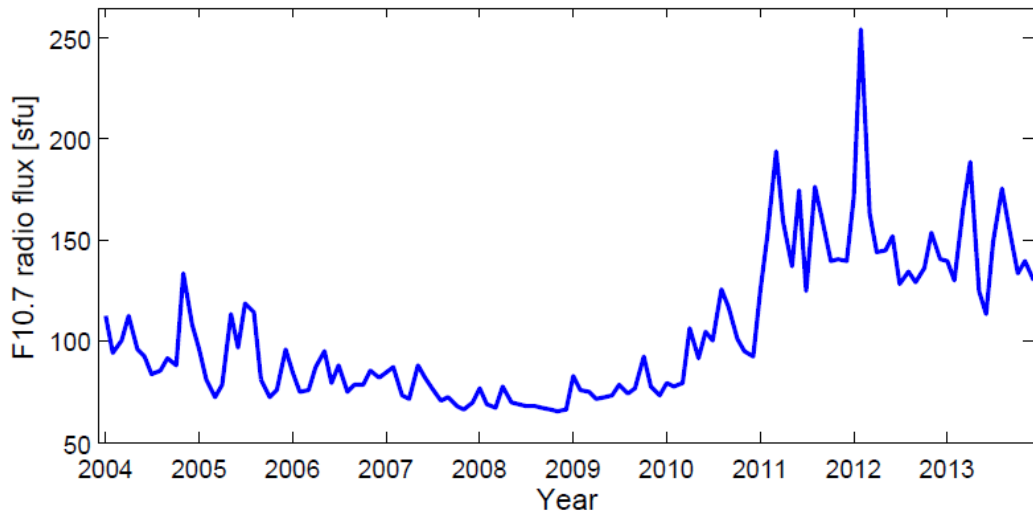


Figure 6-7: Mean monthly F10.7 radio flux for 2004-2013 period.

Another indicator of the solar cycle is temperature; higher temperatures are associated with solar maximum conditions, and vice versa. SABER global vertical temperatures profiles for solar maximum and minimum conditions are presented in Figure 6-8, along with the temperature differences as a function of altitude. In general, the MLT region is very sensitive to changes in the solar cycle with temperature differences of up to 9 K observed between solar maximum and minimum.

However, temperature is also dependent on other factors, e.g. dynamical effects, variations in local chemical heating etc. which may make temperature more variable. Temperature data for this study is derived from SABER observations and presented in Figure 6-9 for three altitudes - 87 km, 90 km, 95 km - used to represent temperatures relevant to the chemistry of the bottom-side, peak region, and top-side of the metal layers, respectively. The figure clearly shows a lot of inter- and intra-annual variation exists in the temperature at each of these altitudes.

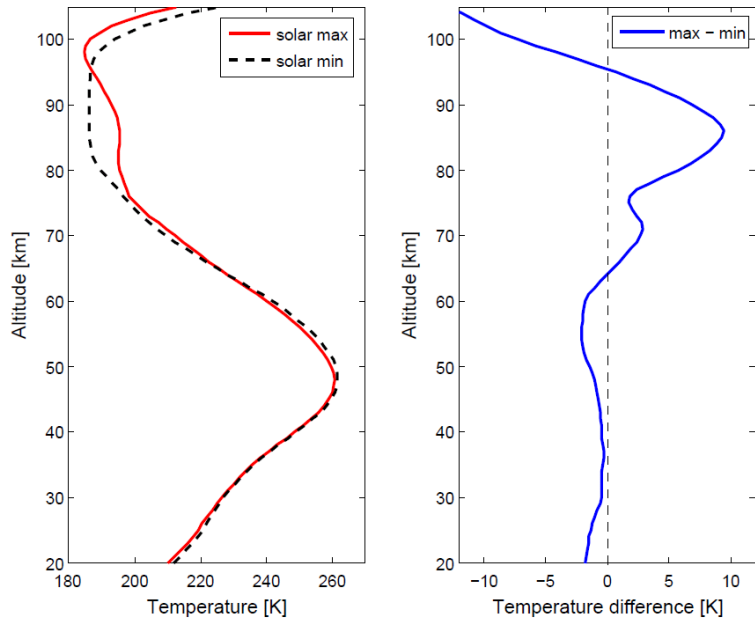


Figure 6-8: 11-year solar cycle variation in the SABER temperature data. [Left panel] Mean global SABER temperature profiles for solar maximum (2012, solid red line) versus solar minimum (2008, broken black line), as a function of height. [Right panel] Temperature difference (solar max - solar min) as a function of altitude. [Units: K].

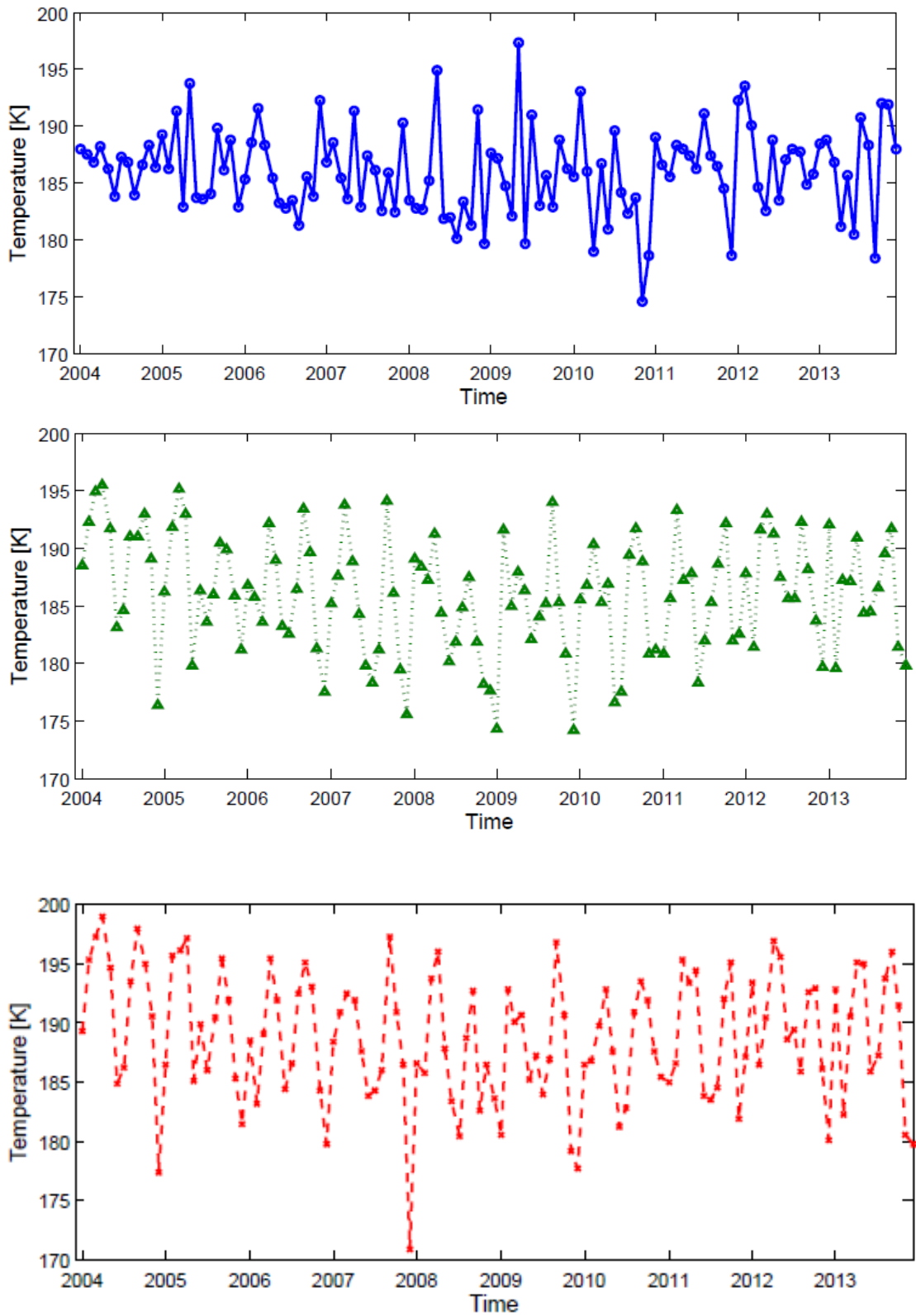


Figure 6-9: Mean monthly global SABER temperatures for 2004-2013, for [top panel] 95 km, [middle] 90 km, and [bottom] 87 km. [Units: K].

A number of correlation analyses were performed to assess the relationship between the global mean OSIRIS and WACCM K column densities and the solar cycle indices, across the full 2004-2013 period. The correlation coefficients and significance values for both the OSIRIS and WACCM K data versus the F10.7 and temperature solar indices are presented in Table 6-1. The equivalent analysis for Na is presented in Table 6-2.

Both the OSIRIS and WACCM K datasets exhibit highly significant weak anti-correlations with the solar F10.7 index, with correlation coefficients of -0.25 and -0.19 respectively. Both datasets also show a relatively weak but significant anti-correlation with the SABER temperatures at 87 and 90 km. Although the correlation coefficients for OSIRIS versus WACCM, versus both of these temperatures do not agree (approximately -0.34 and -0.52, respectively regardless of altitude), they are self-consistent with one another; the correlation coefficients for OSIRIS versus both the temperatures at 87 and 90 km are -0.35 and -0.34 respectively, while the equivalent for WACCM are -0.53 and -0.52. Neither the OSIRIS nor the WACCM datasets shows any significant correlation with the temperature at 95 km. The possible mechanisms for these correlation patterns are reviewed in Section 6.2.3.3 .

The correlation analyses for Na are quite different to those for K. Neither the OSIRIS nor the WACCM Na data exhibit any significant correlation with the F10.7 index. However, in contrast to K, both datasets show highly significant positive correlations with SABER temperatures at 87 and 90 km. As for K, the absolute magnitude of these correlations at the two altitudes is self-consistent for each of the OSIRIS and WACCM datasets. The OSIRIS Na data shows positive equivalent positive correlations of +0.33 and +0.32. As is the case for K, neither the OSIRIS nor WACCM Na datasets show any overall correlation with the SABER temperature at 95 km.

Table 6-1: Correlation analysis between OSIRIS and WACCM global mean K column densities and the solar F10.7 flux (F10.7) and global mean SABER temperatures at 87 km (T87), 90 km (T90) and 95 km (T95) respectively. All data covers the period 2004-2013. The significance values of each correlation coefficient is indicated in brackets. Results in bold indicate a significance with a confidence level of $\geq 95\%$. Blue cell shading represents a significant anti-correlation. Red cell shading indicates a significant positive correlation. All correlations to 2 d.p.

K	OSIRIS	WACCM
F10.7	-0.25 (p<0.01)	-0.19 (p<0.05)
T87	-0.35 (p<0.01)	-0.53 (p<0.01)
T90	-0.34 (p<0.01)	-0.52 (p<0.01)
T95	0.08 (p=0.39)	-0.09 (p=0.34)

Table 6-2: As above, but for Na.

Na	OSIRIS	WACCM
F10.7	0.05 (p=0.63)	-0.01 (p=0.93)
T87	0.33 (p<0.01)	0.50 (p<0.01)
T90	0.32 (p<0.01)	0.47 (p<0.01)
T95	0.01 (p=0.95)	-0.14 (p=0.13)

6.2.3.3 Why do Na and K behave differently?

As shown above in Section 6.2.3.2, both Na and K appear to respond quite differently to the solar cycle. Both OSIRIS and WACCM K data exhibits highly significant anti-correlations with the F10.7 flux, and temperatures at 87 and 90 km, but no overall correlation with the temperature at 95 km. Meanwhile both OSIRIS and WACCM Na data exhibit highly significant positive correlations with the temperature at 87 and 90 km only, and no overall correlation with either the F10.7 index or temperature at 95 km. These differential solar cycle responses can be explained by considering the different K and Na chemistries described in Chapter 5.

The following chemical reactions are those most relevant to the metal atom (here, designated Mt) response to the solar cycle:



The above resulting $Mt^+.N_2$ ion can switch with the ligands CO_2 and H_2O to form more stable complex ions. Alternatively, it may react with atomic O to form $Mt^+.O$. Any of these cluster ions can undergo dissociative recombination to form neutral Mt, via,



The impact of the solar cycle can be divided into two categories: changes in photo-ionisation and photo-dissociation rates, and changes in temperature. Both changes in photo-ionisation and photo-dissociation affect the K and Na metal layers equally. During solar maximum conditions, an increased rate of photo-ionisation occurs resulting in both an enhanced concentration of metal ions via reaction R6.5, and via R6.6 and R6.7 due to an associated increase in the amount of ambient *E* region ions and the corresponding increase in the rate of charge transfer reactions. All of these result in a greater fraction of K and Na atoms converted to K^+ and Na^+ ions, respectively, during solar maximum. Conversely, during solar minimum conditions, reduced rates of photo-ionisation, and the associated charge transfer reactions, result in a lower proportion of metal ions relative to the neutral atoms.

Changes in the rate of photo-dissociation may also be important for the metal chemistry of the underside. During solar maximum, increased photo-dissociation rates (via R6.4) result in increased cycling of various metal reservoir compounds back into the neutral metal atoms. The reverse is seen during solar minimum conditions, with relatively less photo-dissociation of the metal compounds. The concentrations of atomic O and H are also lower during solar minimum, and these species convert metal compounds back to the neutral atoms (via R6.2 and R6.3).

The critical factor in explaining the difference in the apparent solar cycle response lies in the temperature dependence of both metal, which manifests itself in two ways. As explained in Chapter 5, reaction R6.3 is only relevant for the Na chemistry; the activation energy for the analogous K reaction is too high to be viable at temperatures within the MLT. Thus, during solar maximum, enhanced temperatures result in

increased neutral Na as a result of reaction R6.3. Conversely, this reaction rate slows down during the cooler temperatures of solar minimum. There is no equivalent effect in K. The second temperature-related dependence occurs as a result of the differences in size of the K and Na metal ions; the larger K^+ ions can form weakly-bound cluster even at low temperatures, which then undergo dissociative recombination to form neutral K, whereas the relatively smaller Na^+ ions require more energy to undergo the same process.

The overall response of the K layer is an anti-correlation with the solar cycle; the reduced rates of photo-ionisation and lower temperatures associated with solar minimum promote enhanced K concentrations. Although photo-dissociation of K reservoir species is a source of neutral K via R6.4, and thus reducing it will reduce the K, it does not appear to be as important here. While both the OSIRIS and WACCM K correlations support an anti-correlation between the F10.7 flux and temperature, care must be taken in the interpretation, as the changes in SABER temperature at 87, 90 and 95 km are not linearly related to the solar flux alone. A schematic overview of this relationship is provided in Figure 6-10.

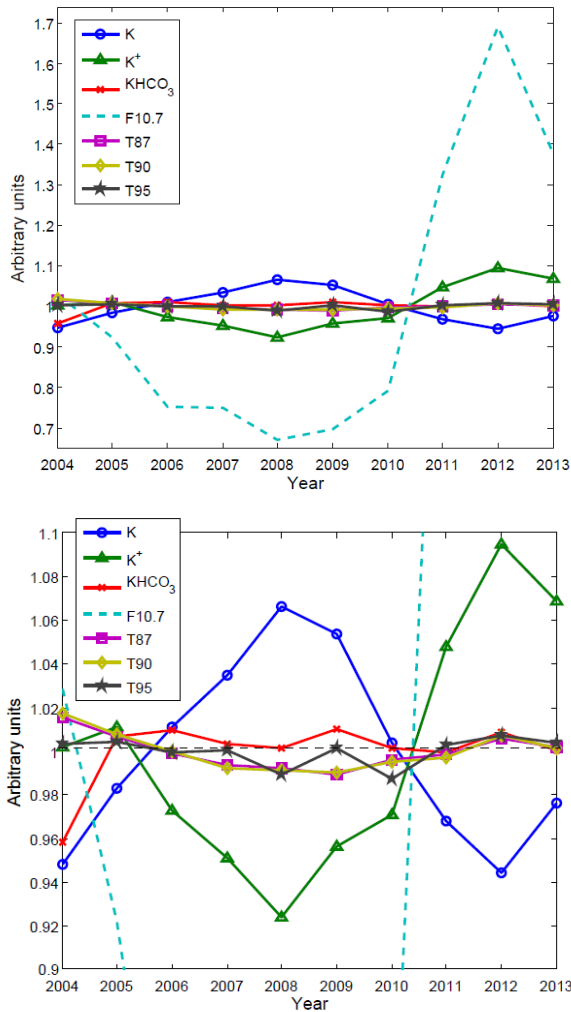


Figure 6-10 [Top panel] Response of the K layer to the 11-yr solar cycle. All results have been normalised (divided by their means) to allow for easy comparison. The solar flux (represented by the F10.7 radio flux) is shown as the light blue dashed line. The normalised modelled K column density (between 75–105 km) is shown as the solid blue line (with circles), the green line (with triangles) and the red lines (with crosses) represent the K⁺ and KHCO₃ column densities, respectively. [Lower panel] As above, but with an expanded y-axis.

The solar cycle response of Na appears to be slightly more complex than that of K, due to the competing influences of temperature and solar flux. The temperature dependence of reaction R6.3 results in an enhancement of the neutral Na layer during the warmer solar maximum conditions, and a reduction in neutral Na during solar minimum as this reaction rate slows down. Meanwhile, the increased rates of photo-ionisation during solar maximum act to deplete the neutral Na layer (and increase the concentration of Na⁺

ions) and vice versa during solar minimum conditions. These competing effects result in little overall solar cycle response, as shown in the non-significant near-zero OSIRIS and WACCM Na versus F10.7 correlation coefficients. A schematic overview of this relationship is shown in Figure 6-11.

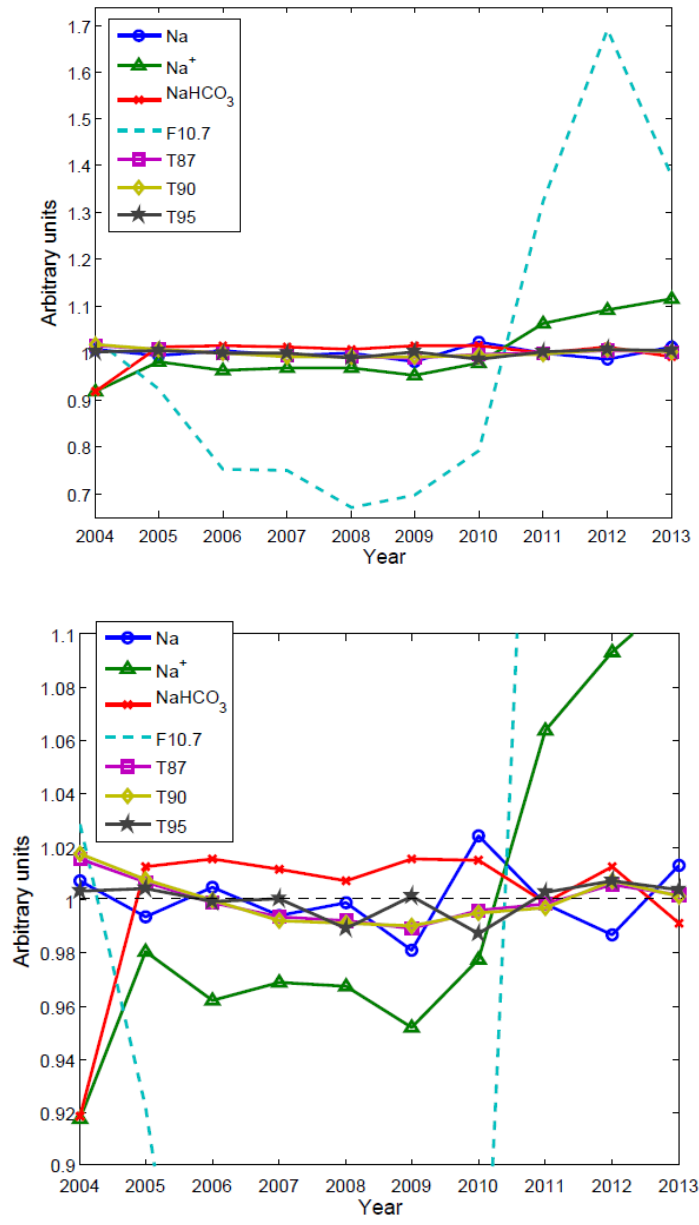


Figure 6-11: [Top panel] The response of the Na layer and related variables to the 11-yr solar cycle. The normalised modelled Na column density (between 75-105 km) is shown as the solid blue line (with circles), the green line (with triangles) and the red lines (with crosses) represent the Na⁺ and NaHCO₃ column densities, respectively. [Lower panel] As above, but with an expanded y-axis.

Overall, despite the issues outlined in Section 6.2 - high spatio-temporal variation in the OSIRIS datasets, only 10 years of data, an unusual solar cycle period - the results indicate that both the observed and modelled K and Na layers show differential responses to the solar cycle; K shows a significant weak anti-correlation with the F10.7 index, and Na shows no overall correlation. The K and Na layers show a negative and positive correlation, respectively, with the temperatures at 87 and 90 km, which is consistent with their differential temperature dependences as discussed in Chapter 5. Neither the OSIRIS nor WACCM results for K or Na show any correlation with the temperature at 95 km. Whether there is any weak correlation which has been masked by a large amount of variation within the modelled and observed metal layers should be the subject of future study.

Although both the OSIRIS and WACCM datasets agree qualitatively on the sign of the changes, there are quantitative differences in the magnitude of the correlation coefficient, with stronger correlations found in the model data. This is to be expected due to the considerably greater variation shown in the OSIRIS data (see Figure 6-3 and Figure 6-5), and it may be that this variation is acting to mask the true extent of the solar cycle response. Additionally, while the model includes known forcings (e.g. daily solar spectral irradiance, surface concentrations of radiatively active species, etc.), the real atmosphere may be doing something different. This should also be a source of further investigation.

6.3 Longer-term trends in the metal layers

In the first half of this chapter, the solar cycle response of the K and Na metal layers has been explored using both the OSIRIS and WACCM datasets. In this section, model data will be used to examine the response of the K, Na, and Fe metal layers to longer-term changes across 50 years, within the MLT region.

6.3.1 Longer-term changes within the MLT region

There has been increasing interest in the middle and upper atmospheric response to anthropogenic climate change ever since the model prediction of Roble and Dickinson [1989] which demonstrated that the global average mesospheric temperature would cool by 10-15 K for a doubled-CO₂ scenario. Since then, modelling studies have helped to identify the main drivers for observed trends, most notably the increase of greenhouse gases [e.g. Akmaev *et al.*, 2006; Garcia *et al.*, 2007], which act as radiative coolers at these altitudes, in contrast to their radiative warming properties within the lower atmosphere. Other identified drivers include O₃ [e.g. Akmaev *et al.*, 2006], changes in atmospheric dynamics [e.g. Jacobi, 2014], changes in solar and geomagnetic activity [e.g. Mikhailov, 2002] and changes in the Earth's magnetic field [e.g. Cnossen and Richmond, 2008]. A number of reviews on these trends have been published in recent years, which include Laštovička [2005], Laštovička *et al.* [2008], Beig *et al.* [2011] and Laštovička *et al.* [2012]. Here an updated review is presented to summarise the state of trend studies to date.

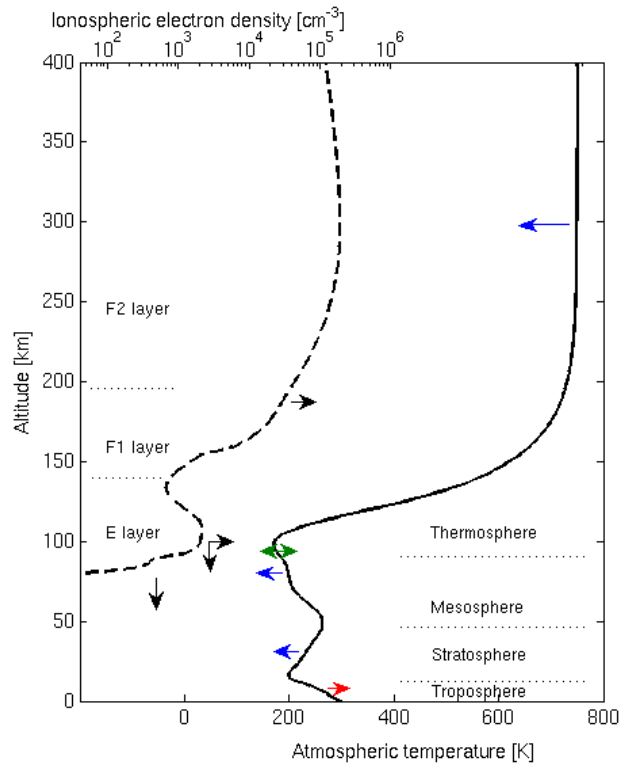


Figure 6-12: Schematic of the long-term changes within the whole atmosphere. Red arrows indicate warming trends, blue arrows indicate cooling, and green arrows indicate regions where the long-term trends are uncertain. Black arrows indicate the sign of changes within the ionospheric electron concentration. Adapted from Lastovicka [2008].

Temperature is the predominant atmospheric parameter which is perturbed by changes in greenhouse gas concentrations [Laštovička *et al.*, 2006]. Cooling trends are apparent in long-term records from ground-based, rocketsonde and satellite data [e.g. Clemesha *et al.*, 1992; Keckhut *et al.*, 1995; Keating *et al.*, 2000; Lübken *et al.*, 2001; Bittner *et al.*, 2002; Nielsen *et al.*, 2002; Semenov *et al.*, 2002; Golitsyn *et al.*, 2006; Kubicki *et al.*, 2006; She *et al.*, 2009; Keckhut *et al.*, 2011]. An overview of the observed and modelled temperature trends within the whole atmosphere is provided in Figure 6-12. Laštovička *et al.* [2008] provided an excellent summary of the available observed temperature trends, with cooling trends of between 1-3 K decade⁻¹ within the lower and middle mesosphere (50-70 km), and 0-10 K decade⁻¹ within the upper mesosphere (70-80 km). This large temperature range for the upper mesosphere is predominantly as a result of the variety of different measurement techniques used, with the greatest cooling rates

derived from rocketsonde data which have significant associated uncertainties. The near-zero results are thought to be as a result of local/regional sampling effects.

Key concerns common to all trend detection studies are data continuity, differences in spatio-temporal sampling, and the associated uncertainties of each observation technique. In addition, the choice of trend analysis employed [e.g. Remsberg, 2007; 2008; 2009; Offermann *et al.*, 2010; Beig, 2011], and whether trends at fixed geometric altitudes or pressure levels are used [e.g. Lübken *et al.*, 2013] must also be considered carefully. Within the MLT region, these considerations are particularly important due to the relatively limited number of observations available, and the need to detect weak trends in what is typically noisy data. A key example of this is in the detection of trends within the mesopause region. Although studies are in general qualitative agreement about the cooling trends within the majority of the mesosphere, there is some contradiction amongst the magnitude and sign of trends observed within the mesopause region. Many of the previous observational studies [e.g. Bittner *et al.*, 2002; She *et al.*, 2002; Signernes *et al.*, 2003; Offerman *et al.*, 2004; Holmen *et al.*, 2014] indicate near-zero trends. These have been further supported by the modelling studies of Akmaev [2002] and Garcia *et al.* [2007] who found similar results. However, a notable number of studies [e.g. Remsberg, 2009; Offerman *et al.*, 2010; Perminov *et al.*, 2014] find cooling trends within the mesopause temperatures, ranging up to approximately 3 K decade⁻¹.

The mesopause region is very sensitive to perturbations and is subject to both the influences of upward propagating atmospheric waves and dynamical forcing from lower altitudes, and also to the effects of solar irradiation, solar wind and ionospheric impacts from above [see review by Plane, 2003]. Various workers [e.g. French and Burns, 2004; Offermann *et al.*, 2004; Remsberg, 2009; Offermann *et al.*, 2010; Beig, 2011] have found significant seasonal and monthly variation within the data records, which makes the derived trend very reliant on choice and length of the analysis period. A key example of this is in a comparison presented in Beig [2011] (see Figure 6-13) which shows a composite of different derived trends for low-latitudes as a function of altitude for a variety of different datasets [e.g. Keckhut *et al.*, 1999 (rocketsonde - US, covering

period 1969-1990); Beig *et al.*, 2012 rocketsonde - India, over 1971-1993); Batista *et al.*, 2009 (lidar - Brazil, over 1993-2006); Sridharan *et al.*, 2009 (lidar - India, over 1998-2009); Remsberg, 2009 (HALOE-satellite, 1991-2005)]. As can be seen, although all datasets qualitatively agree - showing cooling trends at all altitudes - they differ in the strength of these cooling trends, and this was attributed predominantly to changes in stratospheric ozone throughout the whole data observation range (1969-2006). The weakest cooling trend is shown by the later HALOE observations, during which the net ozone effect was close to zero [Remsberg, 2009].

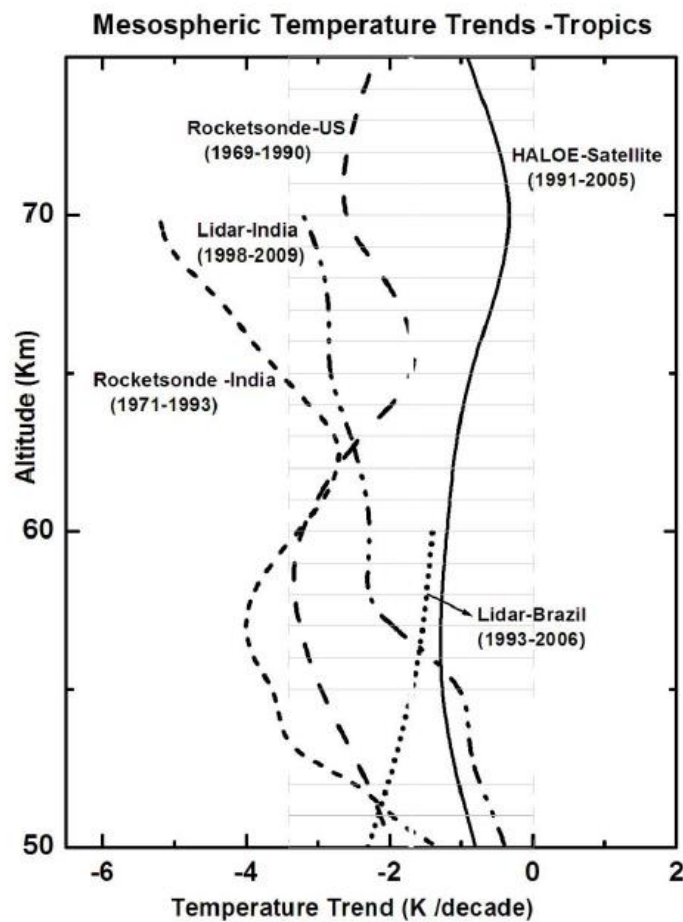


Figure 6-13: Comparison of differential estimates of the mean long-term temperature trend [$K \text{ decade}^{-1}$] within the mesosphere across the tropics, covering four decades of different measurements (1969-2009). The shaded horizontal lines represent the approximate range of trends as revealed within the last two decades. Reproduced from Beig *et al.* [2011].

Changes in stratospheric ozone have an important influence on mesospheric behaviour (both constituents and dynamics) [e.g. Akmaev and Fomichev, 2000; Bremer and Berger, 2002; Akmaev *et al.*, 2006; Bremer and Peters, 2008; Laštovička *et al.*, 2008; Lübken *et al.*, 2013] and are thought to be the predominant cause for the observed non-linearity in a number of derived trends [e.g. Bremer and Berger, 2002; Akmaev *et al.*, 2006; Laštovička *et al.*, 2008; Schwarzkopf and Ramaswamy, 2008; Remsberg, 2009; Qian *et al.*, 2011; Venkat Ratnam *et al.*, 2013; Lübken *et al.*, 2013]. While CO₂ is the main driver and accounts for the largely monotonic linear background in the long-term trends of a variety of parameters, modelling studies by Lübken *et al.* [2013] indicate that O₃ may contribute approximately one third to predicted changes and to the decadal variation. Ozone depletion prior to the mid-1990s will have resulted in strong cooling trends. Since then, a recovery or positive trends in O₃ concentration have been observed [e.g. Fioletov *et al.*, 2002; Chiou *et al.*, 2014; Remsberg, 2014].

The dynamical forcing in the MLT region is dependent on the complex chemical, dynamical and radiative processes occurring at lower altitudes [e.g. Gruzdev and Brasseur, 2005]. A consequence of middle and upper atmospheric cooling (both by changes in greenhouse gases, and ozone) is a change in the global winds. Atmospheric waves (gravity waves, planetary waves, and tides) also play a role in trends (indeed, any changes in the mean circulation may be indicative of long-term changes in wave activity [Qian *et al.*, 2011]) and these are regionally and seasonally variable, very uncertain and are likely to be spatio-temporally unstable [Gavrilov *et al.*, 2002; Baumgaertner *et al.*, 2005; Qian *et al.*, 2011; Jacobi, 2014]. Some studies [e.g. Gavrilov *et al.*, 2002] suggest that there is no apparent trend in MLT gravity wave activity, whilst others [e.g. Jacobi *et al.*, 2006; 2014] point to possible changes, e.g. weak positive trends. There has been no clear pattern in planetary wave activity trends (as summarised by Laštovička *et al.* [2008]), although Jacobi *et al.* [2008] suggested a possible increase in the MLT region, although but that this was high variable and intermittent. There is some controversy in the sign and magnitude apparent trends in tidal activity; a number of observations [e.g. Bremer *et al.*, 1997] have indicated weaker and negative trends in tidal amplitudes, whilst the data of Baumgaertner *et al.* [2005] suggest a positive trend.

There is no overall clear trend in the zonal and meridional winds [e.g. see Bremer *et al.*, 1997; Portnyagin *et al.*, 2006; Qian *et al.*, 2011]. Similar to atmospheric wave activity, there is a large amount of temporal and latitude-specific variation present and an overall non-linearity in the observed trends [Portnyagin *et al.*, 2006]. There was an apparent weakening of the zonal mean winds in the MLT region prior to the 1980s-1990s [e.g. Jacobi *et al.*, 2009; Venkat Ratnam *et al.*, 2013; Jacobi, 2014]. Following this period, there were a number of transition periods during which there was either no significant trend [e.g. Portnyagin *et al.*, 2006] or a tendency towards positive trends [e.g. Jacobi *et al.*, 2009; Jacobi, 2014]. Meanwhile, Portnyagin *et al.* [2006] indicate that the mean meridional winds at a number of NH mid-latitude ground stations exhibit positive increasing trend until the 1990s before exhibiting no overall trend. They indicated that there were seasonal differences though, with no overall significant trend in the winter meridional wind, while the summer meridional winds began to increase from the 1970s onwards.

Observed and projected changes in atmospheric dynamics represent a key area of uncertainty in MLT trend studies. However, the inclusion of dynamical processes - such as wave activity, vertical transport by eddy and molecular diffusion, neutral winds and tides - have produced modelled temperature trends in much better agreement with observations [e.g. see Gruzdev and Brasseur, 2005; Beig, 2011] and the role of gravity waves play a key part in understanding the variation in trends within the mesopause region [Beig, 2011].

Polar mesospheric clouds (PMCs) have received an increasing amount of interest in recent years as they are thought to be sensitive indicators of climate change due to their dependence on temperature and water vapour [e.g. Thomas, 2003; Thomas and Olivero, 2011]. They form at very cold temperatures (<150 K) found within the summer mesopause region, and typically occurring at altitudes between 82-85 km [Lübken, 1999]. Thomas *et al.* [1989] theorised that the increase of CH_4 , and its subsequent oxidation, would increase the amount of water vapour in the upper atmosphere. Indeed Rosenlof *et al.* [2001] showed that stratospheric water vapour - itself a greenhouse gas -

increased at a rate of about $1\% \text{ yr}^{-1}$ across the period 1954-2000. Other observations and model results indicate that middle atmosphere and upper mesospheric water vapour content is also experiencing a general long-term increase [e.g. see Chandra *et al.*, 1997; Nedoluha *et al.*, 1998; Marsh *et al.*, 2007; Remsberg, 2011; Qian *et al.*, 2011; Nedoluha *et al.*, 2013; Russell *et al.*, 2014]. In addition to the cooling temperature trends, this increasing water vapour content was predicted to result in an increase in both PMC brightness/albedo and the occurrence frequency. Further, Thomas [1989] suggested that long-term increases in water vapour or decreases in mesospheric temperature may also expand the latitude range of PMC occurrence.

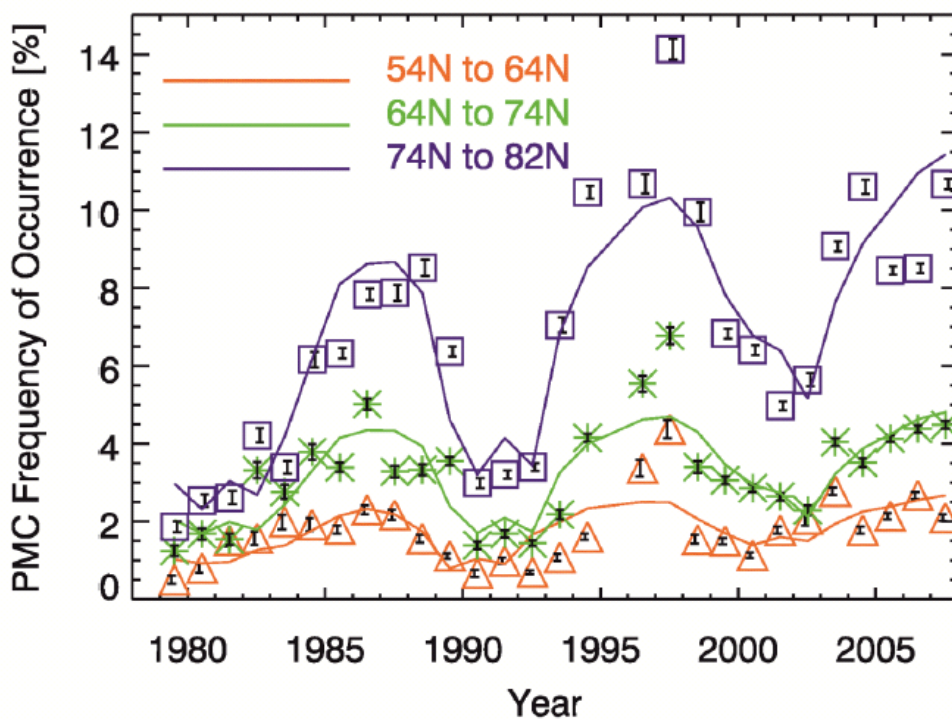


Figure 6-14: Comparison of the seasonal PMC frequency of occurrence as observed by the SBUV and SBUV2 instruments, as a function of latitude band (54-64°N, 64-74°N, 74-82°N). The solid lines represent a linear regression fit. The vertical error bars represent the confidence limits in the individual seasonal mean values based on counting statistics. Reproduced from Shettle *et al.* [2009].

Whilst PMCs are typically observed by satellite, noctilucent clouds (or 'night-shining' clouds, NLCs) can be detected by the naked eye or from ground-based lidar. The

distinction between PMCs and NLCs is significant for trend studies, as observations of NLCs are very limited and often subject to human/weather factors. In recent years, NLCs have been observed at latitudes as low as 37.2°N [e.g. see Russell *et al.*, 2014]. Whether this is indicative of an expanding range as in the prediction of Thomas [1989], or rather due to an increasing interest and number of observations being made, is unclear. Kirkwood *et al.* [2008] found no statistically significant long-term trend in the NLC occurrence rate during a 43 year observation period. However, the authors acknowledge that due to the high observed inter-annual variation and limited observations, any trend $<1\% \text{ yr}^{-1}$ will likely be impossible to determine. Using satellite observations of PMCs from the Solar Backscatter Ultraviolet (SBUV/SBUV2) instrument, DeLand *et al.* [2007] demonstrated that the PMC albedo/brightness had increased across three latitude bands (50-64°, 64-74° and 74-82°) between 1979-2006, with increases ranging from +12% to +20% decade⁻¹ dependent on hemisphere and latitude band. They found that the PMC albedo trend at the lowest latitude band (50-64°) was smaller than at higher latitudes, contrary to the prediction of Thomas (1989). Similar findings were also made by Shettle *et al.* [2009] who analysed trends in PMC frequency occurrence using the same satellite data. Again, they found that the largest trends occurred within the highest latitude band (74-82°) (see Figure 6-14), with a statistically significant increase of 20% decade⁻¹. Modelled results by Russell *et al.* [2014] demonstrated a statistically significant increase in PMC occurrence between 40-55°N, in agreement with observations by the Odin/OSIRIS satellite instrument, which they attributed to the corresponding temperature decreases observed by the TIMED/SABER instrument.

Polar mesospheric summer echoes (PMSEs) are a radar phenomenon that occur as a result of plasma inhomogeneities that occur in response to negatively charged ice particles, present within the summer mesopause region [Latteck and Bremer, 2013]. Similar to PMCs, their appearance is related to mesospheric temperature and water vapour content. While Smirnova *et al.* [2010] found both positive and negative trends in PMSE occurrence rates over 68°N, Bremer *et al.* [2009] found a weak increasing trend in PMSE occurrence rate between 1994-2008, and Latteck and Bremer [2013] found a

significant upward trend between 1994-2012, both at 69°N, indicating a general upward trend in PMSE frequency occurrence.

Long-term satellite drag studies have indicated that thermospheric neutral densities are decreasing, with trends of between -1.7% and -3% decade⁻¹ at 400 km [e.g. see Qian *et al.*, 2011]. This has resulted in a global mean reduction of -0.29 ± 0.20 km decade⁻¹ of the observed altitude of the *E* layer region peak, consistent with the hydrostatic contraction of the middle atmosphere [Qian *et al.*, 2011]. Bremer and Peters [2008] found a correlation between the altitude changes in the ionospheric low-frequency (LF) reflection height and long-term changes in stratospheric ozone; with the greatest decrease in LF reflection height during the 1979-1995 period coinciding with the most pronounced ozone decrease. Changes within the middle atmosphere are not so apparent. Long-term lidar measurements of mesospheric Na at around 90 km by Clemesha *et al.* [1992] found that the centroid height of the layer lowered by ~0.7 km between 1972-1987, which was initially attributed to the cooling and contraction of the middle atmosphere. However, a subsequent study [Clemesha *et al.*, 2003] has indicated that this declining trend in centroid height from the previous 22-year time period was later compensated by a slight upwards trend since 1988. The overall linear trend for the 1972-2001 period is around -93 ± 53 m decade⁻¹ and the authors remain circumspect about whether this might still be as a consequence of global cooling trends.

6.3.2 Longer-term trends in the modelled metal layers

In this section, WACCM model output is employed to investigate long-term trends in the Na, Fe and K metal layers over a 50-year period (1955-2005). The WACCM model is free-running and the output is provided by Dr. Wuhu Feng (University of Leeds). The longer-term changes in these metal layers will be examined in context with longer-term changes in the MLT region in terms of temperature and minor chemical constituents. Key questions to be addressed are:

1. Do the metal layers display different long-term trends in column density to one another?

2. Are these trends consistent with changes in the relevant parameters, such as temperature?
3. Are there changes in the metal layer characteristics, such as the centroid altitude and RMS width, and is this consistent with the observed and modelled changes in the MLT region?

6.3.2.1 The use of WACCM for long-term trend studies within the MLT region

Previous work by Garcia *et al.* [2007] has shown that WACCM is capable of adequately simulating the observed long-term trends in both temperature and ozone. An example of the mid-latitude (30-60°N) WACCM-simulated decadal temperature trend is presented in Figure 6-15, which shows that there is a warming trend within the troposphere, with a maximum warming of $+0.25 \text{ K decade}^{-1}$ at $\sim 6-7 \text{ km}$ altitude. Beyond the tropopause, cooling trends dominate with a maximum cooling rate of $-1.3 \text{ K decade}^{-1}$ at $\sim 45 \text{ km}$, which is associated with the long-term changes in the stratospheric O_3 layer. Cooling trends of between -0.25 to $-0.5 \text{ K decade}^{-1}$ are simulated within the mesopause region, which is of an equivalent magnitude to the tropospheric warming trend.

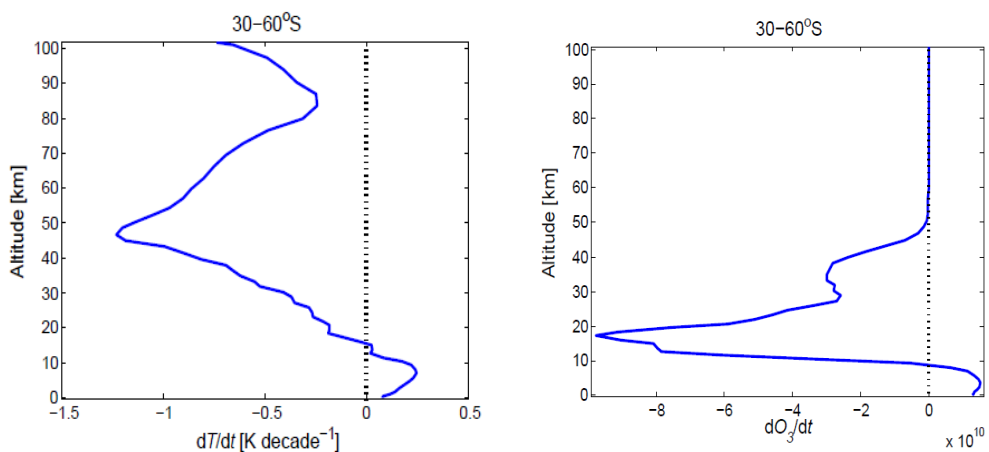


Figure 6-15: [Left panel] Example decadal temperature trend [K decade^{-1}] as simulated by WACCM for 30-60°S, across the period 1955-2005. [Right panel] Equivalent plot for decadal O_3 trend.

A similar decadal trend is seen within the simulated O₃ layer, also shown in Figure 6-15.; within the troposphere there is a positive O₃ trend (maximum of 1x10¹⁰ Dobson units decade⁻¹), which becomes a large negative decadal trend within the stratosphere (maximum of -9x10¹⁰ Dobson units decade⁻¹). Both the observed and modelled temperature and ozone trends are highly variable spatially, which is of relevance to the Section 6.3.2.3 .

6.3.2.2 Detecting linear trends in the metal layers

In order to detect longer-term linear trends in a data set (i.e. over a 50-year period), it is important to first remove other sources of variation within the data. The dominant sources include both the monthly variation, and any variation associated with the solar cycle. The former source (monthly variation) is addressed by only considering annual means.

However, a different approach must be used to account for the solar cycle variation; in this case, a non-linear regression technique is employed to fit an algebraic expression to the WACCM data time series. This expression (*yfit*) takes the form of;

$$yfit = x(1) \times t + x(2) + x(3) \times SolarFlux$$

where *t* is the time (in years), *SolarFlux* is the F10.7 solar flux, and the *x(1)*, *x(2)* and *x(3)* terms represent the coefficients of fit. The linear part of this fit is then inferred as the linear trend component of the data over the full time period. Figure 6-16 provides an example of the technique applied to individual times series of the WACCM K, Na and Fe annual zonal mean column densities for 60-90°N. The non-linear model results in a satisfactory fit with the WACCM K column density data, and this is deemed adequate for purpose even though it does not quite capture the peak-to-peak variation seen in the original data. The linear component of this fit is extracted and indicates that the K column density is increasing at a rate of +0.30% yr⁻¹. In order to estimate the uncertainty associated with this value, a simple linear regression line is also fitted to the original

data, and the uncertainty is given as the difference between the extracted linear trend (using the non-linear fitting technique) and the simple regression line.

The same technique is also used for WACCM modelled output for Na and Fe (also shown in Figure 6-16). In these cases, the non-linear expression does not adequately capture the temporal variation seen in the annual WACCM data, notably so with respect to the Fe data. As seen in the case of the observed and modelled Na layer in 6.2.3.2 , this is most likely as a result of a complex solar cycle dependence in the Na and Fe metal layers.

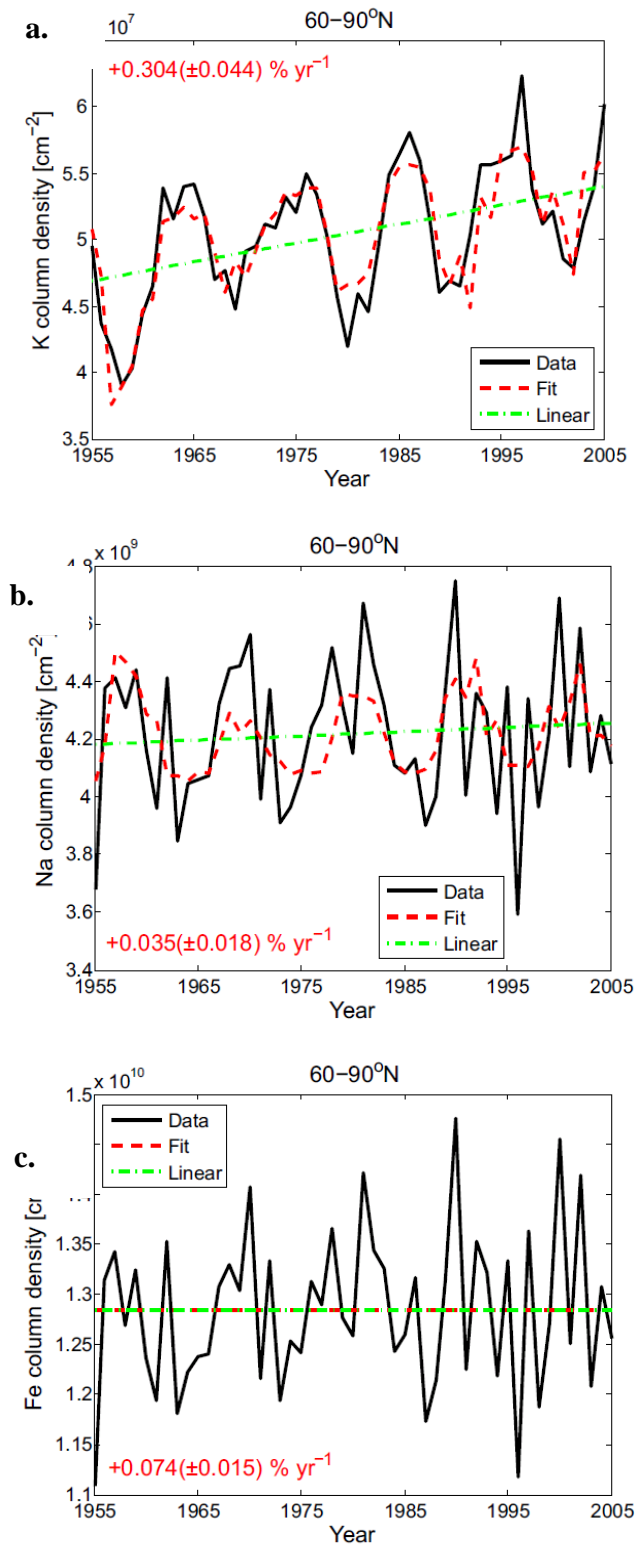


Figure 6-16: Example fitting routine for K [panel a], Na [panel b] and Fe [panel c]. The original metal annual mean column time series is shown as a solid black line [Units: metal atoms cm^{-2}]. The non-linear regression model is shown as the red dashed line. The linear component of the fitted model is shown in a green line. The annual linear trend (across 50-years) indicated in red text [Units: $\% \text{ yr}^{-1}$].

A Fast Fourier transform (FFT) was performed for each of the example (60-90°N) plots to analyse whether there are any hidden variations not accounted for within the Na and Fe data, which would result in an improved non-linear model fit. The results for these FFTs are presented in Figure 6-17. For each metal, there is a dominant annual periodicity component. However, while K shows an additional frequency which corresponds to the solar cycle response, neither Na nor Fe show any other notable underlying dominant frequencies. Thus, no further improvement of the non-linear model was made.

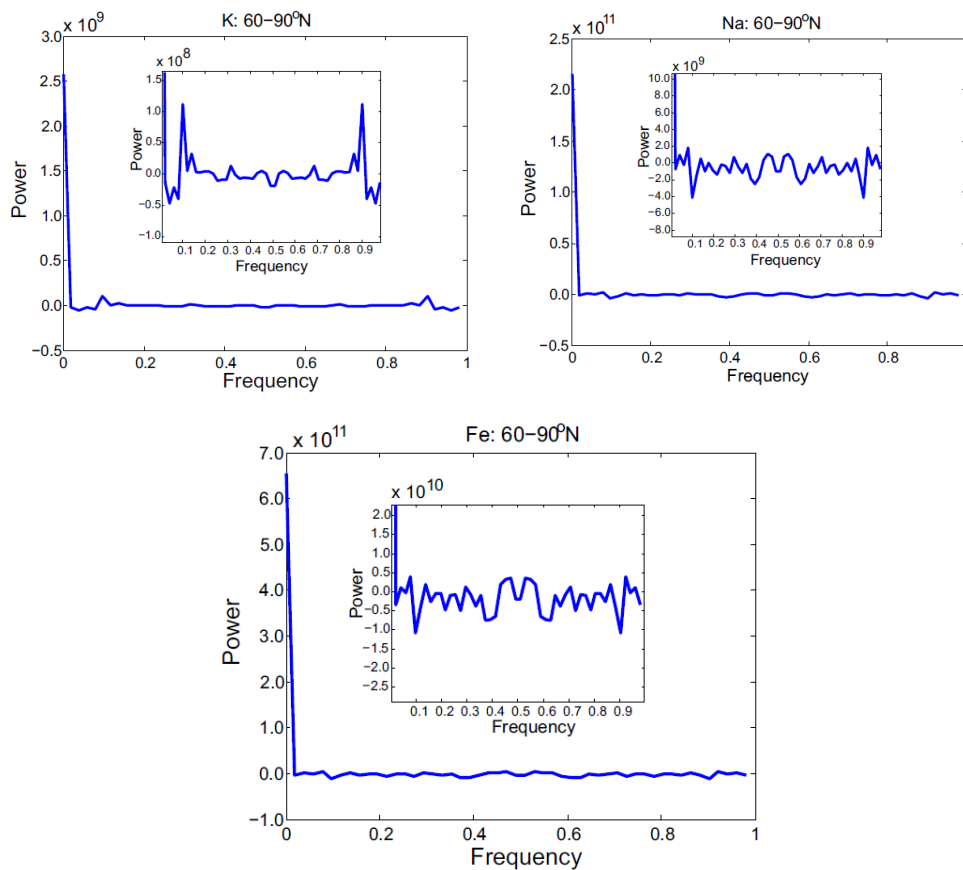


Figure 6-17: Fast-Fourier transform analysis of periodicities of K, Na and Fe WACCM model output. Each inset plot presents an expanded y-axis for clarity. [Units of frequency: yr^{-1}].

6.3.2.3 Long-term changes in the modelled metal layers

Long-term trends within the WACCM simulated Na, K and Fe metal layers were analysed as a function of zonal mean latitude band (binned into 30° bands) across the time period 1955-2005. Each dataset is normalised by its respective multi-year mean in order to facilitate an easier comparison. These are presented in Figure 6-18 to Figure 6-23, along with their derived linear trends determined using the technique described above.

K has a markedly different pattern to both Na and Fe (which both exhibit behaviour that is more similar to one another), with a clear solar-cycle effect, a larger peak-to-trough amplitude, and overall linear trend.

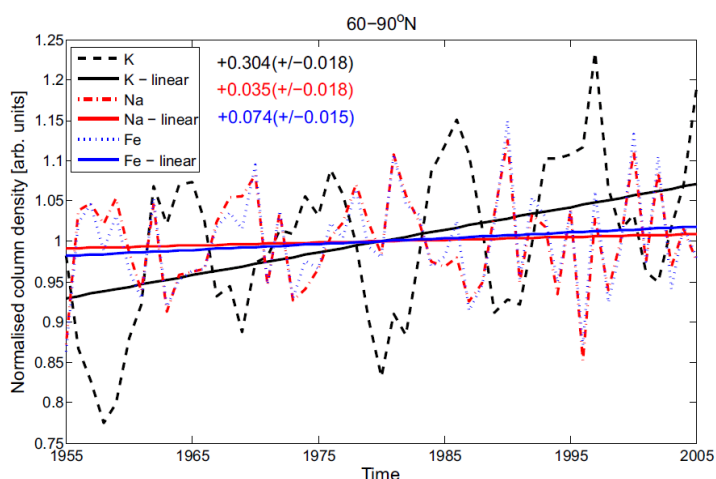


Figure 6-18: Normalised time-series of the K, Na and Fe annual mean column densities for 60-90°N. The normalised time-series is presented as colour-coded broken lines, and the corresponding linear trends are presented as solid lines. The uncertainty associated with each derived linear trend is provided in brackets.

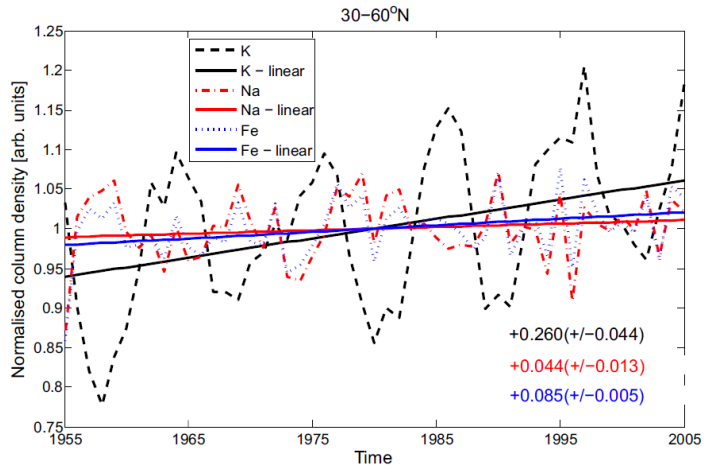


Figure 6-19: As above, but for 30-60°N.

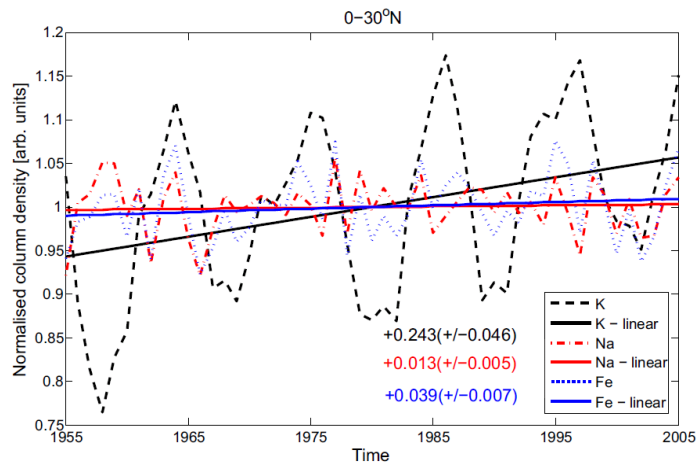


Figure 6-20: As above, but for 0-30°N.

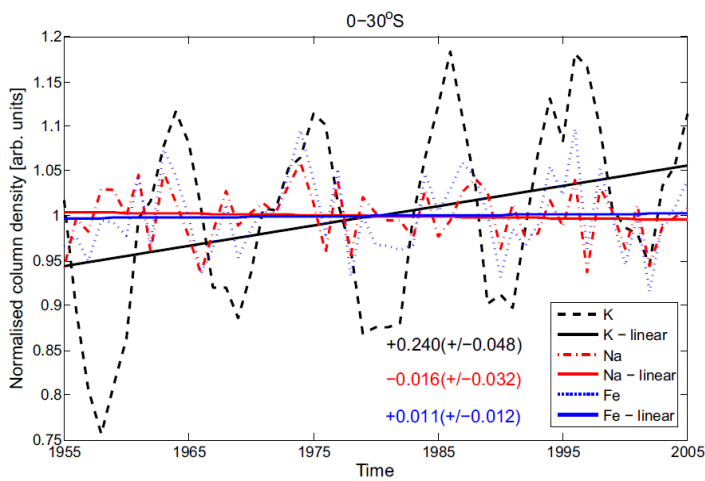


Figure 6-21: As above, but for 0-30°S.

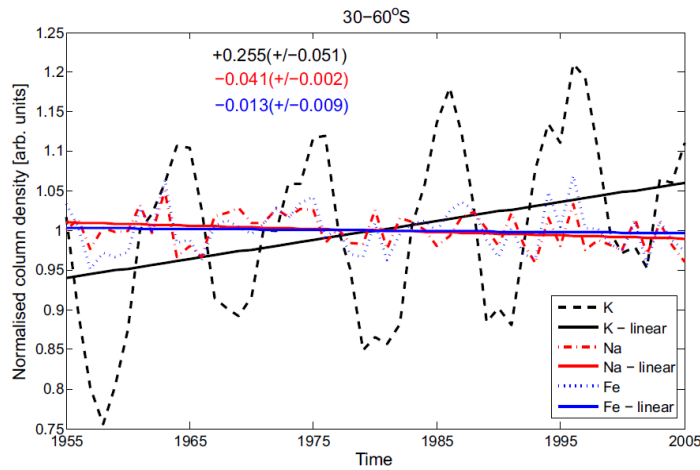


Figure 6-22: *As above, but for 30-60°S.*

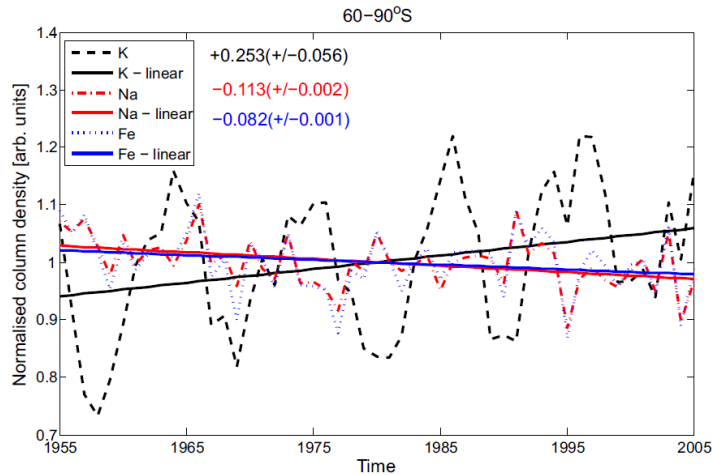


Figure 6-23: *As above, but for 60-90°S.*

A summary of the linear trends for each metal as a function of latitude is provided in Table 6-3. K is the only metal which exhibits increasing trends in column density at all latitudes; both Na and Fe generally show positive trends within the Northern hemisphere, but negative trends within the Southern hemisphere. The K trends are typically a factor ten larger in magnitude than those of Na and Fe, irrespective of latitude. The only exception to this is within the 60-90°S latitude band where the K trend is approximately twice as large as those of the other metals. Overall, the results indicate that the K column densities have increased by approximately 12-15% at all latitudes compared to the Na layer where trends vary between -5% and +2% decade⁻¹, or the Fe layer which varies between ±4%, dependent on latitude.

Table 6-3: Linear trends in the WACCM metal layers [Units: % yr⁻¹] as a function of latitude band (90°N to 90°S, in 30° intervals). The associated uncertainty is indicated in brackets. This has been calculated by determining the difference in a linear trend which takes into account the solar cycle contribution (as used here) and a simple first-order polynomial fit. Positive trends are indicated by red shading whilst negative trends are indicated by blue shading. All values are provided to 3 d.p.

Linear trend in WACCM metal layers [units: % change yr ⁻¹]			
Latitude band	K	Na	Fe
60-90°N	+0.304(±0.044)	+0.035 (±0.018)	+0.074 (±0.015)
30-60°N	+0.260(±0.044)	+0.044(±0.013)	+0.085 (±0.005)
0-30°N	+0.243 (±0.046)	+0.013(±0.005)	+0.039(±0.007)
0-30°S	+0.240(±0.048)	-0.016 (±0.032)	+0.011(±0.012)
30-60°S	+0.255(±0.051)	-0.041 (±0.002)	-0.013(±0.009)
60-90°S	+0.253(±0.056)	-0.113(±0.002)	-0.082(±0.001)

In order to better understand the causal mechanisms behind these different trends, it is important to examine the long-term changes in temperature and other chemical species relevant to the metal chemistries across the same study period. Table 6-4 provides a summary of the mean linear annual trends in the WACCM simulated temperatures at 87, 90 and 95 km, both stratospheric (10-50 km) and MLT region O₃ (75-105 km) column densities and MLT region CO₂ and H₂O column density trends, all as a function of latitude band.

The simulated temperatures indicate a global cooling at the three selected mesopause region altitudes of between approximately -0.01% and -0.07% yr⁻¹. The stratospheric O₃ column densities have been decreasing at a mean rate of -0.05% to -0.65% yr⁻¹

dependent on latitude, with the greatest decreases in the high latitude bands. The MLT region O₃ column density exhibits a more uniform global decrease of approximately -0.07% yr⁻¹ at all latitudes. Finally, both the CO₂ and H₂O mesospheric column densities exhibit increasing annual linear trends of approximately +0.4% yr⁻¹ and +0.35% yr⁻¹ respectively, seen across all latitude bands.

Table 6-4: Summary of derived linear trends for the metals and associated variables, within the 50-year WACCM time-series, as a function of latitude band. The associated uncertainties are given in brackets. As before, negative trends are colour-coded blue, while positive trends are shaded red. All values provided to 3 d.p.

Term	Latitude band					
	60-90°N	30-60°N	0-30°N	0-30°S	30-60°S	60-90°S
T - 95 km	-0.013 (±0.002)	-0.022 (±0.007)	-0.054 (±0.024)	-0.070 (±0.021)	-0.060 (±0.017)	-0.026 (±0.004)
T - 90 km	-0.013 (±0.004)	-0.015 (±0.004)	-0.015 (±0.004)	-0.015 (±0.004)	-0.013 (±0.004)	-0.018 (±0.004)
T - 87 km	-0.020 (±0.003)	-0.013 (±0.003)	-0.012 (±0.004)	-0.012 (±0.003)	-0.009 (±0.003)	-0.011 (±0.003)
Strat. O ₃	-0.100 (±0.002)	-0.075 (±0.003)	-0.069 (±0.002)	-0.079 (±0.002)	-0.181 (±0.000)	-0.633 (±0.000)
MLT O ₃	-0.087 (±0.008)	-0.082 (±0.009)	-0.053 (±0.010)	-0.072 (±0.009)	-0.118 (±0.005)	-0.074 (±0.006)
MLT CO ₂	+0.420 (±0.012)	+0.401 (±0.010)	+0.399 (±0.010)	+0.398 (±0.010)	+0.403 (±0.011)	+0.403 (±0.009)
MLT H ₂ O	+0.382 (±0.017)	+0.342 (±0.011)	+0.336 (±0.008)	+0.348 (±0.010)	+0.359 (±0.014)	+0.391 (±0.014)

Once again, care must be taken when attributing causation due to the interdependence of temperature and the concentrations of O₃, H₂O and CO₂; changes in greenhouse gases such as CO₂ and H₂O, along with changes in O₃ have a direct effect on temperature within the mesopause region. Table 6-5 shows the correlations between temperature and these species. The results suggest that CO₂ is the dominant source of the MLT

temperature decreases, which is in agreement with other observation and modelling studies (see section 6.3.1). There is a highly significant strong negative correlation (-0.842) between temperature and CO₂ at 87 km, which is consistent with enhanced greenhouse cooling associated with increasing CO₂ concentrations. At 95 km, there is a strong highly significant positive correlation (+0.856) between temperature and CO₂. This surprising correlation is likely as a result of the background temperature profile within the upper atmosphere. The temperature within the mesosphere region is characterised by decreasing temperature with increasing altitude. Above the mesopause, temperature begins to increase once more with increasing altitude within the thermosphere. Any hydrostatic atmospheric contraction (which occurs as a result of cooling temperatures and associated changes in the altitude of fixed pressure levels) will result in an apparent increase of temperature.

The correlations between both O₃ and H₂O, and temperature are not significant. However, other studies [e.g. Lübken *et al.*, 2013] have shown that local variations in O₃ contribute up to a third of modelled temperature trends.

Table 6-5: Correlations between temperature (at 87, 90, and 95 km) and stratospheric and mesospheric O₃, and MLT region CO₂ and H₂O. All simulated by WACCM. All to 3 d.p.

Term	T – 95 km	T – 90 km	T – 87 km
Strat. O ₃	-0.136 (p=0.798)	+0.721 (p=0.106)	-0.271 (p=0.603)
MLT O ₃	-0.058 (p=0.913)	-0.613 (p=0.196)	-0.188 (p=0.721)
MLT CO ₂	+0.856 (p<0.05)	+0.464 (p=0.355)	-0.842 (p<0.05)
MLT H ₂ O	+0.577 (p=0.230)	-0.1997 (p=0.704)	-0.326 (p=0.528)

Correlation analyses are performed (shown in Table 6-6) in order to better understand the relationship between the trends in the simulated metal layers and long-term trends in

temperature and these main chemical species. K is the only metal which exhibits a significant correlation with temperature, with a very strong positive correlation (+0.887) at 95 km, and a strong negative correlation (-0.836) at 87 km.

As with the solar cycle, the anti-correlation between K column density and the temperature at 87 km can be explained as a result of the temperature independence of the conversion of K^+ cluster ions to neutral K via dissociative recombination (reaction R6.9). The positive correlation between the temperature at 95 km and K column density is rather more complex, particularly as no such correlation was found between either K or Na column densities and the SABER temperature at 95 km in Section 6.2.3.2 . One possible reason for this strong positive relationship could be due to the positive correlation between increasing CO_2 and increasing temperature at 95 km, due to the shape of the background temperature profile, as discussed above.

Table 6-6: Correlation coefficients between the metals and various related parameters.

The significance values are indicated in brackets. Red shading indicates significant (>95% confidence) positive correlations, blue shading indicates significant negative correlations. All to 3 d.p.

Term	K	Na	Fe
T – 95 km	+0.887 (p<0.05)	+0.277 (p=0.595)	+0.345 (p=0.503)
T – 90 km	+0.545 (p=0.264)	+0.663 (p=0.152)	+0.656 (p=0.157)
T – 87 km	-0.836 (p<0.05)	-0.542 (p=0.267)	-0.569 (p=0.238)
Strat. O ₃	+0.108 (p=0.839)	+0.894 (p<0.05)	+0.856 (p<0.05)
MLT O ₃	-0.327 (p=0.527)	+0.106 (p=0.842)	+0.084 (p=0.875)
MLT CO ₂	+0.982 (p<0.01)	+0.263 (p=0.615)	+0.304 (p=0.558)
MLT H ₂ O	+0.542 (p=0.267)	-0.553 (p=0.255)	-0.503 (p=0.309)

Care must be taken not to confuse cause and effect when performing correlation analyses between the metals. An example for this is the strong positive correlation between the Na and Fe column densities and stratospheric O₃ column density. Decreasing stratospheric O₃ cools the stratosphere and MLT region, which removes both Na and Fe (but not K). This results in this positive correlation between stratospheric O₃ and Na and K.

Overall, temperature appears to be the dominant factor in explaining long-term trends in the K layer, which is supported by the solar cycle responses of the observed and modelled K layers earlier in the chapter. The trends in the Na and Fe layers are rather more complex, and appear to be dependent upon the subtle latitude-specific changes in

temperature, O₃, CO₂ and H₂O. The complex interaction between these different variables result in much weaker and varied trends in the modelled Na and Fe layers, than is seen in the K layer. To aid in the interpretation, this latitudinal dependence is visualised in Figure 6-24. A clear hemispheric asymmetry is apparent in the Na and Fe datasets with both exhibiting relatively similar behaviour to one another in contrast to K. While the hemispheric differences in trends for Na and Fe appear prominent, they are very small compared to K (see Figure 6-25); K is the only metal which exhibits a noticeable long-term linear trend, which equates to a response ($\delta K/\delta T$) of approximately $-6\% \text{ K}^{-1}$ over the 50-year period.

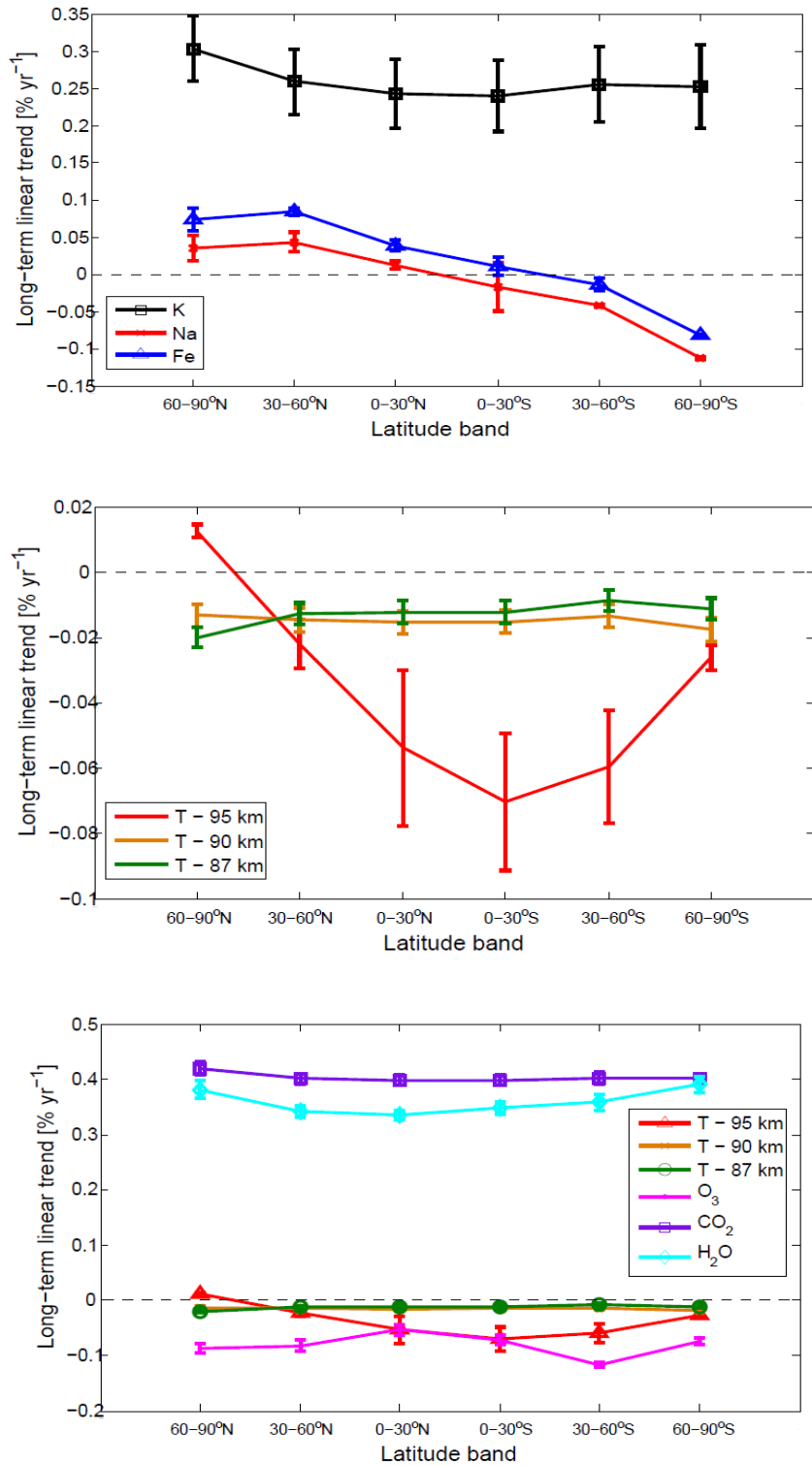


Figure 6-24: Long-term linear trends in modelled metals [top panel], temperature [middle panel] and temperature and MLT region O₃, CO₂ and H₂O. All as a function of latitude band. [Units: $\% \text{ yr}^{-1}$].

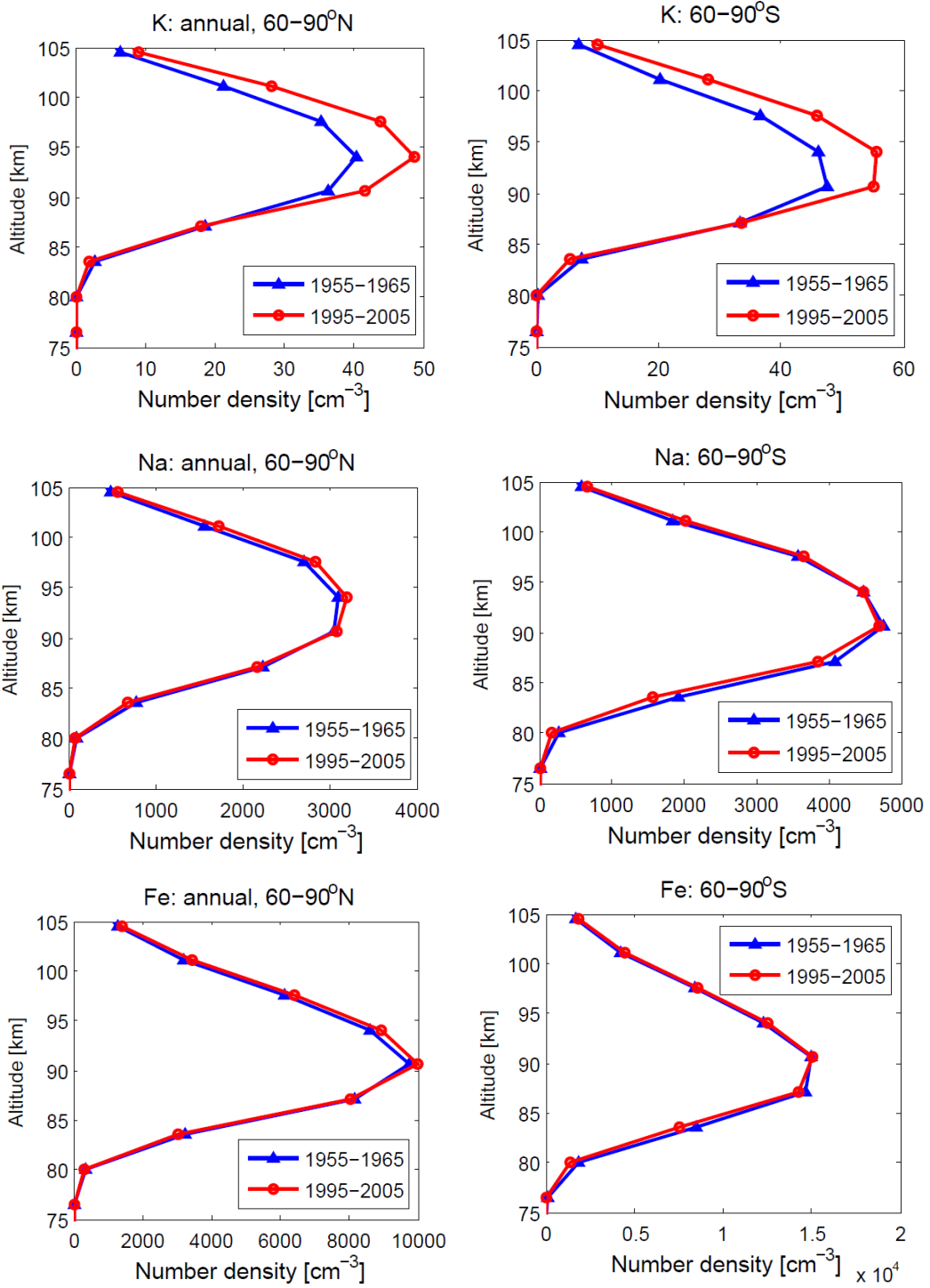


Figure 6-25: A comparison of the long-term response of K (top panel), Na (middle panels) and Fe (lowest panels) across a 50-year period (1955-2005). All profiles show the respective mean metal number density across either 1955-1965 (blue profiles) or 1995-2005 (red profiles), as a function of altitude. The left-hand column indicates zonal mean profiles for 60-90°N, and the right-hand column indicates zonal mean profiles for 60-90°S.

6.3.2.4 Long-term changes in the centroid altitude and RMS layer width

In this section, long-term trends in the modelled metal layer centroid altitude and RMS-width are examined. A trend analysis is performed in the same way as in the previous section for the metal column densities, and an example trend analysis plot for the normalised centroid altitudes is shown in the figure below

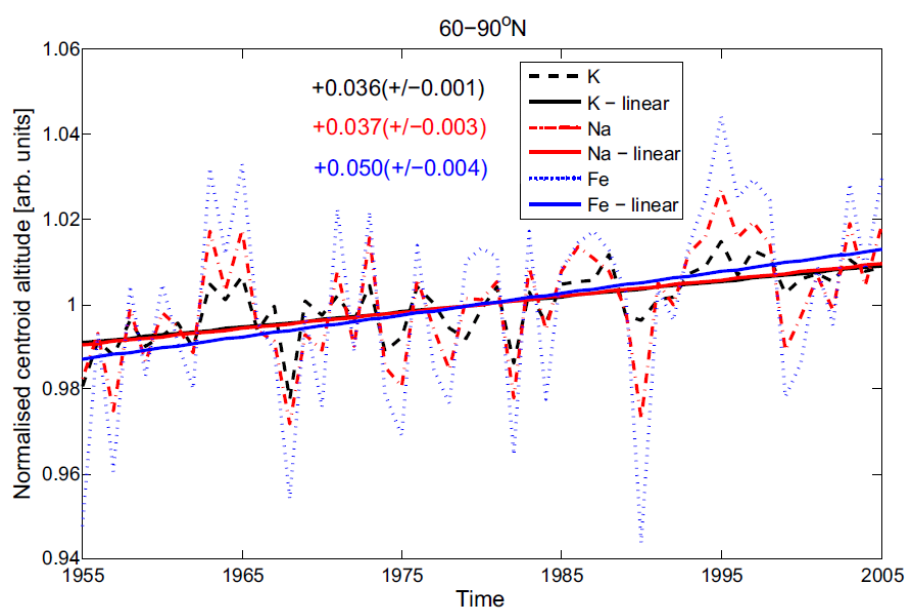


Figure 6-26: Normalised time-series for Na, K and Fe centroid altitude, as a function of latitude. For each plot, the normalised time-series is presented (colour-coded broken lines), along with the associated linear trend (solid lines).

A summary of the linear trends in metal layer centroid altitude is provided in Table 6-7 and the correlation analyses are presented in Table 6-8. In all cases, the changes in centroid altitude are very small (equating to a maximum of 2-3% change over the full 50-year period in the modelled data), with the K changes typically a factor ten greater than those of Na and Fe. Overall, the K layer centroid altitude is increasing at a rate of approximately $0.03\% \text{ yr}^{-1}$ at all latitudes. For the majority of latitudes, Na also shows an increase in the centroid altitude, although the values show much greater latitudinal variation than for K, ranging from approximately $+0.037\% \text{ yr}^{-1}$ at 60-90°N, $+0.002\% \text{ yr}^{-1}$

within the low latitude bands, and a very weak trend of $-0.009\% \text{ yr}^{-1}$ at $60\text{-}90^\circ\text{S}$. The Fe trend data presents a more complicated picture with weak positive trends $>30^\circ\text{N}$ of approximately $+0.03\% \text{ yr}^{-1}$, but even weaker negative trends ($\sim -0.005\% \text{ yr}^{-1}$) between 30°N and 60°S , and a larger negative trend of $-0.0260\% \text{ yr}^{-1}$ at $60\text{-}90^\circ\text{S}$.

Table 6-7: Long-term linear trends in the centroid altitude of the metal layers, as a function of latitude band [units: $\% \text{ yr}^{-1}$]. Associated uncertainties are provided in brackets. All to 3 d.p.

Metal	Latitude band					
	60-90°N	30-60°N	0-30°N	0-30°S	30-60°S	60-90°S
K	+0.036 (±0.001)	+0.044 (±0.003)	+0.023 (±0.002)	+0.027 (±0.002)	+0.033 (±0.004)	+0.014 (±0.003)
Na	+0.037 (±0.003)	+0.015 (±0.002)	+0.001 (±0.003)	+0.003 (±0.003)	+0.010 (±0.003)	-0.009 (±0.003)
Fe	+0.050 (±0.004)	+0.012 (±0.002)	-0.004 (±0.003)	-0.005 (±0.003)	-0.005 (±0.004)	-0.026 (±0.004)

Table 6-8: Summary of correlations between the metal layer centroid altitudes and temperature and relevant chemical species. The associated significance values are provided in brackets. All those significant at the >95% level are shaded and in bold.

Centroid altitude	K	Na	Fe
T – 95 km	+0.327 (p=0.527)	+0.657 (p=0.157)	+0.690 (p=0.130)
T – 90 km	+0.792 (p=0.06)	+0.829 (p<0.05)	+0.738 (p=0.094)
T – 87 km	-0.320 (p=0.537)	-0.773 (p=0.071)	-0.870 (p<0.05)
Strat. O ₃	+0.692 (p=0.128)	+0.551 (p=0.257)	+0.571 (p=0.236)
MLT O ₃	-0.424 (p=0.402)	-0.368 (p=0.474)	-0.168 (p=0.751)
MLT CO ₂	+0.300 (p=0.564)	+0.811 (p=0.051)	+0.813 (p<0.05)
MLT H ₂ O	-0.343 (p=0.506)	+0.119 (p=0.823)	+0.089 (p=0.866)

Table 6-8 indicates a highly significant strong anti-correlation between the Fe layer centroid altitude and the temperature at 87 km; temperature decreases and centroid altitude increases. The Fe centroid altitude is strongly positively correlated with MLT region CO₂ concentration, with both increasing. One possible interpretation of these is that the correlation between CO₂ and Fe centroid altitude is as a result of an indirect effect; the rising CO₂ concentrations are anti-correlated with the temperature, which is likely the dominant control on the Fe layer height. The Fe layer peak altitude is approximately 3-4 km lower (centred around 87 km) than that of either Na or K, as a result of differential ablation. As the temperature at 87 km decreases, the temperature-dependent reaction $\text{FeOH} + \text{H} \rightarrow \text{Fe} + \text{H}_2\text{O}$ becomes less efficient, and more Fe may

remain in the stable FeOH reservoir form, rather than the neutral form. This would likely cause a small change in the centroid altitude.

A strong highly significant positive correlation is shown between the Na centroid altitude and the temperature at 90 km; as temperature decreases, so should the centroid altitude. This appears to be in conflict with the previous negative correlation between Fe centroid altitude and temperature and it is not obvious why this is the case.

Another possible explanation for changes in centroid altitude at high latitudes would be the impact of changes in PMC occurrence through time. A number of authors [e.g. DeLand *et al.*, 2009; Shettle *et al.*, 2009] have reported increasing PMC brightness and frequency of occurrence, thought to be as a result of long-term changes in temperature and water vapour within the mesopause region. Unfortunately, no PMC chemistry exists within the 50-year free-running WACCM model run, and as such, this theory cannot be investigated any further.

Overall, the changes in centroid altitude for all the metals is very small, typically between -0.009 and $+0.050\%$ yr^{-1} which equates to a maximum change of 2-3% across the 50-year study period (also see Figure 6-25). This is in approximate agreement with other studies which found very small overall changes in the mesospheric Na layer between 1972-2001 [Clemesha *et al.*, 2003] of between -99 ± 53 m decade^{-1} which equates to an annual linear trend of about -0.010% yr^{-1} .

Summaries of the linear trends in the RMS-width of the metal layers, and the associated correlation analyses are presented in Table 6-9 and Table 6-10. The majority of data suggest that the RMS-width of the Na and K layers are decreasing (i.e. the layers are becoming narrower) at all latitudes, but this trend is much more prominent in the K data where the values are typically an order of magnitude greater than for Na. Additionally, the uncertainties are relatively larger for Na than for K. As was the case for the centroid altitude trend, trends in the Fe layer width vary between positive and negative, depending on latitude, ranging from between approximately $\pm 0.2\%$ yr^{-1} at high latitudes, with much smaller trends within the mid- and low-latitude bands.

Table 6-9: Long-term linear trends in the RMS-width of the metal layers, as a function of latitude band [units: % yr⁻¹]. Associated uncertainties are provided in brackets. All to 3 d.p.

Metal	Latitude band					
	60-90°N	30-60°N	0-30°N	0-30°S	30-60°S	60-90°S
K	-0.532 (±0.029)	-0.440 (±0.026)	-0.381 (±0.045)	-0.429 (±0.045)	-0.368 (±0.040)	-0.087 (±0.044)
Na	-0.252 (±0.014)	-0.083 (±0.007)	-0.006 (±0.021)	-0.023 (±0.021)	-0.081 (±0.020)	+0.089 (±0.027)
Fe	-0.204 (±0.013)	-0.060 (±0.002)	+0.027 (±0.022)	+0.039 (±0.023)	+0.022 (±0.026)	+0.288 (±0.035)

Table 6-10: Summary of correlations between the metal layer centroid altitudes and temperature and relevant chemical species. The associated significance values are provided in brackets. All those significant at the >95% level are shaded and in bold. All to 3 d.p.

Term	RMS-width		
	K	Na	Fe
T – 95 km	-0.168 (p=0.751)	-0.568 (p=0.249)	-0.413 (p=0.415)
T – 90 km	-0.837 (p<0.05)	-0.880 (p<0.05)	-0.872 (p<0.05)
T – 87 km	+0.542 (p=0.267)	+0.739 (p=0.100)	+0.669 (p=0.146)
Strat. O3	-0.930 (p<0.01)	-0.601 (p=0.207)	-0.817 (p<0.05)
Meso O3	+0.130 (p=0.807)	+0.402 (p=0.429)	+0.211 (p=0.688)
CO2	-0.359 (p=0.484)	-0.781 (p=0.067)	-0.571 (p=0.237)
H2O	+0.436 (p=0.388)	-0.076 (p=0.887)	+0.244 (p=0.641)

All three metals show highly significant strong anti-correlations between layer width and the temperature at 90 km, all between -0.80 and -0.90. The chemistry of the top- and

bottom-sides of the layer influence the layer width. On the bottom-side, changes in the chemical cycling as a result of changes in the concentration of relevant species or temperature; a decrease in temperature and an increase in CO₂ and H₂O concentrations may act to increase the amount of a metal atom stored in a reservoir compound, which will reduce the layer width. Changes in dynamics may also play an important role in the layer width. However, the use of annual means, rather than monthly or seasonal means will likely minimise the impact that such changes may have.

As discussed in relation to the centroid altitudes, any changes in PMC occurrence and extent is likely to affect the metal layer widths, producing a general reduction as a result of removal of metal atoms on the bottom-side of the layer in the so-called 'bite-out' process. However, as no PMC chemistry is included in this run of the model, this is not relevant to the modelled time series presented here.

A highly significant anti-correlation exists between the stratospheric O₃ column abundance and the RMS-width of both K (-0.930) and Fe (-0.817). There is also an anti-correlation of -0.601 between stratospheric O₃ and Na RMS-width, but this is not significant. As the reduction in MLT temperatures as a result of stratospheric O₃ decreases results in a compression of the layer thus resulting in the anti-correlation.

The latitude-specific trends in both the centroid altitude and RMS-width are presented in Figure 6-27 and Figure 6-28, respectively. The largest positive trends in centroid altitude are seen at high northern latitudes for all metals. As latitude decreases poleward towards the south, these positive trends become smaller, and in the case of Fe become increasingly negative within the southern hemisphere. The reverse pattern is seen in the RMS-width trends; at high northern latitudes, the RMS-width trend is negative for all three metals. As latitudes become more southern, the magnitude of this negative trend reduces and becomes increasingly positive for K. However, as was the case for long-term changes in the metal column densities, the nature of these hemispheric differences are very small (see Figure 6-25).

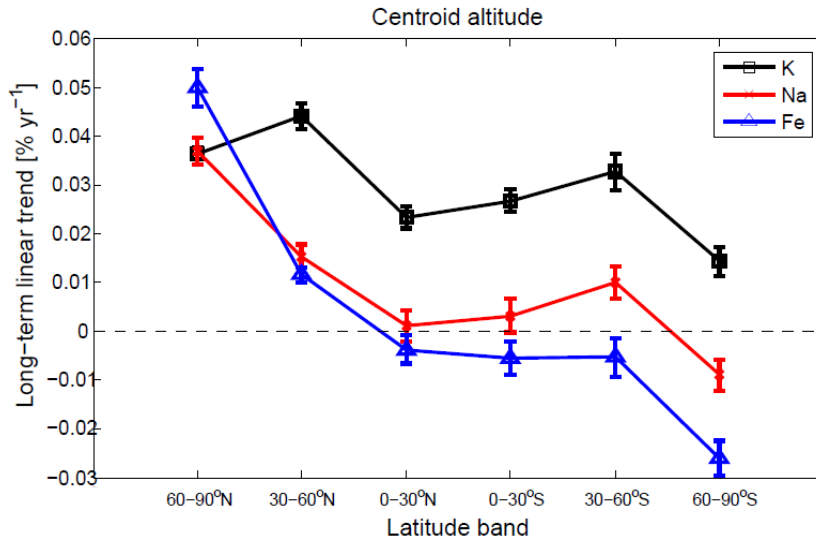


Figure 6-27: Long-term linear trends in the centroid altitude of the WACCM modelled K, Na, and Fe metal layers for 1955-2005, as a function of latitude band. [Units: % yr⁻¹].

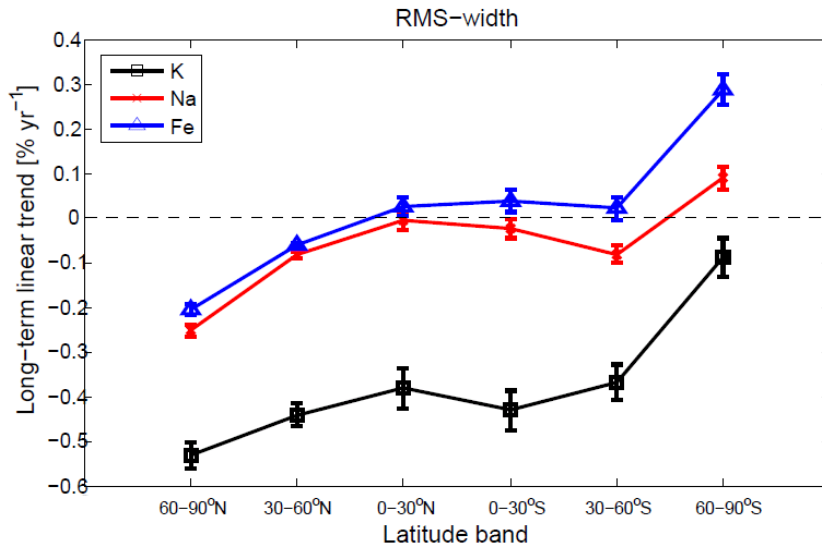


Figure 6-28: Long-term linear trends in the RMS-width of the WACCM modelled K, Na, and Fe metal layers for 1955-2005, as a function of latitude band. [Units: % yr⁻¹].

6.4 Chapter summary

There is increasing interest in the response of the climate to both solar cycle variations and to longer-term changes as a result of anthropogenic climate change. The solar cycle remains one of the fundamental sources of natural variation within the Earth's atmosphere, and its influence must be understood in order to determine accurate longer-term trends. The first half of this chapter sought to examine whether there was any solar cycle response in the observed and modelled Na and K metal layers. The results presented represent only a tentative analysis, for three reasons; 1) the metal datasets do not cover a full solar cycle, instead only covering a ten-year period from 2004-2013, b) an ideal trend analysis requires data extending over multiple solar cycles to aid robust conclusions being drawn, and finally 3) the latter half of solar cycle 23 and the current cycle 24 are unusually quiet which may make any solar cycle response harder to detect.

Nevertheless, the OSIRIS and WACCM Na and K datasets were examined in response to the solar F10.7 index and temperatures from the TIMED/SABER instrument. Both the observed and modelled datasets indicate that the Na and K layers exhibit very different responses to the solar cycle, which supports the K chemistry scheme described in Chapter 5. K shows a highly significant anti-correlation (reduced neutral K during solar maximum, enhanced K during solar minimum). Meanwhile, Na shows a more complex solar cycle response, due to the competing influences of temperature and photo-ionisation on its chemistry.

Both the OSIRIS and WACCM datasets qualitatively agree, but not quantitatively. The OSIRIS metal datasets show considerably more natural variation than seen in the WACCM data, which is likely to account for many of the differences in the absolute strengths of the trends, and the results of the correlation analyses.

The second half of the chapter explores longer-term trends within the MLT region. To date, the majority of research has focused on the impacts of anthropogenic climate change within the lower atmosphere. However, there is increasing evidence that changes

in greenhouse gas concentrations are impacting all parts of the atmosphere, with the middle and upper atmosphere particularly sensitive to such changes.

WACCM data is used to assess the long-term response of the K, Na and Fe metal layers within the MLT region. K is the only layer which shows prominent long-term changes in column density, thought to be as a result of the temperature-independence of the reservoir reaction ($\text{KHCO}_3 \rightarrow \text{K}$) on its underside and also as a result of the size of its ion, which allows efficient conversion of K^+ clusters back to the neutral K layer at cold temperatures, which is not the case for either Na or Fe. The long-term trends in Na and Fe column density are rather more complex; they are much more sensitive to the subtle interaction of latitude-specific changes in temperature and O_3 , CO_2 and H_2O within the MLT region.

Changes in other metal layer characteristics – the centroid altitudes and RMS-widths – are also considered. Very weak increases are seen in the centroid altitude of the Na and K metal layers. Fe exhibits a more complicated latitude-specific trend and this is thought to be related to the lower peak height of the mean layer relative to the other metals, as a result of differential ablation. A general decrease of the RMS layer width is also seen in both Na and K. The Fe RMS-width appears to be more sensitive to long-term changes.

Based on the quantitative differences between the OSIRIS and WACCM datasets response to the solar cycle, it is likely that any observed trend will differ from the modelled trends presented here due to the natural variation that WACCM cannot yet simulate. However, key messages are that the K layer is the only metal which shows both prominent solar cycle and longer-term responses, as a result of its unusual chemistry within the MLT region. While the Na and Fe layers do show some response to longer-term changes, these are typically an order of magnitude smaller than those of K, and mostly near-zero in nature.

7 CONCLUSIONS AND RECOMMENDATIONS

7.1 Major findings

The previous lack of observations of the mesosphere/lower thermosphere (MLT) region has meant that this important region has been relatively poorly understood to date, compared with other parts of the Earth's atmosphere. Although there have been numerous lidar studies of the metal layers produced by meteoric ablation, a key limitation of such data is that they represent point measurements. Remote sensing by satellites makes it possible to construct a near-global picture of these metals, which act as excellent tracers for atmospheric chemistry and dynamics within the MLT region. Of these meteoric metals, K has been the least well understood, displaying a unique semi-annual seasonality not seen in the other observable metals. The overall aim of this thesis has been to produce the first near-global K retrieval to both assess and evaluate this semi-annual seasonality, as well as providing a new dataset with which to test our understanding of the MLT region.

The major findings of this thesis are as follows.

1. The first satellite K retrieval scheme has been developed, which derives K number density profiles using Odin/OSIRIS limb radiance dayglow data. The dataset extends from 2004 to June 2013, has a latitude coverage of 82°N-82°S and provides data at two local sampling times (with local equator crossing times of approximately 0600 and 1800). The K number density profiles have a vertical resolution of 2 km, a total retrieval error of $\pm 15\%$ within the peak layer region, and compare well to available (but limited) K lidar station data.
2. The first near-global look at the K layer has been presented, which shows that the unusual semi-annual seasonality (previously observed only at limited lidar station locations) extends across the full latitude range of the satellite dataset. The greatest seasonal variability is seen at mid- and high-latitudes.

3. In this work, the OSIRIS K dataset has been used to provide the first near-global validation of the WACCM modelled K layer, and provides further support for the K chemistry scheme proposed by Plane *et al.* [2014a].
4. The largest K semi-annual variation occurs at latitudes with the largest annual temperature variability i.e. at mid- and high-latitudes. WACCM data was used to demonstrate the different temperature responses of the Na and K layers, as a function of latitude and altitude. Na was found to be positively correlated with temperature, within the peak layer region, at all latitudes. This relationship results from the positive temperature dependence of the reaction $\text{NaHCO}_3 + \text{H} \rightarrow \text{Na} + \text{H}_2\text{CO}_3$. In contrast, the K layer exhibits a largely negative correlation with temperature within the peak layer region, for the majority of latitudes. This results from both a temperature independence on the underside of the K layer (no analogous $\text{KHCO}_3 + \text{H}$ reaction) and the significance of the formation of weakly-bound K^+ clusters at low temperatures; as temperatures cool (e.g. during the summertime MLT) the $\text{K}:\text{K}^+$ ratio increases. At high latitudes, the temperature anti-correlation with K density was much weaker, due to the competing influence of K exhibiting a maximum during both the colder summertime MLT and during the warmer wintertime MLT as a result of convergence and compression of the K layer due to the residual circulation downwelling and the seasonal peak input of meteoric material.
5. Both OSIRIS and WACCM data have been used to examine the response of K and Na to the 11-year solar cycle. Highly significant negative correlations (approximately -0.35 and -0.52, for OSIRIS and WACCM, respectively, $p < 0.01$) are found between the global K column density and SABER temperatures at 87 and 90 km. Additionally, a weaker, but still highly significant, anti-correlation was found between K and the solar F10.7 flux (-0.25 and -0.19 again for OSIRIS and WACCM, respectively). In contrast, both the OSIRIS and WACCM Na column

density data indicate a positive correlation (approximately +0.33 and +0.49, respectively) with SABER temperature data for the same altitudes, and no overall correlation with the solar F10.7 flux. Overall, the Na layers exhibit a weak 11-year solar cycle response; during solar minimum conditions, reduced temperatures result in a decrease of the Na:NaHCO₃ balance, which is tempered by the associated decrease in photo-ionisation rates (increased relative Na:Na⁺ balance), and vice-versa during solar maximum conditions. In contrast, the reduced temperatures during solar minimum result in an enhancement of the K:K⁺ ratio, which is further enhanced by the reduced rates of photo-ionisation. During solar maximum conditions, the increased rate of photo-ionisation result in a reduction of the K:K⁺ ratio. This trend is reinforced by the warmer temperatures, which prevent K⁺ forming clusters and then being neutralized by dissociative electron recombination. These results support the different temperature responses discussed above.

6. WACCM data was used to examine the response of the K, Na and Fe metal layers to longer-term changes within the MLT region, over a 50-yr period (1955-2005). K is the only modelled metal to exhibit a pronounced response to the long-term cooling trends which have occurred as a result of increasing concentrations of CO₂ and changes to the stratospheric O₃ layer over this period. The underlying mechanism for this is that while Na and Fe are both positively correlated with temperature, K exhibits an anti-correlation with temperature due to the ion molecule chemistry, and the long-term response of K to temperature ($\delta K/\delta T$) is approximately -6% K⁻¹.
7. Across the 50-year period, changes in the centroid altitude for K and Na are predicted to be minimal, with a maximum change of 2-3%. Fe exhibits a more complicated latitude-specific trend, and this is likely as a result of both its lower peak layer height (as a result of differential ablation) and latitude-specific changes in chemical species relevant to it. Changes in the longer-term modelled layer-width (RMS-width) are an order of magnitude larger for K than for either Na or Fe. Both

the Na and K layers exhibit a decrease in their RMS-widths in response to the changing MLT climate.

These points have achieved the specific aims set out in Chapter 1,; namely: producing and validating the first near-global satellite K dataset, assessing the extent of the semi-annual seasonality in K, the sensitivity of the K layer to a number of atmospheric phenomena, and examining whether the metals are sensitive to both the 11-year solar cycle and longer-term atmospheric changes across a 50-yr period.

7.2 Recommendations

Future work could include extending the Na and K datasets for as long as the Odin/OSIRIS instrument remains in operation. A clear limitation of the solar cycle work presented here is that the available OSIRIS data period does not extend over a full 11-year solar cycle. This, combined with the unusually weak solar cycle, and the high inter-annual variability seen within the OSIRIS metal datasets, mean that all correlation results are indicative only. An extended OSIRIS dataset will allow a more robust comparison, although many more years would be necessary. An independent K retrieval is currently in development which uses data from the NASA Upper Atmospheric Research Satellite (UARS). Launched in September 1991, UARS remained in operation for 14 years before it was decommissioned in December 2005. The combination of K time-series from different instruments presents a lot of new challenges, but a combination of these datasets could provide a dataset of >21 years which would be more suitable for this type of analysis.

A couple of applications of the new OSIRIS K dataset were presented in Chapter 5: detection of the depletion of the K layer polar mesospheric clouds (PMC), and an apparent correlation between the occurrence of sporadic K and sporadic *E* layers. Both of these offer scope for future work. The OSIRIS data can be used to assess the seasonal and latitudinal extent of PMCs via their depletion of the K layer. This indirect data can be compared with direct measurements of PMCs by lidar and space-borne instruments such as the SOFIE instrument (Solar Occultation for Ice Instrument) on-board the AIM

(Aeronomy of Ice in the Mesosphere) satellite. It is likely that the indirect OSIRIS PMC observations may form a complementary dataset for the study of PMCs. Additionally, the dataset can be used to validate a future run of the WACCM model which will include PMC chemistry.

Further work can also be done on assessing the spatio-temporal occurrence correlation between sporadic K (K_s) and sporadic E (E_s). Some differences exist between the occurrence of OSIRIS Na_s and K_s ; Fan *et al.* (2007b) found that Na_s were more prevalent in the southern hemisphere, but the opposite was true for the K_s layer. Additionally, the global percentage occurrence frequency was found in this thesis to be higher for K_s (~12%) than the ~5% value reported by Fan *et al.* [2007b] for Na_s . Further examination of the nature of these differences may prove fruitful in identifying the relative importance of other mechanisms for the production of sporadic metal layers, e.g. the dissociation of metal reservoir species [von Zahn and Murad, 1990], the sputtering of metal atoms from cosmic dust particles [von Zahn *et al.*, 1987; Beatty *et al.*, 1989] or temperature fluctuations which produce an enhancement from some unknown source [Zhou *et al.*, 1993].

Future improvements to the OSIRIS K retrieval will be carried out. Due to the challenge of the retrieval of K, very strict quality control criteria were imposed so as to only consider the best possible spectra from the start. This meant that only limb spectra with associated errors that fell within the 1.5σ mean error cut-off criteria were considered. Future work will examine the impact of relaxing such quality-control criteria and enhancing and extending the existing OSIRIS K dataset.

Satellite datasets now exist for Na, Mg and K. As Fe is both the most abundant metal in the MLT and a major constituent of meteoroids, it would be highly desirable to develop an Fe layer retrieval in the future. Work has been performed (not shown in this thesis) on trying to extract information on the Fe layer at 372 nm, which was found to be the most prominent emission feature in the OSIRIS spectra. However this is an extremely difficult problem, due to the presence of other strong lines and very prominent Fraunhofer line features within this wavelength region. Only single-scattering is considered within the K

retrieval, but the explicit treatment of multiple scattering may help solve this problem. This is likely to be a significant piece of research.

Finally, it may be possible to use the OSIRIS Na and K datasets to provide a further constraint on the influx of cosmic dust entering the Earth's atmosphere. This can be done via comparison of the satellite observations with a model, to determine the total flux of ablated material. However, due to the critical dependence of any such result on the strength of vertical transport in the model, this is likely to be a significant amount of work.

7.3 Concluding remarks

Overall, this work has developed a new K dataset, which has been used to show that the semi-annual seasonal behaviour - previously only seen at a limited number of lidar stations - is near-global in extent. The OSIRIS K dataset has been used to validate WACCM with a new module for K chemistry as described in Plane *et al.* [2014a]. Consistent differences are shown between the observed and modelled K and Na (and modelled Fe) layers at all temporal scales, as a result of the unique chemistry of K. Study of the MLT region is gaining prominence as the sensitivity of this region to anthropogenic climate change is being recognised. In response to this, the upper altitude limits of atmospheric circulation models are being increased. This new K dataset can now be utilised to the fullest extent, investigating various phenomena via their interaction with the mesospheric metal layers and also being used to validate such models by using the metal layers as tracers. The ultimate aim of this is to improve our understanding of this fascinating, but much neglected, region and to develop a more complete understanding of processes affecting our atmosphere as a whole.

8 REFERENCES

- Akmaev, R. A., & Fomichev, V. I. (2000). A model estimate of cooling in the mesosphere and lower thermosphere due to the CO₂ increase over the last 3–4 decades. *Geophysical Research Letters*, 27(14), 2113-2116.
- Akmaev, R. A., (2002). Modeling the cooling due to CO₂ increases in the mesosphere and lower thermosphere. *Physics and Chemistry of the Earth, Parts A/B/C*, 27(6-8), 521–528.
- Akmaev, R. A., Fomichev, V. I., and Zhu, X. (2006). Impact of middle-atmospheric composition changes on greenhouse cooling in the upper atmosphere. *Journal of Atmospheric and Solar-Terrestrial Physics*, 68(17), 1879–1889.
- Akmaev, R. A. (2011). Whole Atmosphere Modeling: connecting terrestrial and space. *Review of Geophysics*, 49, RG4004.
- Allen, M., Yung, Y. L., & Waters, J. W. (1981). Vertical transport and photochemistry in the terrestrial mesosphere and lower thermosphere (50–120 km). *Journal of Geophysical Research: Space Physics (1978–2012)*, 86(A5), 3617-3627.
- Alpers, M., Höffner, J., and von Zahn, U. (1990). Iron atom densities in the polar mesosphere from lidar observations. *Geophysical Research Letters*, 17(13), 2345-2348.
- Alpers, M., Gerding, M., Höffner, J., and Schneider, J. (2001). Multiwavelength lidar observation of a strange noctilucent cloud at Kühlungsborn, Germany (54°N). *Journal of Geophysical Research: Atmospheres (1984–2012)*, 106(D8), 7945-7953.
- Batista, P. P., Clemesha, B. R., Batista, I. S., and Simonich, D. M. (1989). Characteristics of the sporadic sodium layers observed at 23 S. *Journal of Geophysical Research: Space Physics (1978–2012)*, 94(A11), 15349-15358.

- Batista, P. P., Clemesha, B. R., and Simonich, D. M. (2009). A 14-year monthly climatology and trend in the 35–65km altitude range from Rayleigh LIDAR temperature measurements at a low latitude station. *Journal of Atmospheric and Solar-Terrestrial Physics*, *71*(13), 1456-1462.
- Baumgaertner, A. J. G., McDonald, A. J., Fraser, G. J., and Plank, G. E. (2005). Long-term observations of mean winds and tides in the upper mesosphere and lower thermosphere above Scott Base, Antarctica. *Journal of Atmospheric and Solar-Terrestrial Physics*, *67*(16), 1480–1496.
- Beatty, T. J., Collins, R. L., Gardner, C. S., Hostetler, C. A., Sechrist, C. F., and Tepley, C. A. (1989). Simultaneous radar and lidar observations of sporadic E and Na layers at Arecibo. *Geophysical Research Letters*, *16*(9), 1019-1022.
- Beig, G. (2003). Trends in the mesopause region temperature and our present understanding - an update. *Physics and Chemistry of the Earth*, *31*, 3–9. doi:10.1029/2002RG000121.
- Beig, G. (2011). Long-term trends in the temperature of the mesosphere/lower thermosphere region: 1. Anthropogenic influences. *Journal of Geophysical Research*, *116*, A00H11. doi:10.1029/2011JA016646.
- Beig, G., Fadnavis, S., Schmidt, H., and Brasseur, G. P. (2012). Inter-comparison of 11-year solar cycle response in mesospheric ozone and temperature obtained by HALOE satellite data and HAMMONIA model. *Journal of Geophysical Research*, *117*, D00P10.
- Bernard, R. (1939). The Identification and the Origin of Atmospheric Sodium. *The Astrophysical Journal*, *89*, 133.
- Bittner, M., Offermann, D., Graef, H.-H., Donner, M., and Hamilton, K. (2002). An 18-year time series of OH rotational temperatures and middle atmosphere decadal variations. *Journal of Atmospheric and Solar-Terrestrial Physics*, *64*, 1147–1166.

- Blamont, J. E., and Donahue, T. M. (1961). The dayglow of the sodium D lines. *Journal of Geophysical Research*, 66(5), 1407-1423.
- Bowman, M. R., Gibson, A. J., and Sandford, M. C. W. (1969). Observation of mesospheric Na atoms by tuner laser radar. *Nature*, 221, 456-458.
- Brasseur, G., & Solomon, S. (1984). *Aeronomy of the Middle Atmosphere, Chemistry and Physics of the Stratosphere and Mesosphere-D*.
- Bremer, J. (1997). Long-term trends in the meso- and thermosphere. *Advances in Space Research*, 20(11), 2075–2083. doi:10.1016/S0273-1177(97)00598-X
- Bremer, J., Schminder, R., Greisiger, K. M., Hoffmann, P., Kürschner, D., & Singer, W. (1997). Solar cycle dependence and long-term trends in the wind field of the mesosphere/lower thermosphere. *Journal of Atmospheric and Solar-Terrestrial Physics*, 59(5), 497–509. doi:10.1016/S1364-6826(96)00032-6
- Bremer, J., & Berger, U. (2002). Mesospheric temperature trends derived from ground-based LF phase-height observations at mid-latitudes: comparison with model simulations. *Journal of atmospheric and solar-terrestrial physics*, 64(7), 805-816.
- Bremer, J., & Peters, D. (2008). Influence of stratospheric ozone changes on long-term trends in the meso- and lower thermosphere. *Journal of Atmospheric and Solar-Terrestrial Physics*, 70(11), 1473-1481.
- Bremer, J., Hoffmann, P., Latteck, R., Singer, W., & Zecha, M. (2009). Long-term changes of (polar) mesosphere summer echoes. *Journal of Atmospheric and Solar-Terrestrial Physics*, 71(14), 1571-1576.
- Cabannes, J., Dufay, J., & Gauzit, J. (1938). Sur la presence du sodium dans la haute atmosphere. *CR Acad. Sci. Paris*, 206, 807-872.
- Ceplecha, Z., Borovička, J., Elford, W. G., ReVelle, D. O., Hawkes, R. L., Porubčan, V., & Šimek, M. (1998). Meteor phenomena and bodies. *Space Science Reviews*, 84(3-4), 327-471.

- Chamberlain, J. W., & Negaard, B. J. (1956). Resonance scattering by atmospheric sodium—II Nightglow theory. *Journal of Atmospheric and Terrestrial Physics*, 9(4), 169-178.
- Chamberlain, J. W., Hunten, D. M., & Mack, J. E. (1958). Resonance scattering by atmospheric sodium—IV abundance of sodium in twilight. *Journal of Atmospheric and Terrestrial Physics*, 12(2), 153-165.
- Chamberlain, J. W., *Physics of the Aurora and Airglow*, Academic Press, New York, 1961.
- Chance, K. V., and Spurr, R. J. (1997). Ring effect studies: Rayleigh scattering, including molecular parameters for rotational Raman scattering, and the Fraunhofer spectrum. *Applied Optics*, 36(21), 5224-5230.
- Chance, K., and Kurucz, R. L. (2010). An improved high-resolution solar reference spectrum for Earth's atmosphere measurements in the ultraviolet, visible, and near infrared. *Journal of Quantitative Spectroscopy and Radiative Transfer*, 111(9), 1289-1295.
- Chandra, S., Jackman, C. H., Fleming, E. L., and Russell, J. M. (1997). The Seasonal and Long Term Changes in Mesospheric Water Vapor. *Geophysical Research Letters*, 24(6), 639–642.
- Chandrasekhar, S. (1960). *Radiative transfer*. Courier Dover Publications. New York.
- Chiou, E. W., *et al.* (2014). Comparison of profile total ozone from SBUV (v8.6) with GOME-type and ground-based total ozone for a 16-year period (1996 to 2011). *Atmospheric Measurement Techniques*, 7(6), 1681–1692.
- Chu, X., Huang, W., Fong, W., Yu, Z., Wang, Z., Smith, J. A., and Gardner, C. S. (2011). First lidar observations of polar mesospheric clouds and Fe temperatures at McMurdo (77.8 S, 166.7 E), Antarctica. *Geophysical Research Letters*, 38(16).

- Chu, Y. H., *et al.* (2014). Morphology of sporadic E layer retrieved from COSMIC GPS radio occultation measurements: Wind shear theory examination. *Journal of Geophysical Research: Space Physics*, 119(3), 2117-2136.
- Clemesha, B. R., Kirchhoff, V. W. J. H., Simonich, D. M., and Takahashi, H. (1978). Evidence of an extra-terrestrial source for the mesospheric sodium layer. *Geophysical Research Letters*, 5(10), 873-876.
- Clemesha, B. R., Kirchhoff, V. W. J. H., and Simonich, D. M. (1979). Concerning the seasonal variation of the mesospheric sodium layer at low-latitudes. *Planetary and Space Science*, 27(6), 909-910.
- Clemesha, B.R., Simonich, D.M., Batista, P.P. and Kirchoff, V.W.J.H. (1982). The diurnal variation of atmospheric sodium. *Journal of Geophysical Research*, 87(A1):181-186.
- Clemesha, B.R., Batista, P.P. and Simonich, D.M. (1988). Concerning the origin of enhanced sodium layers. *Geophysical Research Letters* 15(11):1267-1270.
- Clemesha, B. R., Simonich, D. M., and Batista, P. P. (1992). A long-term trend in the height of the atmospheric sodium layer: possible evidence for global change. *Geophysical Research Letters*, 19(5), 457–460.
- Clemesha, B. R. (1995). Sporadic neutral metal layers in the mesosphere and lower thermosphere. *Journal of Atmospheric and Terrestrial Physics*, 57(7), 725-736.
- Clemesha, B. R., Batista, P. P., and Simonich, D. M. (2003). Long-term variations in the centroid height of the atmospheric sodium layer. *Advances in Space Research*, 32(9), 1707-1711.
- Clemesha, B. R., Batista, P. P., Simonich, D. M., and Batista, I. S. (2004). Sporadic structures in the atmospheric sodium layer. *Journal of Geophysical Research: Atmospheres (1984–2012)*, 109(D11).

- Cnossen, I., and Richmond, A. D. (2008). Modelling the effects of changes in the Earth's magnetic field from 1957 to 1997 on the ionospheric hmF2 and foF2 parameters. *Journal of Atmospheric and Solar-Terrestrial Physics*, 70(11-12), 1512–1524.
- Collins, S. C., *et al.* (2002). A study of the role of ion–molecule chemistry in the formation of sporadic sodium layers. *Journal of Atmospheric and Solar-Terrestrial physics*, 64(7), 845-860.
- Collis, P. N., and Turunen, T. (1987). Horizontal extent and vertical motions of a mid-latitude sporadic E-layer observed by EISCAT. *Physica Scripta*, 35(6), 883.
- Cox, R. M., and Plane, J. M. (1997). An experimental and theoretical study of the clustering reactions between Na⁺ ions and N₂, O₂ and CO₂. *Journal of the Chemical Society, Faraday Transactions*, 93(16), 2619-2629.
- Cox, R. M., and Plane, J. (1998). An ion-molecule mechanism for the formation of neutral sporadic Na layers. *Journal of Geophysical Research: Atmospheres (1984–2012)*, 103(D6), 6349-6359.
- Cox, R. M., Self, D. E., and Plane, J. (2001). A study of the reaction between NaHCO₃ and H: Apparent closure on the chemistry of mesospheric Na. *Journal of Geophysical Research: Atmospheres (1984–2012)*, 106(D2), 1733-1739.
- Curtius, J., *et al.* (2005). Observations of meteoric material and implications for aerosol nucleation in the winter Arctic lower stratosphere derived from in situ particle measurements. *Atmospheric Chemistry and Physics*, 5(11), 3053-3069.
- Cziczo, D. J., Thomson, D. S., and Murphy, D. M. (2001). Ablation, flux, and atmospheric implications of meteors inferred from stratospheric aerosol. *Science*, 291(5509), 1772-1775.
- Daire, S.E., Plane, J.M.C., Gamblin, S.D., Soldan, P., Lee, E.P.F. and Wright, T.G. (2002). A theoretical study of the ligand-exchange reactions of Na⁺.X complexes (X

- = O, O₂, N₂, CO₂ and H₂O): Implications for the upper atmosphere. *Journal of Atmospheric and Solar-Terrestrial Physics* 64:861-865.
- Dee, D. P., *et al.* (2011). The ERA-Interim reanalysis: Configuration and performance of the data assimilation system. *Quarterly Journal of the Royal Meteorological Society*, 137(656), 553-597.
- DeLand, M. T., Shettle, E. P., Thomas, G. E., and Olivero, J. J. (2006). A quarter-century of satellite polar mesospheric cloud observations. *Journal of Atmospheric and Solar-Terrestrial Physics*, 68(1), 9-29.
- Delgado, R., Weiner, B. R., and Friedman, J. S. (2006). Chemical model for mid-summer lidar observations of mesospheric potassium over the Arecibo Observatory. *Geophysical research letters*, 33(2).
- Delgado, R. (2011). Observations and modeling of sporadic metal layers over the Arecibo Observatory. *PhD thesis*.
- Delgado, R., Friedman, J. S., Fentzke, J. T., Raizada, S., Tepley, C. A., & Zhou, Q. (2012). Sporadic metal atom and ion layers and their connection to chemistry and thermal structure in the mesopause region at Arecibo. *Journal of Atmospheric and Solar-Terrestrial Physics*, 74, 11–23. doi:10.1016/j.jastp.2011.09.004
- Donahue, T. M., and Meier, R. R. (1967). Distribution of sodium in the daytime upper atmosphere as measured by a rocket experiment. *Journal of Geophysical Research*, 72(11), 2803-2829.
- Ern, M., Preusse, P., Alexander, M. J., and Warner, C. D. (2004). Absolute values of gravity wave momentum flux derived from satellite data. *Journal of Geophysical Research: Atmospheres (1984–2012)*, 109(D20).
- Eska, V., Höffner, J., and von Zahn, U. (1998). Upper atmosphere potassium layer and its seasonal variations at 54°N. *Journal of Geophysical Research*, 103, 29207–29214.

- Eska, V., and von Zahn, U. (1999). The terrestrial potassium layer (75-110 km) between 71°S and 54°N: Observations and modeling. *Journal of Geophysical Research*, *104*, 17173–17186.
- Fahrutdinova, A. N., Ganin, V. A., Berdunov, N. V., Ishmuratov, R. A., and Hutorova, O. G. (1997). Long-term variations of circulation in the mid-latitude upper mesosphere-lower thermosphere. *Advances in Space Research*, *20*(6), 1161–1164.
- Fan, Z. Y., Plane, J. M. C., and Gumbel, J. (2007a). On the global distribution of sporadic sodium layers. *Geophysical Research Letters*, *34*(15), L15808.
- Fan, Z. Y., Plane, J. M. C., Gumbel, J., Stegman, J., and Llewellyn, E. J. (2007b). Satellite measurements of the global mesospheric sodium layer. *Atmospheric Chemistry and Physics Discussions*, *7*(2), 5413–5437.
- Feng, W., Marsh, D. R., Chipperfield, M. P., Janches, D., Höffner, J., Yi, F., and Plane, J. M. C. (2013). A global atmospheric model of meteoric iron. *Journal of Geophysical Research: Atmospheres*, *118*(16), 9456–9474.
- Fiedler, J., Baumgarten, G., and von Cossart, G. (2003). Noctilucent clouds above ALOMAR between 1997 and 2001: Occurrence and properties. *Journal of Geophysical Research: Atmospheres (1984–2012)*, *108*(D8).
- Fioletov, V. E., Bodeker, G. E., Miller, A. J., McPeters, R. D., and Stolarski, R. (2002). Global and zonal total ozone variations estimated from ground-based and satellite measurements: 1964–2000. *Journal of Geophysical Research: Atmospheres*, *107*(D22), 4647.
- Fleming, E. L., Chandra, S., Barnett, J. J., and Corney, M. (1990). Zonal mean temperature, pressure, zonal wind and geopotential height as functions of latitude. *Advances in Space Research*, *10*(12), 11-59.
- Forbes, J. M. (1995). Tidal and planetary waves. *The upper mesosphere and lower thermosphere: a review of experiment and theory*, 67-87.

- Forbes, J. M., Zhang, X., and Marsh, D. R. (2014). Solar cycle dependence of middle atmosphere temperatures. *Journal of Geophysical Research: Atmospheres*.
- Fraser, G. J. (1990). Long-term variations in mid-latitude southern hemisphere mesospheric winds. *Advances in Space Research*, 10(10), 247–250.
- French, W. J. R., and Burns, G. B. (2004). The influence of large-scale oscillations on long-term trend assessment in hydroxyl temperatures over Davis, Antarctica. *Journal of atmospheric and solar-terrestrial physics*, 66(6), 493-506.
- Fricke-Begemann, C., Höffner, J., and von Zahn, U. (2002). The potassium density and temperature structure in the mesopause region (80–105 km) at a low latitude (28 N). *Geophysical research letters*, 29(22), 24-1.
- Friedman, J. S., Collins, S. C., Delgado, R., and Castleberg, P. A. (2002). Mesospheric potassium layer over the Arecibo Observatory, 18.3 N 66.75 W. *Geophysical Research Letters*, 29(5), 15-1.
- Fritts, D. C., and Alexander, M. J. (2003). Gravity wave dynamics and effects in the middle atmosphere. *Reviews of Geophysics*, 41(1).
- Fröhlich, C., and Lean, J. (1998). The Sun's total irradiance: Cycles, trends and related climate change uncertainties since 1976. *Geophysical Research Letters*, 25(23), 4377-4380.
- Fussen, D. (2004). Global measurement of the mesospheric sodium layer by the star occultation instrument GOMOS. *Geophysical Research Letters*, 31(24), L24110.
- Fussen, D., *et al.* (2010). A global climatology of the mesospheric sodium layer from GOMOS data during the 2002–2008 period. *Atmospheric Chemistry and Physics*, 10(19), 9225–9236.
- Gabrielli, P., *et al.* (2004). Meteoric smoke fallout over the Holocene epoch revealed by iridium and platinum in Greenland ice. *Nature*, 432(7020), 1011-1014.

- Garcia, R. R. (1989). Dynamics, radiation, and photochemistry in the mesosphere: Implications for the formation of noctilucent clouds. *Journal of Geophysical Research: Atmospheres (1984–2012)*, *94*(D12), 14605-14615.
- Garcia, R. R., and Boville, B. A. (1994). “Downward control” of the mean meridional circulation and temperature distribution of the polar winter stratosphere. *Journal of the Atmospheric Sciences*, *51*(15), 2238-2245.
- Garcia, R. R., Lieberman, R., Russell III, J. M., and Mlynczak, M. G. (2005). Large-scale waves in the mesosphere and lower thermosphere observed by SABER. *Journal of the Atmospheric Sciences*, *62*(12), 4384-4399.
- Garcia, R. R., Marsh, D. R., Kinnison, D. E., Boville, B. A., and Sassi, F. (2007). Simulation of secular trends in the middle atmosphere, 1950–2003. *Journal of Geophysical Research*, *112*, D09301.
- Gardner, C. S., Voelz, D. G., Philbrick, C. R., and Sipler, D. P. (1986). Simultaneous lidar measurements of the sodium layer at the Air Force Geophysics Laboratory and the University of Illinois. *Journal of Geophysical Research: Space Physics (1978–2012)*, *91*(A11), 12131-12136.
- Gardner, C. S., Senft, D. C., and Kwon, K. H. (1988). Lidar observations of substantial sodium depletion in the summertime Arctic mesosphere. *Nature*. 332:142-144.
- Gardner, C. S., Kane, T. J., Senft, D. C., Qian, J., and Papen, G. C. (1993). Simultaneous observations of sporadic E, Na, Fe, and Ca⁺ layers at Urbana, Illinois: Three case studies. *Journal of Geophysical Research: Atmospheres (1984–2012)*, *98*(D9), 16865-16873.
- Gardner, J. A., Viereck, R. A., Murad, E., Knecht, D. J., Pike, C. P., Broadfoot, A. L., and Anderson, E. R. (1995). Simultaneous observations of neutral and ionic magnesium in the thermosphere. *Geophysical Research Letters*, *22*(16), 2119–2122.
- Gardner, C. S., Plane, J., Pan, W., Vondrak, T., Murray, B. J., and Chu, X. (2005). Seasonal variations of the Na and Fe layers at the South Pole and their implications

- for the chemistry and general circulation of the polar mesosphere. *Journal of Geophysical Research: Atmospheres* (1984–2012), 110(D10).
- Gardner, C. S., and Liu, A. Z. (2010). Wave-induced transport of atmospheric constituents and its effect on the mesospheric Na layer. *Journal of Geophysical Research: Atmospheres* (1984–2012), 115(D20).
- Gardner, C. S., Chu, X., Espy, P. J., Plane, J. M. C., Marsh, D. R., and Janches, D. (2011). Seasonal variations of the mesospheric Fe layer at Rothera, Antarctica (67.5°S, 68.0°W). *Journal of Geophysical Research*, 116(D2), D02304.
- Gavrilov, N. M., Fukao, S., and Nakamura, T. (1999). Peculiarities of interannual changes in the mean wind and gravity wave characteristics in the mesosphere over Shigaraki, Japan. *Geophysical Research Letters*, 26(16), 2457–2460.
- Gavrilov, N. M., Fukao, S., Nakamura, T., Jacobi, C., Kürschner, D., Manson, A. H., and Meek, C. E. (2002). Comparative study of interannual changes of the mean winds and gravity wave activity in the middle atmosphere over Japan, Central Europe and Canada. *Journal of Atmospheric and Solar-Terrestrial Physics*, 64(8), 1003-1010.
- Gerding, M., Alpers, M., Höffner, J., and Zahn, U. V. (1999). Sporadic Ca and Ca⁺ layers at mid-latitudes: Simultaneous observations and implications for their formation. In *Annales geophysicae* (Vol. 19, No. 1, pp. 47-58). Copernicus GmbH.
- Gerding, M., Alpers, M., Zahn, U. V., Rollason, R. J., and Plane, J. M. C. (2000). Atmospheric Ca and Ca⁺ layers: Midlatitude observations and modeling. *Journal of Geophysical Research: Space Physics* (1978–2012), 105(A12), 27131-27146.
- Gibson, A. J., and Sandford, M. C. W. (1971). The seasonal variation of the night-time sodium layer. *Journal of Atmospheric and Terrestrial Physics*, 33(11), 1675-1684.
- Gleissberg, W. (1967). Secularly smoothed data on the minima and maxima of sunspot frequency. *Solar Physics*, 2(2), 231-233.

- Golitsyn, G. S., Semenov, A. I., Shefov, N. N., and Khomich, V. Y. (2006). The response of middle-latitude atmospheric temperature on the solar activity during various seasons. *Physics and Chemistry of the Earth, Parts A/B/C*, 31(1), 10-15.
- Grainger, J. F., and Ring, J. (1962). Anomalous Fraunhofer line profiles. *Nature*, 193, 762.
- Gruzdev, A. N., and Brasseur, G. P. (2005). Long-term changes in the mesosphere calculated by a two-dimensional model. *Journal of Geophysical Research: Atmospheres (1984–2012)*, 110(D3).
- Gumbel, J., Fan, Z. Y., Waldemarsson, T., Stegman, J., Witt, G., Llewellyn, E. J., and Plane, J. M. C. (2007). Retrieval of global mesospheric sodium densities from the Odin satellite. *Geophysical Research Letters*, 34(4), L04813.
- Hansen, G., and Von Zahn, U. (1990). Sudden sodium layers in polar latitudes. *Journal of Atmospheric and Terrestrial physics*, 52(6), 585-608.
- Haley, C. S., et al. (2004). Retrieval of stratospheric O₃ and NO₂ profiles from Odin Optical Spectrograph and Infrared Imager System (OSIRIS) limb-scattered sunlight measurements. *Journal of Geophysical Research: Atmospheres (1984–2012)*, 109(D16).
- Hartogh, P., Jarchow, C., and Hallgren, K. (2013). Investigations of the Solar Influence on Middle Atmospheric Water Vapour and Ozone During the Last Solar Cycle - Analysis of the MPS Data Set. In F.-J. Lübken (Ed.), *Climate and Weather of the Sun-Earth System (CAWSES)* (pp. 109–124). Springer Netherlands.
- Hartogh, P., Sonnemann, G. R., Grygalashvily, M., Song, L., Berger, U., and Lübken, F.-J. (2010). Water vapor measurements at ALOMAR over a solar cycle compared with model calculations by LIMA. *Journal of Geophysical Research*, 115, D00I17.
- Hedin, A. E. (1991). Extension of the MSIS thermosphere model into the middle and lower atmosphere. *Journal of Geophysical Research: Space Physics (1978–2012)*, 96(A2), 1159-1172.

- Hedin, J., and Gumbel, J. (2011). The global mesospheric sodium layer observed by Odin/OSIRIS in 2004–2009. *Journal of Atmospheric and Solar-Terrestrial Physics*, 73(14), 2221-2227.
- Heinselman, C. J. (2000). Auroral effects on the gas phase chemistry of meteoric sodium. *Journal of Geophysical Research: Atmospheres (1984–2012)*, 105(D10), 12181-12192.
- Hervig, M. E., *et al.* (2009). First satellite observations of meteoric smoke in the middle atmosphere. *Geophysical Research Letters*, 36(18).
- Höffner, J., Fricke-Begemann, C., and Lübken, F. J. (2003). First observations of noctilucent clouds by lidar at Svalbard, 78 N. *Atmospheric Chemistry and Physics*, 3(4), 1101-1111.
- Höffner, J., and Lübken, F.-J. (2007). Potassium lidar temperatures and densities in the mesopause region at Spitsbergen (78°N). *Journal of Geophysical Research*, 112(D20), D20114.
- Holmen, S. E., Dyrland, M. E., and Sigernes, F. (2014). Long-term trends and the effect of solar cycle variations on mesospheric winter temperatures over Longyearbyen, Svalbard (78 N). *Journal of Geophysical Research: Atmospheres*, 119, 6596–6608.
- Holton, J. R. (1983). The influence of gravity wave breaking on the general circulation of the middle atmosphere. *Journal of the Atmospheric Sciences*, 40(10), 2497-2507.
- Hughes, D. W. (1978). Meteors. *Cosmic dust*, 1, 123-185.
- Hunten, D. M. (1954). A study of sodium in twilight. I. Theory. *Journal of Atmospheric and Terrestrial Physics*, 5(1), 44-56.
- Hunten, D. M., and Shepherd, G. G. (1954). A study of sodium in twilight. II. Observations on the distribution. *Journal of Atmospheric and Terrestrial Physics*, 5(1), 57-62.

- Hunten, D. M. (1967). Spectroscopic studies of the twilight airglow. *Space Science Reviews*, 6(4), 493-573.
- Hunten, D. M., Turco, R. P., and Toon, O. B. (1980). Smoke and dust particles of meteoric origin in the mesosphere and stratosphere. *Journal of the Atmospheric Sciences*, 37(6), 1342-1357.
- Jacobi, C., Hoffmann, P., and Kürschner, D. (2008). Trends in MLT region winds and planetary waves, Collm (52 N, 15 E). In *Annales Geophysicae* (Vol. 26, No. 5, pp. 1221-1232). Copernicus GmbH.
- Jacobi, C. (2013). Long-term trends and decadal variability of upper mesosphere/lower thermosphere gravity waves at midlatitudes. *Journal of Atmospheric and Solar-Terrestrial Physics*, 118, 90–95.
- Kane, T. J., and Gardner, C. S. (1993). Lidar observations of the meteoric deposition of mesospheric metals. *Science*, 259(5099), 1297–1300.
- Keating, G. M., Tolson, R. H., and Bradford, M. S. (2000). Evidence of long term global decline in the Earth's thermospheric densities apparently related to anthropogenic effects. *Geophysical Research Letters*, 27(10), 1523–1526.
- Keckhut, P., Hauchecorne, A., and Chanin, M. L. (1995). Midlatitude long-term variability of the middle atmosphere: Trends and cyclic and episodic changes. *Journal of Geophysical Research: Atmospheres*, 100(D9), 18887–18897.
- Keckhut, P., Schmidlin, F. J., Hauchecorne, A., and Chanin, M. L. (1999). Stratospheric and mesospheric cooling trend estimates from US rocketsondes at low latitude stations (8 S–34 N), taking into account instrumental changes and natural variability. *Journal of Atmospheric and Solar-Terrestrial Physics*, 61(6), 447-459.
- Keckhut, P., *et al.* (2011). An evaluation of uncertainties in monitoring middle atmosphere temperatures with the ground-based lidar network in support of space observations. *Journal of Atmospheric and Solar-Terrestrial Physics*, 73(5-6), 627–642.

- Kirchhoff, V. W. J. H., and Clemesha, B. R. (1983). The atmospheric neutral sodium layer: 2. Diurnal variations. *Journal of Geophysical Research: Space Physics* (1978–2012), 88(A1), 442-450.
- Kirkwood, S., and Collis, P. N. (1989). Gravity wave generation of simultaneous auroral sporadic E layers and sudden neutral sodium layers. *Journal of Atmospheric and Terrestrial Physics*, 51(4), 259-269.
- Kirkwood, S., Dalin, P., and Réchou, A. (2008). Noctilucent clouds observed from the UK and Denmark – trends and variations over 43 years. *Annales Geophysicae*, 26, 1243–1254.
- Kramida, A., Ralchenko, Y., and Reader, J. (2012). NIST Atomic Spectra Database (ver. 5.0), 2013. *National Institute of Standards and Technology, Gaithersburg, MD, USA. Available online: <http://physics.nist.gov/asd> (accessed on 3 January 2014).*
- Kubicki, A., Keckhut, P., Chanin, M.-L., Hauchecorne, A., Lysenko, E., and Golitsyn, G. S. (2006). Temperature trends in the middle atmosphere as seen by historical Russian rocket launches: Part 1, Volgograd (48.68° N, 44.35° E). *Journal of Atmospheric and Solar-Terrestrial Physics*, 68(10), 1075–1086.
- Kwon, K.H., Senft, D.C. and Gardner, C.S. (1988). Lidar observations of sporadic sodium layers at Mauna Kea observatory, Hawaii. *Journal of Geophysical Research*, 93(D11):14199-14208.
- Kyte, F. T., & Wasson, J. T. (1986). Accretion rate of extraterrestrial matter: Iridium deposited 33 to 67 million years ago. *Science*, 232(4755), 1225-1229.
- Lachlan-Cope, T. A., Connolley, W. M., Turner, J., Roscoe, H., Marshall, G. J., Colwell, S. R., Höpfner, M. and Ingram, W. (2009). Antarctic winter tropospheric warming—The potential role of polar stratospheric clouds, a sensitivity study. *Atmospheric Science Letters*, 10(4), 262-266.
- Lanci, L., and Kent, D. V. (2006). Meteoric smoke fallout revealed by superparamagnetism in Greenland ice. *Geophysical Research Letters*, 33(13).

- Lanci, L., Delmonte, B., Kent, D. V., Maggi, V., Biscaye, P. E., and Petit, J. R. (2012). Magnetization of polar ice: a measurement of terrestrial dust and extraterrestrial fallout. *Quaternary Science Reviews*, 33, 20-31.
- Langowski, M., Sinnhuber, M., Aikin, A. C., von Savigny, C., and Burrows, J. P. (2014a). Retrieval algorithm for densities of mesospheric and lower thermospheric metal atom and ion species from satellite-borne limb emission signals. *Atmospheric Measurement Techniques*, 7(1), 29–48.
- Langowski, M., von Savigny, C., Burrows, J. P., Feng, W., Plane, J. M. C., Marsh, D. R., Sinnhuber, M. and Aikin, A. C. (2014b). Global investigation of the Mg atom and ion layers using SCIAMACHY/Envisat observations between 70 km and 150 km altitude and WACCM-Mg model results. *Atmospheric Chemistry and Physics Discussions*, 14(2), 1971–2019.
- Laštovička, J. (2005). On the role of solar and geomagnetic activity in long-term trends in the atmosphere–ionosphere system. *Journal of Atmospheric and Solar-Terrestrial Physics*, 67(1-2), 83–92.
- Laštovička, J. (2006). Global change in the upper atmosphere. *Science*, 314(5803), 1253–1254.
- Laštovička, J., Akmaev, R. A., Beig, G., Bremer, J., Emmert, J. T., Jacobi, C., Jarvis, M.J., Nedoluha, G., Portnyagin, Y.I. and Ulich, T. (2008). Emerging pattern of global change in the upper atmosphere and ionosphere. *Annales Geophysicae*, 26, 1255–1268.
- Laštovička, J., Solomon, S. C., and Qian, L. (2012). Trends in the neutral and ionized upper atmosphere. *Space Science Reviews*, 168(1-4), 113-145.
- Latteck, R., and Bremer, J. (2013a). Long-term changes of polar mesosphere summer echoes at 69°N. *Journal of Geophysical Research: Atmospheres*, 118(18), 10,441–10,448. doi:10.1002/jgrd.50787

- Latteck, R., and Bremer, J. (2013b). Occurrence frequencies of polar mesosphere summer echoes observed at 69° N during a full solar cycle. *Advances in Radio Science*, 11(2006), 327–332.
- Leighton, H. I., Shapley, A. H., and Smith Jr, E. K. (1962). The occurrence of sporadic E during the IGY. *Ionospheric Sporadic E*, 1, 166.
- Llewellyn, E. J., et al. (2004). The OSIRIS instrument on the Odin spacecraft. *Canadian Journal of Physics*, 82(6), 411-422.
- Lockwood, M., Owens, M. J., Barnard, L., Davis, C. J., and Steinhilber, F. (2011). The persistence of solar activity indicators and the descent of the Sun into Maunder Minimum conditions. *Geophysical Research Letters*, 38(22).
- Love, S. G., and Brownlee, D. E. (1993). A direct measurement of the terrestrial mass accretion rate of cosmic dust. *Science*, 262(5133), 550-553.
- Lübken, F. J. (1999). Thermal structure of the Arctic summer mesosphere. *Journal of Geophysical Research: Atmospheres (1984–2012)*, 104(D8), 9135-9149.
- Lübken, F. J., and Höffner, J. (2004). Experimental evidence for ice particle interaction with metal atoms at the high latitude summer mesopause region. *Geophysical Research Letters*, 31(8).
- Lübken, F. J., Berger, U., Kiliani, J., Baumgarten, G., and Fiedler, J. (2013). Solar variability and trend effects in mesospheric ice layers. In *Climate And Weather of the Sun-Earth System (CAWSES)* (pp. 317-338). Springer Netherlands.
- Lübken, F. J., Berger, U., and Baumgarten, G. (2013). Temperature trends in the midlatitude summer mesosphere. *Journal of Geophysical Research: Atmospheres*, 118(24), 13-347.
- Macleod, M. A. (1966). Sporadic E theory. I. Collision-geomagnetic equilibrium. *Journal of the Atmospheric Sciences*, 23(1), 96-109.

- Marsh, D. R., Garcia, R. R., Kinnison, D. E., Boville, B. A., Sassi, F., Solomon, S. C., and Matthes, K. (2007). Modeling the whole atmosphere response to solar cycle changes in radiative and geomagnetic forcing. *Journal of Geophysical Research: Atmospheres (1984–2012)*, 112(D23).
- Marsh, D. R., Janches, D., Feng, W., and Plane, J. M. C. (2013). A global model of meteoric sodium. *Journal of Geophysical Research: Atmospheres*, 118(19), 11,442–11,452. doi:10.1002/jgrd.50870
- Mathews, J.D., Zhou, Q., Philbrick, C.R., Morton, Y.T. and Gardner, C.S. (1993). Observations of iron and sodium layer coupled processes during AIDA. *Journal of Atmospheric and Solar-Terrestrial Physics*, 55(3):487-498.
- Mathews, J. D., Janches, D., Meisel, D. D., and Zhou, Q. H. (2001). The micrometeoroid mass flux into the upper atmosphere: Arecibo results and a comparison with prior estimates. *Geophysical Research Letters*, 28(10), 1929-1932.
- McCracken, K. G., Beer, J., Steinhilber, F., and Abreu, J. (2013). A phenomenological study of the cosmic ray variations over the past 9400 years, and their implications regarding solar activity and the solar dynamo. *Solar Physics*, 286(2), 609-627.
- McLinden, C. A., McConnell, J. C., Griffioen, E., and McElroy, C. T. (2002). A vector radiative-transfer model for the Odin/OSIRIS project. *Canadian journal of physics*, 80(4), 375-393.
- McNutt, D. P., and Mack, J. E. (1963). Telluric absorption, residual intensities, and shifts in the Fraunhofer D lines. *Journal of Geophysical Research*, 68(11), 3419-3429.
- Megie, G., Allain, J. Y., Chanin, M. L., and Blamont, J. E. (1977). Vertical profile of stratospheric ozone by lidar sounding from the ground.
- Megie, G., and Blamont, J. E. (1977). Laser sounding of atmospheric sodium interpretation in terms of global atmospheric parameters. *Planetary and Space Science*, 25(12), 1093-1109.

- Megie, G., Bos, F., and Chanin, M. L. (1978). Simultaneous nighttime lidar measurements of atmospheric sodium and potassium. *Planetary Space Science*, 26, 27–35.
- Megner, L., Rapp, M., and Gumbel, J. (2006). Distribution of meteoric smoke—sensitivity to microphysical properties and atmospheric conditions. *Atmospheric Chemistry and Physics*, 6(12), 4415-4426.
- Merkel, A. W., Harder, J. W., Marsh, D. R., Smith, A. K., Fontenla, J. M., and Woods, T. N. (2011). The impact of solar spectral irradiance variability on middle atmospheric ozone. *Geophysical Research Letters*, 38(13), n/a–n/a. doi:10.1029/2011GL047561
- Mikhailov, A. V. (2002). The geomagnetic control concept of the F2-layer parameter long-term trends. *Physics and Chemistry of the Earth*, 27, 595–606. doi:10.1016/S1474-7065(02)00042-6
- Mlynczak, M. G., *et al.* (2010). Observations of infrared radiative cooling in the thermosphere on daily to multiyear timescales from the TIMED/SABER instrument. *Journal of Geophysical Research*, 115(A3), A03309.
- Molina, M. J., Zhang, R., Wooldridge, P. J., McMahon, J. R., Kim, J. E., Chang, H. Y., and Beyer, K. D. (1993). Physical chemistry of the H₂SO₄/HNO₃/H₂O system: Implications for polar stratospheric clouds. *Science*, 261(5127), 1418-1423.
- Morris, R., and Murphy, D. (2008). The polar mesosphere. *Physics Education*, 43(4), 366.
- Murphy, D. M., Thomson, D. S., and Mahoney, M. J. (1998). In situ measurements of organics, meteoritic material, mercury, and other elements in aerosols at 5 to 19 kilometers. *Science*, 282(5394), 1664-1669.
- Murtagh, D., *et al.* (2002). An overview of the Odin atmospheric mission. *Canadian Journal of Physics*, 80(4), 309-319.

- Nagasawa, C., and Abo, M. (1995). Lidar observations of a lot of sporadic sodium layers in mid-latitude. *Geophysical research letters*, 22(3), 263-266.
- Namboothiri, S. P., Manson, A. H., and Meek, C. E. (1993). Variations of mean winds and tides in the upper middle atmosphere over a solar cycle, Saskatoon, Canada, 52°N, 107°W. *Journal of Atmospheric and Terrestrial Physics*, 55(10), 1325–1334.
- Namboothiri, S. P., Meek, C. E., and Manson, A. H. (1994). Variations of mean winds and solar tides in the mesosphere and lower thermosphere over time scales ranging from 6 months to 11 yr: Saskatoon, 52°N, 107°W. *Journal of Atmospheric and Terrestrial Physics*, 56(10), 1313–1325.
- Nedoluha, G. E., Bevilacqua, M., Gomez, R. M., Siskind, D. E., Hicks, B. C., Russell, J. M., and Connor, B. J. (1998). Increases in middle atmospheric water vapor as observed by the Halogen Occultation Experiment and the ground-based Water Vapor Millimeter-wave Spectrometer from 1991 to 1997. *Journal of Geophysical Research*, 103, 3531–3543.
- Nedoluha, G. E., Gomez, R. M., Hicks, B. C., Wrotny, J. E., Boone, C., and Lambert, A. (2009). Water vapor measurements in the mesosphere from Mauna Loa over solar cycle 23. *Journal of Geophysical Research*, 114, D23303.
- Nedoluha, G. E., Michael Gomez, R., Allen, D. R., Lambert, A., Boone, C., and Stiller, G. (2013). Variations in middle atmospheric water vapor from 2004 to 2013. *Journal of Geophysical Research: Atmospheres*, 118(19), 11,285–11,293.
- Nesvorný, D., Janches, D., Vokrouhlický, D., Pokorný, P., Bottke, W. F., and Jenniskens, P. (2011). Dynamical model for the zodiacal cloud and sporadic meteors. *The Astrophysical Journal*, 743(2), 129.
- Newman, A. L. (1988). Nighttime Na D emission observed from a polar-orbiting DMSP satellite. *Journal of Geophysical Research: Space Physics (1978–2012)*, 93(A5), 4067-4075.

- Nielsen, K. P., Sigernes, F., Raustein, E., and Deehr, C. S. (2002). The 20-year change of the Svalbard OH-temperatures. *Physics and Chemistry of the Earth, Parts A/B/C*, 27(6), 555-561.
- Offermann, D., Donner, M., Knieling, P., and Naujokat, B. (2004). Middle atmosphere temperature changes and the duration of summer. *Journal of Atmospheric and Solar-Terrestrial Physics*, 66(6-9), 437-450.
- Offermann, D., Hoffmann, P., Knieling, P., Koppmann, R., Oberheide, J., and Steinbrecht, W. (2010). Long-term trends and solar cycle variations of mesospheric temperature and dynamics. *Journal of Geophysical Research*, 115(D18), D18127.
- Oikarinen, L. (2001). Polarization of light in UV-visible limb radiance measurements. *Journal of Geophysical Research: Atmospheres (1984-2012)*, 106(D2), 1533-1544.
- Olivero, J. J., and Thomas, G. E. (1986). Climatology of polar mesospheric clouds. *Journal of the atmospheric sciences*, 43(12), 1263-1274.
- Perminov, V. I., Semenov, A. I., Medvedeva, I. V., and Zheleznov, Y. A. (2014). Variability of mesopause temperature from the hydroxyl airglow observations over mid-latitudinal sites, Zvenigorod and Tory, Russia. *Advances in Space Research*.
- Peucker-Ehrenbrink, B. (1996). Accretion of extraterrestrial matter during the last 80 million years and its effect on the marine osmium isotope record. *Geochimica et Cosmochimica Acta*, 60(17), 3187-3196.
- Picone, J. M., Hedin, A. E., Drob, D. P., and Aikin, A. C. (2002). NRLMSISE-00 empirical model of the atmosphere: Statistical comparisons and scientific issues. *Journal of Geophysical Research: Space Physics (1978-2012)*, 107(A12), SIA-15.
- Plane, J., Gardner, C. S., Yu, J., She, C. Y., Garcia, R. R., and Pumphrey, H. C. (1999). Mesospheric Na layer at 40 N: Modeling and observations. *Journal of Geophysical Research: Atmospheres (1984-2012)*, 104(D3), 3773-3788.

- Plane, J. M. C. (2003). Atmospheric chemistry of meteoric metals. *Chemical Review*, *103*, 4963–4984. doi:10.1021/cr0205309
- Plane, J. M. C., Murray, B. J., Chu, X., and Gardner, C. S. (2004). Removal of meteoric iron on polar mesospheric clouds. *Science (New York, N.Y.)*, *304*(5669), 426–8.
- Plane, J. M. C. (2004). A time-resolved model of the mesospheric Na layer: constraints on the meteor input function. *Atmospheric Chemistry and Physics*, *4*(3), 627–638.
- Plane, J. M. C. (2012). Cosmic dust in the earth's atmosphere. *Chemical Society Reviews*, *41*(19), 6507–18. doi:10.1039/c2cs35132c
- Plane, J. M. C., Feng, W., Dawkins, E., Chipperfield, M. P., Höffner, J., Janches, D., and Marsh, D. R. (2014a). Resolving the strange behavior of extraterrestrial potassium in the upper atmosphere. *Geophysical Research Letters*, *41*(13), 4753–4760.
- Plane, J. M. C., Feng, W. and Dawkins, E. C. M., (2014b). Mesosphere and Metals: Chemistry and Changes. *Chemical Reviews*. Submitted: 4th September 2014.
- Poole, L. R., and McCormick, M. P. (1988). Polar stratospheric clouds and the Antarctic ozone hole. *Journal of Geophysical Research: Atmospheres (1984–2012)*, *93*(D7), 8423–8430.
- Portnyagin, Y. I., Merzlyakov, E. G., Solovjova, T. V., Jacobi, C., Kürschner, D., Manson, A., and Meek, C. (2006). Long-term trends and year-to-year variability of mid-latitude mesosphere/lower thermosphere winds. *Journal of Atmospheric and Solar-Terrestrial Physics*, *68*(17), 1890–1901.
- Qian, L., Laštovička, J., Roble, R. G., and Solomon, S. C. (2011). Progress in observations and simulations of global change in the upper atmosphere. *Journal of Geophysical Research*, *116*(January), A00H03.
- Qian, L., Solomon, S. C., and Roble, R. G. (2014). Secular changes in the thermosphere and ionosphere between two quiet Sun periods. *Journal of Geophysical Research: Space Physics*, *119*(3), 2013JA019438.

- Raizada, S., Tepley, C. A., Janches, D., Friedman, J. S., Zhou, Q., and Mathews, J. D. (2004). Lidar observations of Ca and K metallic layers from Arecibo and comparison with micrometeor sporadic activity. *Journal of Atmospheric and Solar-Terrestrial Physics*, 66(6-9), 595–606.
- Raizada, S., Rapp, M., Lübken, F.-J., Höffner, J., Zecha, M., and Plane, J. M. C. (2007). Effect of ice particles on the mesospheric potassium layer at Spitsbergen (78°N). *Journal of Geophysical Research*, 112(D8), D08307.
- Raizada, S., Tepley, C. A., Aponte, N., and Cabassa, E. (2011). Characteristics of neutral calcium and Ca⁺ near the mesopause, and their relationship with sporadic ion/electron layers at Arecibo. *Geophysical Research Letters*, 38(9).
- Raizada, S., Tepley, C. A., Williams, B. P., and García, R. (2012). Summer to winter variability in mesospheric calcium ion distribution and its dependence on Sporadic E at Arecibo. *Journal of Geophysical Research: Space Physics (1978–2012)*, 117(A2).
- Rishbeth, H., and Roble, R. G. (1992). Cooling of the upper atmosphere by enhanced greenhouse gases—modelling of thermospheric and ionospheric effects. *Planetary and space science*, 40(7), 1011-1026.
- Remsberg, E. E. (2007). A reanalysis for the seasonal and longer-period cycles and the trends in middle-atmosphere temperature from the Halogen Occultation Experiment. *Journal of Geophysical Research*, 112(D9), D09118.
- Remsberg, E. E. (2008). On the observed changes in upper stratospheric and mesospheric temperatures from UARS HALOE. *Annales Geophysicae*, 26, 1287–1297.
- Remsberg, E. E. (2009). Trends and solar cycle effects in temperature versus altitude from the Halogen Occultation Experiment for the mesosphere and upper stratosphere. *Journal of Geophysical Research*, 114(D12), D12303.

- Remsberg, E. E. (2010). Observed seasonal to decadal scale responses in mesospheric water vapor. *Journal of Geophysical Research*, 115(D6), D06306.
- Remsberg, E. E. (2014). Decadal-scale responses in middle and upper stratospheric ozone from SAGE II version 7 data. *Atmospheric Chemistry and Physics*, 14(2), 1039–1053.
- Roble, R. G., and Dickinson, R. E. (1989). How will changes in carbon dioxide and methane modify the mean structure of the mesosphere and thermosphere? *Geophysical Research Letters*, 16(12), 1441–1444.
- Rodgers, C. D. (1976). Retrieval of atmospheric temperature and composition from remote measurements of thermal radiation. *Reviews of Geophysics*, 14(4), 609-624.
- Rodgers, C. D. (1990). Characterization and error analysis of profiles retrieved from remote sounding measurements. *Journal of Geophysical Research: Atmospheres (1984–2012)*, 95(D5), 5587-5595.
- Rodgers, C. D. (2000). *Inverse methods for atmospheric sounding: theory and practice* (Vol. 2, p. 256). Singapore: World scientific.
- Rosenlof, K. H., Oltmans, S. J., Kley, D., Russell III, J. M., Chiou, E.-W., Chu, W. P., Johnson, D.G., Kelly, K.K., Michelsen, H.A., Nedoluha, G.E., Remsberg, E.E., Toon, G.C. and McCormick, M. P. (2001). Stratospheric water vapor increases over the past half-century. *Geophysical Research Letters*, 28(7), 1195–1198.
- Russell III, J. M., Rong, P., Hervig, M. E., Siskind, D. E., Stevens, M. H., Bailey, S. M., and Gumbel, J. (2014). Analysis of northern midlatitude noctilucent cloud occurrences using satellite data and modeling. *Journal of Geophysical Research: Atmospheres*, 119, 3238–3250.
- Saunders, R. W., Dhomse, S., Tian, W. S., Chipperfield, M. P., and Plane, J. M. C. (2012). Interactions of meteoric smoke particles with sulphuric acid in the Earth's stratosphere. *Atmospheric Chemistry and Physics*, 12(10), 4387-4398.

- Scharringhausen, M. (2007). *Investigation of mesospheric and thermospheric magnesium species from space* (Doctoral dissertation, Ph. D. thesis, University of Bremen, Institute of Environmental Physics).
- Scharringhausen, M., Aikin, A. C., Burrows, J. P., and Sinnhuber, M. (2008a). Spaceborne measurements of mesospheric magnesium species – a retrieval algorithm and preliminary profiles. *Atmospheric Chemistry and Physics*, 8(7), 1963–1983.
- Scharringhausen, M., Aikin, A. C., Burrows, J. P., and Sinnhuber, M. (2008b). Global column density retrievals of mesospheric and thermospheric Mg I and Mg II from SCIAMACHY limb and nadir radiance data. *Journal of Geophysical Research*, 113(D13), D13303.
- Schwarzkopf, M. D., and Ramaswamy, V. (2008). Evolution of stratospheric temperature in the 20th century. *Geophysical Research Letters*, 35(3), L03705.
- Schoeberl, M. R., Strobel, D. F., and Apruzese, J. P. (1983). A numerical model of gravity wave breaking and stress in the mesosphere. *Journal of Geophysical Research: Oceans (1978–2012)*, 88(C9), 5249-5259.
- Semenov, A. I., Shefov, N. N., Lysenko, E. V., Givishvili, G. V., and Tikhonov, A. V. (2002). The season peculiarities of behaviour of the long-term temperature trends in the middle atmosphere on the mid-latitudes. *Physics and Chemistry of the Earth, Parts A/B/C*, 27(6), 529-534.
- She, C. Y., *et al.* (2006). Simultaneous observation of sodium atoms, NLC and PMSE in the summer mesopause region above ALOMAR, Norway (69° N, 12° E). *Journal of Atmospheric and Solar-Terrestrial Physics*, 68(1), 93-101.
- She, C.-Y., Krueger, D. A., Akmaev, R., Schmidt, H., Talaat, E., and Yee, S. (2009). Long-term variability in mesopause region temperatures over Fort Collins, Colorado (41°N, 105°W) based on lidar observations from 1990 through 2007. *Journal of Atmospheric and Solar-Terrestrial Physics*, 71(14-15), 1558–1564.

- Shettle, E. P., DeLand, M. T., Thomas, G. E., and Olivero, J. J. (2009). Long term variations in the frequency of polar mesospheric clouds in the Northern Hemisphere from SBUV. *Geophysical Research Letters*, 36(2).
- Sigernes, F., Shumilov, N., Deehr, C. S., Nielsen, K. P., Svenøe, T., and Havnes, O. (2003). Hydroxyl rotational temperature record from the auroral station in Adventdalen, Svalbard (78°N, 15°E). *Journal of Geophysical Research: Space Physics*, 108(A9), 1342.
- Simonich, D. M., Clemesha, B. R., and Kirchoff, V. W. J. H. (1979). The mesospheric sodium layer at 23 S: Nocturnal and seasonal variations. *Journal of Geophysical Research: Space Physics (1978–2012)*, 84(A4), 1543-1550.
- Sioris, C. E., and Evans, W. F. (1999). Filling in of Fraunhofer and gas-absorption lines in sky spectra as caused by rotational Raman scattering. *Applied Optics*, 38(12), 2706-2713.
- Slipher, V. M. (1929). Emissions in the spectrum of the light of the night sky. *Publ. Astron. Soc. Pac*, 41, 262-263.
- Sloan, L. C., and Pollard, D. (1998). Polar stratospheric clouds: A high latitude warming mechanism in an ancient greenhouse world. *Geophysical Research Letters*, 25(18), 3517-3520.
- Smirnova, M., Belova, E., Kirkwood, S., and Mitchell, N. (2010). Polar mesosphere summer echoes with ESRAD, Kiruna, Sweden: Variations and trends over 1997–2008. *Journal of Atmospheric and Solar-Terrestrial Physics*, 72(5), 435-447.
- Solomon, S., Garcia, R. R., Rowland, F. S., and Wuebbles, D. J. (1986). On the depletion of Antarctic ozone. *Nature*, 321(6072), 755-758.
- Solomon, S., and Chanin, M. L. (2011). The Antarctic ozone hole: a unique example of the science and policy interface. *Science Diplomacy: Antarctica, Science, and the Governance of International Spaces*, 189-196.

- Sprenger, K., and Schindler, R. (1969). Solar cycle dependence of winds in the lower ionosphere. *Journal of Atmospheric and Terrestrial Physics*, 31(1), 217–221.
- Sridharan, S., Vishnu Prasanth, P., and Bhavani Kumar, Y. (2009). A report on long-term trends and variabilities in middle atmospheric temperature over Gadanki (13.5° N, 79.2° E). *Journal of Atmospheric and Solar-Terrestrial Physics*, 71(13), 1463-1470.
- Strong, K., *et al.* (2002). Retrieval of vertical concentration profiles from OSIRIS UV visible limb spectra. *Canadian Journal of Physics*, 80(4), 409-434.
- Sullivan, H. M., and Hunten, D. M. (1964). Lithium, sodium, and potassium in the twilight airglow. *Canadian Journal of Physics*, 42(5), 937-956.
- Summers, M. E., and Siskind, D. E. (1999). Surface recombination of O and H₂ on meteoric dust as a source of mesospheric water vapor. *Geophysical Research Letters*, 26(13), 1837-1840.
- Thayer, J. P., Thomas, G. E., and Lübken, F. J. (2003). Foreword: Layered phenomena in the mesopause region. *Journal of Geophysical Research: Atmospheres* (1984–2012), 108(D8).
- Thayer, J. P., and Pan, W. (2006). Lidar observations of sodium density depletions in the presence of polar mesospheric clouds. *Journal of Atmospheric and Solar-Terrestrial Physics*, 68(1), 85-92.
- Thomas, G. E., Olivero, J. J., Jensen, E. J., Schroeder, W., and Toon, O. B. (1989). Relation between increasing methane and the presence of ice clouds at the mesopause. *Nature*, 338(6215), 490–492.
- Thomas, G. E., and Olivero, J. (2001). Noctilucent clouds as possible indicators of global change in the mesosphere. *Advances in Space Research*, 28(7), 937-946.
- Thomas, G. E. (2003). Are noctilucent clouds harbingers of global change in the middle atmosphere?. *Advances in Space Research*, 32(9), 1737-1746.

- Venkat Ratnam, M., Kishore Kumar, G., Venkateswara Rao, N., Krishna Murthy, B. V., Laštovička, J., and Qian, L. (2013). Evidence of long-term change in zonal wind in the tropical lower mesosphere: Observations and model simulations. *Geophysical Research Letters*, 40(2), 397-401.
- von Cossart, G., Fiedler, J., Von Zahn, U., Hansen, G., and Hoppe, U. P. (1997). Noctilucent clouds: One-and two-color lidar observations. *Geophysical Research Letters*, 24(13), 1635-1638.
- von Zhan, U. and Hansen, T.L. (1988). Sudden neutral sodium layers: a strong link to sporadic E layers. *Journal of Atmospheric and Terrestrial Physics*, 50(2):93-104.
- von Zahn, U., and Murad, E. (1990). NaHCO₃: A source of Na atoms for sudden sodium layers?. *Geophysical research letters*, 17(2), 147-149.
- von Zahn, U., and Höffner, J. (1996). Mesopause temperature profiling by potassium lidar. *Geophysical Research Letters*, 23(2), 141-144.
- von Zahn, U. (2003). Are noctilucent clouds a “Miner's Canary” for global change?. *EOS, Transactions American Geophysical Union*, 84(28), 261-264.
- Vondrak, T., Plane, J. M. C., Broadley, S., & Janches, D. (2008). A chemical model of meteoric ablation. *Atmospheric Chemistry and Physics*, 8(23), 7015-7031.
- Warshaw, G., Desaulniers, D. L., and Degenstein, D. (1996). Optical design and performance of the Odin UV/visible spectrograph and infrared imager instrument.
- Wickwar, V. B., Taylor, M. J., Herron, J. P., and Martineau, B. A. (2002). Visual and lidar observations of noctilucent clouds above Logan, Utah, at 41.7 N. *Journal of Geophysical Research: Atmospheres (1984–2012)*, 107(D7), ACL-2.
- Willson, R. C., and Hudson, H. S. (1991). The Sun's luminosity over a complete solar cycle. *Nature*, 351(6321), 42-44.
- Willson, R. C. (2014). ACRIM3 and the Total Solar Irradiance database. *Astrophysics and Space Science*, 352:341-352.

- Wu, D. L., Ao, C. O., Hajj, G. A., de La Torre Juarez, M., and Mannucci, A. J. (2005). Sporadic E morphology from GPS-CHAMP radio occultation. *Journal of Geophysical Research: Space Physics (1978–2012)*, 110(A1).
- Xu, J., *et al.* (2007). Mesopause structure from Thermosphere, Ionosphere, Mesosphere, Energetics, and Dynamics (TIMED)/Sounding of the Atmosphere Using Broadband Emission Radiometry (SABER) observations. *Journal of Geophysical Research: Atmospheres*, 112(D9), D09102.
- Zhou, Q., Mathews, J. D., and Tepley, C. A. (1993). A proposed temperature dependent mechanism for the formation of sporadic sodium layers. *Journal of Atmospheric and Terrestrial Physics*, 55(3), 513-521.